Dissertation
submitted to the
Combined Faculties of the Natural Sciences and for Mathematics
of the Ruperto-Carola University of Heidelberg, Germany
for the degree of
Doctor of Natural Sciences

Put forward by
Dipl.-Phys. Holger Gerhards
Born in Köthen, Germany

Oral examination: 30.10.2008

Ground Penetrating Radar as a Quantitative Tool with Applications in Soil Hydrology

Referees: Prof. Dr. Kurt Roth

Prof. Dr. Bernd Jähne

Kurzfassung

Diese Arbeit beschäftigt sich mit der Erkundung der Georadar-Methode im Hinblick auf die Anwendbarkeit in der Hydrologie oberflächennaher Bodenschichten. Die Motivation besteht darin, die Grenzen der Auswertbarkeit von Georadarmessungen zu erweitern, weswegen ein detaillierter Überblick der Ausbreitung elektromagnetischer Wellen gegeben wird. Begonnen wird hierbei mit einer Einführung in die theoretischen und experimentellen Beschreibungsmöglichkeiten der relevanten dielektrischen Materialeigenschaften. Fortgesetzt wird dies mit einer Übersicht verschiedener Simulationsansätze in der Elektrodynamik, welche sich in ihrer physikalischen Komplexität unterscheiden. So wird der Strahlenansatz, die Beschreibung durch ebene Wellen sowie die Anwendung von Greenschen Funktionen vorgestellt, wobei letzteres an einen vertikalen Dipol in einem horizontal geschichteten Medium angepaßt ist. Mit diesen Modellansätzen werden einige spezielle Sachverhalte der Wellenausbreitung in der Elektrodynamik beleuchtet. So zum Beispiel, wird die Reflektion von und die Brechung an kontinuierlichen dielektrischen Übergängen analysiert, die zum Beispiel durch die Wasserverteilung im Boden herrühren können. Weiterhin wird die Bodenwelle hinsichtlich ihrer evaneszenten Eigenschaften untersucht. Diese treten auf, wenn die Bodenwelle in den Luftraum einkoppelt. Als Resultat der theoretischen Betrachtungen werden zwei neue Messmethoden und deren Auswertbarkeit vorgestellt. Eine Messmethode stellt die Anhebemessung dar, welche die Detektion von evaneszenten Wellen erlaubt. Die zweite Messtechnik ist die Mehrkanalmethode, welche einen gleichzeitigen Zugriff auf die Reflektortiefe und den mittleren Wassergehalt auf Messstrecken über mehrer hundert Meter bietet.

Abstract

This work concentrates on the investigation of ground penetrating radar (GPR) with respect to applications in soil hydrology. The motivation is to expand the boundaries of processability and evaluability of GPR measurements. Therefore, a detailed review of the fundamentals for electromagnetic wave propagation is given. First, theoretical and experimental descriptions of the dielectric material models are introduced. This is followed by an overview of different modeling approaches in electrodynamics which differ in their physical complexity. The ray approach, a plane wave description and a Green's function approach are presented, where the last simulates a vertical dipole in a horizontally layered medium. With the help of these modeling approaches, some specific electromagnetic wave phenomena are studied. For instance the reflection and the refraction at continuously varying dielectric properties are analyzed, which can stem for example from the water distribution in soils. Furthermore, the ground wave is studied regarding its evanescent wave behavior. This can be observed, when the wave couples into the air. As an outcome of the theoretical considerations, two novel measurement techniques and their evaluation approaches are presented. One technique is the lift measurement, which enables the detection of evanescent waves. The other technique is the multi-channel method, which allows a simultaneous access to reflector depth and average water content up to several hundred meters.

Contents

1 Introduction **1**
1.1 Introduction to Soil Hydrology . . . 1
1.2 Introduction to Ground Penetrating Radar . . . 2
1.3 Outline . . . 3
1.4 Advises for the Reader . . . 4

2 Material Models **7**
2.1 Dielectric Properties - A General Description . . . 7
2.1.1 Dielectric Permittivity . . . 7
2.1.2 Electric Conductivity . . . 10
2.2 Dielectric Properties of Soils . . . 12
2.2.1 Dielectric Mixing Models . . . 13
2.2.2 Dielectric Permittivity Functions for Specific Media . . . 16
2.3 Water Content Distribution in Soils . . . 19
2.3.1 Short Introduction to Soil Physics . . . 19
2.3.2 Description of the Capillary Fringe . . . 20

3 Electromagnetic Theory - Modeling Approaches **23**
3.1 Introduction / Overview . . . 23
3.2 Travel Path Analysis using the Ray Approach . . . 24
3.2.1 Analytical Solutions for Few Layer Setups . . . 25
3.2.2 Multi-Layer Modeling . . . 28
3.3 Plane Wave Descriptions . . . 32
3.3.1 Propagation in Homogeneous Media . . . 32
3.3.2 Reflection and Transmission at a Sharp Dielectric Transition . . . 33
3.3.3 Multi-Layer Modeling . . . 35
3.4 Near Field Analysis / Greens Function Approach . . . 39
3.5 Multi-Layer Model Validation . . . 43
3.5.1 Plane Wave Modeling . . . 43
3.5.2 Green's Approach Modeling . . . 45

4 Ground Penetrating Radar - Basics **47**
4.1 Measurement Principle . . . 47
4.2 Standard Measurement Techniques . . . 49
4.2.1 Surface Ground Penetrating Radar . . . 49
4.3 Origination of Ground Penetrating Radar Signals . . . 52
4.3.1 Travel Paths in Ground Penetrating Radar Applications . . . 52
4.3.2 Attenuation and Absorption of Electromagnetic Waves . . . 55
4.3.3 Propagation in Dispersive Media . . . 56
4.3.4 Refraction at Sharp and Smooth Permittivity Changes . . . 59
4.3.5 Reflection from Sharp and Smooth Permittivity Changes . . . 63
4.3.6 Evanescent Waves . . . 74

4.4 Pre-Processing and Filtering Procedures 78
4.4.1 Amplification / Gain 79
4.4.2 Runmean-Filter 79
4.4.3 Dewow-Filter 80
4.4.4 Gauss-Filter 82
4.4.5 Ringing Removal 82
4.5 Processing Procedures 85
4.5.1 Time Zero Correction 85
4.5.2 Normal Moveout Correction 91
4.5.3 Windowed Fourier Analysis 96
4.5.4 Evanescent Wave Evaluation / Ground Wave Evaluation 99

5 Multi-Channel Ground Penetrating Radar 107
5.1 Overview / Introduction 107
5.2 Multi-Channel Technique and Evaluation 108
5.2.1 Measurement Technique 108
5.2.2 Two-Point Evaluation of the Multi-Channel Measurement 108
5.2.3 Multi-Point Evaluation of the Multi-Channel Measurement 109
5.2.4 Multi-Layer Evaluation 110
5.2.5 Inverse estimation of reflector depth: Synthetic Example 111
5.2.6 Air Wave Adaption Method 113
5.2.7 Application of the Air Wave Adaption Method 115
5.2.8 Synthetic Example for the Multi-Layer Evaluation 116
5.3 Multi-Channel Surveys 118
5.3.1 Single-Layer Example from the Tibetan Plateau 118
5.3.2 Two-Layer Example from the Tibetan Plateau 121
5.3.3 Multi-Layer Evaluation from the Hirschacker Testsite 124

6 Summary 129

A Calculations and Derivations I
A.1 Small Calculations I
A.1.1 Travel Time from a Dipping Reflector I
A.1.2 Attenuation of Plane Waves III
A.2 Hertzian Potential and Hertzian Dipole III

Bibliography IX

1 Introduction

> Each day is a little life; every waking and rising a little birth; every fresh morning a little youth; every going to rest and sleep a little death.
>
> *(Arthur Schopenhauer)*

1.1 Introduction to Soil Hydrology

Soil hydrology describes a scientific field, which focuses primarily on water distribution and water movement in soils. This research can be done on almost all scales. For instance, the near surface water content at scales of a few tenth square meters is relevant for the contamination processes of the groundwater. For several hundreds of square meter, the near surface water content distribution is relevant for agricultural purposes as well as for local climatic conditions. At a regional scale, the groundwater flow and the groundwater recharge is important for urban managements, for example. This results from the importance of groundwater as a source for drinking water. But the near surface water is also of high significance at the global scale. Because of its properties as an energy storage, it drastically determines extended climatic conditions. For instance, the dramatical day and night time temperature changes in deserts compared to the temperate zone can be traced back to the lack of water. One determining factor is the evaporation of the water at the soil surface in the daytime. This leads to a cooling of the soil surface. Therefore, the soil surface temperature becomes not as hot as without water. Furthermore, the water in the soils stores the thermal energy in the daytime. In the nighttime, this energy is emitted again.

Another aspect of water in soils can be found in permafrost regions. In high latitude regions, the annual freezing and thawing of the upper soil, makes every kind of surface feature unstable and fragile. In regions of high altitude permafrost, such as the Tibetan Plateau, the permafrost conditions led to a compact layer of frozen ground in a depth of a few meters. This frozen layer prevents infiltrating water from runoff processes through the subsurface rock formations. Therefore, the water stays near the surface. This conditions vegetation, which influences the nutrition of animals and men. Especially on the Tibetan Plateau, this frozen layer is melting due to increasing temperatures resulting from climate change. Therefore, the whole environmental system is changing in these regions, which is not invertible.

All these examples for the significance of the water in soils show the necessity of its determination and quantification. Analogous to almost all environmental research activities, this quantification can log a status of an environmental system. It can also help to predict the development of this system.

The measurement of the water content in soils and the distribution of the water content is done by geophysical methods. For almost all scales, measurement techniques or at least measurement approaches exist. For localized water content measurements at scales up to several decimeters, one can use gravimetric measurements or time domain reflectometry, for instance. In laboratory experiments, X-ray tomography, the nuclear magnetic reso-

nance (NMR) method or neutron probes can be used to obtain the moisture content of an extracted soil sample. At larger scales up to several hundred meters, one can either use seismic applications or ground penetrating radar. For scales of some kilometers, remote sensing measurements are applied, which are provided by airborne or satellite techniques.

1.2 Introduction to Ground Penetrating Radar

A General Perspective

Ground Penetrating Radar (GPR) is a measurement device. Its advantage is the controlled radiation and measurement of free electromagnetic waves. This enables a GPR operator to a remote access to structures, objects and material properties of interest. One could directly imagine applications in archaeology, forensic research or for landmine detection. But also researchers in sedimentology, permafrost studies, glaciology and hydrology are interested in this measurement device. They all need an insight into the subsurface, which should be fast and non-invasive. The same properties are also recommended in engineering fields, which analyze the state of buildings, bridges, motorways, dikes or waste disposal sites.

Although this list of possible and actual application fields is not complete, one statement should be made. Common GPR methods are not capable to detect either oil deposits[1] or to scan the Earth's deep interior. Both legitimate research questions often occur in discussions with outsiders. This at least evokes further questions: "What can be resolved with GPR measurements?" and "What are the restrictions and limits of this method?". Furthermore, one can ask: "What is the difference between GPR and seismics?", because seismic research is capable to analyze the earth interior and to detect oil?"

All these questions give a glimpse, why there is a whole research field on this measurement device. The answers for all these upcoming questions should not only address the measurement parameters, but also the basic physical effects of electromagnetic wave propagation.

Under these aspects of electromagnetic wave propagation, GPR studies are embedded in the much more general research field of electrodynamics. For instance, the interaction of the electromagnetic fields with materials and the propagation of the waves through inhomogeneous media is studied. But Maxwell's equations are not restricted to any spatial or temporal scale. Under this perspective, any research field dealing with electromagnetic waves in a given frequency range can benefit from the research in other fields with a different frequency spectrum. Only the material properties and the relevant structures must be adapted to the corresponding application. For example, GPR applications can profit from the pioneering work in optics, but also from the research on radio waves.

Ground Penetrating Radar Applications and Promises

GPR is highly demanded in hydrological research questions. This stems from the dielectric properties of the involved materials: air, water and the soil matrix in the frequency spectrum of GPR. Frequencies between 10 MHz to 1 GHz are mainly applied. In this range, the air and the soil matrix have a relative permittivity value, which is low in comparison to water ($\varepsilon_{air} = 1$, $\varepsilon_{matrix} \approx 5$, $\varepsilon_{water} \approx 80$). This relative permittivity determines the

[1] Actually, there were ideas given by Löwy (1927), who proposed to use electromagnetic waves for the detection of oil reservoirs, but there are no realizations of these ideas.

propagation velocity of electromagnetic waves and therefore the travel times, which are measured with GPR.

GPR applications can be found on measurement scales between a few tens of meters up to several hundred meters. Standard measuring devices provide a scanning depth between a few to several tens of meter. This depth depends on the clay, water, iron and salt content, but also on the used frequencies. In arid regions, for instance, the scanning depth can be much higher corresponding to the soils of the temperate zone. The absorbing properties of the soil in arid regions are much lower due to the lack of water. Otherwise, high surface salt concentrations can also totally prohibit any GPR application. The other limit for the scanning depth is the bedrock of the antarctic continent, which can be detected under the ice of a thickness between one or two kilometers.

As already indicated by the title, this work focuses on GPR applications in soil hydrology. Because of its usage for scales up to several hundred meters, this method is situated between local water content measurements and remote sensing techniques, such as airborne or satellite measurements. With respect to its application scale, it provides promises for calibration and upscaling techniques. In this context, calibration means that airborne or satellite remote sensing measurements can be calibrated due to the water content with the help of GPR. For this purpose, the ground wave[2], which is observed in GPR applications, and its influence depth is studied in detail. The abstract concept of upscaling techniques means that projections of hydrological properties to larger scales are examined. Typically, these hydrological properties are either determined in laboratory experiments or on localized points at a test field. An instrumentation of a whole test field for the determinations of the hydraulic properties with standard methods would be too expensive. Therefore, the remote detection of soil boundary layers and the water content distribution promise the determination of effective hydraulic properties at the field scale.

1.3 Outline

This work is structured in four main chapters framed by an introduction and a summary chapter. The content of these chapters are shortly sketched in the following.

Chapter 2 - Material Models: Theoretical and experimental descriptions of dielectric properties are presented. The focus lies on the relative permittivity and the conductivity. Furthermore, mixing models are considered. They provide a conversion of a water content values into a relative permittivity value, which determines the propagation of electromagnetic waves. At last, a short introduction into soil physics is given, which can predict the water content distribution in porous media.

Chapter 3 - Modeling Approaches: This this chapter, three different electromagnetic modeling approaches are presented: a ray approach, a plane wave description and a Green's function approach. These methods are set up for the simulation of electromagnetic wave propagation in layered media. The content can be considered as a toolbox for all further discussions on GPR. It contains the main theory for the mathematically interested reader. Therefore, this chapter itself gives no insights for GPR applications.

Chapter 4 - Ground Penetrating Radar: A detailed overview of the aspects concerning GPR applications in soil hydrology is given. The measurement principle and different measurement techniques are presented. Then, a set of electromagnetic wave

[2]The ground wave is a characteristic wave, which propagates in the ground parallel to the surface.

phenomena is discussed, which influences the results of GPR measurements. For instance, the reflection and refraction at sharp and smooth dielectric transitions are analyzed. Furthermore, the ground wave with respect to its evanescent wave behavior in air is studied. At last, some filter routines for measured GPR signals and some processing methods of different GPR techniques are examined. Such a processing method is the analysis of lift measurements, which provides the detection of waves with an evanescent wave behavior. But also the normal moveout method, which is adapted from seismic applications for GPR measurements, is presented.

Chapter 5 - Multi-Channel GPR: The multi-channel GPR technique and its evaluation procedure is presented. This evaluation procedure is based on an inversion algorithm, which compares measured with modeled ray approach travel times for dipping reflectors. This method is analyzed with synthetic but also with experimental examples. These experiments show a glimpse of the diversity of the subsurface structure and the water content distribution.

1.4 Advises for the Reader

Advises for Text Reading

If you are only interested in the major outcomes, then you are referred to the summary. But you are also invited to read the small closing outcome subsections. They can be found in framed boxes and only for selected topics. They shall highlight the important findings without reading the whole section.

If you are generally interested in GPR, then you are referred to Chapter 4 and 5. Especially, Chapter 4 is considered as a list of aspects on GPR. Here, the most sections should be understandable without reading the previous. At some places, you can find an outcome subsection in a framed box. You can use them to decide to read in more detail or to jump to the next aspect. Chapter 5 gives a detailed introduction to the multi-channel analysis, which was developed in this thesis. In the experiments section 5.3, you can obtain an overview of the possibilities of this method, but you should read at least Sec. 5.2.3 to get the main ideas of the evaluation concept.

If you are interested in the material models related to GPR studies, then you are referred to Chapter 2. Here, you will find a general description for the dielectric permittivity and the electric conductivity. This description shall give the major aspects to understand the physical background for both values. Afterwards, the dielectric permittivity for soils is analyzed. This chapter closes with an introduction to soil physics, which explains dielectric permittivity gradients and permittivity jumps in soils.

If you are interested in simulation tools for GPR, then Chapter 3 is the right address. Here, the reader should use some scratch paper and a pencil to follow the derivations and calculations. The aim of this chapter is that the reader gets acquainted with each method and that he could implement the approach himself.

Mathematical Formalism

An overview of all used variables and substitutions is omitted in this thesis, because this list would not be instructive. Furthermore, some symbols have multiple meanings depending on the context. In order to understand the mathematics without a detailed reading, one has to look in the proximity of the formulas, where in the most cases the symbols are explained. If not, one has to look in the surrounding of the previous formulas.

In the text, some general conventions for the notation are used:

- Scalars are written as cursive letters (e.g. t for the time).
- Vectors are bold written (e.g. $\mathbf{E}$ for the electric field). The components of the vector are given as cursive letters with an index. This index can represent the component of the 3D-domain, such as E_x for the x-component of the electrical field. It also can be represented as an integer value, such as n_i, which is the ith component of the vector $\mathbf{n}$.
- Matrices are bold written with an extra underline (e.g. $\underline{\mathbf{g}}$ for the Dyadic Green's function).
- A derivative of a function $f(x)$ after the variable x is written as $\partial_x f$. The second derivative of a function $g(x, y)$ after the variales x and y is given as $\partial^2_{x,y} g(x, y)$. Throughout the text, this notation can be considered as a partial derivative. An absolute derivative assuming implicit functionalities does not occur.
- Fourier-transformed quantities are not marked separately. They are indicated by the variables the function depends on. For example the Fourier-transformation of a function $f(t)$ yields $f(\omega)$.
- The speed of light in vacuum is always notated as c_0.
- The imaginary unit $\sqrt{-1}$ is always given as $\mathtt{i}$.
- For the summation over two integers, a special abbreviation was used in Chapter 5:

$$\sum_{(l,k)}^{(L,K)} \ldots := \sum_{l=1}^{L} \sum_{k=1}^{K} \ldots$$

- For every other unusual notation, the reader is referred to its first occurrence. If it is not explained their, then the author might have forgotten it. Sorry, if this happen.

Abbreviations in the Text

There are only a few abbreviations in the text, which occur very often. Here is an overview:

CMP:	Common Midpoint (Measurement)
GPR:	Ground Penetrating Radar
TDR:	Time Domain Reflectometry
TE:	Transversal Electric
TM:	Transversal Magnetic
WARR:	Wide Angle Reflection and Refraction (Measurement)

2 Material Models

2.1 Dielectric Properties - A General Description

In order to describe electromagnetic phenomena, at least three material properties are required: the conductivity σ, the permeability μ and the permittivity ε. While the permeability is a quantity of the magnetization of the material, the permittivity is a quantity for the polarization. Furthermore, the conductivity can be traced back to the movement of free charges.

In the following, a closer view on the permittivity and the conductivity will be given, but a discussion concerning the permeability is neglected. A reason for this is that the permeability is only a function of frequency for magnetizable media, otherwise it is near the free space permeability. In soils a magnetization occurs for a significant amount of iron content (Olhoeft and Capron, 1994), which is not considered in the context of this work.

2.1.1 Dielectric Permittivity

The dielectric permittivity can be recognized as a result of the polarizability of the medium, which could be associated with the movement of bounded charges in an oscillating electric field[1]. This can be illustrated by the following derivation, which gives an impression of the physical background.

The derivation shall start from Ampère's law in the time domain given as

$$\nabla \times \mathbf{H}(\mathbf{r}, t) = \mathbf{J}(\mathbf{r}, t) \quad , \tag{2.1}$$

which links the magnetic field $\mathbf{H}$ with the current density $\mathbf{J}$. Assuming an oscillating field, the current density can stem from free moving charge carriers $\mathbf{J}_{\text{free}}$ or from the movement of bounded charges $\mathbf{J}_{\text{bound}}$. The term for the bounded charges can be given as the temporal change of the displacement current $\mathbf{D}$, which leads to a general current density

$$\mathbf{J}(\mathbf{r}, t) = \mathbf{J}_{\text{free}}(\mathbf{r}, t) + \partial_t \mathbf{D}(\mathbf{r}, t) \quad . \tag{2.2}$$

Now, this displacement current is written as

$$\mathbf{D}(\mathbf{r}, t) = \varepsilon_0 \, \mathbf{E}(\mathbf{r}, t) + \mathbf{P}(\mathbf{r}, t) \quad . \tag{2.3}$$

which is a function of the electric field $\mathbf{E}$ and the polarization $\mathbf{P}$, which is induced by the electric field. This polarization describes the effect of displaced charges due to electric fields, but which can also be caused by magnetic fields. In most cases, the effect of the magnetic field is neglected. Furthermore, the response due to the polarization induced by an incoming electric field is assumed to be linear, which is only violated in the research field

[1] Here, the oscillation and rotation of molecules will be subsumed under the aspect of the movement of bounded charges.

of high energy laser physics. This response of the polarization need not to be instantaneous and it can have an aftereffect, which leads to a general description given as

$$\mathbf{P}(\mathbf{r},t) = \int_{-\infty}^{t} R(\mathbf{r},t-t')\,\mathbf{E}(\mathbf{r},t')\,dt' \quad , \tag{2.4}$$

which is a convolution of a response function R and the electric field.

This expression leads to a simple product in the frequency domain, which yields

$$\mathbf{P}(\mathbf{r},\omega) = \chi(\mathbf{r},\omega)\,\mathbf{E}(\mathbf{r},\omega) \quad , \tag{2.5}$$

where χ represents the Fourier transformation of the response function R. Then, Eq. (2.3) leads in the frequency domain with Eq. (2.5) to

$$\mathbf{D}(\mathbf{r},\omega) = \varepsilon_0\,\big(1+\chi(\mathbf{r},\omega)\big)\,\mathbf{E}(\mathbf{r},\omega) = \varepsilon_0\,\varepsilon(\mathbf{r},\omega)\,\mathbf{E}(\mathbf{r},\omega) \quad . \tag{2.6}$$

Here, $\varepsilon(\mathbf{r},\omega) := 1+\chi(\mathbf{r},\omega)$ is defined as the relative permittivity of the medium.

This relative permittivity gives a quantity for the energy storage of the medium, because a higher value denotes a higher polarization, which indicates a higher energy storage. Furthermore, the transformation of the response function into frequency domain only yields a constant, when the polarization reacts instantaneously on the incoming field without any aftereffect. Otherwise, the relative permittivity is a complex function of frequency ν, which can be written as a function of angular frequency $\omega = 2\,\pi\,\nu$ given as

$$\varepsilon(\omega) = \varepsilon'(\omega) - \mathtt{i}\,\varepsilon''(\omega) \quad , \tag{2.7}$$

where ε' and ε'' are the real and the imaginary part of the permittivity, respectively. This relationship indicates that both parts can vary individually, but for all linear materials, they are linked with each other by the Kramers-Kronig-relationship, which is given among others in Cole and Cole (1941). Here, a linear material denotes that Eq. (2.4) is valid.

Description of the Relative Permittivity

An equation for the complex dielectric permittivity as a function of the angular frequency ω, which fulfills the Kramers-Kronig-relationship, is given by Debye (1929)

$$\varepsilon(\omega) = \varepsilon_\infty + \frac{\varepsilon_{\text{stat}} - \varepsilon_\infty}{1+\mathtt{i}\,\omega\,\tau_{\text{rel}}} \quad , \tag{2.8}$$

where $\varepsilon_{\text{stat}}$, ε_∞ and τ_{rel} are the static dielectric permittivity at low frequencies, the dielectric permittivity at high frequencies[2] and the relaxation time. This equation can be deduced by the assumption that an incoming electric field causes an instantaneous polarization increase and an exponential decay with time, which is called dielectric aftereffect (Wagner, 1913, 1914). At the relaxation time τ_{rel} the polarization decayed to a relative value of $1/e$. Furthermore, at the relaxation frequency $\nu_{\text{rel}} = (2\,\pi\,\tau_{\text{rel}})^{-1}$ the imaginary part of the permittivity function has its maximum.

For most polar liquids a single relaxation exists in specific frequency ranges (Cole and Cole, 1941). Here, a single relaxation can be interpreted as a single oscillator system within the medium. For other liquids and solids, Eq. (2.8) is not valid (Cole and Cole, 1941). In this case, multiple oscillator systems within the same frequency range can be found. If they are separated, Eq. (2.8) can be extended as a sum of discrete relaxations

$$\varepsilon(\omega) = \varepsilon_\infty + (\varepsilon_{\text{stat}} - \varepsilon_\infty)\sum_i \frac{\gamma_i}{1+\mathtt{i}\,\omega\,\tau_i} \quad \text{with} \quad 1 = \sum_i \gamma_i \quad . \tag{2.9}$$

[2]Here, low and high frequencies mean a low or high frequency limit of the considered range.

Here, $\gamma_i \in [0,1]$ are weights for the ith relaxation with the relaxation time τ_i.

Depending on the internal structure of the material and the energy states within, there might be a continuous distribution of relaxation times (Sposito and Prost, 1982). This is described by the Cole-Cole-model (Cole and Cole, 1941)

$$\varepsilon(\omega) = \varepsilon_\infty + \frac{\varepsilon_{\text{stat}} - \varepsilon_\infty}{1 + (\mathtt{i}\,\omega\,\tau_{\text{rel,c}})^{1-\alpha}} \quad , \tag{2.10}$$

where $\tau_{\text{rel,c}}$ is the Cole-Cole relaxation time and α is a measure of the distribution of the relaxation times (Sposito and Prost, 1982). Originally, this equation was set up, because there were a lot of experimental data, which did not fit the Debye-model.

Although, Eq. (2.8) and Eq. (2.10) represent the historical roots for the description of the complex relative permittivity, there are some further models, which can be used. One class of models are modified Cole-Cole-relationships, such as the Cole-Davidson or Gavril'yak-Negami function (Nigmatullin and Ryabov, 1997). Another model is called Jonscher model (Jonscher, 1977; Grégoire and Hollender, 2004).

Generalized Dielectric Permittivity

The derivation for the relative dielectric permittivity was based on the response of the material due to an internal polarization, but current densities, which result from free charge carriers were neglected. This effect can also be included into a generalized dielectric permittivity function. Its derivations uses Eq. (2.1) in frequency domain together with Eq. (2.2), which yields

$$\nabla \times \mathbf{H}(\mathbf{r},\omega) = \mathbf{J}_{\text{free}}(\mathbf{r},\omega) + \mathtt{i}\,\omega\,\mathbf{D}(\mathbf{r},\omega) \quad . \tag{2.11}$$

This current density $\mathbf{J}_{\text{free}}$ is a result of the movement of charges due to a local electric field. When these charges can move freely in all directions, which means that there are no barriers within the moving distance, then the current density and the electric field point in the same direction. Here, the moving distance depends on the frequency of the electric field, the field strength and the energetic surrounding of the charges. Now, with the assumption that the electric field and the current density are proportional to each other, this leads to Ohm's law

$$\mathbf{J}_{\text{free}}(\mathbf{r},\omega) = \sigma(\mathbf{r},\omega)\,\mathbf{E}(\mathbf{r},\omega) \quad , \tag{2.12}$$

where the proportionality constant σ denotes the conductivity. In general, the conductivity can also be a complex function of frequency. Then, Eq. (2.11) leads with (2.6) and (2.12) to

$$\nabla \times \mathbf{H}(\mathbf{r},\omega) = \left[\,\sigma(\mathbf{r},\omega) + \mathtt{i}\,\omega\,\varepsilon_0\,\varepsilon(\mathbf{r},\omega)\,\right]\,\mathbf{E}(\mathbf{r},\omega) = \mathtt{i}\,\omega\,\varepsilon_0\,\varepsilon_{\text{gen}}(\mathbf{r},\omega)\,\mathbf{E}(\mathbf{r},\omega) \quad , \tag{2.13}$$

where ε_{gen} denotes the general relative permittivity function given as

$$\varepsilon_{\text{gen}}(\mathbf{r},\omega) = \frac{\sigma(\mathbf{r},\omega)}{\mathtt{i}\,\omega\,\varepsilon_0} + \varepsilon(\mathbf{r},\omega) \quad . \tag{2.14}$$

With respect to Eq. (2.13), a general conductivity function σ_{gen} can also be defined as

$$\sigma_{\text{gen}}(\mathbf{r},\omega) = \sigma(\mathbf{r},\omega) + \mathtt{i}\,\omega\,\varepsilon_0\,\varepsilon(\mathbf{r},\omega) \quad . \tag{2.15}$$

This shows that a conductivity and relative permittivity can be used congruently. By separating both values, it depends on the definition, which physical phenomena should be subsumed under one of these functions. From an experimental point of view, the definitions depend on the values, which can be accessed separately.

2.1.2 Electric Conductivity

In this section, the dielectric conductivity σ will be understood as a parameter, which determines the linear movement of free charge carriers. This conductivity is introduced by Ohm's law, which is given in Eq. (2.12). Under a general perspective, the conductivity is a complex function, which depends on the frequency. On the other hand, in research fields using frequencies lower than 1 GHz such as time domain reflectometry and ground penetrating radar, the conductivity is assumed to be constant. Here, this constant is the direct current conductivity (e.g. al Hagrey and Müller, 2000; Bittelli *et al.*, 2008).

Although this finding seems to be a proven fact (Olhoeft and Capron, 1994)[3], a short introduction into the theory describing the conductivity will be given, which highlights its physical background. Afterwards, in order to obtain an insight into the describing parameters, a simple example will be presented, which describes the conductivity in a potassium chloride (KCl) solution. This example validates that for a frequency range below 1 GHz the complex conductivity function reduces to the simple direct current conductivity.

Mathematical Description of Electric Conductivity

An approach to study the electric conductivity as a function of frequency is based on the equation of motion (Drude, 1900; Tip, 2004)

$$\partial_t^2 \mathbf{s}(\mathbf{r},t) + g\,\partial_t \mathbf{s}(\mathbf{r},t) = \frac{q}{m}\,\mathbf{E}(\mathbf{r},t) \quad , \tag{2.16}$$

where particles with a charge q and a mass m behave like moving charge carriers damped through friction, which is described by $g\,\partial_t \mathbf{s}$. This means that the particles can move freely within a medium. Here, g is a damping constant and $\mathbf{s}$ corresponds to the elongation of the particles, caused by an external force proportional to the electric field $\mathbf{E}$.

The movement of all particles with a particle density N leads to a resulting current density $\mathbf{J}$, which is given as

$$\mathbf{J}(\mathbf{r},t) = -N\,q\,\partial_t \mathbf{s}(\mathbf{r},t) \quad . \tag{2.17}$$

This leads to the first order differential equation

$$\partial_t \mathbf{J}(\mathbf{r},t) + g\,\mathbf{J}(\mathbf{r},t) = \frac{q^2\,N}{m}\,\mathbf{E}(\mathbf{r},t) \quad , \tag{2.18}$$

which yields after Fourier transformation

$$-\mathtt{i}\,\omega\,\mathbf{J}(\mathbf{r},\omega) + g\mathbf{J}(\mathbf{r},\omega) = \frac{q^2\,N}{m}\,\mathbf{E}(\mathbf{r},\omega) \tag{2.19}$$

$$\Longrightarrow \quad \mathbf{J}(\mathbf{r},\omega) = \frac{q^2\,N}{(g-\mathtt{i}\,\omega)\,m}\,\mathbf{E}(\mathbf{r},\omega) \quad \overset{\text{with (2.12)}}{\Longrightarrow} \quad \sigma(\omega) = \frac{q^2\,N}{(g-\mathtt{i}\,\omega)\,m} \quad . \tag{2.20}$$

This means that the direct current conductivity σ_{dc} yields

$$\sigma_{\mathrm{dc}} := \sigma(\omega=0) = \frac{q^2\,N}{g\,m} \quad , \tag{2.21}$$

which is a function of physical quantities.

[3] In Olhoeft and Capron (1994), the fact of a constant conductivity is stated without giving any further references.

Conductivity of Potassium Chloride Solution

Although, Eq. (2.20) predicts the complex frequency behavior of the conductivity, there is no intuition for the order of magnitude of the damping factor g. To overcome this problem, a simple example will be examined. But before going into details, Eq. (2.20) is rewritten using Eq. (2.21)

$$\sigma(\omega) = \frac{\sigma_{\mathrm{dc}}\, g}{g - \mathtt{i}\,\omega} = \frac{\sigma_{\mathrm{dc}}}{g^2 + \omega^2}\,(g^2 + \mathtt{i}\, g\,\omega) \quad . \tag{2.22}$$

This leads to the relative permittivity contribution for the free charge carriers

$$\varepsilon_{\mathrm{r,free}} = \frac{1}{\mathtt{i}\,\omega\,\varepsilon_0}\,\frac{\sigma_{\mathrm{dc}}\, g}{g - \mathtt{i}\,\omega} \tag{2.23}$$

$$\Longrightarrow \quad \varepsilon'_{\mathrm{r,free}} = \frac{\sigma_{\mathrm{dc}}\, g}{\varepsilon_0\,(g^2 + \omega^2)} \quad \text{and} \quad \varepsilon''_{\mathrm{r,free}} = \frac{\sigma_{\mathrm{dc}}\, g^2}{\omega\,\varepsilon_0\,(g^2 + \omega^2)} \quad , \tag{2.24}$$

where σ_{dc} is the direct current conductivity. This value can be found in the literature for a lot of different solutions and fluids.

Now, in order to obtain a value for the damping factor g, the salt potassium chloride (KCl) resolved in water will be roughly analyzed. Analogous to Drude (1900), the total direct current conductivity is a sum of the direct current conductivity of both compounds / ions. This leads with Eq. (2.21) to

$$\sigma_{\mathrm{dc}} = \sigma_{\mathrm{dc,K^+}} + \sigma_{\mathrm{dc,Cl^-}} = \left(\frac{q^2\, N}{g\, m}\right)_{\mathrm{K^+}} + \left(\frac{q^2\, N}{g\, m}\right)_{\mathrm{Cl^-}} \quad . \tag{2.25}$$

It is obvious that the particle densities of both components and the charges are equal. The particle densities are $N_{\mathrm{K^+}} = N_{\mathrm{Cl^-}} = N$ and the charges are $q_{\mathrm{K^+}} = -q_{\mathrm{Cl^-}} = q \approx 1.602 \cdot 10^{-19}$ C, which is the elementary charge. With the assumption that both ions do not interact with the water[4], the damping factor of both ions is almost equal ($g_{\mathrm{K^+}} = g_{\mathrm{Cl^-}} = g$). This leads to

$$\sigma_{\mathrm{dc}} = \frac{q^2\, N}{g}\,\left(\frac{1}{m_{\mathrm{K^+}}} + \frac{1}{m_{\mathrm{Cl^-}}}\right). \tag{2.26}$$

With the relationships $N = n\, N_{\mathrm{A}}$ and $N_{\mathrm{A}}\, m = M$, we obtain the equation

$$g = \frac{q^2\, N_{\mathrm{A}}^2\, n}{\sigma_{\mathrm{dc}}}\,\left(\frac{1}{M_{\mathrm{K^+}}} + \frac{1}{M_{\mathrm{Cl^-}}}\right), \tag{2.27}$$

which is a function, where all parameters are known. Here, $N_{\mathrm{A}} = 6.022 \cdot 10^{23}\,\mathrm{mol}^{-1}$, $M_{\mathrm{K^+}} = 39.09\,\mathrm{g\,mol}^{-1}$, $M_{\mathrm{Cl^-}} = 35.453\,\mathrm{g\,mol}^{-1}$ and n is the Avogadro constant, the molar mass of potassium, the molar mass of chloride and the amount of substance in mol per volume. When a concentration $c_{\mathrm{KCl}} = n\, M_{\mathrm{KCl}}$ for resolved potassium chloride is given, then Eq. (2.27) yields

$$g = \frac{q^2\, N_{\mathrm{A}}^2\, c_{\mathrm{KCl}}}{\sigma_{\mathrm{dc}}\, M_{\mathrm{K^+}}\, M_{\mathrm{Cl^-}}} \quad . \tag{2.28}$$

In order to use a reasonable example to highlight the magnitude of the damping term, the experimental data from Ferré *et al.* (2003) will be used, who studied a KCl-tracer movement in a soil with time domain reflectometry. The initial concentration of the KCl

[4] The assumption that both ions do not interact with the water is not true, but it is set, because the objective is to obtain a reasonable value and especially an order of magnitude for the damping factor g.

solution was $c_{\mathrm{KCl}} = 0.67$ g/l with a conductivity of $\sigma_{\mathrm{dc}} = 0.142$ S/m. With Eq. (2.28), this leads to a damping term $g \approx 3.17 \cdot 10^{13}$ s^{-1}.

Therefore, the damping term is much larger than the considered frequencies of this work ($g \gg \omega$), which yields

$$\sigma(\omega) \approx \sigma_{\mathrm{dc}} \quad \text{and} \quad \varepsilon'_{\mathrm{r,free}} \approx 0$$
$$\varepsilon''_{\mathrm{r,free}} \approx \frac{\sigma_{\mathrm{dc}}}{\omega\,\varepsilon_0} \quad . \tag{2.29}$$

This leads to a simple function between the imaginary part of the relative permittivity resulting from free charge carriers and frequency, which is illustrated in Fig. 2.1.

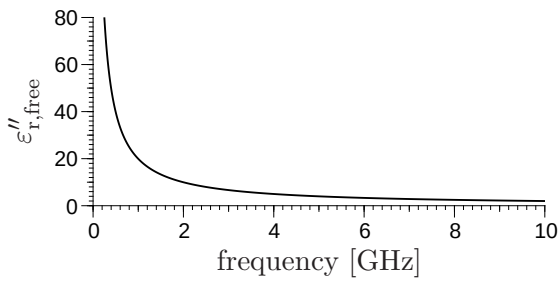

Figure 2.1: *Imaginary part of the relative permittivity for free charge carriers assuming a constant conductivity of $\sigma_{dc} = 12.2$ mS/cm.*

It can be concluded that a frequency dependent conductivity needs not to be considered in research fields like time domain reflectometry and ground penetrating radar, because the relevant frequencies are below 1 GHz. Furthermore, the damping term can be assumed to be larger within soils, because the pore space geometry restricts the movement of the charge carriers.

Outcome: Electrical Conductivity

In this section, the derivation of a complex and frequency dependent electrical conductivity function was presented, considering moving charges. These movements are damped due to collision processes with other particles / molecules. The damping term determines the complex conductivity function. The numerical value of this damping term was analyzed assuming a potassium chloride solution (KCl). It is used as a substitute for a conductive solution in a soil, where a smaller damping term is assumed. It was found that for the KCl-solution the damping term is much larger than the frequencies of interest up to some giga-Hertz. Therefore, the conductivity function reduces to the real direct current conductivity value.

2.2 Dielectric Properties of Soils

A soil can be recognized as a multi-phase system. In the most examples of this work, three phases are assumed consisting of air, water and the solid soil matrix. In literature, a fourth phase is considered such as the ice phase in permafrost studies or an oil phase in petrophysical research. In hydrology, some publications also distinguish between a phase of bounded and free water.

In this section, an overview of descriptions for the dielectric properties in soils will be given. It starts with a small list, which gives the main physical processes determining the relative permittivity in soils. Then, common mixing formulas for the relative permittivity as well as for the dielectric conductivity will be presented. In the end, the relative permittivity as a function of frequency will be given for water, dry sand and two clay materials.

Physical Processes of the Relative Permittivity

Relaxation due to rotation of molecules: The relaxation process comes from an oscillating system, which is excited by the incoming electromagnetic wave. This removes energy from the incoming wave. This energy is emitted undirected and not instantaneously. The most prominent example is the relaxation of water, which leads to the typical relative permittivity behavior as a function of frequency. Here, the relaxation of water can be deduced from oscillation of the water molecules.

While the relative permittivity of pure water is discussed in section 2.2.2, which reveals a temperature dependency and an almost constant value for frequencies below 1 GHz, the relaxation behavior can change, when water interacts with the soil matrix. Then, the Debye model Eq. (2.8) cannot be used any longer, because the water within the soil can have different energy states, which lead to different relaxation processes (Sposito and Prost, 1982).

Maxwell-Wagner-effect: Another effect is the Maxwell-Wagner-effect (Wagner, 1914), which is based on the assumption that a medium is a mixture of different dielectric materials separated by numerous interfaces (Chen and Or, 2006a), where each material itself has no relaxation, but could have a conductivity. The dielectric response of such a medium has a relaxation. In historical studies, layered media and spheres within a solute were analyzed (Wagner, 1914). Because of this finding, this process is different to relaxation processes resulting from oscillating molecules, atoms or electrons. On the other hand, the frequency dependent relative permittivity resulting from the Maxwell-Wagner-effect can also be described by the Debye-model (Maetzler, 1998).

In contrast to the relaxation of water, which influences frequencies above 1 GHz, the Maxwell-Wagner-effect affects the dielectric permittivity spectrum of wet soils especially at frequencies below 100 MHz (Chen and Or, 2006b).

A short qualitative overview over all influencing phenomena, which determines the frequency behavior of the imaginary part of the relative dielectric permittivity below 10^{14} Hz is given in Robinson *et al.* (2003), Fig. 34.

2.2.1 Dielectric Mixing Models

Because soil is a mixture of different phases (e.g. water, air and soil matrix), there is a need to predict either the permittivity or the conductivity, when the properties of each constituent are known. Otherwise, a huge effort must be undertaken to obtain the site specific dielectric properties of the soil material for different water content values. This is difficult, because the water content cannot be adjusted arbitrarily. The reason for this is that the water content distribution is determined by the soil hydraulic properties and the actual hydraulic state which will presented in Sec. 2.3. Furthermore, a uniform distribution of the water content for the unsaturated case cannot be easily achieved, because this is no equilibrium state and gravity flow will occur.

An introduction of the mixing formulas for the dielectric permittivity and the electric conductivity will be given.

Relative Dielectric Permittivity

Semiempirical Model: One of the most popular mixing formula is the semiempirical model

$$\varepsilon_c^{\eta} = \sum_{i=1}^{N} \theta_i \, \varepsilon_i{}^{\eta} \quad \text{with} \quad \sum_{i=1}^{N} \theta_i = 1 \quad \text{and} \quad \eta \in [-1, 1] \quad , \tag{2.30}$$

which was presented by Dobson *et al.* (1985). θ_i and ε_i are the volume fraction and relative permittivity of the ith constituent, when analyzing a mixture of N materials. Furthermore, the shape factor η is a measure for orientation and mixture of these materials (Roth *et al.*, 1990). ε_c is the bulk relative permittivity of the mixture. In general, the relative permittivity values can be complex.

Eq. (2.30) is based on the refractive volumetric mixing proposed by Birchak *et al.* (1974). It is derived from plane wave considerations. It applies an exponent of $\eta = 0.5$. With this exponent, the relationship Eq. (2.30) is known as the complex refractive index model (CRIM).

Experimental Studies: Dobson *et al.* (1985) modified Eq. (2.30)

$$\varepsilon_c^{\alpha} = 1 - \theta_{\mathrm{w}} + \frac{\rho_{\mathrm{c}}}{\rho_{\mathrm{s}}} \, (\varepsilon_{\mathrm{s}}^{\alpha} - 1) + \theta_{\mathrm{w}}^{\beta} \, \varepsilon_{\mathrm{fw}}^{\alpha} \tag{2.31}$$

in order to apply it on measured data. Here, θ_{w} is the volumetric water content. ρ_{c} and ρ_{s} are the bulk density and the specific density of the soil matrix, respectively. $\varepsilon_{\mathrm{fw}}$ is the relative permittivity of free water. The exponent β was introduced to encounter for the different dielectric behavior of bounded and free water. To fit the measured data, the shape factor was set to $\eta = 0.65$. Furthermore, empirical relationships were introduced to define the real and imaginary part of β as a function of clay and sand content. Dobson *et al.* (1985) applied this equation on measured relative permittivity values for different water contents measured with frequencies between 1.4 and 18 GHz. In this publication, it was found that for the lower frequencies the semiempirical model overestimates the measurement.

Peplinski *et al.* (1995) applied (2.31) to a similar data set measured at frequencies between 0.3 and 1.3 GHz. In this publication also the shape factor was used as $\eta = 0.65$. With only small modifications in the empirical relationships, the model fits reasonably well.

Theoretical Four-Component Model: In the publication of de Loor (1968), a general relationship for the relative permittivity for mixtures is given assuming a host medium and different inclusions. Dobson *et al.* (1985) adapted this relationship to soils assuming a four phase medium assuming the soil matrix as the host medium. As inclusions, an air phase, bounded and free water were used. The discrimination into two water phases is done, because in the proximity of the soil particles, it can be assumed that the water is influenced by surface charges.

In Dobson *et al.* (1985), the inclusions are assumed to be disc-shaped, because "the plate-like clay mineral fraction dominates both the distribution and nature of soil water". For these assumptions, the mixing model is given as

$$\varepsilon_{\mathrm{c}} = \frac{3\,\varepsilon_{\mathrm{s}} + 2\,\theta_{\mathrm{fw}}\,(\varepsilon_{\mathrm{fw}} - \varepsilon_{\mathrm{s}}) + 2\,\theta_{\mathrm{bw}}\,(\varepsilon_{\mathrm{bw}} - \varepsilon_{\mathrm{s}}) + 2\,\theta_{\mathrm{a}}\,(\varepsilon_a - \varepsilon_{\mathrm{s}})}{3 + \theta_{\mathrm{fw}}\left(\dfrac{\varepsilon_{\mathrm{s}}}{\varepsilon_{\mathrm{fw}}} - 1\right) + \theta_{\mathrm{bw}}\left(\dfrac{\varepsilon_{\mathrm{s}}}{\varepsilon_{\mathrm{bw}}} - 1\right) + \theta_{\mathrm{a}}\left(\dfrac{\varepsilon_{\mathrm{s}}}{\varepsilon_{\mathrm{a}}} - 1\right)} \quad , \tag{2.32}$$

where θ_i and ε_i stands for the volume fraction and the relative permittivity of the ith constituent. The indices "s", "fw", "bw" and "a" denote the soil matrix, the free water, the bounded water and the air, respectively.

Similar mixing formulas are presented in Robinson *et al.* (2003), which are also derived from the general relationship given by de Loor (1968).

Experimental Studies: Dobson *et al.* (1985) applied Eq. (2.32) to experimental data measured at frequencies between 1.4 and 18 GHz. For the free water, a modified Debye-type relaxation was used. For the bounded water, the best fit was obtained with $\varepsilon_{\mathrm{bw}} = 35 - \mathtt{i}\,15$.

Calculation of the Water Content: In a lot of GPR studies, site specific calibrations of the dielectric permittivity as a function of volumetric water content were not conducted. The reason for this is that, on the one hand, these measurements are time consuming. On the other hand, they could not cover lateral and horizontal changes of the soil types. Although, this effort could be done, for the evaluation techniques nowadays, these information cannot be included.

Commonly, two relationsships are used. The first one is the semiempirical model given in Eq. (2.30) for a three-phase medium. The bulk permittivity is given as

$$\varepsilon_c^\eta = \theta\,\varepsilon_{\mathrm{water}}^\eta + (1-\phi)\,\varepsilon_{\mathrm{matrix}}^\eta + (\phi-\theta)\,\varepsilon_{\mathrm{air}}^\eta \quad , \tag{2.33}$$

where θ, ϕ is the volumetric water content and the porosity. $\varepsilon_{\mathrm{air}}$, $\varepsilon_{\mathrm{water}}$ and $\varepsilon_{\mathrm{matrix}}$ are the relative permittivity of air, water and the soil matrix, respectively. In the frequency range of GPR all relative permittivity values can be assumed to be constant. From this equation, the formula for the volumetric water content can be derived

$$\theta = \frac{\varepsilon_c^\eta - \varepsilon_{\mathrm{matrix}}^\eta - \phi\left(\varepsilon_{\mathrm{air}}^\eta - \varepsilon_{\mathrm{matrix}}^\eta\right)}{\varepsilon_{\mathrm{water}}^\eta - \varepsilon_{\mathrm{air}}^\eta} \quad , \tag{2.34}$$

which requires knowledge about the permittivity values of the three constituents, the porosity ϕ and the exponent η. Except of a few studies, e.g. Roth *et al.* (1990), this exponent is set to $\eta = 0.5$ in analogy to Birchak *et al.* (1974) and Herkelrath *et al.* (1991).

Because Eq. (2.34) requires four parameters, which must be determined individually, a modification is used in some studies (Herkelrath *et al.*, 1991) within the research field of time domain reflectometry (TDR) and GPR. This modification uses the exponent of $\eta = 0.5$, which leads to a general function

$$\theta = A\sqrt{\varepsilon_c} + B \quad , \tag{2.35}$$

where A and B are calibration parameters. These calibration parameters are obtained by comparing the square root of the relative permittivity with volumetric water content values determined with external methods, for instance gravimetric measurements.

The second commonly used equation, which relates volumetric water content and the bulk relative permittivity, is the Topp-formula, presented by Topp (1980). It is given by a polynomial of third order

$$\theta = A + B\,\varepsilon_c + C\,\varepsilon_c^2 + D\,\varepsilon_c^3 \tag{2.36}$$

with the parameters

$$A = -5.3\cdot 10^{-2} \quad B = 2.92\cdot 10^{-2} \quad C = -5.5\cdot 10^{-4} \quad D = 4.3\cdot 10^{-6} \quad . \tag{2.37}$$

The author states that 95% of all measured data points are inbetween a range of ± 0.026 in water content and that the scatter of the data points were due to the different soil types and not a result of noise. Furthermore, the publication of Topp (1980) presented that there are deviations of the fitting parameters for different soils, especially when organic soils are investigated. Therefore, the disadvantage of Eq. (2.36) is that there is no physical intuition behind this formula and that it is extracted from a small set of measurements of mineral soils in a coaxial transmission line.

Electric Conductivity

In contrast to the relative permittivity of soils it is assumed that the electric conductivity is almost determined by the water phase through the transport of ions. As long as the concentration of these ions is not to high, one can assume that they do not interact with each other, which leads to a sum of the conductivity values for each ion type. For the investigation of the soil with geophysical instruments, the single constituents cannot be determined.

Another aspect, which should be mentioned is that the conductivity of the water phase σ_w within the pore space cannot be simply scaled to the bulk conductivity of the soil σ_s by knowing the water content θ. It was observed that a geometry factor F_g must be included, which leads to a relationship

$$\sigma_s = \theta \, F_g \, \sigma_w \tag{2.38}$$

presented by Amente *et al.* (2000). The geometry factor is also a function of water content, which can be estimated from the hydraulic conductivity of the soil (Amente *et al.*, 2000). In this publication, it was found that for sandy soils the geometry factor F_g is close to θ^b with $b = 0.5$.

From empirical studies, the well known Archie's law

$$\sigma_s = \frac{\sigma_w \, S^n}{F} \tag{2.39}$$

was found, which is widely used in electric resistivity surveys (Samouëlian *et al.*, 2005). S is the saturation, which describes the water content with respect to the porosity of the soil. And n is a fitting parameter with respect to the saturation degree. F is the formation factor, which also reflects the pore geometry. It can be measured at full saturation.

Both presented equations for the bulk conductivity of the soil are equivalent. They can be applied to a large range of soil types, as long as the conductivity contribution of the soil fraction can be neglected (Amente *et al.*, 2000). For example, for clayey soils this contribution has an impact to the total conductivity. Furthermore, it must be noticed that the conductivity is a function of temperature due to changes of the viscosity of the fluid.

2.2.2 Dielectric Permittivity Functions for Specific Media

The Relative Permittivity of Water

Water mainly determines the relative permittivity of soils within the frequency range of ground penetrating radar applications (between 10 MHz and 1 GHz). Because of this, the relative permittivity of pure water and its dependency on frequency and temperature will be presented in the following. These relationships can be used for dielectric mixing formulas assuming that there is no interaction between the water molecules and the soil matrix.

The relative permittivity of pure water for frequencies between 1.1 and 57 GHz is presented by Kaatze (1989). Here, the author used a large data set to fit the parameters of the Debye model, cf. Eq. (2.8), as a function of temperature T, measured in Kelvin (K). They are given as

$$\log_{10} \varepsilon_{\mathrm{s}} = 1.94404 - 1.991 \cdot 10^{-3}\ \mathrm{K}^{-1} \cdot (T - 273.15\,\mathrm{K}) \tag{2.40}$$

$$\varepsilon_{\infty} = 5.77 - 2.74 \cdot 10^{-2}\ \mathrm{K}^{-1} \cdot (T - 273.15\,\mathrm{K})$$

$$\tau_{\mathrm{rel}} = \left(3.745 \cdot 10^{-15}\,s\right) \cdot \left(1 + 7 \cdot 10^{-5}\ \mathrm{K}^{-1} \cdot (T - 300.65\,\mathrm{K})^2\right) \cdot \exp\left\{\frac{2.2957 \cdot 10^3\,\mathrm{K}}{T}\right\}.$$

In order to obtain an impression of the complex behavior of the relative permittivity of water, an example is shown in Fig. 2.2. Here, the real and imaginary part of the relative permittivity up to 30 GHz are presented for two different temperatures ($\vartheta_1 = 20°\mathrm{C}$ and $\vartheta_2 = 10°\mathrm{C}$).

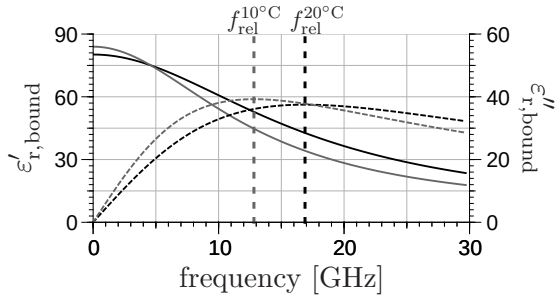

Figure 2.2: *Real (solid) and imaginary (dashed) part of the relative permittivity of water at a temperature of $T = 293.15$ K (20 °C) (black) and $T = 283.15$ K (10 °C) (gray).*

For pure water, in the above mentioned frequency domain the relaxation process can be traced back to a rotation of the water molecules (Robinson *et al.*, 2003). The temperature dependency stems from the random thermal movement of the molecules. For higher temperatures, this random movement is larger and therefore, the energy storage due to the polarization process is lower for the low frequency limit. This can be seen in the behavior of the static permittivity ε_{s}. Furthermore, the imaginary part of the relative permittivity at relaxation frequency, which determines the energy absorption, decreases for increasing temperatures. This is also an effect of the random movement of the particles due to temperature.

For the dielectric behavior of water for frequencies below 1.1 GHz, the static permittivity can be used (Kaatze, 1989). Furthermore, relaxation processes for lower frequencies are unlikely for pure water. This can be underlined by the publication of Vidulich *et al.* (1967), who determined the dielectric constant of water between 0.5 and 100 kHz, which equals the same equation of the static permittivity given in Eq. 2.40.

The Relative Permittivity of Dry Sand

The complex relative permittivity of dry sand (desert sand from Tunisia) was studied by Maetzler (1998). Here, the imaginary part of Debye model with a correction term α

$$\varepsilon(\omega) = \varepsilon_{\infty} + \frac{\varepsilon_{\mathrm{stat}} - \varepsilon_{\infty}}{1 + \mathtt{i}\,\omega\,\tau_{\mathrm{rel}}} + \mathtt{i}\,\alpha \tag{2.41}$$

was fitted to experimental data. The obtained parameters were $\varepsilon_{\infty} = 2.53$, $\varepsilon_{\mathrm{stat}} = 2.79$, $\alpha = 0.002$ and a relaxation frequency $\nu_{\mathrm{rel}} = 0.27$ GHz, from which the relaxation time can be calculated as

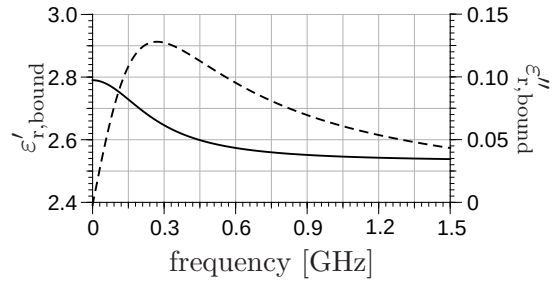

Figure 2.3: *The real (solid) and imaginary (dashed) part of the relative permittivity of dry sand measured by Maetzler (1998).*

$\tau_{\mathrm{rel}} = (2\,\pi\,\nu_{\mathrm{rel}})^{-1}$. The correction term was introduced to fit the data and it was assumed to be due to losses of the main sand component. Furthermore, the relaxation process was explained by the Maxwell-Wagner-effect. The frequency behavior for both real and imaginary part of the relative permittivity for the dry sand is shown in Fig. 2.3.

From this example, it can be concluded that the relative permittivity can be assumed to be constant for ground penetrating radar measurements, because a relative permittivity difference of about 0.2 is approximately our measurement accuracy, which is shown in the experimental studies of this work.

The Relative Permittivity of Clay

The relative permittivity of clay under moist conditions as a function of frequency was measured and presented by Ishida *et al.* (2000). Here, the complex shape of the relative permittivity results from coupling of water molecules with its surrounding (Sposito and Prost, 1982).

Ishida *et al.* (2000) measured the relative permittivity of different clay minerals under moist conditions. In this study, the water content of each sample was adjusted using a pressure plate apparatus to a water potential of 33 kPa. Before this procedure, the samples were oven dried at 110°C.

For two clay minerals, the complex functions of the relative permittivity are given in Fig. 2.4 for a frequency range between 1 MHz and 10 GHz. This figure results from the findings presented in Ishida *et al.* (2000), which are given as:

$$\text{Kaolinite:}\quad \varepsilon(\omega) = \varepsilon_\infty + \frac{\triangle\varepsilon_l}{(1+\mathtt{i}\,\omega\,\tau_l)^{\alpha_l}} + \frac{\triangle\varepsilon_m}{1+(\mathtt{i}\,\omega\,\tau_m)^{\beta_m}} + \frac{\triangle\varepsilon_h}{1+(\mathtt{i}\,\omega\,\tau_h)^{\beta_h}} \tag{2.42}$$

$$\begin{aligned}
\triangle\varepsilon_l &= 335.0 \pm 21.4 & \log_{10}\tau_l\ [\mathrm{s}] &= -\ 5.52 \pm 0.38 & \alpha_l &= 0.71 \pm 0.04\\
\triangle\varepsilon_m &= 23.6 \pm 1.6 & \log_{10}\tau_m[\mathrm{s}] &= -\ 7.72 \pm 0.21 & \beta_m &= 0.92 \pm 0.02\\
\triangle\varepsilon_h &= 47.7 \pm 1.9 & \log_{10}\tau_h\ [\mathrm{s}] &= -11.12 \pm 0.21 & \beta_h &= 0.98 \pm 0.01\\
\varepsilon_\infty &= 5.3 \pm 0.6
\end{aligned}$$

$$\text{Allophane:}\quad \varepsilon(\omega) = \varepsilon_\infty + \frac{\triangle\varepsilon_l}{(1+\mathtt{i}\,\omega\,\tau_l)^{\alpha_l}} + \frac{\triangle\varepsilon_m}{(1+\mathtt{i}\,\omega\,\tau_m)^{\alpha_m}} + \frac{\triangle\varepsilon_h}{1+(\mathtt{i}\,\omega\,\tau_h)^{\beta_h}} \tag{2.43}$$

$$\begin{aligned}
\triangle\varepsilon_l &= 24.6 \pm 2.8 & \log_{10}\tau_l\ [\mathrm{s}] &= -\ 7.51 \pm 0.21 & \alpha_l &= 0.95 \pm 0.03\\
\triangle\varepsilon_m &= 5.6 \pm 1.5 & \log_{10}\tau_m[\mathrm{s}] &= -\ 8.69 \pm 0.18 & \alpha_m &= 0.65 \pm 0.03\\
\triangle\varepsilon_h &= 51.8 \pm 2.5 & \log_{10}\tau_h\ [\mathrm{s}] &= -11.07 \pm 0.23 & \beta_h &= 0.97 \pm 0.01\\
\varepsilon_\infty &= 4.0 \pm 0.7
\end{aligned}$$

Here, the relative permittivity function consists of a sum of relaxation processes described by the Cole-Cole model and the Cole-Davidson model (Nigmatullin and Ryabov, 1997).

Fig. 2.4 reveals a high real part of the relative permittivity, $\varepsilon_c' \approx 50-60$ for frequencies between 50 MHz and 1 GHz. Here, the difference in the dielectric properties compared to sand can be clearly seen. The real permittivity of saturated sand is reported to be between 20 and 30 (Davis and Annan, 1989). Furthermore, the imaginary part of the clay minerals is $\varepsilon_c'' \approx 2-10$ for frequencies between 50 MHz and 1 GHz. This is is much larger compared to the dry sand (Fig. 2.3).

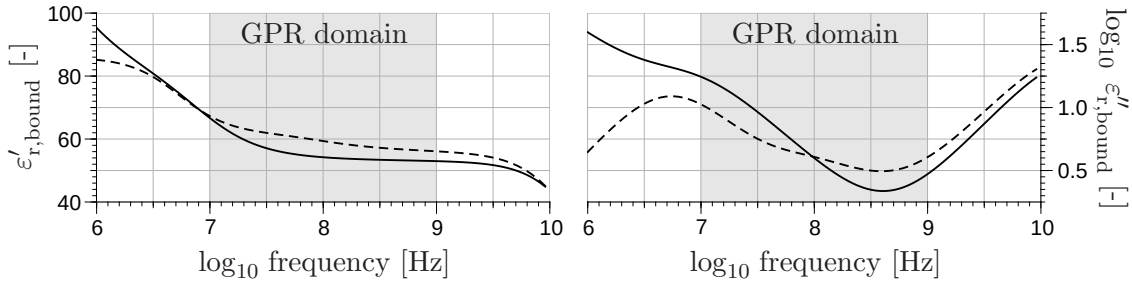

Figure 2.4: *Relative permittivity of two clay minerals (kaolinite – solid, allophane – dashed) under moist conditions. The direct current conductivity part is removed.*

2.3 Water Content Distribution in Soils

In this section, a short introduction to soil physics will be given to obtain an insight in the description of fluids in porous media. To be more specific, the main interests concern the distribution of water in soils, which determines the bulk dielectric permittivity and therefore the propagation of electromagnetic waves. As an example for a possible water distribution, the equilibrium state will be shortly described, which leads to the evolution of a capillary fringe.

2.3.1 Short Introduction to Soil Physics

The basic ideas in soil physics can be derived from pore size considerations. Here, the mass balance and a flux law can be formulated for fluids within the porous medium, where a flux can be driven by a pressure gradient or by gravity. When a whole pore space is given, then these equations can predict the behavior of the system, which includes water distribution and water movement. For scales larger than a few centimeters, a pore space description cannot be used, because of experimental and numerical limits. Therefore, these relationships need to be averaged over a specific volume. This volume is called representative elementary volume (REV), which is defined as a space, where an averaging of the material properties over a slightly larger domain will not change. As an example, an averaged porosity can be calculated by choosing a sphere with a radius and an arbitrary midpoint within the porous medium. For different radii in the order of the grain sizes, the fraction between pore space and total sphere volume will change significantly. For much larger radii, these changes will decrease until a constant value is reached. The sphere with that radius encloses a volume, which can be defined as an REV.

Although, this REV is a theoretical construct, it helps to average the mass balance equation and flux law, which also correspond to the introduction of state variables analogous to thermodynamics. The mass balance for an incompressible fluid yields

$$\partial_t \theta + \nabla \mathbf{j}_w = 0 \quad , \tag{2.44}$$

where θ is the water content and $\mathbf{j}_w$ the water flux. In this equation, source and sink terms are neglected. If necessary, these terms can be included on the right hand side representing infiltration or pumping for example.

The flux law becomes

$$\mathbf{j}_w = -K(\theta)\, \nabla \psi_w \quad , \tag{2.45}$$

where K and ψ_w are the hydraulic conductivity and the water potential, respectively. Here, ψ_w is an energy density. Its changes in space drive the water movement. It depends

on gravity, but it is also a function of pressure. This yields to the mathematical expression for the water potential

$$\psi_w = -\rho_w \, g \, (z - z_0) + \psi_m \quad , \tag{2.46}$$

where ρ_w, g, z and z_0 are the mass density of water, the acceleration number due to gravity (9.81 m/s^2), the depth of the observation point and a reference depth, respectively. ψ_m is the matric potential and it includes the pressure dependency, which can be given as

$$\psi_m = p_w - p_a \quad . \tag{2.47}$$

This is only the pressure difference between the water and the air phase, assuming that all grains of the soil matrix are completely covered by a small water film.

Now, continuing the discussion of Eq. (2.45), the flux is driven by the change of the water potential and scales with a proportionality constant, which is the hydraulic conductivity. Although, the hydraulic conductivity is written as a scalar value, in a generalized sense, it must be assumed as a matrix. This is because the water flow need not be equal in all directions, which is the case for a layered structure of grains with a preferred orientation, for instance. Furthermore, the hydraulic conductivity must be considered as a function of water content. This is obvious, because water can only be transported through the water phase. When the soil is dry, the water can move only in the small films around the grains, which leads to a very low hydraulic conductivity.

If the Eqns. (2.44)-(2.46) are combined, Richards equation

$$\partial_t \theta - \nabla \cdot \Big[K(\theta) \big[\nabla \psi_m - \rho_w \, g \big] \Big] = 0 \tag{2.48}$$

is obtained, which describes water distribution and water transport in porous media and was first presented by Richards (1931). The difficulties of this equation are that it is non-linear, because of the dependency of the hydraulic conductivity on the water potential. Furthermore, a relationship between the matric potential and the water content is required as well as a relationship between the hydraulic conductivity and water content. These relationships must be determined experimentally for each soil and can only be predicted by knowing the pore-size distribution and pore connectivity (Vogel and Roth, 1998). On the other hand, there are a few mathematical expressions for these relationships, where some of the required parameters are pure fitting parameters without any physical meaning (Fuentes *et al.*, 1992).

2.3.2 Description of the Capillary Fringe

The capillary fringe will be examined in more detail, because it is the easiest example to illustrate gradual changes of the water content within the soil, but it only occurs under conditions of the hydraulic equilibrium.

In this context, one can understand a capillary fringe as a range above a water table, where the water is moved upwards due to capillary rise. Assuming a porous medium with a huge distribution of different pore radii, one can imagine that there is a functionality between height above the water table and water content. This comes from the fact that the water rises higher in small pores compared to larger ones.

In the following, two descriptions for the capillary fringe will be presented. But before, the matric head is introduced, which is a more intuitive measure than the matric potential. The matric head h_m is defined as

$$h_m := \frac{\psi_m}{\rho_w \, g} \quad , \tag{2.49}$$

which is given in units of centimeters above a reference surface. In most cases, this is the water table. In hydraulic equilibrium, the matric head gives a height above the ground / free water table, measured in negative values. This can be illustrated, because at the free water table the pressure difference between air and water phase is zero, which leads to a matric head equal to zero. For water above the free water table, the energy density of the water equals the potential energy density in hydraulic equilibrium. But this energy density is given in negative values, because, due to the capillary rise, energy must be introduced to the system to free the water from its bounded state. Because the potential energy is a function of height, Eq. (2.49) defines this height, but it is given in negative values.

With this matric head, the capillary fringe can be described by the van-Genuchten parameterization (van Genuchten, 1980)

$$\theta(h_m) = \left(\theta_s - \theta_r\right)\left[1 + (\alpha_g\, h_m)^{n_g}\right]^{-m_g} + \theta_r \quad , \tag{2.50}$$

where θ_s, θ_r, α_g, n_g and m_g are the van-Genuchten-parameters, which the restrictions $\alpha_g < 0$, $n_g > 1$ and $m_g > 0$. Here, θ_s is the saturated water content, which is the highest possible water content in the soil. It can be lower than the porosity of the system due to entrapped air. θ_r describes the residual water content. It is the amount of water, which cannot be removed from the soil due to small films on the grains. In most cases m_g is expressed as $m_g = 1 - 1/n_g$. Here, as a physical explanation $1/\alpha_g$ corresponds to an air entry value and $1/n_g$ indicates the width of the capillary fringe, which gives the distribution of the relevant radii within the porous medium.

Another parameterization for the capillary fringe was described by Brooks and Corey, which is given as

$$\Theta(h_m) = \begin{cases} [h_m/h_0]^{-\lambda} & \text{, for} \quad h_m < h_0 \\ 1 & \text{, for} \quad h_m \geq h_0 \end{cases} \qquad \text{with} \quad \Theta = \frac{\theta - \theta_r}{\theta_s - \theta_r} \quad . \tag{2.51}$$

Here, Θ and h_0 describe the saturation of soil and the air entry pressure. In contrast to the van-Genuchten parameterization, this air entry pressure is well defined and corresponds to the capillary rise due to the largest pores in the medium. The parameter λ is only a fitting parameter, which describes the curvature and therefore, the pore size distribution.

3 Electromagnetic Theory - Modeling Approaches

3.1 Introduction / Overview

Every kind of modeling is a tool to verify a scientific theory and therefore helps to evaluate measured data. Each model requires a theory, which should reflect the reality to a certain extent based on the assumptions defined in this model.

Because this work deals with ground penetrating radar (GPR), which is an application of the electromagnetic theory, models are required, which represent this theory. For the prediction of electromagnetic wave phenomena, one can find at least four different modeling approaches:

Ray Approaches are the most simple models, which assume the electromagnetic waves to propagate on straight lines within a homogeneous medium.

Plane Wave Approaches solve the electromagnetic wave equation for the absence of sources, such as radiating dipoles. Therefore, these approaches are far-field methods, because the radiation field of an antenna cannot directly be addressed. It must be approximated for full wave studies.

In most applications concerning GPR, only the solution for the reflection coefficient for simple material setups is analyzed and used for data interpretation (e.g. Bradford and Deeds, 2006). However, multi-layer approaches exist, such as described in Strobbia and Cassiani (2007), where the waveguiding behavior of the near subsurface is examined.

Green's Function Approaches solve the electromagnetic wave equation with respect to a source term, which can be placed and designed almost arbitrarily in a predefined material model. This predefined medium is necessary to calculate the Green's functions, which are solutions for an arbitrary orientation of an infinitesimal radiating dipole.

In the research field of surface GPR applications, there are at least two main applications of Green's functions. Some researchers use them, in order to describe the backscattered electric field from pipes or other spherical objects placed in an homogeneous background (Hansen and Johansen, 2000; Meincke, 2001). Furthermore, Green's functions are calculated for horizontally layered media (Lambot, 2003) in order to determine the near surface volumetric water content (Lambot *et al.*, 2004).

The disadvantage of these approaches is that Green's functions for arbitrary media are difficult to determine. Therefore, this method is restricted to a small set of material structures. Furthermore, these approaches are challenging in the mathematical description.

The advantage of these methods is that a full wave solution, which includes the near field (due to the antenna radiation) and the far field, can be obtained in shorter calculation times compared to other numerical approaches.

Numerical Approaches offer the highest potential to model arbitrary material structures or dielectric property distributions. Furthermore, the antenna and its radiation can be modeled in great detail (Lampe *et al.*, 2003), which leads to more realistic representations of GPR measurements.

In the research field of full wave electromagnetic modeling, two approaches exist to solve Maxwell's equations in the time domain. These equations can either be solved on regular and structured grids with the finite difference method (Taflove and Hagness, 2000), or they can be solved on unstructured grids using finite element methods (Volakis *et al.*, 1998). These finite element methods offer the possibility to adapt the representing grid by refining the spatial discretization of highly interesting or numerically challenging areas. In many cases, this allows an increase of modeling performance with superior numerical efficiency relative to methods based on structured grids.

For full wave simulations of GPR, the finite difference method is widely used such as presented by Roberts and Daniels (1997), Chen and Huang (1998) and Cassidy (2007). They all solve Maxwell's equation in the time domain, because most of the GPR measurements work in this domain.

The difficulties of the numerical methods are that the accuracy depends on the discretization of the domain, which has a significant impact on the runtime. Furthermore, the domain must be truncated, because an infinite domain cannot be modeled with these approaches. Therefore, extra boundary algorithms must be implemented, which simulate an infinite domain.

In this work, examples for the first three modeling approaches will be presented, which vary in complexity and the electromagnetic phenomena they are able to represent. The advantage in using different modeling approaches is that each method is based on some aspects of wave propagation. For instance, while a simple ray approach only focuses on travel paths and times, the plane wave approach additionally includes amplitude behavior, wavelet distortion, the applicability for dispersive material properties etc. This means that the aspect of a travel time is superposed by the amplitude behavior in a plane wave approach, leading to an extraction of travel times, which is a bit more difficult. Furthermore, the ray approach allows the determination of travel times for distinct travel paths. The plane wave approach represents all possible wave modes for a given material model, which could complicate the assignment of the different travel paths. This small example demonstrates that different modeling approaches can help each other for the interpretation, the validation and the evaluation of simulations.

3.2 Travel Path Analysis using the Ray Approach

The ray approach is the simplest model to predict travel times of electromagnetic wave propagation. It only accounts for reflection and refraction at layer boundaries. The limit of this approach is that neither the amplitude behavior nor the wavelet distortion can be analyzed.

Assuming a multi-layered model, the ray approach can predict travel paths through the system, but it can not distinguish which travel paths are likely to be detected. For this purpose simple plane wave predictions must be included, such as done in Goodman (1994).

In this section, a description of the elementary wave types, which are observable in GPR studies, will be given. Here, two- or three-layer structures will be assumed. In a next step, two approaches are presented, predicting the travel path and the travel time through a

multi-layered medium, which can represent the gradients of the relative permittivity due to water content changes in the subsurface.

3.2.1 Analytical Solutions for Few Layer Setups

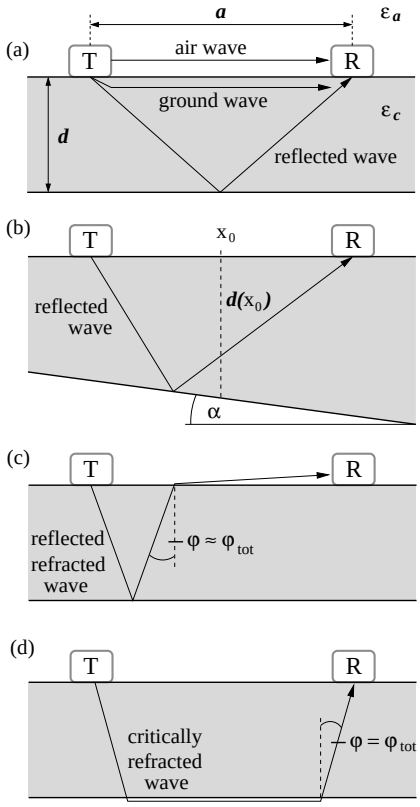

Figure 3.1: *Selected travel paths, which are all observable in GPR applications. For a better overview, these travel paths are scetched separately.*

In this subsection, the focus is on the travel paths, which are most relevant for ground penetrating radar applications. A set of them is presented in Fig. 3.1. Here, one can distinguish between three categories: (i) direct waves, (ii) reflected waves, and (iii) refracted waves.

Direct Waves

Direct waves are all waves, where the travel paths go directly from the transmitter to the receiver. In a homogeneous medium, one would expect a single ray. When the transmitter and the receiver are placed above an interface between two half-spaces with different dielectric properties, then two direct waves can be observed (Fig. 3.1a). The travel times t_{dir} of these waves are only a function of distance a (antenna separation) and relative permittivity ε_r of the medium the wave travels through. It is given as

$$t_{\text{dir}} = \frac{a}{c_0}\sqrt{\varepsilon_r} \quad , \tag{3.1}$$

where c_0 is the speed of light in vacuum.

When both waves are detected, then the fastest wave, which propagates through the air is denoted as the air wave (Fig. 3.1a). The second fastest wave, which travels through the ground is called ground wave.

Reflected Waves

With respect to the material model given in Fig. 3.1, a reflected wave is the result of one or more reflections. The travel time t_{refl} of a single reflection at a horizontal layer boundary with a depth d (Fig. 3.1a) can be described as:

$$t_{\text{refl}} = \frac{\sqrt{a^2 + 4\,d^2}}{c_0}\sqrt{\varepsilon_c} \quad . \tag{3.2}$$

Here, ε_c is the relative permittivity of the medium in which the reflected wave travels. Furthermore, one can assume multiple reflections within this layer. Then the travel time becomes

$$t_{\text{refl},n} = \frac{\sqrt{a^2 + (2\,n\,d)^2}}{c_0}\sqrt{\varepsilon_c} \quad , \tag{3.3}$$

where n denotes the number of reflections at the lower boundary.

In a more general case, the lower layer can be assumed as a dipping reflector (Fig. 3.1b). Then, the travel time $t_{\mathrm{refl},\alpha}$ depends on the measurement position x_0 and the dipping of the reflector described by the angle α. This yields[1]

$$t_{\mathrm{refl},\alpha}(x_0) = \frac{\sqrt{\varepsilon_c}}{c_0} \cos\alpha \sqrt{4\,d(x_0)^2 + a^2} \quad , \tag{3.4}$$

where the reflector depth $d(x_0)$ defines the reflector depth below the midpoint x_0 between transmitter and receiver. α is the dipping angle. If this midpoint is moved to a position x, we obtain

$$t_{\mathrm{refl},\alpha}(x) = \frac{\sqrt{\varepsilon_c}}{c_0} \sqrt{(4d^2 + a^2)\,\cos^2\alpha + 4\,(x_0 - x)^2\,\sin^2\alpha + 8\,d\,(x_0 - x)\,\sin\alpha\,\cos\alpha} \quad , \tag{3.5}$$

where d is still the reflector depth below the position x_0.

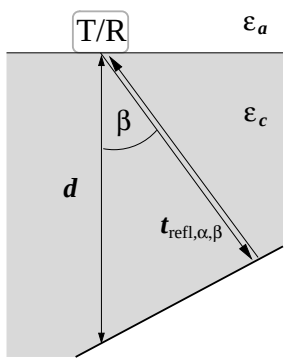

Figure 3.2: *Dipping reflector orthogonal to transmitter-receiver direction.*

In all the examples above, it is assumed that the reflector depth does not change perpendicularly to the transmitter-receiver direction. When there is a dip with an angle β introduced orthogonally to the transmitter-receiver direction, Eq. (3.4) becomes

$$t_{\mathrm{refl},\alpha,\beta}(x_0) = \frac{\sqrt{\varepsilon_c}}{c_0} \cos\alpha\,\cos\beta \sqrt{4\,d(x_0)^2 + a^2} \quad , \tag{3.6}$$

where $t_{\mathrm{refl},\alpha,\beta}(x_0)$ denotes the travel time from a single reflection caused by a boundary layer with the dipping angle α in survey direction and β orthogonal to the survey direction.

Refracted Waves

As illustrated in Fig. 3.1c-d, there are two different types of refracted waves in three-layer systems. One wave is first reflected at the lower interface and then it is refracted at the air-ground interface (Fig. 3.1c). Therefore, it is called "reflected-refracted wave" (Strobbia and Cassiani, 2007), but in the literature one can find the nomenclature "critically refracted wave" (Huisman *et al.*, 2003) or "air-refracted phase" (Bohidar and Hermance, 2002). The second wave (Fig. 3.1d) is critically refracted at the lower interface, which requires that the lower medium has a lower dielectric permittivity than the intermediate layer. This wave is named "critically refracted wave" (Rucker and Ferré, 2003; Strobbia and Cassiani, 2007), but also denoted as a "refracted wave" (Huisman *et al.*, 2003) or the "subsurface refracted wave" (Bohidar and Hermance, 2002).

It must be noted that in the following description the refracted waves are assumed to be detectable as separated wavelets. This cannot be guaranteed in general because both wavetypes can occur as waveguiding modes (van der Kruk, 2006; van der Kruk *et al.*, 2007).

[1]The derivation of this relationship can be found in Appendix A.1.1.

Reflected-Refracted Waves: The travel path of the reflected-refracted wave is presented in Fig. 3.1c. This wave is reflected at a dielectric boundary in the subsurface and is refracted at the ground surface. Therefore, one can determine two travel path sections, one within the soil and the other one in air. Assuming the receiver to be placed directly on the surface, these characteristic waves occur when the incoming angle φ from soil to air is approximately the total reflection angle φ_{tot}, which is given as

$$\sin \varphi_{\text{tot}} = \sqrt{\varepsilon_a / \varepsilon_c} \quad . \tag{3.7}$$

Assuming a horizontal reflector, the travel time $t_{\text{refl-refr}}$ of the reflected-refracted wave is given as

$$t_{\text{refl-refr}} = \frac{\sqrt{\varepsilon_c}}{c_0} \frac{2\,d}{\cos \varphi_{\text{tot}}} + \frac{\sqrt{\varepsilon_a}}{c_0} \big(a - 2\,d\,\tan \varphi_{\text{tot}}\big) = \frac{a}{c_0} \sqrt{\varepsilon_a} + \frac{2\,d}{c_0} \sqrt{\varepsilon_c - \varepsilon_a} \quad . \tag{3.8}$$

If multiple reflections occur previous the refraction into the air, then the travel time becomes

$$\begin{aligned} t_{\text{refl-refr},n} &= \frac{\sqrt{\varepsilon_c}}{c_0} \frac{2\,n\,d}{\cos \varphi_{\text{tot}}} + \frac{\sqrt{\varepsilon_a}}{c_0} \big(a - 2\,n\,d\,\tan \varphi_{\text{tot}}\big) \\ &= \frac{a}{c_0} \sqrt{\varepsilon_a} + \frac{2\,n\,d}{c_0} \sqrt{\varepsilon_c - \varepsilon_a} \quad , \end{aligned} \tag{3.9}$$

where n is the number of reflections at the lower boundary.

Critically Refracted Waves: These waves are reported in borehole GPR applications (Rucker and Ferré, 2003) as well as in surface GPR surveys (Strobbia and Cassiani, 2007). While in borehole applications only a single wave can be found, because in most cases a simple two-layer medium can be assumed, in surface GPR applications multiples can occur, which can be associated with guiding wave phenomena (Strobbia and Cassiani, 2007; van der Kruk, 2006).

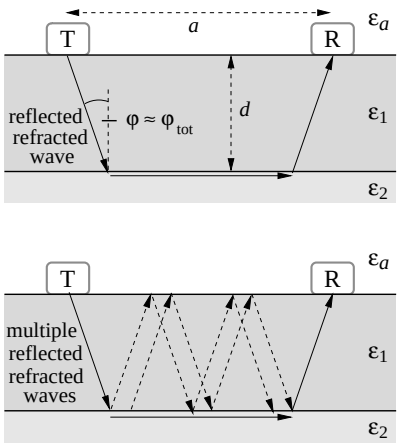

Figure 3.3: *Single critically refracted wave travel path and a representation of multiples.*

As presented in Fig. 3.3, the travel paths of critically refracted waves can be divided into three sections. The two sections in the intermediate layer are equal. The occurrence of the coupling from the lower medium in the intermediate layer can be argued by Huygens principle. Again, a total reflection at the bottom interface must be assumed, which requires that the lower half-space has a lower relative permittivity than the intermediate layer ($\varepsilon_1 > \varepsilon_2$). Again, the total reflection angle is defined as

$$\sin \varphi_{\text{tot}} = \sqrt{\frac{\varepsilon_2}{\varepsilon_1}} \quad , \tag{3.10}$$

where the definition of the notation can be extracted from Fig. 3.3. This leads to a travel path in the intermediate layer s_1 and a travel path in the lower half-space s_2 given as

$$\begin{aligned} s_1 &= \frac{2d}{\cos \varphi_{\text{tot}}} = \frac{d\sqrt{\varepsilon_1}}{\sqrt{\varepsilon_1 - \varepsilon_2}} \quad \text{and} \\ s_2 &= a - 2\,d\,\tan \varphi_{\text{tot}} = a - \frac{2\,d\sqrt{\varepsilon_2}}{\sqrt{\varepsilon_1 - \varepsilon_2}} \quad , \end{aligned} \tag{3.11}$$

where d and a correspond to the depth of the intermediate layer and the distance between transmitter T and receiver R, respectively. Therefore, the total travel time can be expressed by

$$t_{\text{c-refr}} = \frac{2\,s_1}{c_0}\sqrt{\varepsilon_1} + \frac{s_2}{c_0}\sqrt{\varepsilon_2} = \frac{2\,d}{c_0}\sqrt{\varepsilon_1 - \varepsilon_2} + \frac{a}{c_0}\sqrt{\varepsilon_2} \quad . \tag{3.12}$$

Again, when multiple reflections are assumed in the intermediate layer either before or after the refraction process, then the travel time for the nth multiple can be written as

$$t_{\text{c-refr},n} = \frac{2\,n\,d}{c_0}\sqrt{\varepsilon_1 - \varepsilon_2} + \frac{a}{c_0}\sqrt{\varepsilon_2} \quad . \tag{3.13}$$

3.2.2 Multi-Layer Modeling

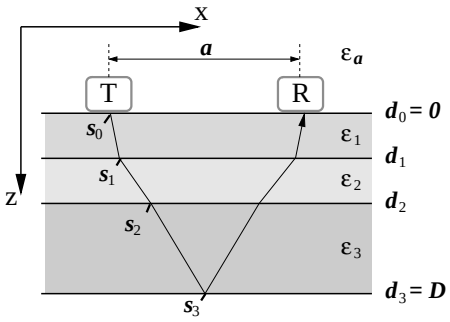

Figure 3.4: *Setup of a multi-layer model.*

This subsection will focus on the travel path of electromagnetic waves in multi-layered media (Fig. 3.4). This layering can simulate the gradients in dielectric permittivity within soils caused by gradients in water content.

Here, two modeling approaches will be presented. One is based on Fermat's principle and the other one on a ray tracing method.

Fermat's Principle

Fermat's principle is a variation principle. It states that a travel path is realized, when small variations of it always increase the travel time (Jones, 1994). In this context, this principle is used in the following way: A travel path is described with a set of parameters. A specific set of parameters is searched, which leads to the smallest travel time. For this purpose, it must be guaranteed, that one and only one travel path with the minimal time is possible.

In the following, a horizontally layered material model will be used (Fig. 3.4). Assuming a detectable reflection from the lower boundary of the n-th layer, one can calculate the travel time

$$t_{\text{refl}} = \frac{2}{c_0}\sum_{i=1}^{n}\sqrt{(s_i - s_{i-1})^2 + (d_i - d_{i-1})^2}\,\sqrt{\varepsilon_i} \tag{3.14}$$

$$\text{with} \quad s_0 = 0 \quad , \quad s_n = \frac{a}{2} \quad , \quad d_0 = 0 \quad \text{and} \quad d_n = D \quad .$$

Referring to Fig. 3.4, s_i $(i = 0, \ldots, n)$ denotes the x-position of the transition points at the interfaces. s_0 is set to 0 and $s_n = a/2$, which is the reflection point. This is a consequence of s_0, the antenna separation a and the assumption of a horizontal layering. All other transition points s_j $(j = 1, \ldots, n-1)$ must be set such, that Fermat's principle is fulfilled.

For this purpose, the travel time, given in Eq. (3.14), can be understood as a function of the unknown transition points

$$t_{\text{refl}} =: f(s_1, \ldots, s_{n-1}) = f(\mathbf{s}) \quad . \tag{3.15}$$

These unknowns themselves can be defined as a vector $\mathbf{s} = (s_1, \ldots, s_{n-1})$. The function f can be expanded into a Taylor-series

$$f(\mathbf{s}) \approx f(\mathbf{s}_0) + \mathbf{B}^{\mathrm{T}}\,(\mathbf{s} - \mathbf{s}_0) + \frac{1}{2}\,(\mathbf{s} - \mathbf{s}_0)^{\mathrm{T}}\,\underline{\mathbf{C}}\,(\mathbf{s} - \mathbf{s}_0) \quad , \tag{3.16}$$

which is truncated after the second derivative. The abbreviation for the vector $\mathbf{B}$ and the matrix $\underline{\mathbf{C}}$ are given as

$$\mathbf{B} = \Big(\partial_{s_1} f(\mathbf{s}_0)\,, \partial_{s_2} f(\mathbf{s}_0)\,, \ldots, \partial_{s_{n-1}} f(\mathbf{s}_0)\Big) \tag{3.17}$$

$$\underline{\mathbf{C}} = \begin{pmatrix} \partial^2_{s_1} f(\mathbf{s}_0) & \partial^2_{s_1,s_2} f(\mathbf{s}_0) & \cdots & \partial^2_{s_1,s_{n-1}} f(\mathbf{s}_0) \\ \partial^2_{s_2,s_1} f(\mathbf{s}_0) & \partial^2_{s_2} f(\mathbf{s}_0) & \cdots & \partial^2_{s_2,s_{n-1}} f(\mathbf{s}_0) \\ \vdots & \vdots & \ddots & \vdots \\ \partial^2_{s_{n-1},s_1} f(\mathbf{s}_0) & \partial^2_{s_{n-1},s_2} f(\mathbf{s}_0) & \cdots & \partial^2_{s_{n-1}} f(\mathbf{s}_0) \end{pmatrix} \quad , \tag{3.18}$$

with the derivatives

$$\frac{c}{2}\,\partial_{s_i} f = \frac{(s_i - s_{i-1})\,\sqrt{\varepsilon_i}}{\sqrt{(s_i - s_{i-1})^2 + (d_i - d_{i-1})^2}} - \frac{(s_{i+1} - s_i)\,\sqrt{\varepsilon_{i+1}}}{\sqrt{(s_{i+1} - s_i)^2 + (d_{i+1} - d_i)^2}} \tag{3.19}$$

$$\frac{c}{2}\,\partial^2_{s_i} f = \frac{(d_i - d_{i-1})^2\,\sqrt{\varepsilon_i}}{\big((s_i - s_{i-1})^2 + (d_i - d_{i-1})^2\big)^{3/2}} + \frac{(d_{i+1} - d_i)^2\,\sqrt{\varepsilon_{i+1}}}{\big((s_{i+1} - s_i)^2 + (d_{i+1} - d_i)^2\big)^{3/2}} \tag{3.20}$$

$$\frac{c}{2}\,\partial^2_{s_k,s_l} f = \begin{cases} -\dfrac{(d_k - d_l)^2\,\sqrt{\varepsilon_k}}{((s_k - s_l)^2 + (d_k - d_l)^2)^{3/2}} & , \quad \text{when} \quad k - l = 1 \\ 0 & , \quad \text{else} \end{cases} \quad . \tag{3.21}$$

The approximated function $f(\mathbf{s})$ corresponds to a paraboloid in $n-1$-dimensions. Its extremum is at the position $\mathbf{s}_e$, where the gradient is zero:

$$\nabla f(\mathbf{s}_e) = \mathbf{B} + \underline{\mathbf{C}}\,(\mathbf{s}_e - \mathbf{s}_0) \stackrel{!}{=} \mathbf{0} \quad . \tag{3.22}$$

The solution of the equation above can be found with the Newton-method for higher dimensions, which can be set up as

$$\mathbf{s}_{m+1} = \mathbf{s}_m - (\underline{\mathbf{C}}^{-1}\,\mathbf{B})_{\mathbf{s}_m} \qquad \text{with} \quad \lim_{m\to\infty} \mathbf{s}_m = \mathbf{s}_e \quad , \tag{3.23}$$

where m, $\mathbf{s}_e$ represent the number of iterations and the resulting parameter vector. The iteration can be stopped if the correction $\triangle\mathbf{s}_{m+1} = |\mathbf{s}_{m+1} - \mathbf{s}_m|$ is smaller than a given vector, where each entry denotes the error of its corresponding transition point. In order to guarantee convergence of the Newton-method, an adequate initial parameter vector must be found.

The initial parameter vector can be obtained at least with two methods. The first one is simply guessing by using a random number generator. When these random numbers are sorted and projected to the interval $[s_0, s_n]$, this leads to an initial parameter vector. Of course, this procedure must be repeated until the algorithm converges. As a second method, one can calculate the initial values with the straight line approach. Unfortunately, these transition points may not lead to a convergence of the algorithm. Especially this is the case, when the changes between the relative permittivity values of the layers or the antenna separation a is too large. But they lead to a convergence, when a relatively small antenna separation is assumed using the same material model. This can be used as an initial step of an iterative procedure, which increases the antenna separation to the desired value. Then, the transition points can be linearly projected to the larger antenna separation in each step, which are close to the actual values.

Straight Line Approach

Under the motive that refraction may not have a measurable influence on the travel times for smooth dielectric permittivity transitions, a travel path of a straight line can be assumed. With respect to Fig. 3.4 the relationship for the sections of this straight line in

each layer can be found as

$$\frac{a}{2\,D} = \frac{s_i - s_{i-1}}{d_i - d_{i-1}} \qquad \text{for} \qquad i = 1, \ldots, n \quad . \tag{3.24}$$

Therefore, the straight line travel time $t_{\text{refl}}^{\text{straight}}$ from a reflection after the transition of multiple layers is given by

$$t_{\text{refl}}^{\text{straight}} = \frac{2}{c}\sqrt{\frac{a^2}{4\,D^2} + 1}\,\left(\sum_{i=1}^{n}(d_i - d_{i-1})\,\sqrt{\varepsilon_i}\right) \quad . \tag{3.25}$$

Ray Tracing Method

The ray tracing method is based on linear ray propagation, refraction and reflection. For simplicity, it is assumed that the reflection, refraction and propagation processes take place on a single plane in two dimensions (Fig. 3.5). In a first step the starting point (x_0, z_0) and the direction angle α_0 must be defined. Furthermore, a material model must be given, which consists of n layers with a relative permittivity $(\varepsilon_1, \varepsilon_2, \ldots, \varepsilon_n)$. The layer boundaries are given by functions $d_i(x)$ $(i = 1, \ldots, n)$, which are not allowed to cross within the area of interest.

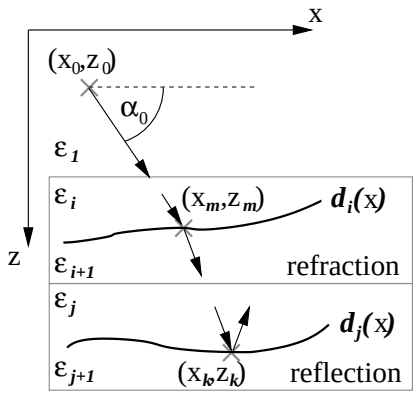

Figure 3.5: *Principle of the ray tracing method.*

The algorithm is performed as followed: From a starting point the ray tracing algorithm calculates the crossing point of the ray with the next layer boundary in propagation direction. There, a new direction angle is calculated depending on whether refraction or reflection shall occur. This crossing point is a new starting point.

Now, this procedure will be described mathematically. A ray starting at a position (x_m, z_m) with a direction angle α_m is written as

$$z(x) = (x - x_m)\,\tan\alpha_m + z_m \quad . \tag{3.26}$$

In the next step, the crossing point x_{m+1} of the m-th ray with the i-th layer boundary given by $d_i(x)$ is calculated with the Newton-method by minimizing the difference function $f(x) := z(x) - d_i(x)$. This yields

$$\begin{aligned} x_{m+1,l+1} &= x_{m+1,l} - \frac{f(x_{m+1,l})}{\partial_x f(x_{m+1,l})} \\ &= x_{m+1,l} - \frac{(x_{m+1,l} - x_m)\,\tan\alpha_m + z_m - d_i(x_{m+1,l})}{\tan\alpha_m - \partial_x d_i(x_{m+1,l})} \end{aligned} \tag{3.27}$$

with $l = 0, 1, 2, 3, \ldots$, which denotes the iteration steps of the Newton-method.

For the calculation of refraction and reflection, the definitions given in Fig. 3.6 are used. Then, the equations for a refraction are given by

$$\tan\gamma = \partial_x d_i(x_{m+1}) \qquad \varphi_1 = \frac{\pi}{4} - \alpha_m - \gamma \qquad \sin\varphi_2 = \sqrt{\frac{\varepsilon_m}{\varepsilon_{m+1}}}\,\sin\varphi_1 \tag{3.28}$$

$$\alpha_{m+1}^{\text{refr}} = \frac{\pi}{4} - \varphi_2 - \gamma \quad , \tag{3.29}$$

where $\alpha_{m+1}^{\text{refr}}$ only exists, when

$$\sqrt{\frac{\varepsilon_m}{\varepsilon_{m+1}}}\,\sin\varphi_1 < 1 \quad . \tag{3.30}$$

Otherwise, total reflection occurs. For reflection, the direction angle is calculated by

$$\begin{aligned} \tan\gamma &= \partial_x d_i(x_{m+1}) \\ \alpha_{m+1}^{\text{refl}} &= \pi - \alpha_m + 2\,\gamma \quad . \end{aligned} \tag{3.31}$$

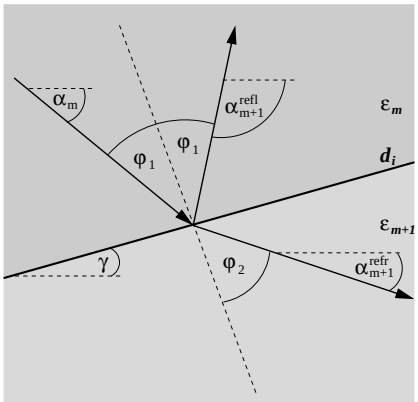

Figure 3.6: *Definitions for the reflection and the refraction description for the ray tracing method.*

With these equations, the travel path through an arbitrary layered medium can be calculated and from this the travel time. Unfortunately, the end point $(x_{\text{end}}, z_{\text{end}})$ can not be given at the beginning of the algorithm. For a given transmitter position and material model, this system has only two free parameters: (i) the direction angle α_0 of ray at the starting point and (ii) the z-position at end point z_{end}. Therefore, for a fixed z_{end} the x-position is a function of the direction angle: $x_{\text{end}} = x_{\text{end}}(\alpha_0)$.

In order to obtain the travel path from a given transmitter position (x_0, z_0) to a given receiver position $(x_{\text{rec}}, z_{\text{rec}} = z_{\text{end}})$, the Newton-method is applied to search the direction angle $\hat{\alpha}_0$, which fulfills

$$g(\hat{\alpha}_0) := x_{\text{rec}} - x_{\text{end}}(\hat{\alpha}_0) \stackrel{!}{=} 0 \quad . \tag{3.32}$$

This is obtained by the algorithm

$$\alpha_{0,l+1} = \alpha_{0,l} - \frac{g(\alpha_{0,l})}{\partial_{\alpha_0} g(\alpha_{0,l})} \qquad (l = 0, 1, 2, \ldots) \quad , \tag{3.33}$$

where the derivative $\partial_{\alpha_0} g(\hat{\alpha}_{0,l})$ can be given numerically as central differences

$$\partial_{\alpha_0} g(\hat{\alpha}_{0,l}) \approx \frac{g(\hat{\alpha}_{0,l} + \delta) - g(\hat{\alpha}_{0,l} - \delta)}{2\,\delta} \quad . \tag{3.34}$$

δ defines a small angle shift. It determines the numerical calculation of the derivation and which therefore must be defined appropriately. Again l gives the iteration number for the Netwon-method.

The limit of this procedure Eq. (3.33) should lead to the true direction angle, depending on the initial value. The convergence depends on the derivative given in Eq. (3.34) and the choice of the value δ. For instance, for refraction processes near the total refraction angles, very small changes of the starting direction angle α_0 can significantly change the result. Here, the angle shift δ, must be chosen very small.

3.3 Plane Wave Descriptions

Plane waves are solutions of the homogeneous Maxwell's equations, which means that there are no sources of the electromagnetic fields. In other words, plane waves are far-field solutions. They are described by an angular frequency[2] ω and a propagation vector $\mathbf{k}$.

In the following, some aspects of plane wave propagation are presented, which are relevant for the description of GPR signal propagation. First, a possibility to describe the propagation of electromagnetic waves in homogeneous and dispersive media will be presented. Afterwards, the reflection process at sharp transitions is analyzed. Finally, a multi-layer modeling approach is presented, which can be used to study plane wave propagation through a fine layered medium, with almost smoothly changing material properties.

3.3.1 Propagation in Homogeneous Media

A single plane wave propagating in a homogeneous medium with a relative dielectric permittivity ε_r is given by

$$\mathbf{C}(\mathbf{r},t) = \mathbf{C}(\mathbf{k},\omega)\; e^{\mathtt{i}(\omega t - \mathbf{k}\cdot\mathbf{r})} \tag{3.35}$$

$$\text{with} \quad \mathbf{C} = \{\mathbf{E},\mathbf{H}\}$$

$$\text{and} \quad \omega = 2\pi\,\nu \quad , \quad |\mathbf{k}| = \frac{\omega}{c_0}\sqrt{\varepsilon_r} \quad . \tag{3.36}$$

Here, Eq. (3.35) is a general notation of the plane wave description for the electric field $\mathbf{E}$ and the magnetic field $\mathbf{H}$. The second part of Eq. (3.36) is called dispersion relationship. ν and ε_r are the physical frequency and the relative permittivity of the material. With Eq. (3.35), the electric field strength is calculated for a given position $\mathbf{r}$ and a given time t.

Now, a set of plane waves (with different angular frequencies) propagating in one dimension (x-direction) is assumed, which leads to the propagation constant $k = \omega\sqrt{\varepsilon_r}/c_0$. At the position $x = 0$, the electric field $\mathbf{E}(0,t)$ as a function of time yields

$$\mathbf{E}(0,t) = \int \mathbf{E}(\omega)\; e^{\mathtt{i}\omega t}\; d\omega \quad . \tag{3.37}$$

On the other hand, if the electric field in time domain is given, than the frequency components can be obtained by

$$\mathbf{E}(\omega) \;\; = \frac{1}{2\pi}\int \mathbf{E}(0,t)\; e^{-\mathtt{i}\omega t}\; dt \quad . \tag{3.38}$$

Now, it is used that the propagation vector in one dimension is a function of frequency. This allows us to calculate the electric field $\mathbf{E}(x,t)$ in time domain at every other position x with

$$\mathbf{E}(x,t) = \int \mathbf{E}(\omega)\; e^{\mathtt{i}(\omega t - k(\omega)\,x)}\; d\omega \quad . \tag{3.39}$$

Here, the propagation constant determines the phase and amplitude term for each frequency, which changes the time signal. If $k(\omega)$ is only a linear function of ω, which means that the medium is not dispersive and that the phase term changes equally for each frequency. This leads to a shift of the time signal. But for dispersive media, the dielectric permittivity is a complex value, which leads to a complex k. This implies that the imaginary part causes an amplitude change and the real part determines the phase or in other words the propagation velocity of the frequency component.

[2] Instead of angular frequency ω, also the frequency $\nu = \omega\,(2\,\pi)^{-1}$ measured in Hz (Hertz) can be used, but this would lead to the additional factor $2\,\pi$ in the descriptions.

3.3.2 Reflection and Transmission at a Sharp Dielectric Transition

The description of reflection and transmission of plane waves is a two dimensional problem (Fig. 3.7). For a single incoming plane wave with a propagation vector $\mathbf{k} = (k_{\mathrm{I},x}, 0, k_{\mathrm{I},z})$, the electric field $\mathbf{E}_\mathrm{I}$ is given as

$$\mathbf{E}_\mathrm{I}(x,z,t) = \mathbf{E}_\mathrm{I}(k_{\mathrm{I},x}, k_{\mathrm{I},z}, \omega)\; e^{\mathrm{i}(\omega t - k_{\mathrm{I},x}x - k_{\mathrm{I},z}z)} \tag{3.40}$$

$$\text{with} \quad k_{\mathrm{I},x}^2 + k_{\mathrm{I},z}^2 = \frac{\omega^2}{c_0^2}\,\varepsilon_1 \quad , \tag{3.41}$$

where ε_1 is the relative permittivity of the medium in which the incoming wave propagates. At the reflection point the x-component of the propagation vector remains constant for the transmitted and reflected field. Therefore, the propagation vectors for all involved waves can be calculated by

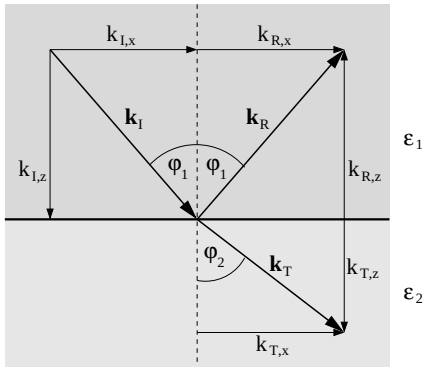

Figure 3.7: *Definition of the propagation vectors for transmission and reflection at a boundary.*

$$\mathbf{k}_\mathrm{I} = (k_{\mathrm{I},x}, k_{\mathrm{I},z}) \quad , \quad \mathbf{k}_\mathrm{R} = (k_{\mathrm{I},x}, -k_{\mathrm{I},z}) \quad \text{and} \quad \mathbf{k}_\mathrm{T} = \left(k_{\mathrm{I},x}, \sqrt{\frac{\omega^2}{c_0^2}\,\varepsilon_2 - k_{\mathrm{I},x}^2}\right) \quad , \tag{3.42}$$

where ε_2 is the relative permittivity of the medium in which the transmitted wave propagates.

For the derivation for the reflection and transmission coefficients, it is necessary to split the incoming electric field into two polarizations, which are given as

$$\mathbf{E}_\mathrm{S} = \mathbf{E}_\mathrm{S}^{(\mathrm{TE})} + \mathbf{E}_\mathrm{S}^{(\mathrm{TM})} \tag{3.43}$$

with $\mathrm{S} = \{\mathrm{I}, \mathrm{R}, \mathrm{T}\}$ and with the definitions

$$\begin{aligned} &\mathbf{E}_\mathrm{S}^{(\mathrm{TE})} \cdot \mathbf{n} = 0 \\ \text{and} \qquad &\left(\mathbf{k} \times \mathbf{E}_\mathrm{S}^{(\mathrm{TM})}\right) \cdot \mathbf{n} = 0 \quad . \end{aligned} \tag{3.44}$$

Here, $\mathbf{n}$ is the normal vector on the boundary. In these equations the abbreviation TE stands for "transversal electric" and TM for "transversal magnetic", which assigns the oscillation plane of the electric and magnetic field.

Now, the reflection coefficient $R^{(\mathrm{TE})}$ and the transmission coefficient $T^{(\mathrm{TE})}$ for TE-polarization are given as

$$R^{(\mathrm{TE})} = \frac{\sqrt{\varepsilon_1}\,\cos\varphi_1 - \sqrt{\varepsilon_2}\,\cos\varphi_2}{\sqrt{\varepsilon_1}\,\cos\varphi_1 + \sqrt{\varepsilon_2}\,\cos\varphi_2} = \frac{\sqrt{\varepsilon_1}\,\cos\varphi_1 - \sqrt{\varepsilon_2 - \varepsilon_1\,\sin^2\varphi_1}}{\sqrt{\varepsilon_1}\,\cos\varphi_1 + \sqrt{\varepsilon_2 - \varepsilon_1\,\sin^2\varphi_1}} \tag{3.45}$$

$$T^{(\mathrm{TE})} = \frac{2\sqrt{\varepsilon_1}\,\cos\varphi_1}{\sqrt{\varepsilon_1}\,\cos\varphi_1 + \sqrt{\varepsilon_2}\,\cos\varphi_2} = \frac{2\sqrt{\varepsilon_1}\,\cos\varphi_1}{\sqrt{\varepsilon_1}\,\cos\varphi_1 + \sqrt{\varepsilon_2 - \varepsilon_1\,\sin^2\varphi_1}} \quad , \tag{3.46}$$

where φ_1 and φ_2 are the incoming and refracted angles as illustrated in Fig. 3.7. Because the TM-polarization has not much relevance in this work, the corresponding formulas are omitted. It must be noted that Eq. (3.45) and (3.46) are the Fresnel equations for TE polarization.

Time Domain Analysis

All considerations above focus on a single plane wave in the frequency domain. In contrast, GPR signals deal with time domain signals. Therefore, the reflection of wavelets / electromagnetic time signals should analyzed in more detail.

General Description: The local and temporal description of an incoming and a reflected wave is given by

$$E_{\mathrm{I}}(x,z,t) = \iint d\omega\, dk_z\; E_{\mathrm{I}}(k_z,\omega)\, e^{\mathtt{i}(\omega t - k_x x - k_z z)} \tag{3.47}$$

$$E_{\mathrm{R}}(x,z,t) = \iint d\omega\, dk_z\; R(k_x,\omega)\, E_{\mathrm{I}}(k_z,\omega)\, e^{\mathtt{i}(\omega t - k_x x + k_z z)} \quad . \tag{3.48}$$

If the complex reflection coefficient is written in an absolute $|R(k_x,\omega)|$ and a phase term with $\xi(k_x,\omega)$, this yields

$$E_R(x,z,t) = \iint d\omega\, dk_z\; |R(k_x,\omega)|\, e^{\mathtt{i}\xi(k_x,\omega)}\, E_I(k_z,\omega)\, e^{\mathtt{i}(\omega t - k_x x + k_z z)} \quad . \tag{3.49}$$

From this equation, it can be concluded that the incoming wavelet stays only constant in shape, when the reflection coefficient is a real number, which is valid when both media are not dispersive and when the incoming angle is not equal to or larger than the total reflection angle. Otherwise, when the reflection coefficient is complex, the shape of the reflected signal will change.

Total Reflection: For total reflection, a specific behavior of the wavelet in time and space is described by the Goos-Hänchen shift (Goos and Hänchen, 1947), which was analyzed and validated by Artmann (1948) and Chiu and Quinn (1972). This effect predicts shifts in the travel time and of the reflection point. The derivation of these shifts presumes that the phase term of the reflection coefficient can be approximated as a linear function.

Arbitrary Reflection: For arbitrary reflections, one could also assume that the absolute part of the reflection coefficient is constant for the applied frequency and propagation vector range. Furthermore, it could be assumed that the phase function can be approximated in a Taylor-series truncated after the linear term. Mathematically, this can be expressed as

$$|R(k_x,\omega)| = |R| = \text{const.} \tag{3.50}$$

$$\xi(k_x,\omega) = \xi_0 + \partial_{k_x}\xi|_{(k_{x,0},\omega_0)}\,(k_x - k_{x,0}) + \partial_\omega \xi|_{(k_{x,0},\omega_0)}\,(\omega - \omega_0)$$

$$\xi(k_x,\omega) = \xi_0 + \xi'_{k_x}\,(k_x - k_{x,0}) + \xi'_\omega\,(\omega - \omega_0) \quad , \tag{3.51}$$

where $\xi_0 = \xi(k_{x,0},\omega_0)$. These assumptions are rough and therefore, if the following equations will be applied to a scientific context, then the assumptions must be verified. Alternatively, the full expression for the reflection coefficient should be used to describe the reflected wave field.

With respect to Eq. (3.45), the reflection coefficient is given as a function of frequency and incoming angle. Because, in the following equations the derivative after the x-component of the propagation vector k_x is required, this derivative can be given as

$$\partial_{k_x}\xi = \partial_\varphi \xi\, \partial_{k_x}\varphi = \partial_\varphi \xi\, \frac{1}{|\mathbf{k}|\,\cos\varphi} \quad \text{with} \quad k_x = |\mathbf{k}|\,\sin\varphi \quad . \tag{3.52}$$

When Eq. (3.51) is inserted into Eq. (3.49), this equation becomes

$$E_R(x,z,t) = |R|\, e^{\mathtt{i}(\xi_0 - \xi'_{k_x}\, k_{x,0} - \xi'_\omega\, \omega_0)} \iint d\omega\, dk_z\;\; \tilde{E}_I(k_z,\omega)\, e^{\mathtt{i}(\omega(t+\xi'_\omega) - k_x(x-\xi'_{k_x}) - k_z z)}$$

$$E_R(x,z,t) = |R|\, \Re\mathrm{e}\Big[e^{\mathtt{i}(\xi_0 - \xi'_{k_x}\, k_{x,0} - \xi'_\omega\, \omega_0)}\Big]\;\; E_I(x-\xi'_{k_x}, z, t+\xi'_\omega) \quad , \tag{3.53}$$

where $\xi'_{k_x} = \partial_{k_x}\xi$ and $\xi'_\omega = \partial_\omega \xi$.

The last equation shows that a reflection of a wavelet can be shifted in time and also in space depending on the derivatives of the phase term of the reflection coefficient. This means that reflections at a boundary between two non-dispersive media do not show this effect, at least when no total reflection occurs.

Evanescent Waves

Electromagnetic waves show another interesting behavior at transitions from a medium with a lower to a medium with a higher permittivity. Using Fig. 3.7 and assuming that $\varepsilon_1 > \varepsilon_2$, then the propagation vector of the transmitted wave yields

$$\mathbf{k}_\mathrm{T} = (k_{\mathrm{T},x}, k_{\mathrm{T},z}) = \left(k_{\mathrm{I},x}, \sqrt{\frac{\omega^2}{c_0^2}\,\varepsilon_2 - k_{\mathrm{I},x}^2}\right) = \left(k_{\mathrm{I},x}, \frac{\omega}{c_0}\sqrt{\varepsilon_2 - \varepsilon_1\,\sin^2\varphi_1}\right) \quad . \tag{3.54}$$

For this relationship, the dispersion relationship Eq. (3.41) for the transmitted field and the refraction law Eq. (3.28) were used. When the incoming angle φ_1 is larger than the total reflection angle, cf. Eq. (3.7), $k_{\mathrm{T},z}$ becomes imaginary, because

$$\varphi_1 > \varphi_\mathrm{tot} \quad\Longrightarrow\quad \varepsilon_1\,\sin^2\varphi_1 > \varepsilon_2 \quad\Longrightarrow\quad k_{\mathrm{T},z} = -\mathtt{i}\,\frac{\omega}{c_0}\sqrt{\varepsilon_1\,\sin^2\varphi_1 - \varepsilon_2} \quad . \tag{3.55}$$

Now, with the complex z-component of the propagation vector, a single transmitted plane wave can be described with

$$\mathbf{E}_\mathrm{T}(x,z,t) = T\,\mathbf{E}_\mathrm{I}(k_{\mathrm{I},x}, k_{\mathrm{I},z}, \omega)\; e^{\mathtt{i}(\omega t - k_{\mathrm{I},x}x)}\; e^{-z\,\omega/c_0\,\sqrt{\varepsilon_1\,\sin^2\varphi_1 - \varepsilon_2}} \quad , \tag{3.56}$$

where T is the transmission coefficient for either TE- or TM-polarization. The very last term shows an exponential decay depending on the position z, the angular frequency ω, the incoming angle φ_1 and the relative permittivities of both media, ε_1 and ε_2. This equation also underlines the negative sign in Eq. (3.55), because otherwise the field strength of the transmitted field would increase exponentially, which violates the energy conservation law.

A special case of Eq. (3.56) exists for $\varphi_1 = \pi/2$. This means that in medium 1 the wave propagates parallelly to the boundary. Then the field in medium 2 is proportional to

$$\mathbf{E}_\mathrm{T}(x,z,t) \sim e^{\mathtt{i}(\omega t - k_{\mathrm{I},x}x)}\; e^{-z\,\omega/c_0\,\sqrt{\varepsilon_1 - \varepsilon_2}} \quad . \tag{3.57}$$

The proportionality is used because for the parallel propagation of a wave in medium 1 the transmission coefficient becomes zero. On the other hand, when this wave is detectable in medium 2, the decay of that field can be described as a function of distance from the interface, frequency and dielectric contrast.

3.3.3 Multi-Layer Modeling

Overview

There are different procedures to model plane wave propagation in a horizontally layered medium and its general reflection and transmission behavior. For instance, one can apply

the before mentioned algorithms for wavelet propagation and for transmission and reflection. Another evaluation approach for multi-layered media is the calculation of a general reflection coefficient by iterative methods (Chew, 1990)

Here, a method will be presented, which is used in optical applications, such as waveguide descriptions (Chen *et al.*, 2000). It was adapted to GPR studies for similar objectives by Strobbia and Cassiani (2007). In contrast to these applications, this method is used to derive a general reflection coefficient. But it allows the calculation of the electric field in the multi-layered medium.

The derivation of this method can be outlined as follows: It is started by describing the propagation of electromagnetic waves in homogeneous media by Maxwell's equations. The fields are split in two polarizations. A procedure using a single matrix is developed, which predicts the propagation of a plane wave in a homogeneous medium from one to another point. When the continuous field components are used, the propagation of a plane wave through a layered medium is formulated as a successive application of this matrix procedure, which leads to a global propagation matrix. Now, a generalized reflection coefficient can be calculated.

Mathematical Formulation

A model setup as presented in Fig. 3.4 is used. The boundaries between media with different dielectric properties are placed in the x-y-plane. And the layered media is only defined between $z \in [0, D]$. In the following, it is assumed that plane waves approach from $z < 0$. Furthermore, the lower end of the layered medium $z = D$ must set appropriately, so that either the medium for $z > D$ is homogeneous or that no further reflections are expected from below.

The derivation starts with the homogeneous Maxwell's equations in frequency domain in the ith layer with the relative permittivity $\varepsilon_{r,i}(\omega)$ and the relative permeability $\mu_{r,i}$. They are given as

$$\varepsilon_0\, \varepsilon_{r,i}(\omega) \nabla \cdot \mathbf{E}(\mathbf{r}, \omega) = 0 \tag{3.58}$$

$$\mu_0\, \mu_{r,i} \nabla \cdot \mathbf{H}(\mathbf{r}, \omega) = 0 \tag{3.59}$$

$$\nabla \times \mathbf{E}(\mathbf{r}, \omega) = -\mathtt{i}\, \omega\, \mu_0\, \mu_{r,i}\, \mathbf{H}(\mathbf{r}, \omega) \tag{3.60}$$

$$\nabla \times \mathbf{H}(\mathbf{r}, \omega) = \quad \mathtt{i}\, \omega\, \varepsilon_0\, \varepsilon_{r,i}(\omega)\, \mathbf{E}(\mathbf{r}, \omega) \quad , \tag{3.61}$$

where $\mathbf{E}$ and $\mathbf{H}$ are the electric and magnetic field in frequency domain, which is denoted by the arguments. Because no sources are present, solutions superposed by plane waves can be assumed, analogous to Eq. (3.35). Then, from Eq. (3.58) and (3.59) the relationships

$$\mathbf{k} \cdot \mathbf{E}(\mathbf{k}, \omega) = \mathbf{k} \cdot \mathbf{H}(\mathbf{k}, \omega) = 0 \tag{3.62}$$

can be obtained. If the reflection phenomenon is studied in the x-z-plane, which leads to $k_y = 0$ and where the normal vector on the boundaries is $\mathbf{n} = (0, 0, 1)$, the fields can be split into two polarizations, which are given as

$$\text{TE:} \qquad \mathbf{E}^{(\mathrm{TE})} = (0, E_y, 0) \qquad \mathbf{H}^{(\mathrm{TE})} = (H_x, 0, H_z) \tag{3.63}$$

$$\text{TM:} \qquad \mathbf{E}^{(\mathrm{TM})} = (E_x, 0, E_z) \qquad \mathbf{H}^{(\mathrm{TM})} = (0, H_y, 0) \quad . \tag{3.64}$$

Because the space is unbounded in x-direction, one can perform the Fourier transformation for k_x

$$\mathbf{C}(x, z, \omega) = \int \mathbf{C}(k_x, z, \omega)\, e^{-\mathtt{i} k_x x}\, dk_x \qquad \text{with} \quad \mathbf{C} = \{\mathbf{E}, \mathbf{H}\} \quad . \tag{3.65}$$

Table 3.1: *Substitutions in Eq. (3.66) and (3.67) for general analysis*

	TE	TM
F	E_y	H_y
G	$-\mathtt{i}\omega\mu_0 H_x$	$\mathtt{i}\omega\varepsilon_0 E_x$
γ_i	$\mu_{r,i}^{-1}$	$\varepsilon_{r,i}^{-1}$

From Maxwell's equations Eq. (3.58)-(3.61), the following equations can be deduced for the continuous components and both polarizations

$$\left(\frac{d^2}{dz^2} + k_{z,i}^2\right) F(z) = 0 \tag{3.66}$$

$$G(z) = \gamma_i \frac{d}{dz} F(z) \quad . \tag{3.67}$$

Here, the substitutions for F, G and γ are listed in Tab. 3.1. The advantage of both equations with the corresponding substitutions is to handle both polarizations in the same manner. Furthermore, the usage of the continuous components allow a stepwise calculation for F and G for each layer without dealing with extra boundary conditions. One has only account for $\lim_{z\uparrow z_b} F = \lim_{z\downarrow z_b} F$ and $\lim_{z\uparrow z_b} G = \lim_{z\downarrow z_b} G$, where z_b denotes the depth of a single boundary.

A general solution of (3.66) and (3.67) is

$$F(z) = C_1\, e^{\mathtt{i}k_{z,i}z} + C_2\, e^{-\mathtt{i}k_{z,i}z} \tag{3.68}$$

$$G(z) = \mathtt{i}\gamma_i k_{z,i} \left(C_1\, e^{\mathtt{i}k_{x,i}z} - C_2\, e^{-\mathtt{i}k_{z,i}z}\right) \quad . \tag{3.69}$$

Using the starting values $F(z_0)$ and $G(z_0)$ at an arbitrary position z_0 within the ith layer, one can obtain its solution on other positions z within the same layer by

$$\begin{pmatrix} F \\ G \end{pmatrix}_z = \begin{pmatrix} m_{11} & m_{12} \\ m_{21} & m_{22} \end{pmatrix} \begin{pmatrix} F \\ G \end{pmatrix}_{z_0} = \hat{\mathbf{m}}_{z,z_0} \begin{pmatrix} F \\ G \end{pmatrix}_{z_0} \tag{3.70}$$

with components

$$\begin{aligned} m_{11} = \cos[k_{z,i}(z-z_0)] \qquad m_{22} &= \cos[k_{z,i}(z-z_0)] \\ m_{12} &= \frac{1}{\gamma_i k_{z,i}} \sin[k_{z,i}(z-z_0)] \\ m_{21} &= -\gamma_i k_{z,i} \sin[k_{z,i}(z-z_0)] \end{aligned} \tag{3.71}$$

of the propagation matrix. Here, the subscript at the vector brackets denotes the position of the vector components.

Because F and G represent continuous field components, no boundary conditions need to be applied for the transition from one medium to another. Therefore, one can project the field at z_1 in layer i to z_2 in layer j by successively propagating the plane wave with the usage of the propagator matrix, which yields

$$\begin{pmatrix} F \\ G \end{pmatrix}_{z_2} = \underbrace{\hat{\mathbf{m}}_{z_2,d_j} \hat{\mathbf{m}}_{d_j,d_{j+1}} \ldots \hat{\mathbf{m}}_{d_{i-1},z_1}}_{\hat{\mathbf{M}}_{z_2,z_1}} \begin{pmatrix} F \\ G \end{pmatrix}_{z_1} \quad . \tag{3.72}$$

Now, a field F_0 in the upper half space $z \in (-\infty, 0]$ can be assumed as a superposition of the incoming (F_I) and the reflected (F_R) wave, which results in

$$F_0(z) = F_I\, e^{\mathtt{i}k_{0z}z} + F_R\, e^{-\mathtt{i}k_{0z}z} \tag{3.73}$$

$$G_0(z) = \mathtt{i}k_{0z}\gamma_0 \left(F_I\, e^{\mathtt{i}k_{0z}z} - F_R\, e^{-\mathtt{i}k_{0z}z}\right) \quad . \tag{3.74}$$

In the lower half space $z \in [D, \infty)$, where D denotes the lower boundary of the multi-layered system, there are no back-traveling field components and therefore, they equal the transmitted field

$$F_N(z) = F_T \, e^{\mathtt{i} k_{Nz}(z-D)} \tag{3.75}$$

$$G_N(z) = \mathtt{i} k_{Nz} \gamma_N \, F_T \, e^{\mathtt{i} k_{Nz}(z-D)} \quad . \tag{3.76}$$

Now, using these field specifications at $z = 0$, one can project the field to $z = D$ with Eq. (3.72) in the following way

$$\begin{pmatrix} F_T \\ \mathtt{i} k_{Nz} \gamma_N F_T \end{pmatrix}_D = \hat{\mathbf{M}}_{D,0} \begin{pmatrix} F_I + F_R \\ \mathtt{i} k_{0z} \gamma_0 (F_I - F_R) \end{pmatrix}_0 . \tag{3.77}$$

This leads to a general reflection coefficient

$$\mathcal{R} = \frac{\gamma_0 k_{0z} M_{22} - \gamma_N k_{Nz} M_{11} - \mathtt{i}(M_{21} + \gamma_0 \gamma_N k_{0z} k_{Nz} M_{12})}{\gamma_0 k_{0z} M_{22} + \gamma_N k_{Nz} M_{11} + \mathtt{i}\,(M_{21} - \gamma_0 \gamma_N k_{0z} k_{Nz} M_{12})} \tag{3.78}$$

with $F_R = \mathcal{R} F_I$ and to a general transmission coefficient

$$\mathcal{T} = \frac{2\,\gamma_0\, k_{0z}}{\gamma_0 k_{0z} M_{22} + \gamma_N k_{Nz} M_{11} + \mathtt{i}\,(M_{21} - \gamma_0 \gamma_N k_{0z} k_{Nz} M_{12})} \tag{3.79}$$

with $F_T = \mathcal{T} F_I$.

With the help of these reflection and transmission coefficients the reflected and the transmitted electric field can be calculated for an arbitrary incoming field. Furthermore, when the total electric field in the upper half-space is known due to the knowledge of the reflected wave, Eq. (3.72) can be applied to calculate the electric field at each position in the layered system.

The calculation of a general reflection and transmission coefficient requires a successive multiplication of matrices, cf. Eq. (3.72). Here, small errors in the calculation may increase significantly for a huge set of layers. In order to obtain an insight in what extent numerical errors occur in this procedure, the energy transfer through the layered medium should be examined. It can be stated that the transported energy by the reflected wave and the transmitted wave equal the incoming wave field. This is mathematically represented by the reflectivity ρ and the transmissivity τ, which leads to

$$\rho + \tau = 1 \quad . \tag{3.80}$$

Both quantities can be obtained from the reflection and transmission coefficient by

$$\rho = |\mathcal{R}|^2 \quad \text{and} \quad \tau = \frac{\Re\mathrm{e}(k_{Nz})}{k_{0z}} \, |\mathcal{T}|^2 \quad . \tag{3.81}$$

Now, the results of this algorithm for plane waves in multi-layered media can be checked by the proof of Eq. (3.80).

3.4 Near Field Analysis / Greens Function Approach

In the following, an approach is presented, which solves Maxwell's equations for a radiating vertical dipole placed in a horizontally layered medium. The theory was published by Hanson (2004a,b), who describes the basic equations to calculate the electric field for arbitrarily layered media doing an eigenvalue decomposition of the corresponding vector wave equation for the Hertzian potential. The additional contribution of this work to this theory is that the explicit eigenfunctions for a vertical dipole will be given.

This section is structured in four parts. The first and second part give an introduction to the Green's function description in electrodynamics and the representation with eigenfunctions. The third part presents the solutions for the eigenfunctions of a horizontally layered medium. The last part gives the equations for the determination of the Green's function of the horizontally layered medium.

Dyadic Green's Function Approach

One possibility for a Green's function approach in electrodynamics is to use the vector wave equation and assume a point excitation, mathematically given as Dirac-δ-function. This yields to the conditional equation for the dyadic-Green's function $\underline{\mathbf{g}}$. It is given by

$$-\left(\nabla^2 + k^2(z)\right)\ \underline{\mathbf{g}}(\mathbf{r},\mathbf{r}') = \underline{\mathbf{I}}\,\delta(\mathbf{r}-\mathbf{r}') \quad , \tag{3.82}$$

where $k^2(z) = \omega^2\,\mu\,\varepsilon(z)$ and $\omega = 2\pi\,\nu$ with the frequency ν measured in units of Hz (Hertz). Here, k and the relative permittivity ε are assumed to be only a function of the z-direction indicating a horizontal layering. The Green's function $\underline{\mathbf{g}}$ is considered as a matrix, where each row corresponds to a solution of an infinitesimal dipole with an orientation either in x, y or z-direction.

Eq. (3.82) gives a general vector wave equation. It can stand for the electric or magnetic field, but also for the Hertzian potential[3] $\boldsymbol{\pi}_e$. In the following, this potential is considered, which can be calculated with help of the Green's function by

$$\boldsymbol{\pi}_e(\mathbf{r},\omega) = -\int_\Omega \underline{\mathbf{g}}(\mathbf{r},\mathbf{r}')\cdot\frac{\mathbf{J}(\mathbf{r}',\omega)}{\mathtt{i}\,\omega\,\varepsilon_0\,\varepsilon_r(z')}\,d\Omega' \quad , \tag{3.83}$$

where $\mathbf{J}$ denotes the current density, which evokes the propagating electromagnetic waves. ε_0 and ε_r are the dielectric constant and the relative permittivity, which vary in z-direction in order to simulate a horizontally layered structure. If a single (infinitesimal) dipole is assumed at a position $\mathbf{r}_0$, Eq. (3.83) can be rewritten as

$$\begin{aligned} &\mathbf{J}(\mathbf{r}',\omega) = \tilde{\mathbf{J}}(\omega)\,\delta(\mathbf{r}'-\mathbf{r}_0) \\ &\Longrightarrow \quad \boldsymbol{\pi}_e(\mathbf{r},\omega) = -\underline{\mathbf{g}}(\mathbf{r},\mathbf{r}_0)\cdot\frac{\tilde{\mathbf{J}}(\omega)}{\mathtt{i}\,\omega\,\varepsilon_0\varepsilon_r(z_0)} \quad . \end{aligned} \tag{3.84}$$

Then, the electric field in frequency domain can be calculated by

$$\mathbf{E}(\mathbf{r},\omega) = \left(k^2(z) + \nabla\nabla\cdot\right)\boldsymbol{\pi}_e(\mathbf{r},\omega) \quad . \tag{3.85}$$

For the study of the vertical dipole $\mathbf{J} = (0,0,J_z)$, the Hertzian vector has only one component $\boldsymbol{\pi}_e = (0,0,\pi_z)$, which also reduces the Green's tensor $\underline{\mathbf{g}}$ to a scalar function g. This

[3] The derivation of the vector wave equation for the Hertzian potential is given in Appendix A.2.

simplifies the expression with the double ∇-operator. Therefore, with this assumption, the components of the electric field are given as

$$E_x(\mathbf{r},\omega) = \frac{\partial^2}{\partial x \partial z}\pi_z \qquad E_y(\mathbf{r},\omega) = \frac{\partial^2}{\partial y \partial z}\pi_z$$
$$E_z(\mathbf{r},\omega) = k^2(z)\pi_z + \frac{\partial^2}{\partial x^2}\pi_z \quad , \tag{3.86}$$

where the derivation can be expressed numerically using for instance central differences. In a mixed case, this derivation is given as

$$\frac{\partial^2 \pi_z(\eta,z)}{\partial \eta \partial z} \approx \frac{1}{\triangle\eta\triangle z}\Big[\pi_z(\eta+\triangle\eta, z+\triangle z) + \pi_z(\eta-\triangle\eta, z-\triangle z)$$
$$- \pi_z(\eta+\triangle\eta, z-\triangle z) - \pi_z(\eta-\triangle\eta, z+\triangle z)\Big] \quad , \tag{3.87}$$

where η stands either x or y. At last, the time domain solution can be obtained with a Fourier transformation of the electric field components given in Eq. (3.86).

Eigenfunction Approach

A horizontally layered medium as shown in Fig. 3.4 is considered. To calculate the Green's function g, it is assumed that it can be expressed as a linear combination of the eigenfunctions of the operator $\mathcal{L} = -(\nabla^2 + k^2)$, which can be understood as Storm-Liouville Problem of the third kind (Dudley, 1994). Because of the model approach of a layered medium, the eigenfunction problem can be reduced to a linear differential equation of second order (Hanson, 2004a)

$$\mathcal{L}u_{\xi,j}(z) = -\left(\frac{d^2}{dz^2} + k_j^2\right) u_{\xi,j}(z) = \xi\, u_{\xi,j}(z) \quad , \tag{3.88}$$

where $u_{\xi,j}$ denotes the eigenfunction for the jth layer and the eigenvalue ξ. At the layer boundaries d_j, these eigenfunctions must fulfill

$$u_{\xi,j}\Big|_{d_j} = \frac{\varepsilon_{j+1}}{\varepsilon_j}\, u_{\xi,j+1}\Big|_{d_j} \quad \text{and} \quad \frac{d\,u_{\xi,j}}{dz}\Big|_{d_j} = \frac{d\,u_{\xi,j+1}}{dz}\Big|_{d_j} \quad , \tag{3.89}$$

which result from the transition conditions of the Hertzian vector potential and can be derived from the conditions for the electric and magnetic field components (Sommerfeld, 1926). To obtain the Green's functions, the adjoint eigenvalue problem must be formulated (Hanson, 2004a; Dudley, 1994), which is given as

$$\mathcal{L}^\star v_{\xi,j}(z) = -\left(\frac{d^2}{dz^2} + \bar{k}_j^2\right) v_{\xi,j}(z) = \bar{\xi}\, v_{\xi,j}(z) \quad , \tag{3.90}$$

where $\mathcal{L}^\star$ is the adjoint operator and $v_{\xi,j}$ the adjoint eigenfunction for the jth layer and the eigenvalues[4] $\bar{\xi}$. The transition conditions for the adjoint eigenfunctions are

$$v_{\xi,j}\Big|_{d_j} = v_{\xi,j+1}\Big|_{d_j} \quad \text{and} \quad \frac{d\,v_{\xi,j}}{dz}\Big|_{d_j} = \frac{\bar{\varepsilon}_i}{\bar{\varepsilon}_{j+1}}\frac{d\,v_{\xi,j+1}}{dz}\Big|_{d_j} \quad , \tag{3.91}$$

which can be derived from the definition of adjoint operator

$$\int_\Omega \mathcal{L}u(z)\ \bar{v}(z)\, d\Omega = \int_\Omega u(z)\ \mathcal{L}^\star\bar{v}(z)\, d\Omega \tag{3.92}$$

[4]The bar denotes the conjugated complex value.

assuming vanishing functions at infinity. Because the eigenfunctions can be determined except for a constant factor, they must be normalized by

$$\int_\Omega u_\xi \, \bar{v}_{\xi'} \, d\Omega = \begin{cases} \delta_{\xi\xi'} & \text{for the discrete spectrum} \\ \delta(\xi - \xi') & \text{for the continuous spectrum} \end{cases} \quad . \tag{3.93}$$

Furthermore, they must fulfill

$$\int_\Omega u_\xi \, \bar{u}_\xi \, d\Omega = \int_\Omega |u_\xi|^2 \, d\Omega < \infty \quad \text{and} \quad \int_\Omega v_\xi \, \bar{v}_\xi \, d\Omega = \int_\Omega |v_\xi|^2 \, d\Omega < \infty \quad . \tag{3.94}$$

The last conditions are set up to guarantee that the eigenfunctions decay to zero for $z \to \pm\infty$ in a way that the integral does not diverge. This is necessary to obtain physically meaningful solutions.

Now, the Green's function results from the eigenfunctions (Hanson, 2004b)

$$\begin{aligned} g(\mathbf{r}, \mathbf{r}') = \frac{1}{4\mathtt{i}} \Bigg[& \sum_{n=1}^{M} u_{\xi_n}(z) \, \bar{v}_{\xi_n}(z') \, H_0^{(2)} \left(\rho \sqrt{-\xi_n} \right) \\ & - 2 \int_{-k_N}^{\mathtt{i}\infty} u_\zeta(z) \, \bar{v}_\zeta(z') \, H_0^{(2)}(-\rho\zeta) \, \zeta \, d\zeta \Bigg] \end{aligned} \tag{3.95}$$

by summing up all contributions from the discrete spectrum and integrating over the continuous spectrum. M denotes the number of discrete eigenvalues. Here, $H_0^{(2)}$ is the Hankel function for complex arguments of second kind and zero order. Furthermore, $k_N = \omega \sqrt{\varepsilon_{r,N}}/c_0$ and $\zeta = \mathtt{i}\sqrt{\xi}$.

Eigenfunctions for Layered Media

Equation (3.88) and (3.90) lead to exponential and oscillating basis-functions, depending on the leading sign of $\xi + k_j^2$. It can be shown that eigenvalues $\xi < -k_1^2$ and $\xi < -k_N^2$ evoke proper basis-functions, where ξ holds discrete values. In order to obtain these discrete values ξ_n, a resulting transcendental equation must be solved (Hanson, 2004a).

Introducing the assumptions

$$\begin{aligned} \varepsilon_j \in \mathbf{R} \quad \text{and} \quad \varepsilon_j \geq 1 \quad \forall\, j = 1, \ldots, N \\ \text{and} \quad \varepsilon_N > \varepsilon_i \quad \forall\, i = 1, \ldots, N-1 \quad , \end{aligned} \tag{3.96}$$

the transcendental equation has no zero points and therefore, only the solutions for $\xi > -k_N^2$ must be found. Thus, all eigenvalues belong to the continuous spectrum. A general approach for these improper eigenfunctions to solve (3.88) and (3.90) can be given by

$$\begin{aligned} u_{\xi,j}(z\,; A_j, B_j) &= A_j \, e^{\mathtt{i}\beta_j(z-d_j)} + B_j \, e^{-\mathtt{i}\beta_j(z-d_j)} \\ v_{\xi,j}(z\,; C_j, D_j) &= C_j \, e^{\mathtt{i}\bar{\beta}_j(z-d_j)} + D_j \, e^{-\mathtt{i}\bar{\beta}_j(z-d_j)} \quad , \end{aligned} \tag{3.97}$$

where $\beta_j = \sqrt{\xi + k_j^2}$. The transition conditions (3.89) and (3.91) lead to an access to the unknown constants in Eq. (3.97), which are

$$A_j = \frac{1}{2} \frac{\varepsilon_{j-1}}{\varepsilon_j} \, u_{\xi,j-1}(d_j\,; A_{j-1}, B_{j-1}) + \frac{\beta_{j-1}}{\beta_j} \, u_{\xi,j-1}(d_j\,; A_{j-1}, -B_{j-1}) \tag{3.98}$$

$$B_j = \frac{1}{2} \frac{\varepsilon_{j-1}}{\varepsilon_j} \, u_{\xi,j-1}(d_j\,; A_{j-1}, B_{j-1}) - \frac{\beta_{j-1}}{\beta_j} \, u_{\xi,j-1}(d_j\,; A_{j-1}, -B_{j-1}) \tag{3.99}$$

$$C_j = \frac{1}{2} \, v_{\xi,j-1}(d_j\,; C_{j-1}, D_{j-1}) + \frac{\beta_{j-1}}{\beta_j} \frac{\varepsilon_j}{\varepsilon_{j-1}} \, v_{\xi,j-1}(d_j\,; C_{j-1}, -D_{j-1}) \tag{3.100}$$

$$D_j = \frac{1}{2} \, v_{\xi,j-1}(d_j\,; D_{j-1}, C_{j-1}) - \frac{\beta_{j-1}}{\beta_j} \frac{\varepsilon_j}{\varepsilon_{j-1}} \, v_{\xi,j-1}(d_j\,; C_{j-1}, -D_{j-1}) \quad . \tag{3.101}$$

Here, for example the notation $u_{\xi,j-1}(d_j\,;A_{j-1},B_{j-1})$ means that the eigenfunction for the $(j-1)$th layer is required at the boundary layer d_j and it depends on the constants A_{j-1} and B_{j-1}.

For the first layer, the coefficients A_1, B_1, C_1 and D_1 must be set (except from a constant) depending on the value of ξ. For the case (1) of $\xi < -k_1^2$ the coefficients are

$$A_1^{(1)} = C_1^{(1)} = 0 \quad \text{and} \quad B_1^{(1)} = D_1^{(1)} = 1 \quad , \tag{3.102}$$

because Eq. (3.88) leads to exponential functions, which must vanish for $z \to \infty$, cf. (3.94). The eigenvalues of $\xi > -k_1^2$ split into two cases [(2) and (3)], which lead to the coefficients

$$A_1^{(2)} = C_1^{(2)} = \frac{1}{2\mathtt{i}} \qquad B_1^{(2)} = D_1^{(2)} = -\frac{1}{2\mathtt{i}} \tag{3.103}$$

$$A_1^{(3)} = C_1^{(3)} = \frac{1}{2} \qquad B_1^{(3)} = D_1^{(3)} = \frac{1}{2} \quad . \tag{3.104}$$

Therefore, case (2) equals a sine-function in the first layer and case (3) a cosine function. If a linear combination of both is used, the eigenvalue problem is overestimated. Furthermore, this splitting is required in order to obtain the same solutions for the free radiating dipole as presented by Hanson (2004b).

For all given coefficients Eq. (3.102)-(3.104), the before mentioned constant was neglected, which would be reproduced in all other functions for the different layers. This constant determines the normalization factor, which is also a function of ξ and which must be calculated for each case. Evaluating the integral Eq. (3.93) leads to

$$\begin{aligned}
\alpha^{(1)} &= 2\pi|\beta_N|\left(A_N^{(1)}\bar{C}_N^{(1)} + B_N^{(1)}\bar{D}_N^{(1)}\right)\\
\alpha^{(2)} &= 2\pi|\beta_1|\left(A_1^{(2)}\bar{C}_1^{(2)} + B_1^{(2)}\bar{D}_1^{(2)}\right) + 2\pi|\beta_N|\left(A_N^{(2)}\bar{C}_N^{(1)} + B_N^{(2)}\bar{D}_N^{(2)}\right)\\
\alpha^{(3)} &= 2\pi|\beta_1|\left(A_1^{(3)}\bar{C}_1^{(3)} + B_1^{(3)}\bar{D}_1^{(3)}\right) + 2\pi|\beta_N|\left(A_N^{(3)}\bar{C}_N^{(3)} + B_N^{(3)}\bar{D}_N^{(3)}\right) \quad .
\end{aligned} \tag{3.105}$$

Green's Functions for Layered Media

For the material model defined in Eq. (**??**), which leads to the eigenfunctions above, Eq. (3.95) yields

$$\begin{aligned}
g(\mathbf{r},\mathbf{r}') &= \frac{\mathtt{i}}{2}\int_{-k_N}^{\mathtt{i}\infty} \underbrace{\frac{u_\zeta(z)\,\bar{v}_\zeta(z')}{\alpha}\,H_0^{(2)}(-\rho\zeta)\,\zeta}_{\mathcal{I}}\,d\zeta\\
&= \frac{\mathtt{i}}{2}\int_{-k_N}^{-k_1}\mathcal{I}^{(1)}\,d\zeta + \frac{\mathtt{i}}{2}\int_{-k_1}^{\mathtt{i}\infty}\left(\mathcal{I}^{(2)}+\mathcal{I}^{(3)}\right)d\zeta
\end{aligned} \tag{3.106}$$

where $\mathcal{I}$ is introduced as a substitution for the integrand and its superscript denotes the corresponding case. Furthermore, α is the normalization factor given in Eq. (3.105). Because all ε_j are assumed to be real values, all k_j can be sorted according to their numerical value

$$\underline{k}_1 < \underline{k}_2 < \cdots < \underline{k}_l = k_1 < \cdots < \underline{k}_N = k_N \tag{3.107}$$

in order to divide the integral into different sections $[-\underline{k}_{j+1}, -\underline{k}_j]$. Here, $\underline{k}_j$ denotes the sorted propagation constants, where in general this ordering does not correspond to the layered structure. Furthermore, the condition $\underline{k}_N = k_N$ stems from the initial assumptions

Eq. (3.96), which were set up to suppress the discrete spectrum of the eigenvalue problem. Now, Eq. (3.106) can be written as

$$g(\mathbf{r},\mathbf{r}') = \frac{\mathtt{i}}{2}\sum_{j=l}^{N-1}\int_{-\underline{k}_{j+1}}^{-\underline{k}_j} \mathcal{I}^{(1)}\,d\zeta + \frac{\mathtt{i}}{2}\sum_{j=1}^{l-1}\int_{-\underline{k}_{j+1}}^{-\underline{k}_j} \left(\mathcal{I}^{(2)}+\mathcal{I}^{(3)}\right)\,d\zeta + \frac{\mathtt{i}}{2}\int_{-\underline{k}_1}^{\mathtt{i}\infty} \left(\mathcal{I}^{(2)}+\mathcal{I}^{(3)}\right)\,d\zeta \quad . \tag{3.108}$$

3.5 Multi-Layer Model Validation

In this section, the plane wave multi-layer and the Green's function modeling approach will be tested. This is done by the simulation for given material models. Then, the results are compared with the ray approach predictions.

3.5.1 Plane Wave Modeling

Setup: The source of the electric field in the plane wave approach is given as a set of plane waves. Here, the initial electric field $\mathbf{E}_\mathrm{I}$ can be given as superposition of plane waves with different frequencies ν or its corresponding angular frequency $\omega = 2\,\pi\,\nu$, which leads to wavelets in the time domain. Furthermore, a radiation pattern can be defined by the usage of different incoming angles of the plane waves.

For the following example, the initial field $\mathbf{E}_\mathrm{I}$ as a function of space $\mathbf{r} = (x, y, z)$ and time t is explicitly given as

$$\mathbf{E}_\mathrm{I}(\mathbf{r},t) = \hat{\mathbf{e}}\int_{\omega_1}^{\omega_2}\int_{-\pi}^{\pi} f(\omega)\,g(\varphi)\,\exp\left\{\mathtt{i}\,\omega - \mathtt{i}\,k(\omega)\,(x\,\sin\varphi + z\,\cos\varphi)\right\}\,d\varphi\,d\omega \tag{3.109}$$

$$\text{with}\quad f(\omega) = (\mathtt{i}\,\omega)^4\,\frac{s\,A_w}{4\sqrt{\pi}}\,\exp\left\{-\frac{\omega^2\,s^2}{4} + \mathtt{i}\,\omega\,\tau_0\right\} \quad \text{and} \quad g(\varphi) = \cos^2\varphi \quad ,$$

where the function $g(\varphi)$ represents the radiation pattern by the angle ϕ. $\phi = 0$ corresponds to a downward radiation (in z-direction). $f(\omega)$ describes the shape of the wavelet, which is here the fourth derivative of the Gaussian in frequency domain. A_w, τ_0 and s determine the maximum amplitude of the wavelet, the starting time and the width of the wavelet and therefore its spectrum. $\hat{\mathbf{e}}$ gives the polarization of the electric field. Here, the oscillating axis of the electric field is chosen to be the y-axis, which leads to TE-polarization. ω_1 and ω_2 represents the boundaries for the angular frequency spectrum. Furthermore, k denotes the propagation constant as a function of angular frequency given as $k = \omega/c_0\,\sqrt{\varepsilon_c(\omega)}$, where ε_c is the relative permittivity in the upper half space. c_0 is the speed of light in vacuum.

This kind of initial electric field definition leads to a source similar to a circular wave, which originates at $\mathbf{r} = (0, 0, 0)$. It is invariant in y-direction. As an example, the following parameters of the initial wavelet are used

$$A_w = 10^{-6}\ [\mathrm{V/m\,s^2}] \quad \text{and} \quad s = 2.25\ \mathrm{ns} \quad \text{and} \quad \tau_0 = 0\ \mathrm{ns} \quad \text{and} \quad \hat{\mathbf{e}} = (0,1,0) \quad , \tag{3.110}$$

which leads to an approximate center frequency of 200 MHz. Now, a material model is set up as presented in Fig. 3.8c. From the simulation, the electric field as a function of time at different positions $\mathbf{r}_i = (a_i, 0, 0)$ for $i = 1, \ldots, N$ is extrated. Here, N=33 observation points were used with the an inteval of 0.1 m starting at $a_1 = 0.8$ m.

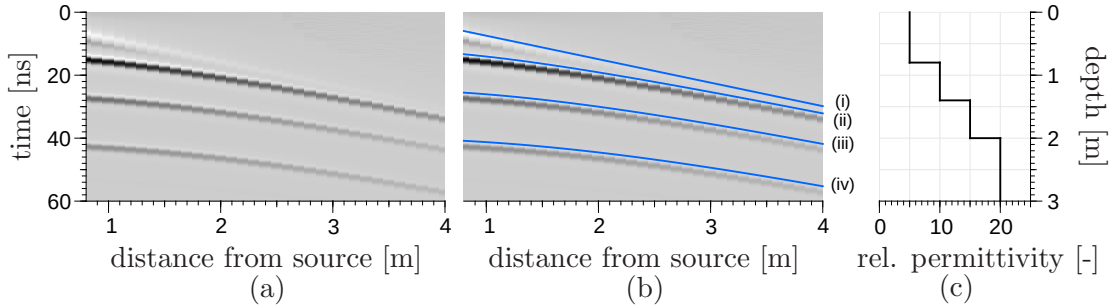

Figure 3.8: *Modeling example with multi-layer plane wave approach. The electric field (a) in the time domain is shown as a function of the distance from the source using the material model given in (c). Subfigure (b) presents the additional ray approach predictions:* (i) *direct wave,* (ii) *reflection from 0.8 m,* (iii) *reflection from 1.4 m,* (iv) *reflection from 2.0 m.*

Results: The results are shown in Fig. 3.8a. Here, all amplitudes of the y-component of the electric field (due to the chosen polarization) are scaled by

$$\tilde{E}_y = \begin{cases} \log_{10} E_y & , \text{ if } \quad E_y > 1 \\ -\log_{10} |E_y| & , \text{ if } \quad E_y < -1 \\ 0 & , \text{ else} \end{cases} \tag{3.111}$$

in order to emphasize reflections from the lower boundaries. In Fig. 3.8a, the identification of the amplitude values was neglected, because in almost all further applications, the phase information is of major interest. It should be mentioned that the white color denotes negative and the black color denotes strong positive amplitudes.

In order to underline the reliability of the phase information, ray approach travel times were inserted in Fig. 3.8b, which are calculated assuming a single reflection from each interface, including refraction at permittivity transitions. Multiple reflections are not considered. These ray approach travel times are only shifted from the reflections obtained from the plane wave approach by a constant value. The reason for this shift stems from the fact that the most visible wavelet feature was not emitted as $t = 0$ ns.

Spurious Waves

For the application of the plane wave modeling, it must be noted that a spurious wave occur, which appear before the start of signal time. This phenomenon is presented in Fig. 3.9 and it is explained in the following.

Setup: The modeled trace in Fig. 3.9 is obtained with the same material model (Fig. 3.8c) and an excitation described by Eq. (3.109) and (3.110). Only the starting time was set to $\tau_0 = 20$ ns, which is assigned to the start of signal time and corresponds to the center time of the used wavelet. Furthermore, the distance from the source point in the horizontal direction (x-direction) was set to 1 m.

Results: In Fig. 3.9, after the start of signal, four characteristic wavelets can be observed, which can be assigned to the direct wave and the reflections from each layer boundary. Additionally, before the start of signal time, another wavelet is visible, which seems to be symmetric to the direct wave.

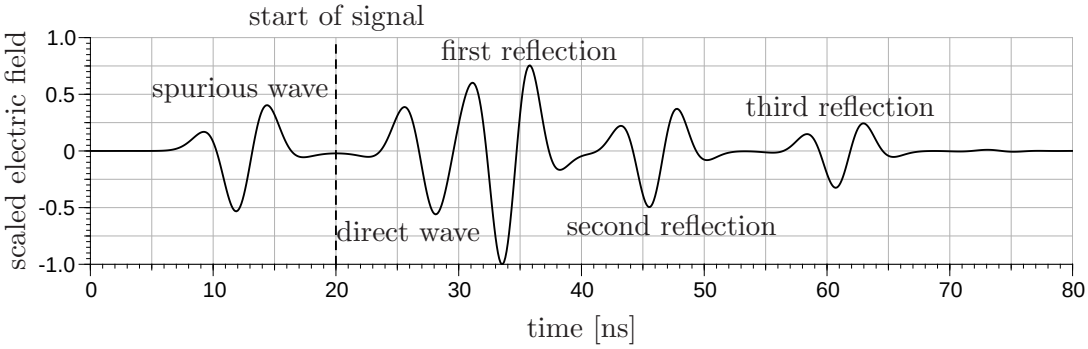

Figure 3.9: *Example of the occurrence of a spurious wave for the plane wave approach. For the modeling, the material setup presented in Fig. 3.8c was used as well as the excitation given in Eq.* (3.109) *and* (3.110) *with a different starting time of* $\tau_0 = 20$ *ns. The observation point was at* $(x, z) = (1, 0)$ *m.*

Explanation / Discussion: The existence of this spurious wave can be explained from the definition of the excitation. It is a superposition of plane waves and therefore, it is no realistic source.

A single plane wave is a steady state function, which exists for all times. Only a set of plane waves with different frequencies creates a localized signal in time. But this signal has no excitation point. Therefore, the defined excitation of a spherical wave at a point (x_0, z_0) is only a localized phenomena, which occurs by a superposition of incoming waves as presented in Fig. 3.10. Then, the outgoing wavefield represents the excitation.

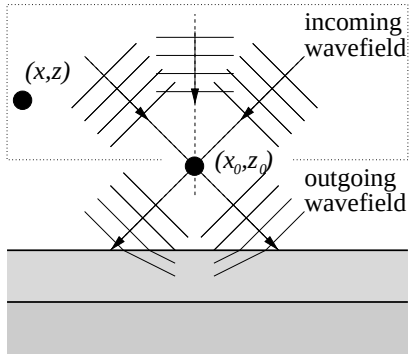

Figure 3.10: *Explanation for the occurrence of spurious waves in plane wave modelings.*

The incoming wavefield is the reason for the spurious wave, which is highlighted in Fig. 3.10. Here, the incoming field crosses the observation point (x, z) before the excitation time. Mathematically, this can be illustrated by the description of a single plane wave, propagating in x-direction. The phase term is given by

$$\ldots \exp\{\mathtt{i}\,\omega\,t - \mathtt{i}\,k_x\,x\} \ldots \quad . \tag{3.112}$$

This shows that a single phase propagates for an increasing time t to an increasing position x, when k_x is a positive value. Now, the same plane wave but with a negative wave constant k_x can be assumed. Then at the same position x, the corresponding phase term to the wave with the positive wave constant can be observed at the negative time.

3.5.2 Green's Approach Modeling

Setup: For the Green's function approach, beside the material model, the only input values are the z-component of the current density, the current density itself and the position of the radiating dipole. For this example, the current density is set to

$$J_z = f(\omega)\,\delta(\mathbf{r} - \mathbf{r}_0) \tag{3.113}$$

$$\text{with} \quad f(\omega) = (\mathtt{i}\,\omega)^3\,\frac{s\,A_w}{4\sqrt{\pi}}\,\exp\left\{-\frac{\omega^2\,s^2}{4} + \mathtt{i}\,\omega\,\tau_0\right\} \quad ,$$

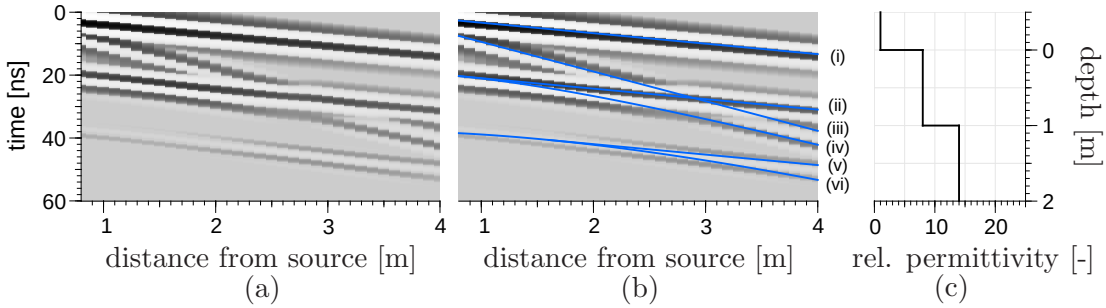

Figure 3.11: *Modeling example with multi-layer Greens function approach. Electric field (a) in time domain is shown as a function of the distance from the source using the material model given in (c). Subfigure (b) presents the additional plane wave predictions:* (i) *direct air wave,* (ii) *reflected-refracted wave,* (iii) *direct ground wave,* (iv) *reflection from 1.0 m,* (v) *double reflected-refracted wave,* (vi) *first multiple of the reflection from 1.0 m.*

where $f(\omega)$ defines the frequency spectrum of the source. Again, the parameters A_w, s and τ_0 define an amplitude value, the spectral composition and the radiation time. As numerical values, these parameters and the radiation position $\mathbf{r}' = (x, y, z)$ are used as

$$A_w = 10^{-24} \quad \text{and} \quad s = 2.25 \text{ ns} \quad \text{and} \quad \tau_0 = 0 \text{ ns} \quad \text{and} \quad \mathbf{r}' = (0, 0, -0.01 \text{ m}) \quad . \tag{3.114}$$

The material model is presented in Fig. 3.11c, which is a three-layer system. The upper layer corresponds to air with $\varepsilon_1 = 1$. The middle and the lower layer are defined by $\varepsilon_2 = 8$ and $\varepsilon_3 = 14$.

Results: In Fig. 3.11a, the z-component of the electric field for different distances from the receiver are shown. Here, the distance from the receiver denotes a growing horizontal / x-position, while keeping $z = -0.01$ m and $y = 0$.

In Fig. 3.11b the corresponding ray approach travel times are inserted. It can be seen that for this setup, almost the whole set of possible wave paths are observable. There are the direct waves (i) and (iii), Eq. (3.1), as well as the single reflection (iv), Eq. (3.2), and the double reflection (vi), Eq. (3.3) with $n = 2$. Furthermore, a reflected-refracted wave (ii), Eq. (3.8) and its second order type (v), Eq. (3.9) with $n = 2$ can be seen.

4 Ground Penetrating Radar - Basics

This chapter aims to provide a deepened analysis of ground penetrating radar (GPR), where the modeling approaches, presented in Chapter. 3, are used to demonstrate and to simulate some electromagnetic phenomena.

In the first sections of this chapter, an introduction to the measurement principle of GPR and some application techniques are presented, which are widely used. Then, some aspects on electromagnetic wave propagation with respect to GPR studies are analyzed. For example, it is focused on refraction and reflection in media with continuously changing dielectric properties, which could originate from the water content distribution in hydrological applications. Afterwards, some pre-processing algorithms for data enhancement of GPR radargrams are presented. Here, their effects and applicability are illustrated.

In the last section, some examples for processing procedures will be given and analyzed. Some of them are mandatory for GPR evaluations, such as the time zero correction. Other processing steps are the normal moveout, the windowed Fourier and the evanescent wave analysis, which are able to give additional information about the material model. For instance, the normal moveout analysis of a common midpoint measurement can provide an estimate of the vertical permittivity distribution at the measurement point. The evanescent wave analysis exploits the evanescent behavior of the ground wave in order to determine the surface permittivity.

4.1 Measurement Principle

A GPR system consists of at least one antenna, which then represents both the transmitter and receiver. Commonly, two antennas are used, where one is the transmitter and the other one is the receiver. The first setup is called monostatic mode and the second bistatic mode. Furthermore, an electronic setup is used, which applies a periodic current pulses to the transmitter, controls the data sampling at the receiving unit and synchronizes both. The current pulses at the transmitting antenna lead to propagating free waves, which are not bound to the electronics. Usually, commonly used GPR systems emit electromagnetic waves, which consist of frequencies between 10 MHz and 1 GHz. These free waves can penetrate the surrounding materials and structures. When they reach the receiver due to transmission, reflection or backscattering processes, they will be transformed into guided waves in the electronics. There, they can be measured as voltage or current values.

As a GPR survey, one can imagine for example that a transmitter-receiver unit is pulled over a distance. The result of a GPR survey yields a radargram, which consists of a set of traces. Each trace is the result of a single GPR measurement, which can be obtained by measuring at a different position, at a certain time or with a modified setup.

A whole trace is obtained in two steps. In the first step, the incoming signal at the receiver, due to transmission and reflection processes, is sampled. This leads to a raw trace, which could be affected by noise. In the next step, several raw traces are averaged[1]

[1] This kind of averaging is also called stacking.

in order to reduce this noise. Because the sampling and averaging requires reproducible time values, the receiving unit must be triggered with the transmitted pulse.

For this kind of data acquisitions, at least four parameters must be externally given for a GPR measurement, which are provided by the measurement software. These parameters are the *time window*, the *sampling number* or alternatively the *sampling frequency*, the *number of traces to average* (stacks) and the *starting time*. The time window determines the radius, wherefrom reflected signals can be measured, depending on the velocity of the waves. The sampling number and the sampling frequency define the temporal resolution of the signal. The starting time declares the initial point of the trigger. Because in the most cases, the time, when the electromagnetic pulse is transmitted, is not measured separately, the starting time can be an arbitrary time before or after the application of the current pulse. Therefore, these GPR measurements have a temporal offset.

At last, the data sampling can be imagined in the following way. For one incoming signal, the electronics opens a shutter at a defined measurement time for a given time period, which depends on the sampling frequency, and measures a single voltage value. Then this measurement time of the shutter is shifted after each sample, until the whole signal is sampled within the time window. For this measurement procedure the time t_{trace}, which is necessary to acquire a single trace, is

$$t_{\text{trace}} = N_{\text{stacks}} \cdot N_{\text{samples}} \cdot t_{\text{pulse}} \quad , \tag{4.1}$$

where N_{stacks} is the number of signals to average, N_{samples} is the number of samples per trace and t_{pulse} is the time between each transmitted pulse.

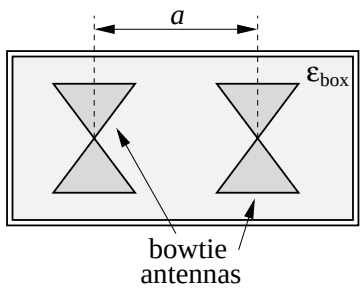

Figure 4.1: *Sketch of a shielded GPR system with two bowtie antennas with an antenna separation a.*

There are also some rigid parameters given by the antenna setup and construction, which determine a GPR measurement. In most GPR applications, mircostrip patch bowtie antennas are used (Fig. 4.1). They can be placed very close to the surface. This leads to a greater amount of energy transfer into the ground. The energy transfer is also determined by the relative permittivity ε_{box}, which surrounds the antenna. Furthermore, the energy transfer into the ground is increased, when the antennas are shielded (Lampe *et al.*, 2003). One property of bowtie antennas is that they have a poor directivity (Balanis, 1997). This can have positive as well as negative effects on GPR measurement depending on the objectives of the GPR survey. The directivity influences the emphasis of side reflections. The induced current pulse into the transmitting antenna is also relevant for GPR measurements, because together with the antenna structure it determines the emitted wavelet in width and frequency composition.

For an optimal or at least a goal-orientated GPR measurement all these parameters should be adapted. For example, the size of the bowtie antennas and the induced current pulse determines the frequency composition, which defines the spatial resolution in a GPR survey due to the corresponding wavelength. Unfortunately, all these parameters cannot be changed arbitrarily. Therefore, the most operators must work with the available commercial GPR systems. For them, including the author, the objective is to extract as many information as possible from radargrams measured with these systems.

4.2 Standard Measurement Techniques

There are two conceptual different GPR techniques, which were first considered by Löwy (1912) to study the subsurface analogous to seismic applications. These techniques are (i) surface GPR and (ii) cross-borehole GPR[2]. Here, surface GPR needs to evaluate reflections, whereas cross-borehole GPR techniques can simply evaluate direct waves, which are obtained from first arrival times.

Nowadays, the principle of surface GPR is not only used for applications on the soil surface. It is also used in underground mines. This arises further difficulties, because reflections can stem from almost every direction. Furthermore, a hybrid method between surface and borehole GPR was developed. It is called vertical radar profiling (Clement and Knoll, 2006). Here, one antenna is placed on the surface, the other one in a nearby borehole.

In this section, an overview of measurement techniques concerning surface GPR will be given, to provide a basis for the following sections.

4.2.1 Surface Ground Penetrating Radar

Common Offset Measurement

The common offset (CO) measurement technique is the most popular, because it is easily applicable for large scale surveys to obtain at least a qualitative insight into the subsurface structure. Its setup consists of a single transmitter-receiver pair, which is pulled along a line (Fig. 4.2). At equidistant intervals, either in space or time, an electromagnetic wave is emitted, which is received after transmission and reflection processes.

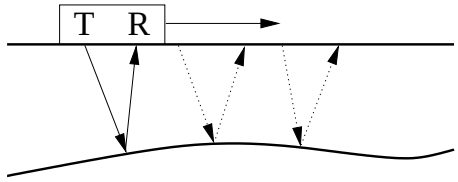

Figure 4.2: *Schematic illustration of a common offset survey with a single transmitter T and receiver R.*

Although, in the historical work of Löwy (1912) a receiving antenna is proposed, which can be orientated in order to distinguish between direct and reflected waves, this technique was not realized. Instead, fixed antennas are used. A reason that this idea was not followed might come from the antenna coupling effect, which determines the energy transfer into the ground as a function of antenna height above the ground (Turner, 1994). Because of this, in most studies transmitter and receiver are placed directly on the ground or even a few centimeters above, in order to emit a high amount of energy into the ground. Here, an increased energy flow into the ground allows the detection of deeper reflections.

The advantage of the common offset technique is its fast and cost-effective applicability. That's why it is widely used and has applications in sedimentology (Ori and Ogliani, 1996; Grasmueck, 1996; Neal, 2004) and archaeology (Nuzzo *et al.*, 2002). It is also applied in hydrological studies, in order to obtain the surface water content by analyzing the ground wave (Grote *et al.*, 2003) or to obtain the water content above reflectors, where the reflector depths were determined by drillings or excavations. For instance, Wollschläger and Roth (2005) showed the temporal change of water content within a soil layer measured by time domain reflectometry (TDR) and GPR. Furthermore, Lunt *et al.* (2005) show the

[2]In contrast to the nowadays established GPR methods, Löwy (1912) assumed the application of much larger antennas (about 100 m length) and proposes the borehole technique for attenuation measurements.

possibility to obtain the water content between surface and reflection with high precision by knowing the depth of the reflector.

The restriction of the knowledge about the reflector depth highlights the major problem of this measurement technique. The measured travel time is a function of reflector depth and relative permittivity, assuming a horizontal reflector. Therefore, it is necessary to determine or even assume one quantity to obtain the other. For long range surveys, this can only be done by an interpolation and extrapolation of a measured quantity due to several drillings or excavations. But this would also lead to uncertainties in the results, because a continuous transition cannot be guaranteed, when small scale heterogeneities are expected.

Common Midpoint Measurement

The common midpoint (CMP) measurement is a technique, which has the largest potential to obtain the distribution of the relative permittivity, which can be translated to water content values. This technique is based on measurements with different antenna separations having the same midpoint (Fig. 4.3). Here, the midpoint means the point between both antennas and need not to refer to a common reflection point.

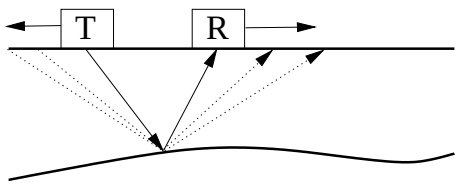

Figure 4.3: *Schematic illustration of a common midpoint measurement.*

Due to the fact that transmitter and receiver must be moved by equidistant steps for a single measurement position, the CMP method is very time consuming. For this reason, it can only be applied within limited ranges. Although, the acquisition time can be improved by using multiple transmitter-receiver pairs, this would introduce multiple unknown travel time offset values. But this is another technique discussed in the "Multi-Channel / Multi-Offset Measurement" section.

The advantage compared to common offset measurements is that standard evaluations of CMP measurements do not require assumptions concerning reflector depth or relative permittivity. Therefore, CMP measurements open the possibility to determine reflector depth and relative permittivity simultaneously.

The most prominent example for the evaluation of a CMP measurement is the normal moveout analysis, which stems from seismic applications Dix (1955); Yilmaz (2001). A short overview about normal moveout analysis will be given in Sec. 4.5.2.

Wide Angle Reflection Refraction Measurement

The wide angle reflection and refraction (WARR) measurement technique is very similar to a CMP measurement, but here only one antenna is moved to adjust larger antenna separations (Fig. 4.4). That's why this method is also called common receiver or common transmitter measurement depending on the stationary antenna. This technique can be applied much faster in field measurements. The disadvantage consists in the fact that lateral changes of the relative permittivity or changes in reflector depth have a larger impact than in a CMP measurement. This comes because the mid-

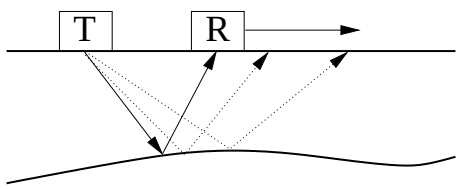

Figure 4.4: *Schematic illustration of a wide angle reflection refraction measurement.*

point between both antennas changes, which can be assigned to have the largest weight on the measurement result.

Multi-Channel / Multi-Offset Measurement

The multi-channel / multi-offset GPR method is a hybrid form of a common offset measurement and a CMP measurement. As sketched in Fig. 4.5, this technique can be understood as a simultaneous measurement of different common offset measurements. Because in a survey, each channel (transmitter-receiver pair) crosses equal measurement points, one can rearrange all measured traces of all channels in local mini-CMP measurements. Although, it is clear that this method is not as accurate as a CMP measurement, it promises a high potential to obtain reflector depth and average relative permittivity or water content simultaneously. Here, the time effort to perform a multi-channel survey is marginally larger than a single common offset measurement.

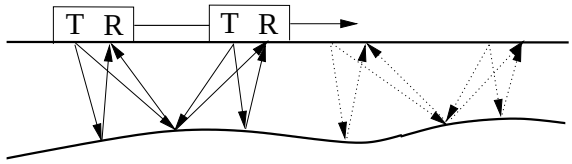

Figure 4.5: *Schematic illustration of a multi-channel / multi-offset measurement.*

Because this technique and its evaluation is a part of this work, the interested reader is referred to chapter 5 or to the corresponding publication (Gerhards *et al.*, 2008).

Off-Ground Radar Measurements

An off-ground radar measurement is very similar to the standard common offset technique. Here, in most applications a single antenna, which is fixed in a specific height above the surface (Fig. 4.6), is used in a monostatic mode.

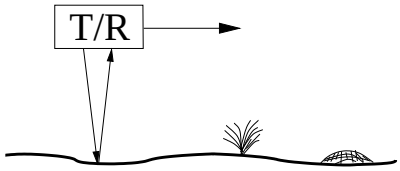

Figure 4.6: *Schematic illustration of an off-ground radar measurement.*

The disadvantage of this method is that the energy transfer into the ground decreases significantly the higher the antenna is lifted (Turner, 1994). Therefore, it can only be used for materials with very low absorption properties and shallow reflections, for instance for the inspection of motorways (Hugenschmidt *et al.*, 1998). Furthermore, surface roughness can also have a huge impact depending on the used frequencies, because it leads to a scattering of the electromagnetic pulse.

In hydrological studies, off-ground GPR can also be used for the estimation of near surface water content. Here, Fresnel's equation for the reflection coefficient can be applied, Eq. (3.45), which only depends on the relative permittivity of air and of the surface assuming a perpendicularly incoming electromagnetic wave. For this purpose, the measurement must be calibrated with a metal plate (Huisman *et al.*, 2003), which yields a reflection coefficient of 1. This calibration must be done, in order to remove the effect of signal attenuation due to geometrical spreading. But this shows that the antenna must be kept in a constant height above the surface to obtain reliable results (Lambot *et al.*, 2006).

Furthermore, full wave inversion techniques can be used to determine the near surface water content (Lambot *et al.*, 2004, 2006). Here, well defined antennas were used, measuring in the frequency domain with a vector network analyzer. Because the description of a measured signal, includes the geometric spreading, the distance between antenna and surface is an additional unknown, which can be obtained from an inversion procedure.

Hence, the near surface relative permittivity and therefore the near surface water content can be determined with a higher accuracy (Lambot *et al.*, 2006).

Lift-Measurements

A lift-measurement is a novel technique used in this work, where either the transmitter, the receiver or both antennas are lifted from the surface (Fig. 4.7). The intention of this method is to determine evanescent waves, which decay more rapidly the more the measurement position is away from the boundary. Furthermore, it was observed that the transmission of energy into the soil follows also an exponential law with the height of the transmitting antenna, which was at least shown for the ground wave (Sec. 4.3.6).

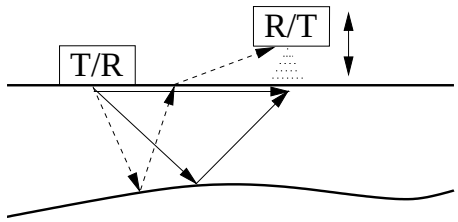

Figure 4.7: *Schematic illustration of a lift measurement. Here, the dots between surface and the lifted antenna indicate evanescent waves.*

Therefore, this techniques has the potential to resolve near surface electric properties by understanding the coupling effect of the transmitting antenna and to distinguish between waves, which couple differently into the air. The last point could also be used to obtain the surface dielectric properties.

4.3 Origination of Ground Penetrating Radar Signals

GPR applies electromagnetic waves for a remote access to subsurface structure and its properties. Therefore, one has to encounter a whole bunch of electromagnetic wave phenomena, which can occur simultaneously and can overlap each other. For instance, such aspects could be the interference of different waves, the distortion of a propagating wave due to dispersive material properties or reflections from continuously changing material properties. In a general GPR study, these electromagnetic phenomena can hardly be separated. Because of this difficulty, this section will focus on a selected set of electromagnetic wave phenomena. They are for instance, the wavelet distortion while propagating through a dispersive medium or the reflection from smooth permittivity transitions. The intention is that the user of a GPR system gains a better insight in the possibilities and difficulties of data interpretation.

4.3.1 Travel Paths in Ground Penetrating Radar Applications

The most popular concept to describe electromagnetic wave propagation is the ray approach. It assumes distinct travel paths. In homogeneous media, these paths are straight lines. Only at boundaries between different dielectric properties they are affected by reflection and refraction processes. If the travel path is known, one can easily calculate the travel time using the dielectric properties of the media the pulse travels through. For the inverse approach using a given travel time, one cannot simply recalculate the travel path and the dielectric properties, because the problem is under-determined. This is the major difficulty of GPR data interpretation.

This difficulty can be faced by using, for instance, the CMP measurement technique to obtain information about the travel paths of the observed waves. This is possible, because the travel path changes characteristically for different antenna separations. Knowing the path and the travel time helps to determine the properties of the examined material.

In order to obtain an insight in possible travel paths in GPR application, first a three-layer model will be analyzed followed by a discussion of multi-layered systems.

Three-Layer System

The three-layer model is the simplest material model, which results in the most significant and observable travel paths (Fig. 4.8). The requirement that the relative permittivity ε_2 of the bottom layer is smaller than of the middle layer ε_1 is only needed for the critically refracted wave. Otherwise, this wave would not occur.

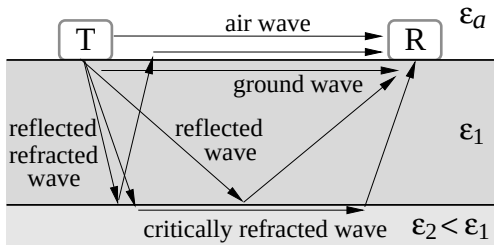

Figure 4.8: *Set of possible travel paths in a three layer medium assuming horizontal reflectors.*

It must be noted that in Fig. 4.8 all kinds of multiple reflected or refracted waves are neglected. Although, multiples can be observered in GPR studies, they mainly have low amplitudes compared to the other waves. Therefore, these waves are also omitted for the further discussion.

In the following, the travel times from these travel paths will be presented obtained from a synthetic CMP measurement. These travel time changes for different antenna separations will give an impression, in which extend distinct waves can be resolved from a CMP measurement.

Setup: For the synthetic three-layer model, an intermediate layer of 0.8 m thickness is assumed. Furthermore, the upper layer respresents air with a relative permittivity $\varepsilon_a = 1$, the middle layer a permittivity zone with $\varepsilon_1 = 15$ and the lower layer a low permittivity material with $\varepsilon_2 = 5$. It is assumed that the transmitter and receiver are placed directly onto the ground. The antenna separations are varied from 0.0 to 8.0 m in 0.1 m steps. The calculations were performed with the formulas given in Sec. 3.2.1.

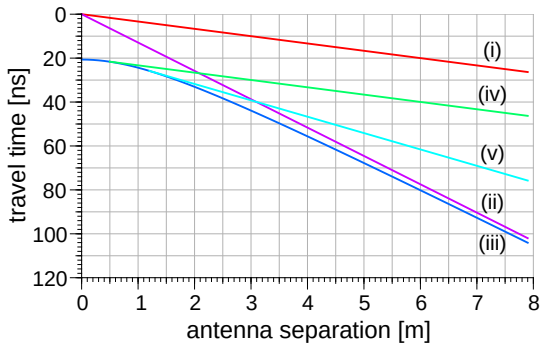

Figure 4.9: *Travel times for the five different travel paths presented in Fig. 4.8. The parameters are chosen to be $d = 0.8$ m and $\varepsilon_a = 1$, $\varepsilon_1 = 15$ and $\varepsilon_2 = 5$. The different travel paths are: (i) air wave, (ii) ground wave, (iii) reflected wave, (iv) reflected-refracted wave and (v) critically refracted wave.*

Results and Discussion: The results are presented in Fig. 4.9. Here, the predicted travel times for different antenna separations and travel paths are shown. It can be seen that the air wave (i) and the reflected-refracted wave (iv) have the same slope. Furthermore, the ground wave (ii) and the reflected wave (iii) are approaching each other for larger antenna separation.

Instead of a single travel time for each antenna separation and travel path, one must consider a whole wavelet. For example, setting a signal with 200 MHz center frequency, this would lead to a wavelet width of about 5 ns, which is a single circle. These wavelets would interfere each other. With this aspect, the observed approaching and also the overlapping between approximately 1.5 and 3.5 m antenna separation would complicate

the data interpretation or makes it nearly impossible with standard techniques, such as the simple ray approach analysis.

The advantage of a such picture, as presented in Fig. 4.9, is that the travel paths of observed wavelets in field studies can be assigned due to the behavior for different antenna separations. This analysis also illustrates that the interpretation of common offset measurements is far from obvious. Here, a fixed antenna separation is used. For instance, when the material model changes along the survey path, the influences of each wave may also vary.

Multi-Layer Systems

The application of the ray concept for multi-layered media can be done by a set of different approaches. One can either use the methods presented in Sec. 3.2.2 or one can face the problem by a straight forward modeling technique (Goodman, 1994). Here, a set of rays with different directions emitted at the transmitter are assumed. At each layer boundary reflection and refraction is calculated. All rays, which approach in the near surrounding of the receiver are considered as potentially measured signals.

This kind of modeling gives an impression, what reflection events can be observed in a radargram. The drawback is that the result do not justifies whether there is a strong or weak reflection. This can be overcome assuming propagating plane waves on each travel path with a defined frequency. The whole wavelet structure is obtained by evaluating a whole set of frequencies with different initial amplitudes, which sets up the wavelet. Losses due to transmission and reflection can be calculated using Fresnel's laws, Eqns. (3.45) and (3.46). Furthermore, absorption processes can be included by assuming a complex relative permittivity for special layers.

The combination of the ray and plane wave approach as presented by Goodman (1994) can be considered as a first order numerical solver for predictions for GPR measurements.

Although, such a solver describing electromagnetic wave propagation is versatile applicable for all kinds of subsurface structures, it requires sharp transitions of the material properties, so that the reflection or refraction point can accurately be assigned. Therefore, for relative permittivity gradients, a fine layered structure must be used instead. But this will lead to further problems, because an incoming ray can split up into a huge amount of travel path possibilities due to multiple reflections.

Another drawback of such a straight forward solver is that some important and used travel paths must be implemented separately, because their origin cannot be explained by the simple recursive application of the reflection and refraction laws.

This statement can be underlined by discussing the observable travel paths using a three layer system as presented in Fig. 4.8. Assuming that the transmitter and the receiver are placed at least a few millimeters in air, then one can only predict the air wave and the reflected-refracted wave. Here, the occurrence or even the excitation of the ground wave and the reflected wave cannot be explained by simple application of the reflection and refraction law under the ray concept. For both waves, at least the incoming angle from the intermediate layer into the air is larger than the total reflection angle, because the reflected-refracted wave couples into the air with an incoming angle, which is only a bit smaller than the total reflection angle. Therefore, also the coupling of the ground- and the reflected wave from the air into the subsurface cannot be explained by the ray approach. But also the travel paths of the critically refracted wave, which, for instance, is described in Rucker and Ferré (2003), is not obvious in a ray concept.

But all these travel paths, presented in Fig. 4.8, are observable in GPR studies. Their origin can be found, when near field effects are included, which are induced by a radiating

antenna. Therefore, more complicated subsurface structures can lead to other waves, which could not be predicted by the ray concept using reflection and refraction processes.

4.3.2 Attenuation and Absorption of Electromagnetic Waves

As stated before, one can understand the transmission and receiving process as an emission of wave pulses, which travel along distinct paths to the receiver, where they are recorded. In this section, a short overview concerning absorption and attenuation processes will be given, which influence GPR signals.

Absorption means the decay of electromagnetic wave energy, which is transformed into thermal energy. With respect to GPR studies, absorption cannot be studied, because the emitted energy by the transmitter in each direction and the energy transfer into the subsurface is unknown for most GPR field studies.

Attenuation denotes the decay of electromagnetic wave amplitudes during the propagation. This amplitude decay need not to result from energy losses (absorption), because reflection and transmission processes split an incoming wave into two different directed waves, for instance. Here, the total energy is still conserved. Furthermore, at the transmitter an excitation of a spherical wave can be assumed. This means that the total emitted energy is located at the boundary of this sphere. Because the radius of this sphere is expanding with time, the wave amplitude along a straight path from the transmitter is attenuated. This is called geometrical spreading. In contrast to the attenuation due to reflection and transmission, the geometrical spreading is equal for all frequencies.

Another frequency dependent attenuation process can be found in dispersive media, which can be described by the propagation of plane waves. This is shown in the following subsection.

Attenuation in Dispersive Media

Mathematical Description: A single plane wave propagating in x-direction is assumed, which is a solution of the electromagnetic wave equation without any source terms. The electric field $\mathbf{E}$ as a function of space x and time t is given by

$$\mathbf{E}(x,t) = \mathbf{E}(k_x,\omega)\, e^{\mathtt{i}\,(\omega\, t - k\, x)} \qquad \text{with} \quad k = \frac{\omega}{c_0}\sqrt{\varepsilon_c} \quad . \tag{4.2}$$

Here, ω and k are the angular frequency and the wave number, respectively. ε_c denotes the relative permittivity of the medium.

Assuming ε_c to be complex ($\varepsilon_c = \varepsilon' - \mathtt{i}\,\varepsilon''$), which could result from relaxation processes or a conductivity (Sec. 2.1.1), this would lead to a complex wave number ($k = \alpha - \mathtt{i}\,\beta$). Then, the phase of Eq. (4.2) becomes

$$e^{\mathtt{i}\,(\omega\, t - k\, x)} = e^{-\beta\, x}\, e^{\mathtt{i}\,(\omega\, t - \alpha\, x)} \quad . \tag{4.3}$$

From this, it is obvious that β is responsible for the attenuation. Here, β cannot be negative, otherwise the amplitudes would increase, which needs an active medium as it is used to build laser.

With the approach

$$\alpha - \mathtt{i}\,\beta = \frac{\omega}{c_0}\sqrt{\varepsilon' - \mathtt{i}\,\varepsilon''} \quad \Longrightarrow \quad \alpha^2 - \beta^2 - 2\,\mathtt{i}\,\alpha\,\beta = \frac{\omega^2}{c_0^2}\,(\varepsilon' - \mathtt{i}\,\varepsilon'') \quad , \tag{4.4}$$

α and β as a function of the real and imaginary part of the relative permittivity are deduced as

$$\alpha = \frac{\omega}{c_0}\sqrt{\frac{\varepsilon' + \sqrt{\varepsilon'^2 + \varepsilon''^2}}{2}} \quad \text{and} \quad \beta = \frac{\omega}{c_0}\sqrt{\frac{-\varepsilon' + \sqrt{\varepsilon'^2 + \varepsilon''^2}}{2}} \quad . \tag{4.5}$$

Result: The factor β introduced in Eq. (4.3) and representing the attenuation of the electromagnetic signal is a function of the real and imaginary part of the relative permittivity as shown in Eq. (4.5). That means that both parameters, the real and imaginary part, are involved in the attenuation process. But for a vanishing imaginary part the attenuation would also vanish.

With respect to β, this calculation highlights that higher frequency components of a wavelet are attenuated much faster, when the real and imaginary part of the relative permittivity are constant.

4.3.3 Propagation in Dispersive Media

In this section, the propagation of an electromagnetic pulse will be discussed and its changes along a travel path within a homogeneous but dispersive medium. Here, one can understand an electromagnetic pulse as a localized signal in time and space, which can be described as a superposition of plane waves with different frequencies and propagation directions.

Propagation Velocity / Phase Velocity

The velocity v of a single plane wave can be derived from Eq. (4.3). The evolution of a constant phase in time and space is described as

$$\omega\, t - \alpha\, x = \text{const.} \quad \Longrightarrow \quad v = \frac{\triangle x}{\triangle t} = \frac{\omega}{\alpha}$$

$$v = \frac{c_0\sqrt{2}}{\sqrt{\varepsilon' + \sqrt{\varepsilon'^2 + \varepsilon''^2}}} \quad . \tag{4.6}$$

Here, the velocity is a function of both, real (ε') and imaginary (ε'') part of the relative permittivity. Only if the material has a pure real relative permittivity, Eq. (4.6) becomes

$$v = \frac{c_0}{\sqrt{\varepsilon'}} \quad . \tag{4.7}$$

Then the propagation velocity do not depend on frequency. This equation is also used, when dispersive materials are assumed, but the compounds of the real and imaginary part cannot be determined separately. This is the case for GPR studies and time domain reflectometry applications. Then, the resultant ε' is called *apparent permittivity* (Topp, 1980).

Examples for Pulse Propagations

In order to get an intuition or even an idea of the propagation of an electromagnetic wave, two examples shall be presented. Here, a one dimensional propagation of an electromagnetic pulse within a homogeneous medium with a complex relative permittivity is assumed. Therefore, geometrical spreading is not considered, which would lead to an additional amplitude decay, but not to a wavelet distortion, because it is assumed to be

Table 4.1: *Setup for the examples in Fig. 4.10.*

	first example (conductivity)	second example (dispersive medium)
wavelet $w(t)$	$A_\mathrm{w} = 10^{-27}$, $t_0 = 10$ ns, $s = 2.25$ ns	
material model	$\varepsilon' = 20, \quad \varepsilon'' = 0,$ $\sigma_\mathrm{dc} = 0.01$ S/m	allophane, Eq. (2.43), without conductivity
figure	4.10a	4.10b

frequency independent. Under these assumptions, the presented process do not reflect the true amplitude behavior. But it shall mirror the wavelet distortion due to a complex relative permittivity.

Setup and Results: Two examples with different dielectric properties will be simulated. In the first example, a constant and real background relative permittivity $\varepsilon_c = 20$ is used with an additional conductivity $\sigma_\mathrm{dc} = 0.01$ S/m. In the second example, the propagation of a wavelet through allophane - a clay mineral is modeled, where the dielectric permittivity is given by Eq. (2.43). Although, clay has also a conductivity, this is neglected here to study the influence of a permittivity, which only results from Maxwell-Wagner effect or bounded ions.

The propagating wavelet is simulated using Eqns. (3.37)-(3.39) presented in Sec. 3.3.1. As a wavelet $w(t)$, the fourth derivative of the Gauss-function is used

$$w(t) = A_\mathrm{w}\, \partial_t^4 \exp\left\{-\frac{(t-\tau_0)^2}{s^2}\right\} \tag{4.8}$$

because it shows similarities to measured wavelets. Here, A_w, τ_0 and s define the wavelet and correspond to amplitude, start time and width (spread) of the wavelet. The used parameters for the initial wavelet are given in Tab. 4.1 as well as the setup for the material model. Here, the spread s is chosen so that the center frequency of the pulse is at 200 MHz.

In both examples the simulated propagation distance is 2 m, where the wavelet as a function of time is calculated at each 0.5 m. The results are given in Fig. 4.10. For both materials, the electromagetic pulse decays with propagation distance due to attenuation. For the first example, the shape of wavelet seems to stay constant along the path (Fig. 4.10a), where the second example shows a distortion of the wavelet (Fig. 4.10b).

Discussion for First Example: In this example, it can be observed that the shape of wavelet seems to stay constant. This can also be seen in the sectrum of the signal in Fig. 4.10a, where the maximum value remains at 0.2 GHz.

This finding can be underlined mathematically by doing a Taylor expansion of α and β, cf. Eq. (4.5), assuming a small imaginary part ε''. This leads to

$$\alpha = \frac{\omega}{c_0\sqrt{2}}\sqrt{\sqrt{\varepsilon'^2+\varepsilon''^2}+\varepsilon'} \;\approx\; \alpha_{\varepsilon''=0} + \left[\partial_{\varepsilon''}\alpha\right]_{\varepsilon''=0}\varepsilon'' \tag{4.9}$$

$$\text{and} \quad \beta = \frac{\omega}{c_0\sqrt{2}}\sqrt{\sqrt{\varepsilon'^2+\varepsilon''^2}-\varepsilon'} \;\approx\; \beta_{\varepsilon''=0} + \left[\partial_{\varepsilon''}\beta\right]_{\varepsilon''=0}\varepsilon'' \tag{4.10}$$

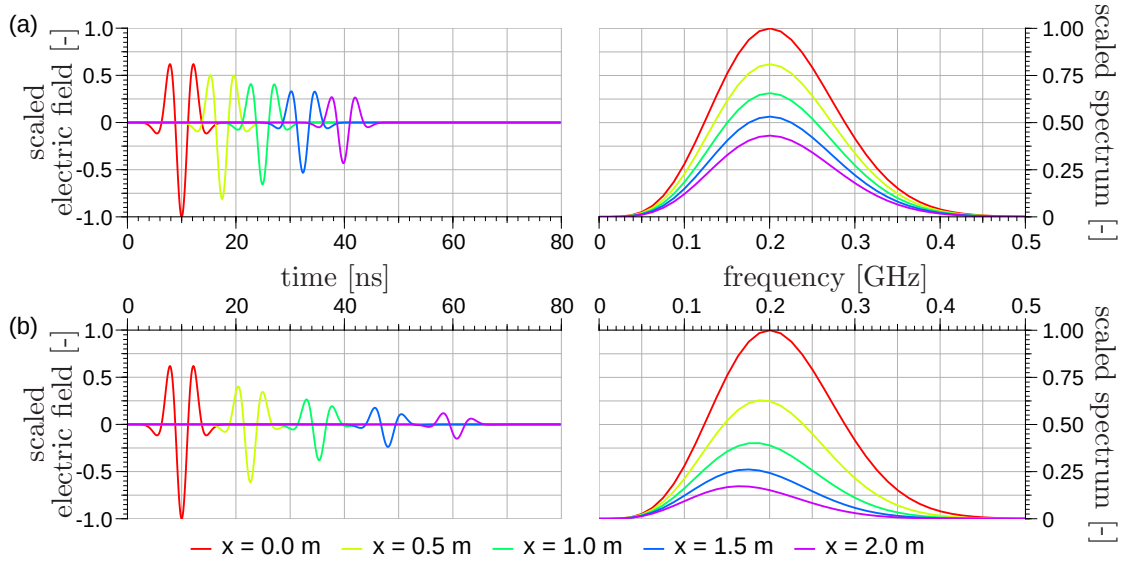

Figure 4.10: *Examples for the propagation of electromagnetic waves within a medium with* $\varepsilon_c = 20$ *and* $\sigma_{dc} = 0.01$ *S/m (a), and within a clay mineral (allophane) given in Eq.* (2.43) *neglecting conductivity (b).*

with

$$\alpha_{\varepsilon''=0} = \frac{\omega\,\sqrt{\varepsilon'}}{c_0} \qquad \text{and} \qquad \left[\partial_{\varepsilon''}\alpha\right]_{\varepsilon''=0} = 0 \tag{4.11}$$

$$\beta_{\varepsilon''=0} = 0 \qquad \text{and} \qquad \left[\partial_{\varepsilon''}\beta\right]_{\varepsilon''=0} = \frac{\omega}{2\,c_0\,\sqrt{\varepsilon'}} \quad . \tag{4.12}$$

With this approximation, Eq. (4.2) becomes

$$\mathbf{E}(x,t) = \mathbf{E}(k_x,\omega)\;\exp\left\{-\frac{\omega\,\varepsilon''\,x}{2\,c_0\,\sqrt{\varepsilon'}}\right\}\;\exp\left\{\mathtt{i}\,\omega\left(t-\frac{\sqrt{\varepsilon'}}{c_0}\,x\right)\right\} \quad , \tag{4.13}$$

where the first exponential term describes the attenuation due to the imaginary part of the relative permittivity. The second exponential term represents the propagation, which is a function of the velocity given in Eq. (4.7).

Now, if the imaginary part of the relative permittivity stems only from the conductivity, then the attenuation term can be rewritten using Eq. (2.29)

$$\ldots\exp\left\{-\frac{\omega\,\varepsilon''\,x}{2\,c_0\,\sqrt{\varepsilon'}}\right\}\cdots = \ldots\exp\left\{-\frac{\sigma_{\mathrm{dc}}\,x}{2\,c_0\,\varepsilon_0\,\sqrt{\varepsilon'}}\right\}\ldots \quad \text{with} \quad \varepsilon'' = \frac{\sigma_{\mathrm{dc}}}{\omega\,\varepsilon_0} \quad . \tag{4.14}$$

This shows that the attenuation is not a function of frequency for small conductivity values according to a low imaginary part of the relative permittivity. Here, a low imaginary part means that the linear Taylor approximation of the attenuation exponent is still valid. For the used 0.01 S/m and 0.2 GHz, the numerical value of ε'' is approximately 5.7.

Discussion for Second Example: In the second example, it can be seen that a dispersive medium distorts the wavelet along the travel path, which is also observable in the spectrum, because each frequency component has a different phase velocity and it is attenuated differently. The shift towards low frequencies is not a general characteristic of dispersive media. Here, it stems from the properties of allophane. With the look on Fig. 2.4, an

increasing imaginary part of the relative permittivity can be observed in the frequency range between 50 MHz and 1 GHz.

Under an experimental perspective, this distortion can have a significant influence on data interpretation. Especially, this can be the case when travel times are extracted from wavelet minima or maxima.

4.3.4 Refraction at Sharp and Smooth Permittivity Changes

The ray approach predicts a refraction of an electromagnetic wave at the interface between two different dielectric materials. This refraction disturbs the travel path, which leads to a travel time which differs from a straight line approach. Furthermore, refraction occurs, when gradients of the dielectric properties exists. This can lead to continuously changing relative permittivity profiles.

Analytically, this travel path disturbance is described by Snell's law, Eq. (3.28) for a two-layer material setup. Refraction of travel paths in multi-layer media can be described, for instance, with the mathematical approaches presented in Sec. 3.2.2.

In order to obtain an impression of the impact of refraction, a material model with sharp transitions will be analyzed in the first step. Afterwards, the refraction is studied, which occurs at a smooth transition of the relative permittivity represented by a capillary fringe.

Refraction at Sharp Transitions

In the field of GPR applications for hydrological purposes, sharp transitions of the dielectric properties could occur, when either the soil texture or only the pore size distribution changes. While a different soil texture can have another relative permittivity, the pore size distribution determines the amount of bounded water due to capillary rise. This amount of water mainly influences the bulk relative permittivity. Here, only a change of the pore size distribution can occur due to compaction or a different deposition. Furthermore, a capillary fringe above a water table could also be interpreted as a sharp transition, when the material has a very narrow pore size distribution.

Influence of Refraction: The influence of refraction will be analyzed in a small example, in order to obtain an insight, to what extend refraction must be considered in GPR applications.

Setup: The plane wave approach and the ray approach for multi-layer media was applied. For the plane wave approach, the same parameters for the incoming pulse were used as described in Sec. 3.5 with the difference that the starting time of the signal τ_0 was set to 10 ns. Furthermore, the same material model was used, which consists of four layers: $\varepsilon_1 = 5$, $\varepsilon_2 = 10$, $\varepsilon_3 = 15$, $\varepsilon_4 = 20$, presented in Fig. 4.11c.

Because refraction is a function of incidence angle, a common midpoint (CMP) measurement was modeled, which means in this context that the distance between excitation and observation point (antenna separation) was increased stepwise. Here, the antenna separation was varied from 0.8 to 4.0 m in 0.1 m steps.

Results and Discussion: The result of the plane wave simulation is shown in Fig. 4.11a. In Fig. 4.11b, additional lines were inserted, where the blue ones correspond to the picked

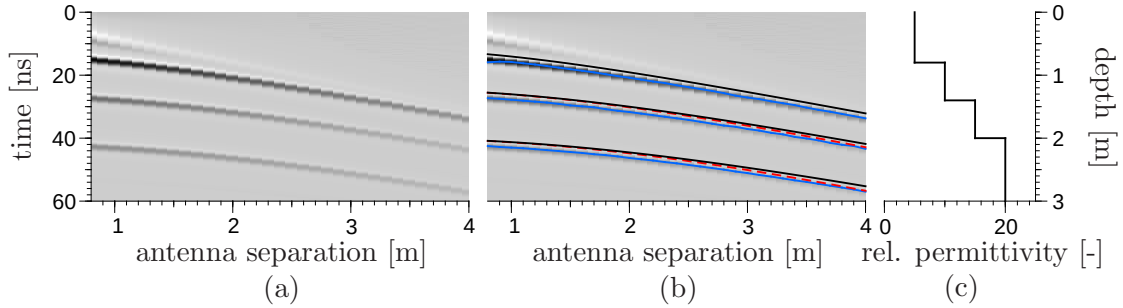

Figure 4.11: *Simulated common midpoint measurement (a) from the synthetic material model given in (c). The plane wave multi-layer approach was used with the settings presented in Sec. 3.5.1. Subfigure (b) shows additional ray approach modeled travel times from the second and third transition using the straight line approach (red dashed) and including refraction (black solid). The blue lines are the picked maxima of the radargram.*

maxima of the plane wave result. Furthermore, the ray approach travel times including refraction were inserted by the black lines. The straight line travel times neglecting refraction are represented by the red dashed lines.

In this example, it can be seen that the ray approach with refraction and the plane wave approach travel times are parallel to each other. Furthermore, the straight line ray approach has deviations of about 0.5 ns from the ray approach with refraction, at about 2.6 m for the second and at about 3 m for the first reflector.

Other simulations with similar structured material models but smaller contrasts, such as presented in Sec. 3.5, were carried out, which are not presented here. It could be observed that there are smaller deviations between the straight line travel times and the travel times including refraction for larger antenna separations.

In summary, refraction has no significant impact in the travel times as long as there are no larger permittivity jumps, which approximately corresponds to the jumps in the example.

Refraction at the Soil-Air-Interface: In the ray approach concept, the most significant refraction has to be assumed at the interface between the soil and the air. When a survey with a rough surface structure is considered, then the air gap between transmitter and receiver changes. This could lead to travel path changes as illustrated in Fig. 4.12.

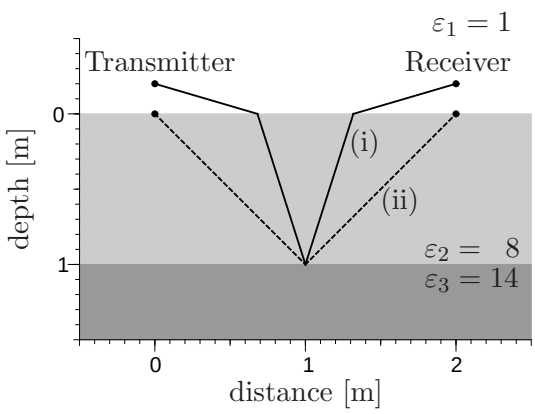

Figure 4.12: *Travel paths for a reflection (i) with and (ii) without an air gap modeled with the ray approach.*

Setup and Results: For the material model presented in Fig. 4.12, the travel time difference between the reflected-reflected (i) ($t_{\text{refl}} = 29.81\ ns$) and the refracted wave (ii) ($t_{\text{refr}} = 26.86\ ns$) is about 2 ns, which could lead to deviations, when either the reflector depth or the average relative permittivity is extracted from these data. Here, the travel times are calculated using Fermat's principle, cf. Sec. 3.2.2.

Discussion: But in real studies both travel paths are observed, because on the one hand, the transmitter radiates in all directions, which can lead to the excitation of the reflected-refracted (i) wave. On the other hand, the reflected wave (ii) is assumed that it couples into the ground and into the air as an evanescent wave, cf. Sec. 3.3.2. Under this perspective, there is no travel time shift for the reflected wave for different air gap thicknesses. For the reflected-refracted wave, a travel time change of about 0.1 ns can be found, when the receiver height over the interface changes between 0 and 0.2 m for the material model presented in Fig. 4.12. This travel time change is about 0.3% of the absolute travel time, which is negligible for experimental studies.

Refraction at Smooth Transitions

In this section, refraction at a smooth transition of the dielectric properties will be analyzed. Here, the focus is here on a varying relative permittivity. These smooth transitions of dielectric properties in soils are directly related to smooth transitions of water content, which could occur due to an infiltration front, evaporation at the soil surface, water uptake by roots or due to a capillary fringe.

Setup: In the following example, the smooth transition is represented by a capillary fringe above a sharp interface. For the simulation, only the ray approach will be used in order to study the travel paths to the sharp transition. The plane wave approach is not applied to this subject, because it would predict an additional reflection from inside the capillary fringe, which could interfere with the reflection from the sharp transition. Furthermore, due to the transition through the capillary fringe, the frequency composition can change, which would alter the shape of the reflected wavelet. This would decrease the possibility to obtain a statement about the impact of refraction on the travel time.

Again, refraction is analyzed for different incoming angles. For this purpose, a common midpoint (CMP) measurement is assumed. The antenna separations are set between 0.4 and 2.0 m each 0.4 m. The synthetic material model is given in Fig. 4.13b. Here, a water table was set at a depth of 0.4 m. Above, the capillary fringe and therefore, the water content distribution can be seen, which is described by the van-Genuchten parameterization given in Eq. (2.50). The parameters are set to $\alpha_g = 0.079$, $n_g = 4.8$, $\theta_r = 0.03$ and $\theta_s = 0.34$, which represents a sand. At a depth of 0.5 m, an artificial interface was set, which shall only stand for a detectable dielectric contrast.

For the calculation of the relative permittivity from the water content values, the mixing formula Eq. (2.33) was used. The exponent was set to $\eta = 0.5$, the porosity to $\phi = 0.34$, the relative permittivity of water to $\varepsilon_{\text{water}} = 80$ and the relative permittivity of the soil matrix (quartz) to $\varepsilon_{\text{matrix}} = 4.7$ (Robinson *et al.*, 2003), respectively.

Results and Discussion: The travel paths to the reflection points are shown in Fig. 4.13a. They show a specific deformation, which results from Fermat's principle. It states that the ray chooses the travel path, where it takes the minimal time. Now, from these travel paths the travel times were calculated, in order to see the differences compared to the expected straight line results. In Tab. 4.2, the travel time from the straight line approach to the same reflection point and the extracted travel time from the travel paths given in Fig. 4.13a are shown. As expected for each antenna separation, the travel time obtained from the straight line approach is larger.

From the travel times presented in Tab. 4.2, an average relative permittivity can be extracted, assuming a homogeneous medium. For the straight line travel times, it is assumed that the whole layer has a relative permittivity of about 10.6. For the refracted

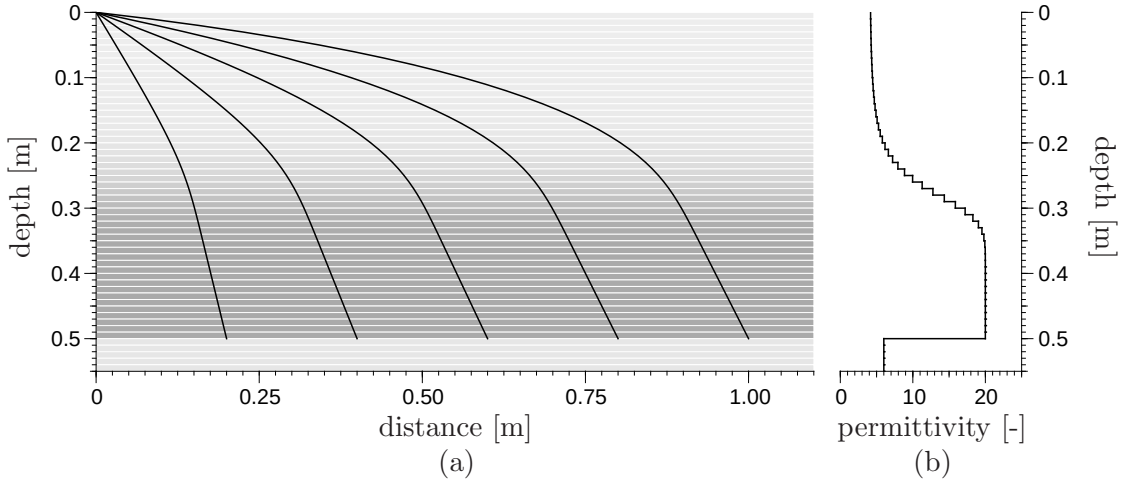

Figure 4.13: *Ray approach travel path (a) to a reflection point at 0.5 m depth for different antenna separations for a material model (b), which simulates a capillary fringe over a water table at 0.4 m given by the van-Genuchten parameterization Eq.* (2.50) *with* $\alpha_g = 0.079$, $n_g = 4.8$, $\theta_r = 0.03$ *and* $\theta_s = 0.34$.

Table 4.2: *Comparison between travel times obtained with straight line approach and with Fermat's principle for the material model given in Fig. 4.13.*

antenna	travel time [ns]		average rel. permittivity [-]	
separation [m]	straight line	with refraction	straight line	with refraction
0.4	11.7	11.6	10.6	10.5
0.8	13.9	13.5	”	10.0
1.2	16.9	15.9	”	9.3
1.6	20.5	18.5	”	8.7
2.0	24.3	21.2	”	8.1

travel paths, the calculated average relative permittivity is decreasing for larger antenna separations. This results because a larger distance of the travel path propagates in the low permittivity domain due to the requirement of Fermat's principle of the realization of the shortest travel times.

This finding reflects a difficulty for GPR applications for hydrological purposes in the presence of continuously varying water contents, because larger antenna separations could lead to an underestimated average relative permittivity, which results in an underestimated average water content value.

Outcome: Refraction from Sharp and Smooth Permittivity Changes

The refraction process was analyzed with respect to the travel times, which can be extracted from GPR data. Refraction has only a little impact on the travel times as long as the relative permittivity jump is comparatively small. Refraction must be considered at the air-soil interface. It has also an impact for changes from dry to water saturated soil, which was shown for a capillary fringe in a shallow depth.

Although, refraction occurs at the air-soil interface, soil roughness is assumed that it does not affect the reflected wave concering travel times. It only affects the reflected-refracted wave, which is an additional travel path.

The analysis of the capillary fringe in shallow depth shows that an estimation of an average relative permittivity from measurements with different antenna separations will lead to different values. This results because for longer antenna separations a larger travel path section takes places in the low permittivity region, which leads to a smaller average permittivity for larger antenna separations.

4.3.5 Reflection from Sharp and Smooth Permittivity Changes

The largest amount of waves occurring in surface GPR applications stems from reflections. Therefore, it is worthwhile to study the reflection phenomena in more detail. For this purpose, reflections from sharp transitions are analyzed in the first step. In the second step, the responses from media with continuously changing relative permittivity profiles are studied. Here, analogous to the refraction analysis (Sec. 4.3.4), the focus will be on the capillary fringe.

Reflection at Sharp Transitions

General Consierations: Reflections from sharp transitions are discussed e.g. in Kung and Lu (1993), because travel times from sharp transitions can be easily obtained, when they are sufficiently separated. Furthermore, the reflection coefficient is fully described by the corresponding Fresnel's law given in Eq. (3.45). For GPR studies the travel time description as well as the amplitude analysis can be used to obtain information about the near subsurface. For example Kung and Lu (1993) presented the possibility to detect objects with sharp permittivity transitions. But also standard normal moveout applications, adapted from seismic applications (Dix, 1955), applies ray approach formulations for the reflection from sharp permittivity contrasts.

The general Fresnel's laws, which predict the whole wavelet behavior of a reflection from a sharp transition, is not often used in GPR applications. But it can be applied at least in a qualitative way. Here, the perpendicular incidence reflection coefficient $R_\perp$ is given as

$$R_\perp = \frac{\sqrt{\varepsilon_1} - \sqrt{\varepsilon_2}}{\sqrt{\varepsilon_1} + \sqrt{\varepsilon_2}} \quad . \tag{4.15}$$

ε_1 is the relative permittivity of the upper half-space, in which the incoming electromagnetic wave propagates. ε_2 denotes the relative permittivity of the lower half-space. This relationship shows that a wavelet, which is reflected at a surface with a larger relative permittivity changes its polarity. This means that maxima turn to minima and vice versa. But also the numerical value of Eq. (4.15) was applied in a few publications in the research field of GPR, where the surface reflection from off-ground GPR applications is analyzed, in order to obtain the surface relative permittivity (Huisman *et al.*, 2003). The disadvantage of this method is that it encounters significant errors. They occur when the distance to the subsurface is determined inaccurately (Lambot *et al.*, 2006), which can be a result from a rough surface.

There are only few publications on the amplitude behavior of reflections for different incoming angles. Reppert *et al.* (2000) as well as Bradford and Deeds (2006) addressed the possibility of its application, but stated difficulties and restrictions for field applications. Here, the disadvantages are the interferences of different wavelets, which avoid the amplitude extraction for a single reflection. Therefore, the reflection coefficient cannot be calculated. Furthermore, the amplitudes are influenced by the radiation pattern of the

antenna, amplitude changes due to geometrical spreading or signal attenuation caused by dispersive materials, which hinder this evaluation method.

Working Plan: Although, the amplitude analysis has a great potential for GPR applications, it can only be applied on either simple material models (Bradford and Deeds, 2006) or with numerical modeling techniques. These techniques should resolve all the difficulties named above.

But instead of going in this direction of the amplitude interpretation of radargrams, the process of reflection shall be examined in more detail, because remote sensing studies reported the occurrence of a penetration depth (e.g. Ulaby *et al.*, 1982; Nolan and Fatland, 2003), which would change the travel time. This penetration depth and therefore its resulting time shift, which could also occur in GPR applications, will be discussed in the following. Some examples will help to underline the occurrence of a penetration depth.

Afterwards, another aspect of reflections from sharp transitions will be analyzed, which will focus on the reflected-refracted wave, because the travel path, which is shown in Sec. 4.3.4 Fig. 4.12 obtained by Fermat's principle differs from the presented travel path in Huisman *et al.* (2003) and Strobbia and Cassiani (2007), which is also illustrated in Fig. 4.8.

Penetration Depth: The idea of a penetration depth δ_p in remote sensing applications was introduced by Ulaby *et al.* (1982). Its derivation is based on the question "At which depth does the electromagnetic energy within the soil decay to an amplitude fraction of $1/e$?", where e denotes the Euler number. Therefore, the decaying term of Eq. 4.13 is used, which ends up in

$$\delta_p = \frac{c_0 \sqrt{\varepsilon'}}{\omega\, \varepsilon''} = \frac{\lambda\sqrt{\varepsilon'}}{2\pi\, \varepsilon''} \quad , \tag{4.16}$$

where $\lambda = 2\pi\, c_0/\omega$ is the wavelength of the incoming wave. ε' and ε'' are the real and imaginary part of the relative permittivity of the soil, respectively. ω is the angular frequency of the signal.

Furthermore, Nolan and Fatland (2003) combines Eq. (4.16) and a 5 GHz equation for the complex permittivity of soils as a function of water content. From this, predictions were made for the penetration depth as a function of water content. The disadvantage of this approach is that in the derivation of the penetration depth no physical insight is given, why the reflection stems from the assumed reflection point.

In optical research, a penetration depth was also observed and discussed, when total reflection occurs. This penetration depth leads to a shift of the reflection point but also in the travel time. The reflection point shift was first measured by Goos and Hänchen (1947), and therefore it is named Goos-Hänchen-shift. Its mathematical explanation was given by Artmann (1948) and Chiu and Quinn (1972).

Because the basic principles of electromagnetic wave propagation in remote sensing and optical applications are the same, a penetration depth observed in remote sensing studies can be derived from the optical approach. This derivation is already given in Sec. 3.3.2. Here, a reflection position shift and a travel time shift can be derived assuming complex permittivity values and that the phase term of the reflection coefficient can be approximated by a linear function of frequency.

In order to obtain an impression of the order of magnitude of these shifts, two examples will be given.

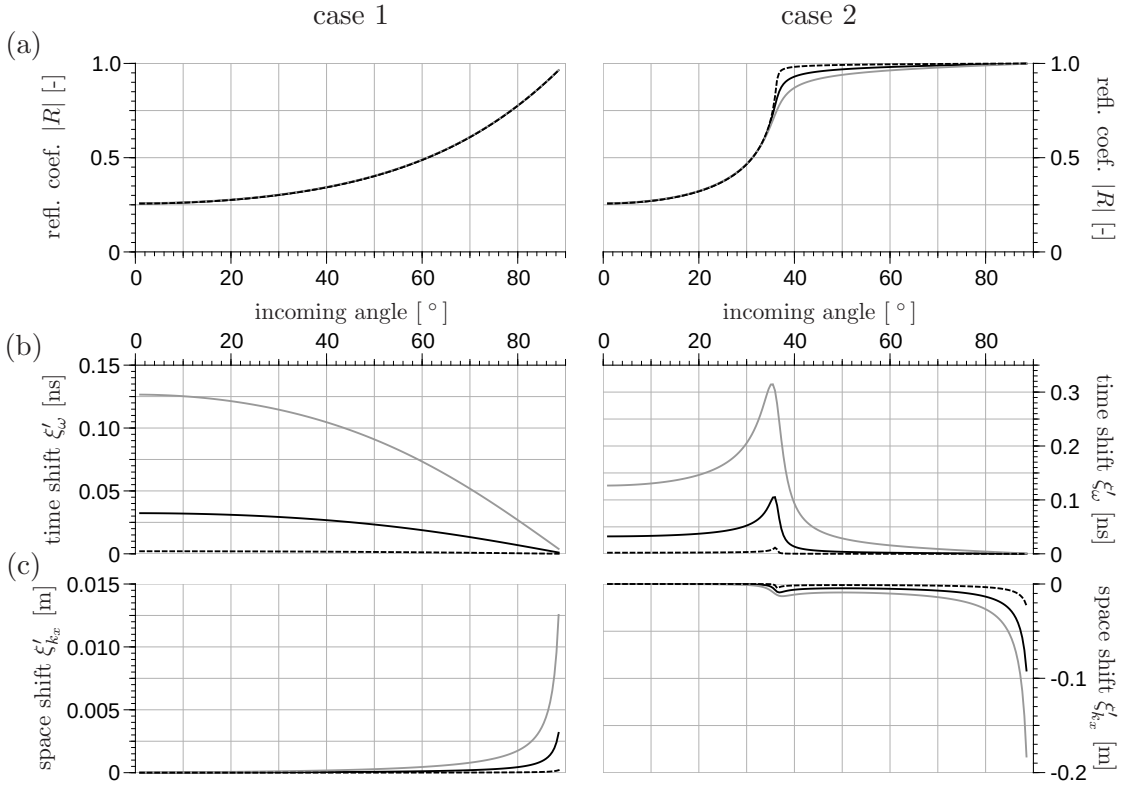

Figure 4.14: *Analysis of the reflection coefficient for three frequencies (0.1 GHz - solid gray, 0.2 GHz - solid black, 0.8 GHz - dashed black) for the first example. A transition between a constant permittivity and a medium with conductivity (case 1) and for the reversed setup (case 2) is assumed. Subfigure (a) represents the absolute part of the reflection coefficient, (b) the time shift and (c) the space shift or shift of the reflection point.*

Setup: Because a complex permittivity must be involved in the reflection process, a two-layer medium is assumed, where the upper half-space has a constant relative permittivity of $\varepsilon_1 = 7$. In the *first example*, the lower half-space is defined using a constant relative permittivity $\varepsilon_s = 20.0$ and an additional direct current conductivity given as $\sigma_{\mathrm{dc}} = 0.01$ S/m. In the *second example*, the clay mineral allophane represents the lower half-space, where the complex relative permittivity is described in Eq. (2.43). An overview can be seen in Tab. 4.3.

Table 4.3: *Settings for both examples to study the penetration depth.*

	first example	*second example*
first layer	$\varepsilon_1 = 7$	
second layer	$\varepsilon_1 = 20$ $\sigma_{\mathrm{dc}} = 0.01$ S/m	allophane Eq. (2.43)
case 1	incoming wave in first layer	
case 2	incoming wave in second layer	
result	Fig. 4.14	Fig. 4.15

Now, for each example two cases are assumed. First, the wave approaches from the upper half-space (case 1) and then from the lower half-space (case 2). The absolute part of the reflection coefficient for the transversal electric (TE) mode, given in Eq. (3.45), for both examples and both approaching directions are presented in Fig. 4.14a and Fig. 4.15a. The transversal magnetic (TM) polarization is not discussed in this context. Because for the purpose of showing the impact of the shifts, there is no additional gain.

In the next step, the time shift ξ'_ω and the shift of the reflection point ξ'_{k_x}, cf. Eq. (3.53) in Sec. 3.3.2, is calculated from the phase term of the complex reflection coefficient using central differences. These shifts are shown in Fig. 4.14b-c and Fig. 4.15b-c for three

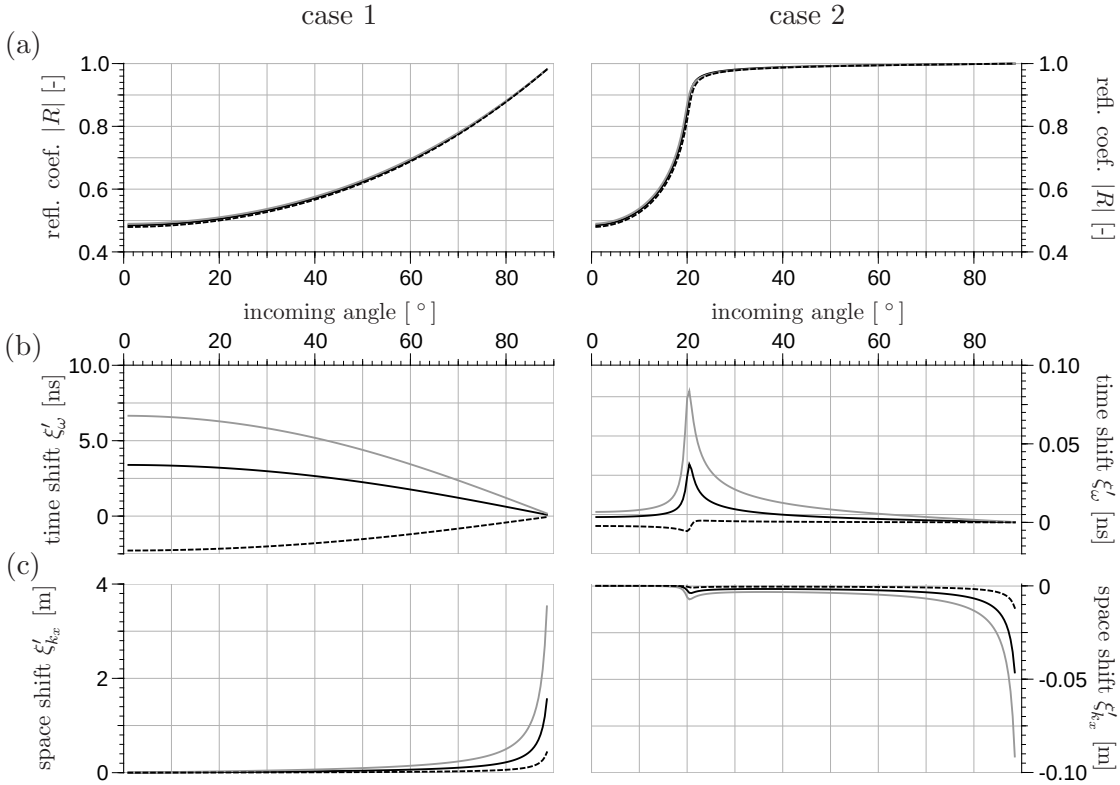

Figure 4.15: *Analysis of the reflection coefficient for three frequencies (0.1 GHz - solid gray, 0.2 GHz - solid black, 0.8 GHz - dashed black) for the second example. A transition between a constant permittivity and the clay type allophane (case 1) and for the reversed setup (case 2) is assumed. Subfigure (a) represents the absolute part of the reflection coefficient, (b) the time shift and (c) the space shift or shift of the reflection point.*

different frequencies (0.1 GHz, 0.2 GHz and 0.8 GHz).

Results and Discussion: From the analysis of the *first example* (Fig. 4.14), it can be concluded that both shifts seem to have no significant impact on GPR applications presented in this work, because of the time resolution. For instance, the time resolution given in chapter 5 is about 0.1 and 0.2 ns. Noise and the picking procedure, which means the extraction of travel times from the radargram, can evoke larger errors.

In the *second example* (Fig. 4.15) using allophane in the lower half-space, the shifts are much larger, when the wave is reflected from the allophane layer. Here, the reflection point shift is very large for glancing incoming angles (0.2 to 3 m for incoming angles larger 70°). These glancing incoming angles can only occur for GPR measurements with a large antenna separation and a detectable shallow reflector. But then other waves, for example the ground wave, would interfere this wave.

But the travel time shifts in the *second example* (case 1) are significant for low incoming angles. For instance, the time shift is about 7 ns for the 0.1 GHz signal for incoming angles lower than 20°. This shift can lead to wrong interpretations of reflector depth or average relative permittivity of the layer above.

Reflection Point of the Reflected-Refracted Wave: For the reflected-refracted wave, cf. Sec. 4.3.1, two different travel paths can be assumed, which are shown in Fig. 4.16. Here, the first travel path (i) is derived from the ray approach, assuming that transmitter and

receiver are located above the interface. The second travel path (ii) is assumed in common GPR literature, e.g. Huisman *et al.* (2003) or Strobbia and Cassiani (2007). Although, there is no significant difference of the travel time, both travel paths have different reflection points, which has an influence, when the lower boundary layer is dipping. Because of this, in the following it will be tried to distinguish, which travel path is likely to occur.

Introductory Considerations: In this work there is no simulation tool which predicts the result of a radiating dipole over a three-layer medium, when the lower interface is dipping. For this reason it is first discussed, how both travel paths could influence the amplitude behavior when the transmitter is lifted above the interface.

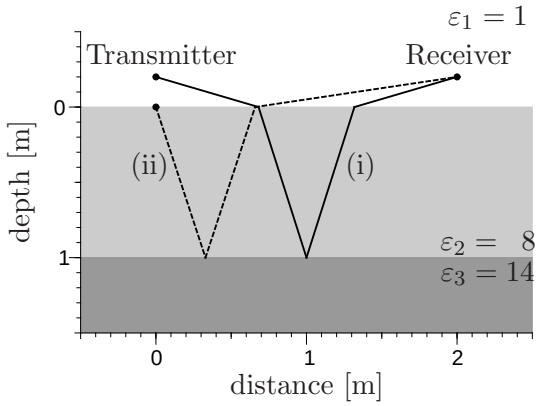

Figure 4.16: *Two possible travel paths for the reflected-refracted wave.*

For the travel path (i) in Fig. 4.16, one can assume that under a plane wave consideration, the amplitude behavior will only be influenced by the transmission coefficients at the air-soil and soil-air interface. Here, small changes of the transmitting antenna height lead to small changes of the incoming angle in the air. This will only affect the amplitudes due to different transmission and reflection coefficients.

For the travel path (ii) in Fig. 4.16, one can assume that the wave is directly excited in the ground. When this excitation is analogous to the excitation of the ground wave, cf. Sec. 4.3.6, then the amplitudes of this wave would decrease exponentially with increasing height of the emitting dipole.

Setup and Results: Simulations with the Green's function method were carried out, where the resultant x-component of the electrical field in time domain are presented in Fig. 4.17. Here, the material model shown in Fig. 4.16 was used. Furthermore, the observation point was set to a horizontal distance of 2 m from the dipole and a height of 0.2 m above the soil-air-interface in air. The excitation was defined in the same way as presented in Sec. 3.5. Now, the vertical position of the dipole was set to three different values. One value is situated in the intermediate layer, very close to the soil-air-interface. The next two positions were placed within the air at -0.1 and -0.2 m above the interface.

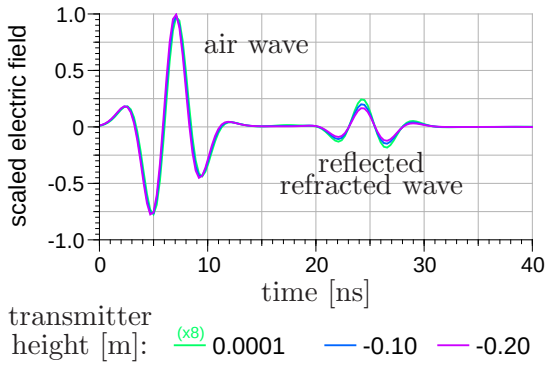

Figure 4.17: *The x-component of the electrical field obtained by the Green's function approach for different transmitter heights and a constant receiver height in order to determine the reflected-refracted wave travel path.*

The resulting traces of the simulation were scaled with the maximum value of the trace, where the transmitter was placed 0.2 m above the interface. Additionally, the trace obtained from the calculation, where the dipole was placed at the interface in the intermediate

layer, was scaled with a factor of 8, which leads to the same air wave amplitudes as for the other traces.

Now, in Fig. 4.17, the results show a small time shift of the air wave wavelet, which has its origin in the different travel paths. Furthermore, a weak decay of the reflected-refracted wave amplitudes relative to the air wave amplitudes can be observed.

Discussion: The changes of the relative amplitudes of the reflected-refracted waves presented in Fig. 4.17 are likely to occur from changing transmission coefficients instead of an exponential decay. Therefore, this study indicates a symmetric travel path (i) of the reflected-refracted wave. Although the asymmetric travel path (ii) in Fig. 4.16 might still exist, it could not be detected with the used modeling tool presented in Sec. 3.4.

Outcome: Reflection at Sharp Transitions

The reflection at sharp transitions was analyzed with respect to travel time shifts, when dispersive media are involved, and with respect to the travel path of the reflected-refracted wave.

The travel time shift was derived in Sec. 3.3.2 using the same consideration for the derivation of the Goos-Hänchen-shift for total reflection. The presented examples show, that a significant time shift can occur from a reflection at a clay mineral, which is highly dispersive. In contrast, the dispersion effects from a conductive layer do not lead to time shifts, larger than the measurement errors of GPR.

Comparing the ray approach analysis prediction for the reflected-refracted wave and common literature, there were two different possibilities for its travel path. Applying the Green's function algorithm, the example show that a symmetric travel path is more likely to occur. Because of the model setup, the asymmetric travel path cannot be excluded.

Reflection at Smooth Transitions

Similar to the analysis of refraction effects in media with continuously varying material properties, the reflection from such media will be analyzed in this section. Although, Nguyen *et al.* (1998) simulates reflection from the capillary fringe, he did not focus on amplitude or phase changes of the reflected wavelet. Furthermore, the reflection at a smooth transition raises the question at which point the main reflection stems from.

Analysis of a Capillary Fringe: To overcome these open questions, the plane wave model was applied to simulate the reflections from a capillary fringe. Here, a single plane wave is assumed, which has a perpendicular incoming angle to the layered structure. These settings do not reflect real measurements, but they allow the separate analysis of wavelet distortion and amplitude decay without influences of the geometrical spreading.

Setup: The wavelet of the incoming wave is defined as Eq. (4.8) with an amplitude parameter $A_w = 10^{-24}$, a time constant $\tau_0 = 10$ ns and a spread of the signal of $s = 2.25$ ns. The capillary fringe is parameterized by the van-Genuchten-model, Eq. (2.50).

In the following, two examples will be analyzed, where the van-Genuchten parameters are given in Tab. 4.4. Furthermore, the water level in both examples was set to 1.8 m. The transition to the relative permittivity values was done with the semiempirical formula Eq. (2.33), where $\eta = 0.5$, $\varepsilon_{\text{matrix}} = 4.7$ and $\varepsilon_{\text{water}} = 80$.

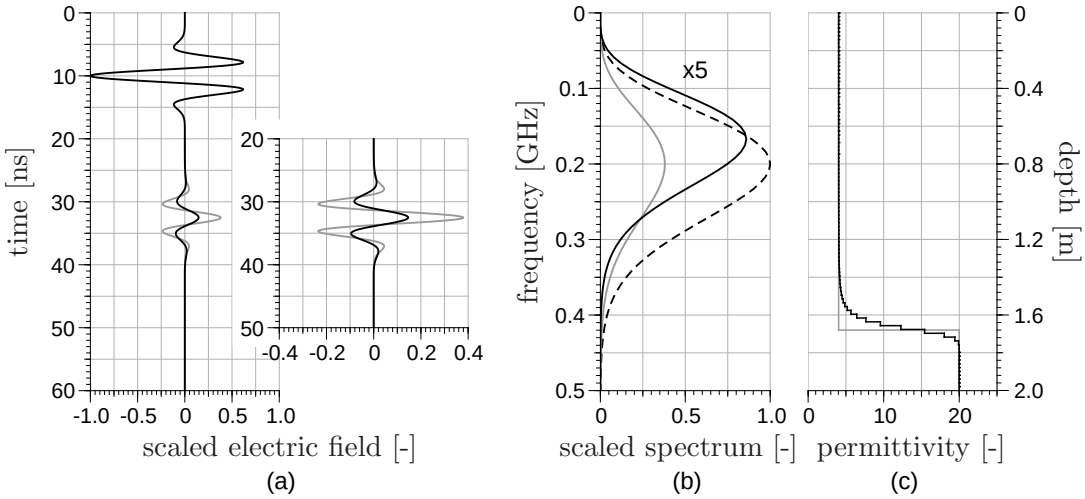

Figure 4.18: *Reflection from a capillary fringe modeled with the plane wave multi-layer approach. Subfigure (a) shows the time signal with the incoming pulse (at 10 ns) and the reflected pulse (at about 33 ns) from the smooth (black) and sharp (gray) transition given in (c). Subfigure (b) shows the corresponding spectra, where the dashed lines is the spectrum from the incoming wavelet. In (c) the material model is given, where the smooth transition is modeled by the van Genuchten parameterization Eq.* (2.50) *with the water table at 1.80 m and* $\alpha_g = 0.079$, $n_g = 4.8$, $\theta_{r,g} = 0.03$ *and* $\theta_{s,g} = 0.34$.

Table 4.4: *Description of the capillary fringe by the van-Genuchten-parameterization for both examples.*

	example 1	example 2
α_g [1/m]	0.079	0.079
n_g [–]	4.8	2.3
θ_s [–]	0.34	0.34
θ_r [–]	0.03	0.03

Results: The results of the plane wave simulation for both examples are shown in Fig. 4.18a and 4.19a. Corresponding to the reflection obtained from a smooth transition, an additional material model with a sharp transition was set up. It jumps from the lowest to the largest relative permittivity value. The depth of this transition was set in a way that the time position of the maximum of the wavelet fits to the reflection from the smooth transition. The resulting material models for the smooth and the sharp transition are shown in Fig. 4.18c and 4.19c. Additionally, in Fig. 4.18b and 4.19b the spectra of the incoming wave and from the reflected wavelets for the smooth and the corresponding sharp reflector are displayed.

Discussion: The difference between both examples is that the transition zone between the low and the high permittivity is larger in Fig. 4.19c compared to 4.18c. In a perspective of soil physics, this larger transition zone stems from a higher amount of small pores in the medium, which leads to a higher capillary rising of water.

From the reflected wavelets in Fig. 4.18a and 4.19a, one can conclude that a smooth dielectric permittivity transition leads to weaker amplitudes compared to a sharp transition as well as to an wavelet distortion. This effect is more pronounced for a more extended transition zone.

With respect to the spectra in Fig. 4.18b and 4.19b, one can see a shift of the frequency with the largest spectral energy. This shift is larger for a wider transition zone, which also indicates a more significant wavelet distortion. The small distortion in Fig. 4.19b is a numerical artefact. It comes when the change of the relative permittivity between the layers near the top boundary is not sufficiently low. This was checked by moving the water

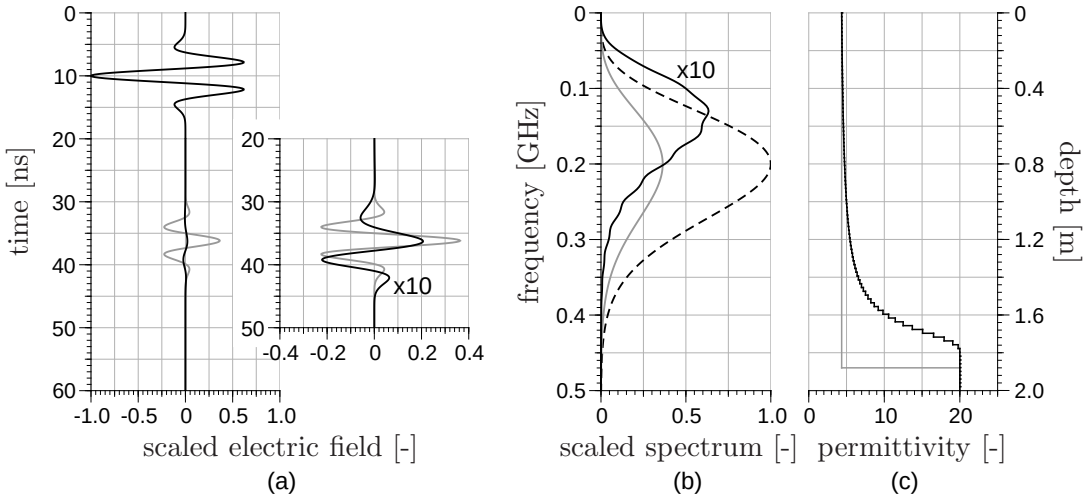

Figure 4.19: *Reflection from a capillary fringe modeled with the plane wave multi-layer approach. Subfigure (a) shows the time signal with the incoming pulse (at 10 ns) and the reflected pulse (at about 33 ns) from the smooth (black) and sharp (gray) transition given in (c). Subfigure (b) shows the corresponding spectra, where the dashed lines is the spectrum from the incoming wavelet. In (c) the material model is given, where the smooth transition is modeled by the van Genuchten parameterization Eq.* (2.50) *with the water table at 1.80 m and* $\alpha_g = 0.079$, $n_g = 2.3$, $\theta_{r,g} = 0.03$ *and* $\theta_{s,g} = 0.34$.

table closer to the top boundary, which amplifies the oscillating disturbances.

Figure 4.18c and 4.19c gives the corresponding reflector depth assuming a sharp transition with a relative permittivity of the upper layer equals to the uppermost relative permittivity of the smooth material model. This corresponding reflector depth is about 1.2 m for the first example and about 1.88 m for the second example. While in the first example this depth corresponds approximately to the depth of the largest gradient of the smooth transition, the corresponding depth is overestimated for the second example. Although, in this example the main reflection could stem from the largest gradient of the permittivity model, the early rise of the permittivity decreases the velocity. This leads to the overestimation. A compensation by adapting the relative permittivity of the upper layer cannot be done, because there are no indicators to set an appropriate values.

Single Frequency Analysis: Because of the frequency shift in the reflection from a smooth relative permittivity transition, the frequency dependent reflection and transmission will be analyzed in this paragraph. The effect of a different incoming angle is also considered.

Instead of using the reflection and transmission coefficient, the reflected and transmitted energy given as the reflectivity and transmissivity given by Eq. (3.81) will be analzed. The reason for this is that the stability of the calculation can be justified, because the reflectivity and transmissivity must sum up to one. This comes because the total incoming energy must either be reflected or transmitted, when no absorption of the medium is presumed.

Setup and Results: For the description of the capillary fringe, the parameters of example 1 (Tab. 4.4, Fig. 4.20c) are used. The reflectivity and transmissivity for incoming angles between 0 and 90 degree and for 200 and 400 MHz are presented in Fig. 4.20a and b. Additionally, the reflectivity and transmissivity for the corresponding sharp transition is

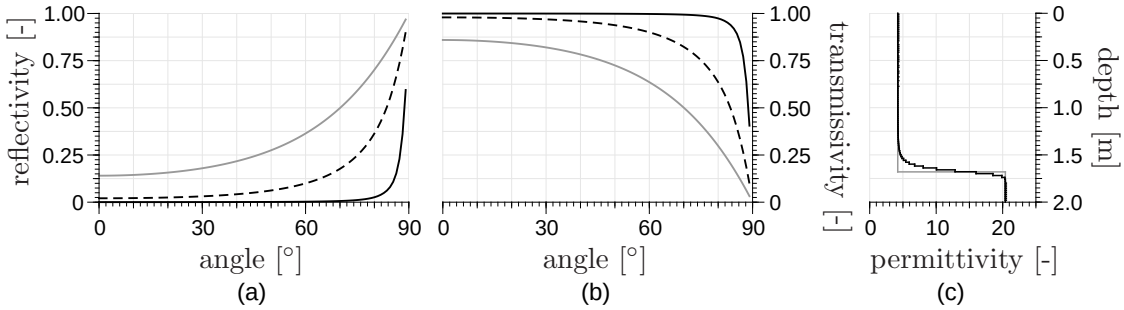

Figure 4.20: *Reflectivity (a) and transmissivity (b) as a function of incoming angle from the continuous material model given in (c). The behavior for 200 MHz (black dashed) and 400 MHz (black solid) is presented. The result from a corresponding sharp transition is also illustrated (gray solid).*

included. The incoming angle of 0 degree means a perpendicular incidence and 90 degree means a glancing incidence.

Discussion: Qualitatively, the reflectivity and transmissivity sum up to one, which was also prooven numerically. This underlines the trustworthiness of the approach.

The results in Fig. 4.20a and b show that an electromagnetic 400 MHz pulse is almost transmitted for a wide range of incoming angles. Furthermore, the reflectivity as well as the transmissivity of the 200 MHz pulse lays between the sharp transition and the 400 MHz pulse. This indicates that higher frequencies passing the transition with less energy loss. This would explain the frequency shift in the examples above. One can also extrapolate this reflectivity behavior for lower frequencies. Then, the reflectivity would approach the sharp transition solution.

Qualitatively, it can be assumed that depending on the width of a transition zone of relative permittivities only a significant reflection can be obtained using comparatively low frequencies.

Reflection from a Linear Ridge: From the examples above, one can see that the reflected wave from a relative permittivity transition seems to be a function of the width of this zone. To underline this observation, the reflection from a linear ridge will be analyzed. This could be considered as a simplified representation of a capillary fringe.

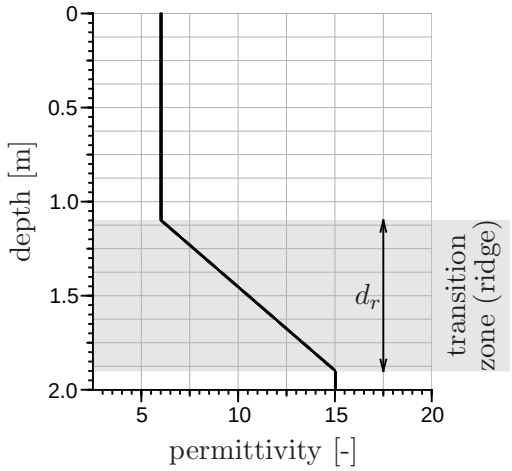

Figure 4.21: *Material model for a linear changing transition zone (ridge).*

Setup: The material model of the following examples is presented in Fig. 4.21. It consists of two layers with a linear transition zone inbetween, which will be called ridge. The relative permittivity of the upper layer was set to 6 and of the lower layer to 15. The ridge is defined by the ridge width d_r, which is the width where the relative permittivity changes from the lower to the larger permittivity. In all examples, the depth of the half ridge width is 1.5 m.

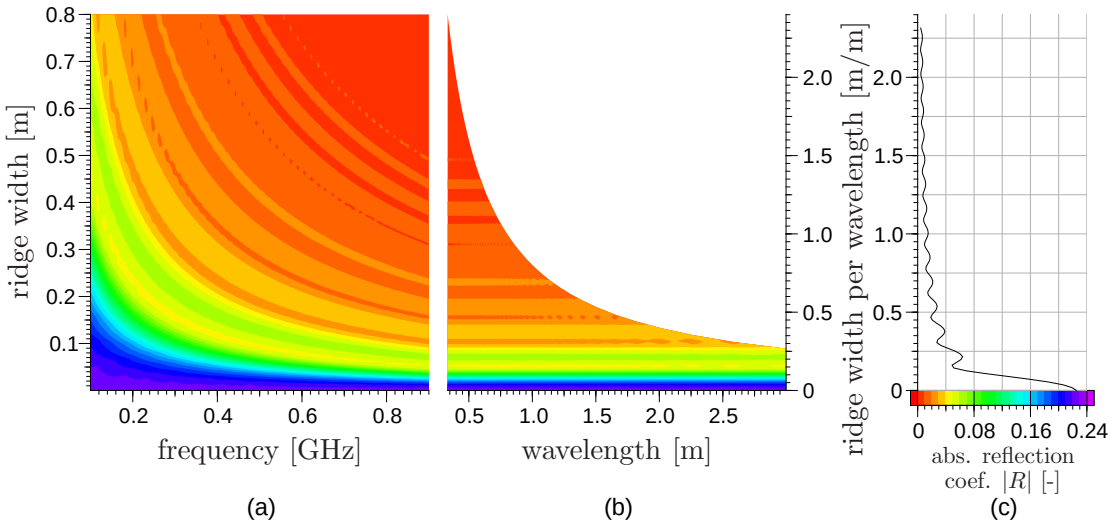

Figure 4.22: *Analysis of the reflection coefficient as a function of frequency and ridge width (a) as well as a function of ridge width per wavelength (b) and (c) using the material model Fig. 4.21.*

Two different calculation will be done. First, the reflection coefficient for different frequencies and perpendicular incidence from ridges with different ridge widths will be analyzed. For the modeling, the plane wave approach is used. The above described material model is discretized in steps according to the incoming wavelength. Using a layered system of $d = 2\ m$ depth, $100 \cdot d/\lambda$ layers are defined with $\lambda = c_0/\nu$, where ν is the frequency. This means that for a wavelength of $\lambda = 2$ m corresponding to 150 MHz in air, the material model was set up by 100 layers.

In the second calculation, the reflected wavelet from a ridge will be analyzed. Here, three different material models will be used: a sharp transition, a ridge width of 0.4 and 0.8 m. The incoming wavelet is defined analogous to the examples of the capillary fringe analysis in Fig. 4.18 and 4.19. In contrast to the described calculation above, the material model is discretized equally for all incoming frequencies. Here, 400 layers are used.

Results and Discussion: The results of the analysis of the reflection coefficient as a function of frequencies and ridge widths are presented in Fig. 4.22a. This figure underlines that higher frequencies are almost transmitted for wider transition zones. Here, only the absolute value of the complex reflection coefficient is used, because it determines the amplitude of the reflected wave. Fig. 4.22b and c in a transformed representation of Fig. 4.22a. Here, the frequencies ν are transposed to the wavelength ($\lambda = c_0/\nu$). The ridge width is transposed to the ridge width per wavelength (d_r/λ). While Fig. 4.22b shows the contour plot, which highlights that the reflection coefficient is only a function of d_r/λ, Fig. 4.22c shows the numerical values as a line plot.

The reflection coefficient as a function of ridge width per wavelength shows an oscillating behavior. Further simulations, which are not presented, show that it depends on the contrast between the minimum and maximum relative permittivity. In this observation, the reason for oscillation can be found. For the explanation, a more simplified model is used. A three layer medium is assumed, where the middle layer has a constant relative permittivity, which corresponds to the mean value of the upper and lower medium. For this setup, one would expect higher and lower reflection coefficients for different wavelength, because this is used in quarter-wave and Bragg-mirrors in optical applications. Although, the material model of a linear ridge is much more complicated, the same phenomenon can

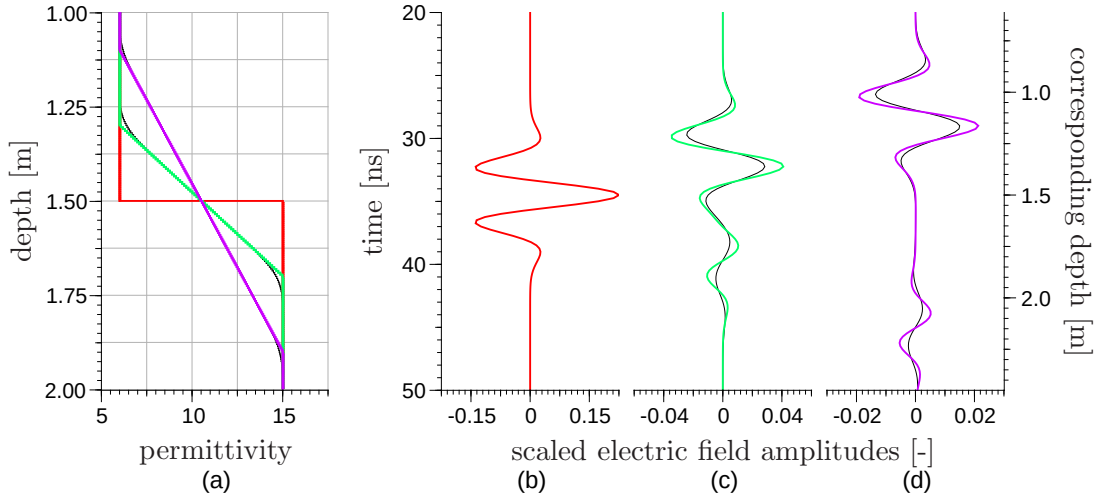

Figure 4.23: *Analysis of the reflection from a linear ridge. The material models are presented in (a). The reflected wavelet for each material model is presented in different colors in (b)-(d) corresponding to (a). The thin black lines represent the smoothed material models as well as their corresponding solution of the reflection.*

be expected. This can explain the oscillating functionality of the absolute value of the reflection coefficient.

The results of the second calculation are presented in Fig. 4.23. The amplitudes of the reflected wavelets are scaled by the maximum value of the incoming wavelet. Therefore, the maximum value of the reflected wavelet corresponds to an effective reflection coefficient. In the case of the sharp transition this equals to the solution of Eq. (4.15), which is in this case $R_\perp \approx 0.23$.

In Fig. 4.23c and d two reflection events can be observed. With respect to the corresponding depth axis using the relative permittivity value of the upper layer, these reflection events seems to stem from the end points of the ridge. At these points the largest second derivative of the relative permittivity distribution occurs.

In order to prove, whether the reflection stems from the sharp cut between the constant and linear relative permittivity behavior, for the material model with the ridge width of 0.4 and 0.8 m the relative permittivity distribution was smoothed a bit. A runmean-filter[3] was used with a width of 0.1 m. The reflected wavelets from these smoothed material models only changes in amplitude and wavelet width. The characteristic maxima seems to stay at the same time. This indicates that for this kind of smooth transition the reflection is likely to occur from the position of the largest second derivative of the relative permittivity.

Outcome: Reflection at Smooth Transitions

In this section, the reflection from smooth changing permittivity models are analyzed. Assuming a capillary fringe, it was shown that neither a water table nor a specific point on the capillary fringe can be detected. This is especially the case for fine textured media, when the capillary fringe is wider than the incoming wavelength. In coarse textured media, when the transition zone is much smaller than the wavelength of the incoming signal, the capillary fringe can be detected as a clear reflection. A

[3]The runmean-filter will be presented in Sec. 4.4.2.

corresponding reflector depth, assuming a sharp transition, depends always on the distribution of the water content, For the capillary fringe in equilibrium, this is a function of the pore size distribution. Furthermore, a smooth transition from low to high permittivity values acts as a low pass filter for the reflected signal.

Assuming a linear transition (ridge), the reflection coefficient is a function of ridge width per wavelength d_r/λ with high reflection coefficients for a small quotient d_r/λ. For this linear ridge model, the reflection can be assigned to the points of the largest second derivative of the relative permittivity distribution.

4.3.6 Evanescent Waves

In ray approach considerations, the existence of some waves and the possibility for their detection cannot be explained (Sec. 4.3.1). Where the excitation of the ground wave or the reflected wave, although the antenna radiates in air, can be traced back to near field properties of the antenna, the detection of these waves in air would be not possible in a ray approach concept. Here, the occurring angles are larger than the total reflection angle.

In order to explain the detection of these waves, the plane wave approach can be used. As shown in Sec. 3.3.2, paragraph "Evanescent Waves", there is an electric field in the neighboring medium, although a wave is reflected totally. This electric field reveals the property that it decays exponentially with an increasing distance to the interface. The same effect is used in optical research for sub-wavelength spectroscopy (Hansma and Tersoff, 1987; Reddick *et al.*, 1989).

This consideration shows that it is necessary that in GPR applications the receiving antenna must be placed close to the ground in order to detect waves like the ground wave or reflected wave.

In the following section, the evanescent wave behavior of the ground wave will be discussed in more detail.

The Ground Wave as a Special Evanescent Wave

The ground wave is studied as a special wave phenomenon in the field of radio waves, which was reviewed by Wait (1998). It is also discussed in several GPR publications (Grote *et al.*, 2003; Galagedara *et al.*, 2005). The propagation velocity of the ground wave depends on the near surface relative permittivity and therefore on the near surface water content. Under this aspect, the GPR ground wave method can be used to calibrate satellite remote sensing techniques, for instance, which focuses on the estimation of the surface water content on the regional scale.

In the research field of GPR, the applicability of the ground wave for the determination of the surface water content was shown by Grote *et al.* (2003). In this publication, it was also presented that the application of different frequencies lead to different water content values. This can be explained when the ground wave has a depth of influence, which is a function of the frequency.

This depth of influence of the ground wave for a three-layer setup was studied by Galagedara *et al.* (2005), who changed the thickness of the intermediate layer and performed standard ground wave evaluations of CMP measurements. This was done by a linear regression of picked ground wave travel times. Here, the interference between the ground wave and the reflected wave is analyzed.

In the following, another aspect of the ground wave will be studied, which focuses on its evanescent behavior.

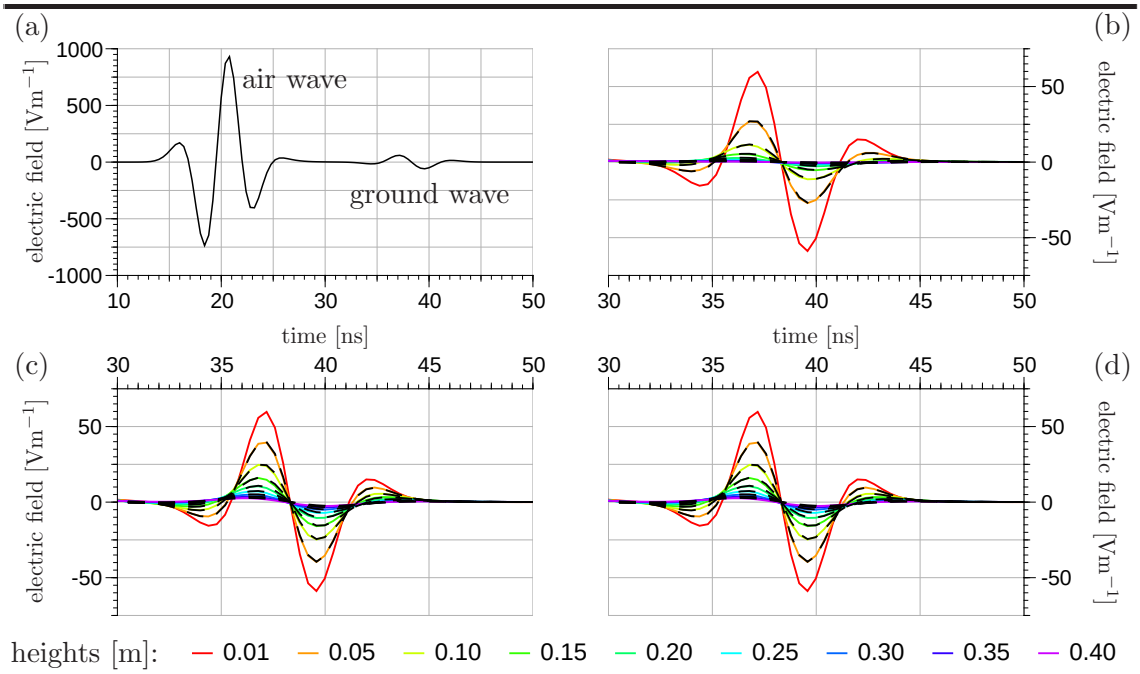

Figure 4.24: *Modeling of a radiating dipole in air above a medium with a relative permittivity of $\varepsilon_r = 8$. (a) shows the electric field at a distance of 3 m and a height of 0.01 m above the interface. In (b), (c) and (d) the color lines represent the full wave modeled results and the black dashed lines represent the plane wave evanescent wave predictions. In (b), both dipole and observation positions were lifted equally. In (c) only the dipole and in (d) only the observation point was lifted.*

Ground Wave Evanescent Wave Behavior In this paragraph it is analyzed, whether the evanescent behavior of the ground wave can be described by a formula derived from plane wave considerations. For this purpose, the ground wave was modeled with a full wave approach (Green's function approach, Sec. 3.4). The electric field at different observation points is calculated, which should result the evanescent decay. These results will be compared with the plane wave prediction.

Full Wave Modeling - Setup: A two-layer medium is assumed. This simple setup avoids difficulties in data interpretation due to interferences with a reflected wave. The upper half-space is air ($\varepsilon_1 = 1$). The lower half-space represents a homogeneous medium with $\varepsilon_2 = 8$. The excitation of the dipole is the same as described in Sec. 3.5.2. Furthermore, the horizontal distance (in x-direction) between dipole and observation point was set to 3 m in order to obtain a separated air and ground wave. The results when both dipole and observation point are located at 0.01 m height above the interface in the upper half space are shown in Fig. 4.24a.

In order to determine the evanescent decay of the ground wave as a function of height above the interface, simulations were carried out, where the observation point was lifted (Fig. 4.24d). This procedure focuses on the coupling of the ground wave from the ground into the air.

Assuming that the coupling of the radiated field by the dipole couples analogous into the ground, additional simulations were done. First, only the dipole (Fig. 4.24c) was lifted and second, the dipole and the observation point (Fig. 4.24b) were lifted simultaneously.

Lifting the dipole or the observation point means that the vertical distance (z-direction) to the interface in the upper half space was increased. The initial position of all simulations for the transmitter and the observation point was $z_0 = 0.01$ m above the interface in the upper half-space.

Full Wave Modeling - Results: Comparing the results of the simulation for the lifted dipole (Fig. 4.24c) and the lifted observation point (Fig. 4.24d), it is noticeable that the graphs seem to be equal. Furthermore, the simulation, where both are lifted simultaneously (Fig. 4.24b), shows a decay, which is twice as strong compared to the other simulations. But before discussing this phenomenon, the decay will be compared to plane wave predictions.

Plane Wave Prediction: The plane wave approach predicts a decay $s_d(z)$ of the ground wave, when it is coupled into the air (cf. Sec. 3.3.2). This results in a function of height z from the interface and angular frequency ω. It is given as

$$s_d(z) := \exp\left\{-\frac{z\,\omega}{c_0}\sqrt{\varepsilon_2 - \varepsilon_1}\right\} \tag{4.17}$$

with the previously defined relative permittivity values. This means that if the frequency components of the ground wave are known directly at the interface, one can obtain the plane wave predictions for an observation height z by multiplying the factor $s_d(z)$ to each frequency component.

In order to apply the plane wave prediction, the simulation of the lifted observation point is analyzed. First, the simulated trace with the closest distance of the observation point to the interface is used. From this trace, the ground wave is cutted and Fourier transformed, such that there is no influence of the air wave, neither in the time nor in the frequency domain. These frequency values are used as the initial values. A modified decay factor $s_d(z; z_0)$ was multiplied to these values for specific heights z. Here, this modified factor is given as

$$s_d(z; z_0) = \exp\left\{-\frac{(z - z_0)\,\omega}{c_0}\sqrt{\varepsilon_2 - \varepsilon_1}\right\} \quad , \tag{4.18}$$

where z_0 defines the height of the initial observation point. The results are transformed backwards into the time domain. This projection of the initial ground wave is shown in Fig. 4.24d by the black dashed lines.

The above described approach for the projection was applied onto the data sets, where the coupling of the radiated field of the dipole into the ground was simulated. Because the decay in Fig. 4.24b was twice as strong compared to the others, here the exponent of the decay factor $s_d(z; z_0)$ was doubled. Again, the results of the projections are indicated by the black dashed lines in Fig. 4.24b and c.

Additionally, the absolute errors between the modeled traces and the projections are presented in Fig. 4.25 for the time domain results and for the lifted observation position. The presentation of relative errors cannot be done in the time domain, because the largest deviations occur near zero crossings.

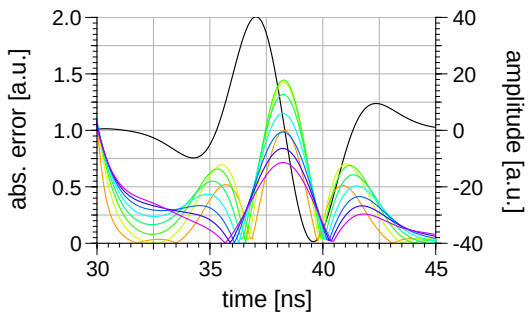

Figure 4.25: *Absolute error between the modeled ground wave with the Green's function approach for a lifted observation position and the projected ground wave by the plane wave prediction. The colors correspond to the observation positions given in Fig. 4.24. The black line is the modelled ground wave for a receiver height of 0.01 m.*

Comparison and Discussion: All the projections fit to the simulated traces, which validates the possibility of this kind of projection. Furthermore, the simulation and the projection shows that the excitation of the ground wave within the ground is

a symmetric process to the coupling from
the ground into the air. This is validated by the simulation, where both dipole and observation point were lifted, which leads to a decay twice as large as the decay factor $s_d(z; z_0)$ given in Eq. (4.18).

It must be noted that there is an error between the modeled and the projected data (Fig. 4.25). This error might be introduced by the modeling with the Green's function approach. Here, a numerical integration must be performed, where the result depends on the number of points for the quadrature. The variation of the number of these points show that deviations can occur. Furthermore, a high number of these points is required, because depending on the frequency the integrand tends either to oscillate or to increase significantly near the boundaries.

Ground Wave in a Multi-Layered Medium While in the paragraph above the ground wave in a two-layer medium was analyzed, here the ground wave in a multi-layered system will be discussed.

From the calculations in Sec. 3.3.2 for evanescent waves, the exponential decay depends on the contrast between the relative permittivity of the near subsurface and the air. For this formula a two-layered medium was assumed. In reality, there are gradients of the relative permittivity near the surface, because of water content changes, which could result from water infiltration, evaporation or water uptake by roots. Therefore, the derivation for the evanescent behavior must be adapted.

Now, a material model as sketched in Fig. 4.26 is given. In one layer, a plane wave is assumed, which propagates only horizontally / in x-direction. For example, it has only a y-component of the electric field, which is given as

$$E_y(x, z, t) = E_i \, \exp\left\{\mathtt{i}\,(\omega\, t - k_x\, x)\right\} \quad . \tag{4.19}$$

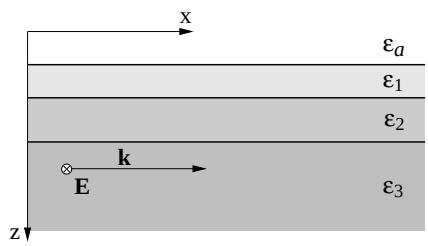

Figure 4.26: *Setup for the argumentation of the ground wave influence depth consideration.*

E_i is an amplitude value. This amplitude value is determined by the propagation through the ith layer and by the induced energy into this layer with this propagation direction by the emitting antenna.

From electromagnetic theory, it is known that the vector components of the electric field and the propagation vector are continuous, when they are parallel to the boundary. This means that the y-component of the electric field of a single plane wave with the angular frequency ω can be expressed within the air

$$E_y(x, z, t) = E_a \, \exp\left\{\mathtt{i}\,(\omega\, t - k_x\, x - k_{z,a}\, z)\right\} \quad . \tag{4.20}$$

The amplitude value E_a depends on the initial value in the layer with the relative permittivity ε_3 (Fig. 4.26) and the transition through the intermediate layers. Here, the z-component of the propagation vector within the air yields

$$k_{z,a} = \sqrt{|\mathbf{k}_a|^2 - k_x^2} = \frac{\omega}{c_0}\,\sqrt{\varepsilon_a - \varepsilon_3} \quad , \tag{4.21}$$

which is a complex value for $\varepsilon_a < \varepsilon_3$ with only an imaginary part and therefore, it determines the evanescent / exponential decaying behavior.

It can be summarized that the decay of a single plane wave component with an angular frequency ω is a function of the relative permittivity, where this wave propagates parallel

to the surface. This propagation is a function of the induction of the waves by the radiating antenna. It can be assumed that waves with different frequencies are induced differently. Furthermore, one can expect that in each layer a pure propagation direction parallel to the layering is induced. This implies that the evanescent coupling of a wave with a single frequency could be a sum of different decay processes. If a main decay process could be assigned due to a main energy induction into a single layer, then this need not to be the case for other frequencies. Therefore with this considerations, the decay function could depend on the frequency.

Note: Neither the two-layer ground wave description as an evanescent wave under plane wave considerations nor the multi-layer description cannot be directly explained with Maxwell's equations. Here, difficulties in the transition conditions of the magnetic field components occur. Furthermore, a description as a bounded surface wave or "Zenneck wave" (Zenneck, 1907; Wait, 1998) cannot be done, because the observed propagation velocity does not correspond to each other.

The only argument for the description above is that the ground wave with the evanescent wave behavior is observable in a full wave analysis. This corresponds to the approximated plane wave prediction.

Outcome: Evanescent Waves

An evanescent wave is a special transmitted wave type, which occurs in the neighboring medium, when a wave is reflected totally. It decays exponentially with the distance from this boundary.

The ground wave in air can be assigned to be an evanescent wave. Its coupling from the ground into the air corresponds to the coupling into the ground near the radiating dipole. The decay of the ground wave in air can be described as a function of frequency, height and dielectric contrast. In multi-layered media, the dielectric contrast is likely to be a function of the frequency. This depends on the vertical distribution of the relative permittivity and on the inducement of waves propagating parallel to the surface by the radiating dipole.

4.4 Pre-Processing and Filtering Procedures

Filter routines try to enhance the measured data quality. In most cases, they are used before the evaluation algorithms. In the following, some filter routines are presented, which are partially used in this work. Furthermore, it will be studied how the raw data is affected by these routines, in what extend they are useful and when they could disturb information.

A measured GPR trace is shown in Fig. 4.27 without any applied pre-processing or filter routines. Here, the amplitudes are measured in digits and they are proportional to voltage values.

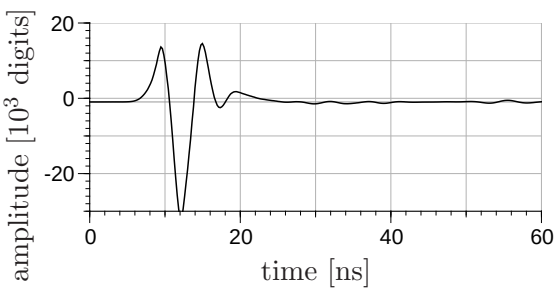

Figure 4.27: *Example of a measured trace without any pre-processing or filtering.*

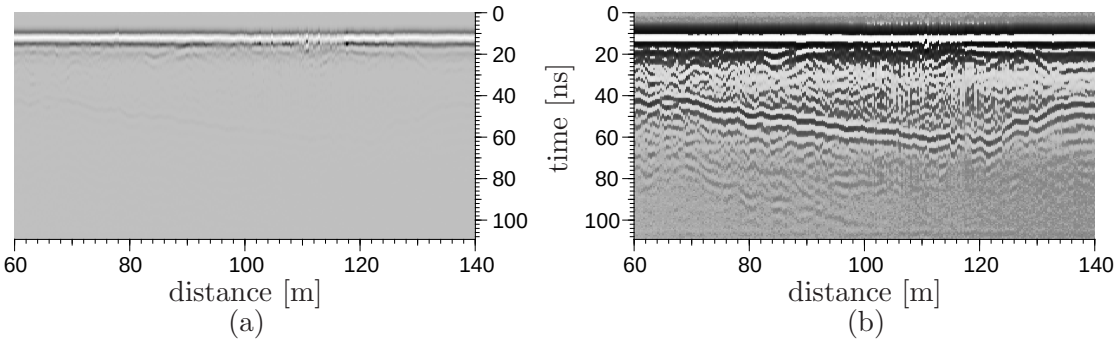

Figure 4.28: *Illustration of an example radargram with only an amplitude shift correction (a) and with logarithmic amplitudes (b) after Eq.* (4.22).

Amplitude Shift: In Fig. 4.27, it can be seen that amplitude values are slightly shifted towards negative amplitudes, which is an artefact from the measurement electronics. For all further examples, this shift should be corrected, so that the base line of the signal corresponds to the zero-amplitude. This correction is done by subtracting the average over all amplitudes within a time interval, where only noise occurs.

4.4.1 Amplification / Gain

As already seen in Fig. 4.27, after the first wiggles no signal can be observed in this kind of presentation, because the electromagnetic waves are strongly attenuated. In order to visualize further reflections, an amplification of the signal is recommended.

In a first step, the amplitudes can be transformed to a logarithmic scale. Notating a measured trace as a function of time as $g(t)$, this transformation is given by

$$\tilde{g}(t) = \begin{cases} \log_{10} g(t) & , \text{ if } \quad g(t) > 1 \\ -\log_{10} |g(t)| & , \text{ if } \quad g(t) < -1 \\ 0 & , \text{ else} \end{cases} , \tag{4.22}$$

where $\tilde{g}(t)$ is the transformed trace. The result of this transformation can be seen in Fig. 4.28. Now, a strong reflection can be observed between 40 and 60 ns.

In some cases, this kind of transformation might not be enough to highlight significant reflections. For this purpose, one can determine an envelope to scale the trace. This envelope can be calculated using the maxima of the trace, where all amplitudes are converted to absolute values. The interpolation between these maxima can be done by linear functions or by fitting a polynomial. Now, by dividing all amplitudes with the corresponding envelope value, this leads to a scaled trace with amplitudes between ± 1.

If the determination of an envelope is done for each trace, this will not distort the maximum positions of the traces. On the other hand, when a global envelope is used or another scaling function is applied to emphasize a specific travel time section, this can slightly change the times of maxima or minima, which might be used for the travel time extraction.

4.4.2 Runmean-Filter

The runmean-filter can be applied to remove noise and it can be considered as a low-pass filter. Mathematically, it is described by a convolution of the a signal $g(t)$ and a kernel

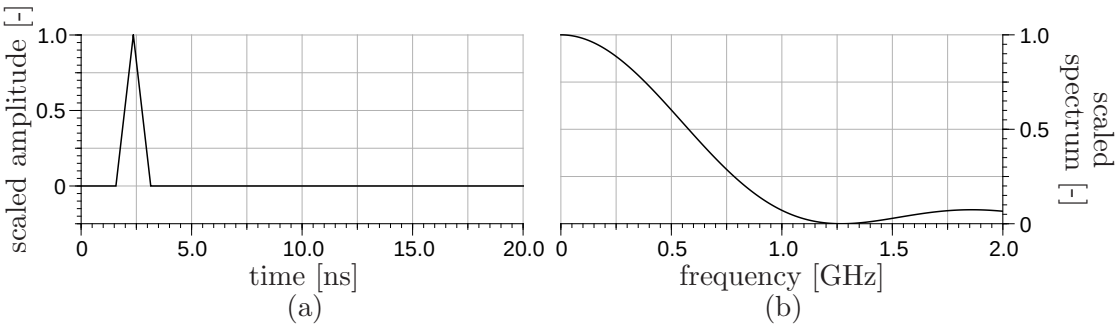

Figure 4.29: *Kernel of the runmean-filter in time domain (a) and its corresponding spectrum (b).*

$k_{\text{rmean}}(t)$, where $k_{\text{rmean}}(t)$ is a hat function (Fig. 4.29a) with a width $2\triangle t$ described as

$$k_{\text{rmean}}(t;\triangle t) = \begin{cases} \frac{1}{\triangle t}\left(1-|t|\right) & , \quad t \in [-\triangle t, \triangle t] \\ 0 & , \quad \text{else} \end{cases} \quad . \tag{4.23}$$

Its corresponding spectrum is presented in Fig. 4.29b The convolution itself is given as

$$g_{\text{rmean}}(t) = \frac{1}{\int k_{\text{rmean}}(t';\triangle t)\, dt'} \int g(t')\, k_{\text{rmean}}(t-t';\triangle t)\, dt' \quad , \tag{4.24}$$

where $g_{\text{rmean}}(t)$ is the filtered signal.

The application of the runmean-filter on the data presented in Fig. 4.28 is shown in Fig. 4.30. In Fig. 4.30c[4], it can be seen that this filter removes noise, while in this kind of illustration the main amplitudes seem to stay unaffected. Although, Fig. 4.30b shows a significant information content (referring to the visible reflectors), it does not contradict the previous statement, because the gray values are not comparable. They only represent scaled amplitudes, where black corresponds to the largest amplitude and white to the lowest.

4.4.3 Dewow-Filter

A dewow-filter is a high-pass filter, which removes low frequencies. It can be recognized as the remainder term of the runmean-filter. Therefore, it is defined as

$$g_{\text{dewow}}(t) = g(t) - \frac{1}{\int k_{\text{rmean}}(t';\triangle t)\, dt'} \int g(t')\, k_{\text{rmean}}(t-t';\triangle t)\, dt' \quad , \tag{4.25}$$

where $g_{\text{dewow}}(t)$ is the dewow-filtered trace.

Figure 4.31 shows the results of an application of a dewow-filter with $\triangle t = 4$ ns on the data presented in Fig. 4.28. Fig. 4.31d illustrates that this filter only affects the first 200 MHz.

Furthermore in Fig. 4.31c, it can be seen that this filter has a large impact of the air-ground-wave between 0 and 20 ns, which is also observable in Fig. 4.31a in comparison with Fig. 4.28. In Fig. 4.28b between 10 and 20 ns two wavelets seem to interfere/overlap. This overlap is not visible in Fig. 4.31a.

The observation of the air-ground wave highlights that after a dewow-filter an overlap of two wavelets, which might have an effective higher amount of lower frequencies in common

[4] Although in Fig. 4.30c the logarithmic amplitudes are presented, the runmean filter was only applied on the raw data.

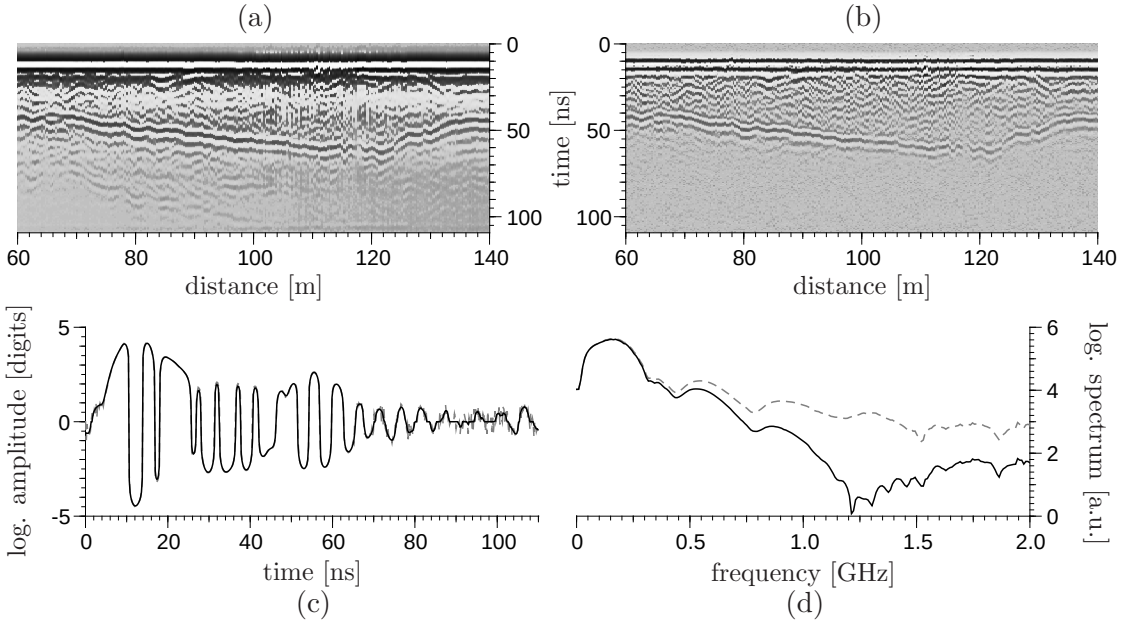

Figure 4.30: *Application of the runmean-filter with $\triangle t = 0.8$ ns on the data presented in Fig. 4.28. (a) is the filtered radargram and (b) shows the differences to Fig. 4.28. Subfigure (c) is an example trace from the distance x=100 m and (d) is the corresponding spectrum. In (c) and (d) the gray dashed line corresponds to the original trace and the black line to the filtered trace.*

could not be resolved. This seems to be contradictory, because the filter can be recognized as a linear operator. When a trace $g(t)$ can be represented as a sum of wavelets $w_i(t)$ given as $g(t) = \sum_i w_i(t)$, then the filter acts on each wavelet on its own. This can also be seen in the frequency domain, where the convolution is a simple product of the trace function and the kernel function

$$g_{\text{dewow}}(\nu) = g(\nu)\; k_{\text{dewow}}(\nu) \tag{4.26}$$

$$\text{with} \quad k_{\text{dewow}}(\nu) = 1 - \frac{1}{\int k_{\text{rmean}}(t'; \triangle t)\; dt'}\; k_{\text{rmean}}(\nu) \quad . \tag{4.27}$$

This leads in a wavelet representation to

$$g_{\text{dewow}}(\nu) = \left(\sum_i w_i(\nu) \right)\; k_{\text{dewow}}(\nu) = \sum_i w_{i,\text{dewow}}(\nu) \quad , \tag{4.28}$$

where $w_{i,\text{dewow}}$ are the dewow-filtered wavelets in the frequency domain.

Although Eq. (4.28) is valid, it cannot be used to give the reason for the above described phenomenon that two wavelets with an overlap cause a higher amount of low frequencies. In order to check this statement, two wavelets w_1 and w_2 are assumed, which are equal in shape and only different in amplitude. A further assumption is that the second wavelet is shifted by a small value τ from the first wavelet, which yields

$$\text{in the time domain:} \qquad w_1(t) + w_2(t) = w_1(t) + \alpha w_1(t+\tau) \tag{4.29}$$

$$\begin{aligned} \text{in the frequency domain:} \qquad w_1(\nu) + w_2(\nu) &= w_1(\nu)\, \left(1 + \alpha e^{-\mathtt{i}\, 2\pi\, \nu\, \tau}\right) \\ &= w_1(\nu)\, \left(1 + \alpha \cos(2\pi\, \nu\, \tau)\right) \quad . \end{aligned} \tag{4.30}$$

When the width of the main wiggle of the wavelet is t_w, then its main frequency is $\nu_w = (2\, t_w)^{-1}$. The cosine term leads to a higher amount of lower frequencies, when the time shift τ is smaller than the width t_w of the main wiggle of the wavelet.

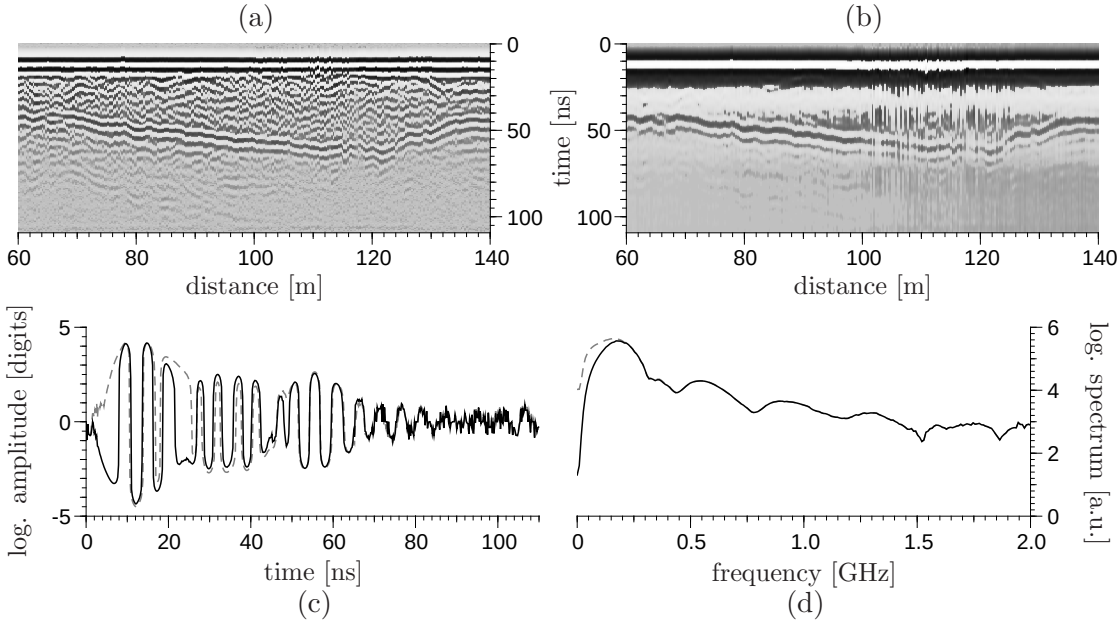

Figure 4.31: *Application of the dewow-filter with $\triangle t = 4.0$ ns on the data presented in Fig. 4.28. (a) is the filtered radargram and (b) shows the differences to Fig. 4.28. Subfigure (c) is an example trace from the distance x=100 m and (d) is the corresponding spectrum. In (c) and (d) the gray dashed line corresponds to the original trace and the black line to the filtered trace.*

4.4.4 Gauss-Filter

A Gauss-filter is a band-pass filter, which can be defined as a convolution analogous to the runmean-filter. Here, the kernel function is the Gauss-function. Instead of a single application in time domain, a Gauss-filter is used in time and space. When a radargram can be defined as a two dimensional function $g(x,t)$, then the Gauss-filter is analytically given as

$$g_{\text{gauss}}(x,t) = \frac{1}{\int k_{\text{gauss}}(x',t';\sigma_x,\sigma_t)\,dt'} \int g(x',t')\,k_{\text{gauss}}(x-x',t-t';\sigma_x,\sigma_t)\,dt'$$
$$\text{with} \quad k_{\text{gauss}}(x,t) = \exp\left\{-\frac{x^2}{2\,\sigma_x^2} - \frac{t^2}{2\,\sigma_t^2}\right\} \quad , \tag{4.31}$$

where σ_x and σ_t define the widths of the two dimensional Gauss-function.

In Fig. 4.32, the application of the Gauss-filter with $\sigma_x = 0.2$ m and $\sigma_t = 0.2$ ns on the data presented in Fig. 4.28 is shown. From the difference plot Fig. 4.32b, it is clear that with this parameter setup almost no structural information from the radargram is removed. Furthermore from the spectrum given in Fig. 4.32d, this filter procedure has better properties in the removal of noise, because in contrary to the runmean-filter, there is a smooth decay for higher frequencies.

4.4.5 Ringing Removal

Ringing is a multiple reflection phenomenon. There are two different sources for ringing in GPR applications. It can be caused by multiple reflections from the subsurface or from side reflections from the antenna box (internal ringing). This internal ringing occurs, when shielded antennas are used. Depending on the reflector depth or the dimensions of the antenna box, ringing can be expressed (i) by a wavelet which occurs in specific intervals or

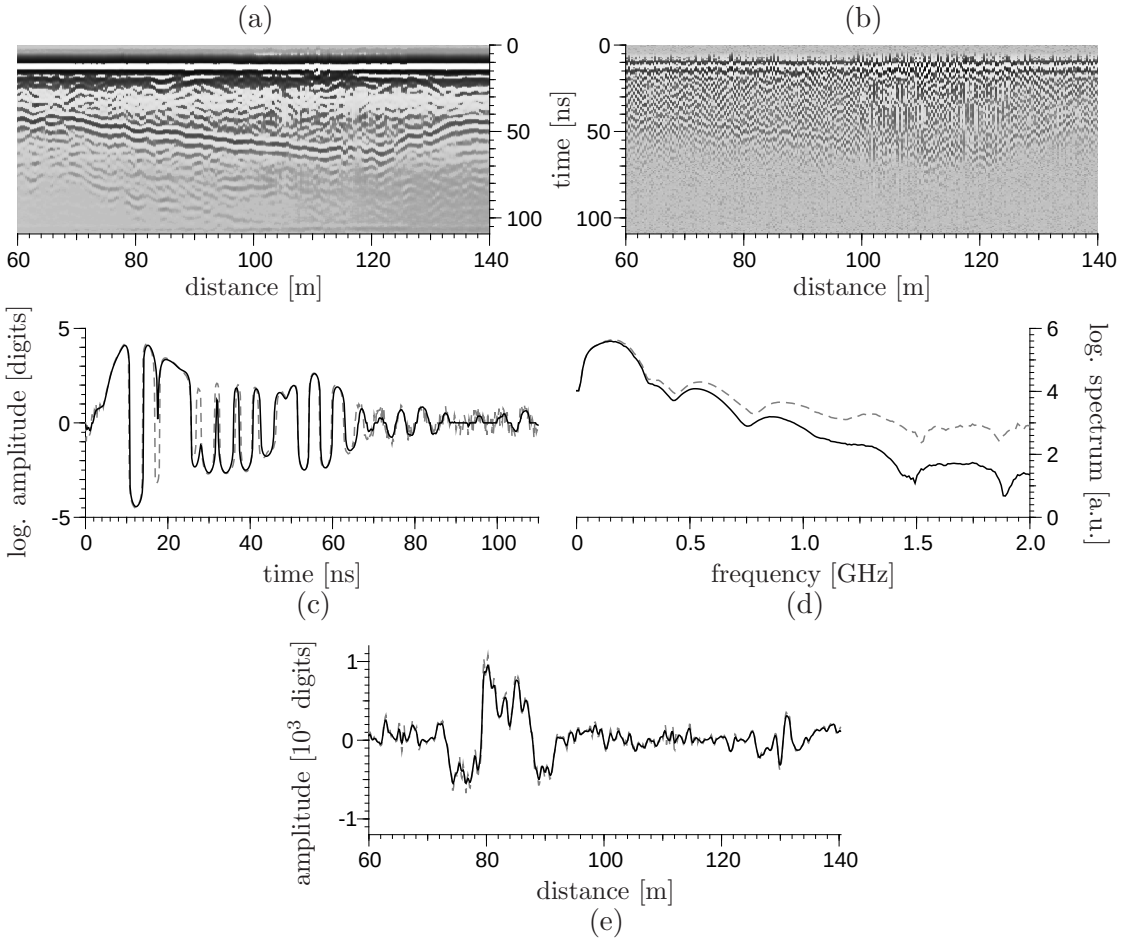

Figure 4.32: *Application of the Gauss-filter with $\sigma_x = 0.2$ m and $\sigma_t = 0.2$ ns on the data presented in Fig. 4.28. Subfigure (a) is the filtered radargram and (b) shows the differences to Fig. 4.28. Subfigure (c) is an example trace from the distance x=100 m and (d) is the corresponding spectrum. (e) shows all amplitudes at the travel time t = 50 ns along the survey. In (c), (d) and (e) the gray dash line corresponds to the original trace and the black line to the filtered trace.*

(ii) by a few dominant frequencies. The first phenomenon is observed, when the reflector depth is much larger than the dominant wavelength of the emitted signal. Dominant frequencies occur, when the travel path between two reflectors (for instance within the antenna box) corresponds to a half wavelength of an emitted frequency component with sufficient energy. Then, resonance can occur.

While the detection of multiple reflections from a subsurface reflector can help for data interpretation, internal ringing can disturb a radargram and therefore its evaluation. An example for the internal ringing is illustrated in Fig. 4.33. Here, the internal ringing is indicated by the horizontal lines. In order to remove this ringing, a simple model is set up for its description.

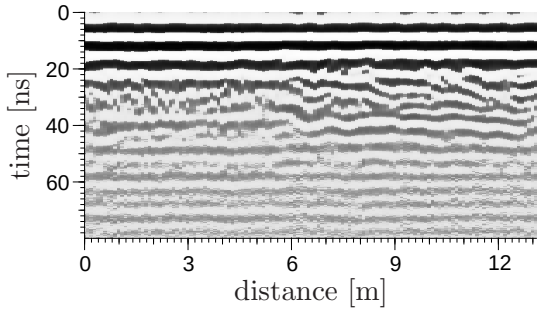

Figure 4.33: *Example radargram with internal ringing.*

In an antenna box with the edge lengths d_i $(i = 1, 2, 3)$, a resonance will

occur, when

$$d_i = n\,\frac{\lambda_i}{2} = \frac{n\,c_0}{2\,\nu_i\,\sqrt{\varepsilon_{\text{box}}}} \quad , \tag{4.32}$$

where λ_i, ν_i $(i = 1, 2, 3)$ are the main wavelengths and the main frequencies, respectively. n denotes the number of multiples of the resonance. This equation gives the condition for standing waves.

With the main frequencies, the internal ringing for each dimension can be described by oscillating terms. Each term has to be scaled differently, because each frequency is emitted with another amplitude by the transmitting antenna within the box. Furthermore, each frequency component will decay with time, due to transmission effects at the boundaries and the absorption from the antennas. This leads to the model describing a trace $r(t)$

$$r(t) = \sum_{i=1}^{3} \sum_{n} A_{i,n}\,\sin\left(2\pi\,\frac{\nu_i}{n} + \vartheta_{i,n}\right)\,e^{-B_{i,n}\,t} \quad , \tag{4.33}$$

which is only affected by the internal ringing. $A_{i,n}$ and $B_{i,n}$ are values for the energy emission and for the energy loss for the nth multiple of the main frequency ν_i, respectively. For completeness, an additional phase shift ϑ_i is introduced.

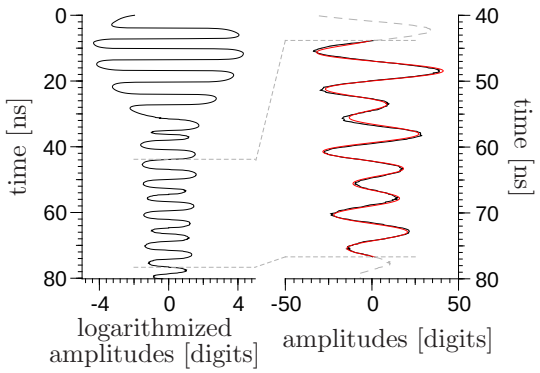

Figure 4.34: *An averaged trace over the whole survey distance of Fig. 4.33 is shown on the left side and a detailed view on the right side. The red curve is a fitted solution with Eq.* (4.34).

For the data given in Fig. 4.33, a mean trace is calculated by averaging each sample over all measurement positions. Then, Eq. (4.33) is fitted in a time window, where the signal almost originates from internal ringing. For simplicity, instead of the general equation (4.33), the modified form

$$\begin{aligned} r(t) = {} & A_1\,\sin(2\pi\,\nu_1 + \vartheta_1)\,e^{-B_1\,t} \\ & + A_2\,\sin(2\pi\,\nu_2 + \vartheta_2)\,e^{-B_2\,t} \end{aligned} \tag{4.34}$$

is used, which results in the solutions given in Fig. 4.34 and Tab. 4.5. These results are obtained from a least square fitting procedure using the Levenberg-Marquardt algorithm (Press *et al.*, 1994).

Table 4.5: *Solutions of the fitting parameter given in Eq.* (4.34) *for the data in Fig. 4.34.*

A_1	[digits]	275	A_2	[digits]	39
B_1	[ns^{-1}]	0.055	B_2	[ns^{-1}]	0.012
ν_1	[GHz]	0.119	ν_2	[GHz]	0.205
ϑ_1	[rad]	3.16	ϑ_2	[rad]	1.93

Although, it is possible to use a single trace for this kind of evaluation, it was decided to use an average trace to overcome noise and to minimize the influence of reflections, which could be shadowed by the ringing.

From the finding in Tab. 4.5, the dielectric permittivity of the material within the antenna box can be calculated. Using the dimensions of the antenna box in width ($d_{\text{w}} = 0.44$ m) and length ($d_{\text{l}} = 0.74$ m), this

leads with Eq. (4.32) to

$$\varepsilon_{\text{box}} = \left(\frac{c_0}{2\, d_i\, \nu_i}\right)^2 \tag{4.35}$$

$$\varepsilon_{\text{box}} \approx 2.90 \tag{4.36}$$

$$\text{with} \quad d_{\text{l}} = 0.74 \text{ m}, \quad \nu_1 \approx 0.119 \text{ GHz}$$

$$\varepsilon_{\text{box}} \approx 2.77 \tag{4.37}$$

$$\text{with} \quad d_{\text{w}} = 0.44 \text{ m}, \quad \nu_2 \approx 0.205 \text{ GHz} \quad .$$

Both values of the relative permittivity of the antenna box are comparable.

The assignment of a frequency and its corresponding dimension of the antenna box can be done in two ways. The first way is a straight forward calculation, where only one assignment leads to comparable results. Furthermore, with a look at the amplitudes A_1 and A_2, it can be seen that the frequency ν_1 contains more energy and therefore, it must lay in a main radiation direction of the transmitting antenna. Its decay (B_1) is also higher, than for the frequency ν_2, which indicates the same. Knowing that the antennas are positioned in the way sketched in Fig. 4.1 and that the used bow-tie antennas radiate the least energy in the principal axis, one can assign the frequency ν_2 with the width d_{w} of the antenna box and ν_1 with the length d_{l}.

Finally, this ringing function can be expanded to the whole time domain of the measured radargram and can be subtract from each trace. For the example given in Fig. 4.33, this results in Fig. 4.35.

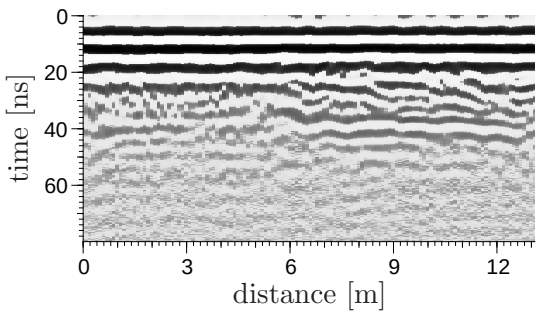

Figure 4.35: *Example radargram with the removed internal ringing.*

4.5 Processing Procedures

4.5.1 Time Zero Correction

A short definition of time zero can be given as:

"Time zero denotes a time, when the radar signal was emitted."

Such a time could be easy to handle, when the transmitter gives a signal to the receiver instantaneously, when it starts radiating. Unfortunately, a lot of available GPR system have no such communication. Commonly, the receiver gets a pulsed signal. It is triggered at a specific value, which is defined by the user or by the software. Now, this start time of the trigger has nothing in common with the time, when the signal was emitted.

Time zero is significant for almost all measurement techniques and their evaluation methods. But where for instance for crosshole GPR this value plays an inferior role, it is of high importance for GPR reflection measurements. Here, this value is needed for evaluation techniques from simple travel time analysis to inverse modeling procedures.

Because of the importance for the evaluation, a lot of effort was undertaken to determine time zero and obtain a stable value (Yelf, 2004). Yelf (2004) concluded in his work that the time zero value "is not a constant value, but must be determined for each surface material type and antenna setup". This finding comes from a statement that "when a 1.5 GHz bow-tie antenna is placed on or near the ground surface, the direct wave is altered in shape and shifts later in time by up to several tenths of nanosecond, due to the dielectric loading of the ground material in the near field of the antenna." (Yelf, 2004)

Time Zero Difficulty for Inversion Procedures

Time zero is also a crucial number in inverse simulations, which is not obvious. To underline this statement, a short example will be given.

Problem: One could assume the travel time equation for the reflected wave

$$t_{\text{refl}} = \frac{\sqrt{\varepsilon_c}}{c_0} \sqrt{4\,d^2 + a^2} + t_{\text{off}} \tag{4.38}$$

with the additional time zero value. d and ε_c are the reflector depth and the relative permittivity above this reflector, respectively. When a hyperbola is observed in a CMP measurement, one could use this function to invert the travel times in order to obtain time zero. This approach can lead to wrong results, which will be shown by the following example.

Setup: With the plane wave approach, a two-layer medium was modeled, where a relative permittivity of $\varepsilon_1 = 3$ and $\varepsilon_2 = 8$ was assigned to the upper and lower half space, respectively. The excitation of the plane waves was set in the same way as presented in Sec. 3.5.1 and it was placed 1 m above the interface in the upper half-space. The observation point was also set 1 m above the interface but with different distances to the excitation, which simulates a CMP measurement. The result of this simulation is shown in Fig. 4.36a.

Evaluation: The observed reflected wave in Fig. 4.36a was picked. Now, a copy of the picked travel times was disturbed with a uniformly distributed error, which varied between ± 0.2 ns. In the next step, on the disturbed and undisturbed travel times a possible offset value in the range of ± 2 ns was added, which denotes the unknown time zero value. For the different offset values, an inversion of the travel times was applied, which minimizes the squared differences between the picked t_{pick} and the modeled t_{model} travel times. Mathematically, this is expressed by the minimization of the cost function ψ defined as

$$\psi = \sum_i \left[t_{i,\text{pick}} - t_{i,\text{model}}\right]^2 \stackrel{!}{=} \min. \quad . \tag{4.39}$$

The modeled travel time as a function of the distance to the source a_i of the ith simulation is given by

$$t_{i,\text{model}} = \frac{\sqrt{\varepsilon_c}}{c_0} \sqrt{4\,d^2 + a_i^2} \quad . \tag{4.40}$$

The minimization was done with the Gauss-Newton method.

Results and Discussion: The results are shown in Fig. 4.36b-d. It can be seen that the solution for reflector depth and relative permittivity reacts linearly to a time zero change. Furthermore, the cost function ψ shows a parabolic shape. When Eq. (4.38) would be

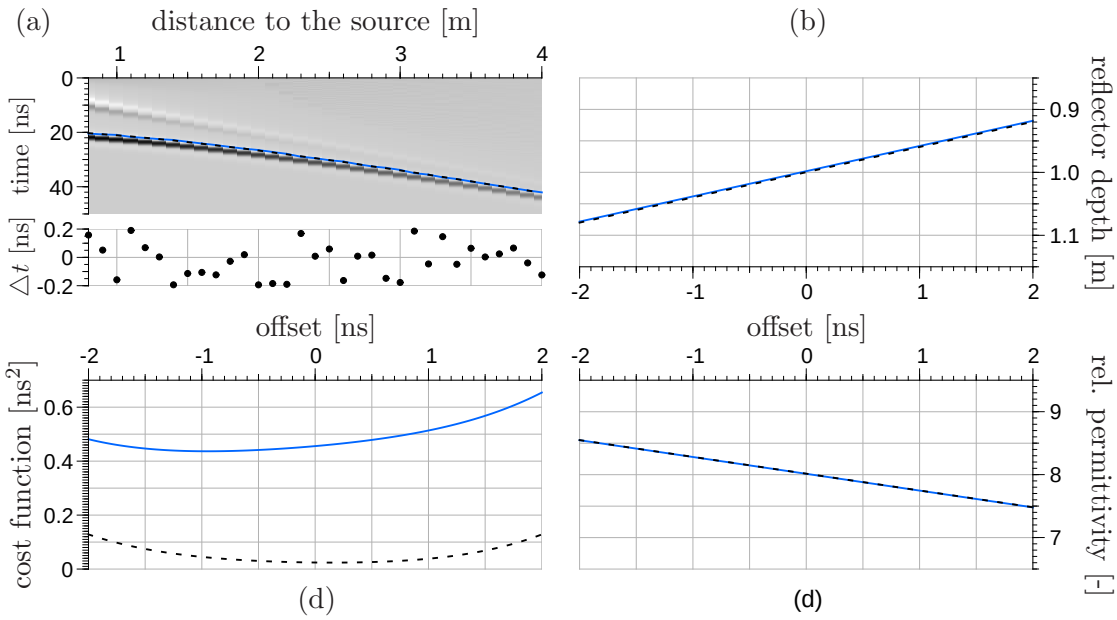

Figure 4.36: *Single reflection analysis, where different offsets are assumed for the reflected wave travel times. The analysis is done by fitting Eq.* (4.40) *to the picked data without (black dashed) and with (blue solid) an additional random error.*

used for an inverse modeling, then the minimum of ψ denotes the corresponding result for the material model. This would not lead to the true material model, especially for noisy data. In the example presented in Fig. 4.36, the minimum of the cost function depending on the offset t_{off} would be at about $t_{\text{off}} = -1$ ns. This leads to an overestimation of the reflector depth ($\triangle d \approx 0.04$ m) and the dielectric permittivity ($\triangle \varepsilon \approx 0.3$).

Time Zero Determination

Based on the assumption for the time zero definition that the starting time of the analyzed wavelet is searched, two methods will be presented, which are capable to provide this value. One method uses the evaluation of a CMP measurement and the other a radiation of an antenna into the air.

Evaluation of CMP measurements: In Fig. 4.37a, a CMP measurement is presented, which was measured in the nature protection area Hirschacker near Schwetzingen, Germany. A clear ground wave is observable throughout the measurement. Furthermore, several reflections and the air wave can be seen. The feature between 3.5 to 5 m and 20 to 40 ns is a bit astonishing, because it shows a constant to slightly decreasing travel time although the antenna separation is increasing. A possible explanation is that this is a reflected-refracted wave, which has a reflection point on a dipping reflector. These dipping reflectors were observed in common offset surveys. They could be assigned to ancient dunes.

Linear Regression of the Direct Wave Picks: In Fig. 4.37b, the picked air and ground wave are shown, where multiple wavelet features are used in order to get information about wavelet distortion. Because of the linear behavior of both waves, it is assumed that the travel time at zero-antenna separation ($a = 0$) refers to the time zero value t_{off} of this corresponding wavelet feature. In order to obtain these values, a linear regression was

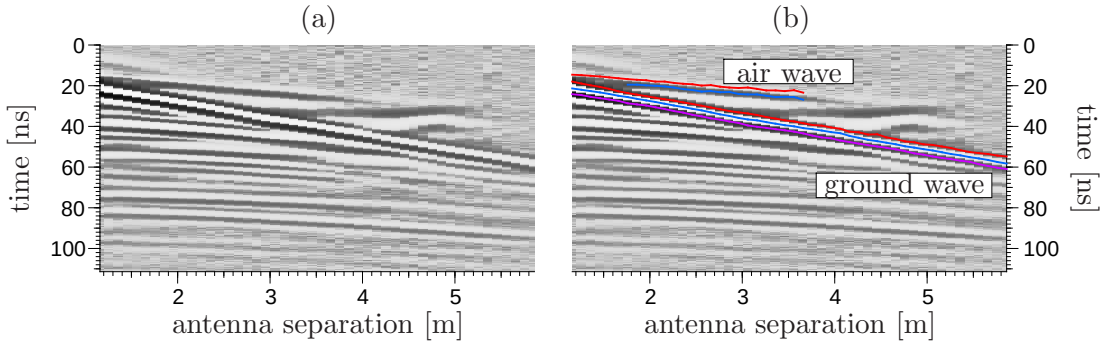

Figure 4.37: *CMP measurement for the determination of time zero.*

Table 4.6: *Parameters of the linear fit for the air and the ground wave of Fig. 4.37. The error is the single standard deviation.*

color	air wave		ground wave	
in Fig. 4.37	v [m/ns]	t_{off} [ns]	v [m/ns]	t_{off} [ns]
red	0.285 ± 0.056	10.53 ± 1.7	0.128 ± 0.007	9.6 ± 1.7
blue	0.260 ± 0.072	12.42 ± 2.9	0.126 ± 0.005	11.9 ± 1.2
purple	-	-	0.127 ± 0.006	14.7 ± 1.3

done using

$$t = A\,a + B \quad \text{with} \quad A = v^{-1} \quad \text{and} \quad B = t_{\text{off}} \quad , \tag{4.41}$$

where $v = c_0/\sqrt{\varepsilon_c}$ is the propagation velocity. For all picks, the results of the linear regression are shown in Tab. 4.6, which reveal a much higher accuracy for the ground wave than for the air wave.

Amplitude and Travel Time Analysis: Now, interferences can be assumed, cf Fig. 4.8, which restrict the reliability of the air and ground wave evaluation. For this reason, the travel times and the amplitudes should be examined in more detail. When some of these information reveal systematic deviations, these picks or small sections should be excluded from the evaluation. Here, the amplitude is considered as a proxy for accuracy, which can indicate the impact for interferences. Furthermore in a far field solution, the decay of the amplitudes should correspond to $1/r^2$, where r is the distance from the transmitter. This functionality comes from a spherical distribution of the energy, which is also called geometrical spreading. The travel time analysis can be done by focusing on the local deviations t_{error} of the picked travel times t_{pick} from the fitted linear function, Eq. (4.41). The deviations are calculated by

$$t_{\text{error}} = t_{\text{pick}} - t_{\text{off}} - \frac{a}{v} \quad . \tag{4.42}$$

The travel time and amplitude analysis for both air and ground wave are shown in Fig. 4.38. Here, for the travel time analysis of the air wave the velocity was set to $v_{\text{air}} = c_0$. Also the time zero was adapted to $t_{\text{off,red}} = 10.83$ ns and $t_{\text{off,blue}} = 13.82$ ns so that all travel times are almost equally distributed around 0 ns. For the evaluation of the ground wave, only all propagation velocities were averaged in order to obtain an equal baseline.

The travel time analysis (Fig. 4.38a,c) shows that the air wave has a high fluctuation in the amplitudes, which can be traced back to the low amplitudes in comparison with the ground wave. Therefore, noise has a much stronger impact. Furthermore, the travel times

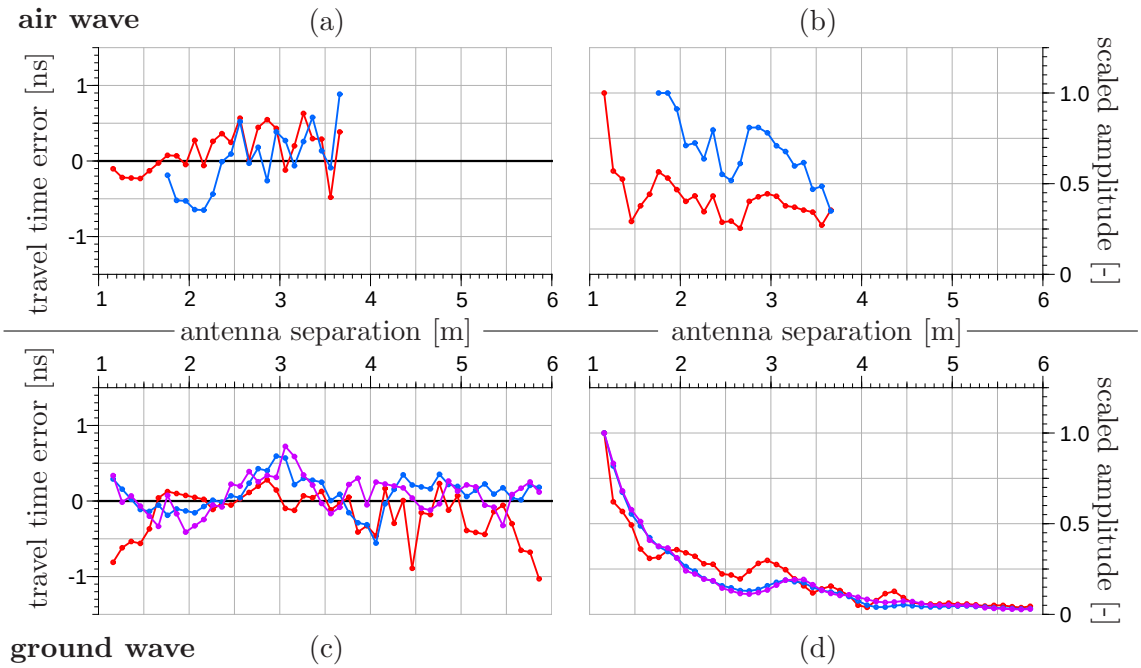

Figure 4.38: *Travel time and amplitude analysis of the air and ground wave from the CMP measurement presented in Fig. 4.37. The amplitudes of (b) and (d) are scaled with the maximum value of each line.*

seem to have a trend, possibly induced by the interference with the ground wave for smaller antenna separations, which leads to the deviation of the air wave velocity (Tab. 4.6). For the ground wave, the upper part (red curves) seems to be be more disturbed than the other ground wave features, which could also be an effect of the low amplitudes.

For the ground wave graphs it is noticeable that the intermediate minimum (blue) and the lower maximum (purple) have a local amplitude maximum at about $a \approx 3.2$ m. In contrast, the travel times show a bit larger deviation from the baseline at about $a \approx 3$ m. A possible explanation is that a reflected-refracted wave interferes / crosses the ground wave. When shortly after the occurrence of the reflected-refracted wave a minimum interferes with a maximum, then the decay of amplitudes can not be detected, but this could lead to a travel time change.

Radiation into the air: Another simple method to obtain a time zero value is to radiate into the air as presented in Fig. 4.39b. Then, the first wavelet can be assigned to the direct travel paths in air. An argument against this method could be the different radiation characteristics, when the antenna radiates into air or when it is placed directly on the ground. If this argument is valid or if this method is applicable, will be proven with a small experiment.

In Fig. 4.39, the measurement setup is shown, where, in a first step, the antennas are placed on the ground surface (Fig. 4.39a). Afterwards, they are positioned as presented in Fig. 4.39b, so that they radiate into the air but still have the same antenna separation and orientation. The resultant traces of both measurements for both plotted channels are given in Fig. 4.40. Here, channel 1 denotes an "internal channel", because transmitter and receiver are within one antenna box, where the antenna separation is $a_1 = 0.36$ m. Channel 3 denotes an "external channel", because transmitter and receiver are in different antenna boxes. It has an antenna separation of $a_3 = 2.20$ m.

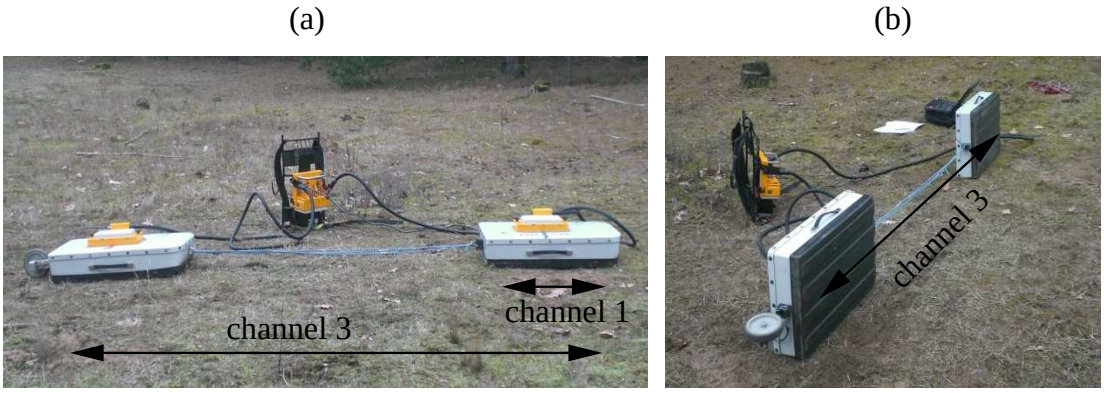

Figure 4.39: *Measurement setup to obtain time zero. The setup uses the difference between the radiation into the ground (a) and into the air (b).*

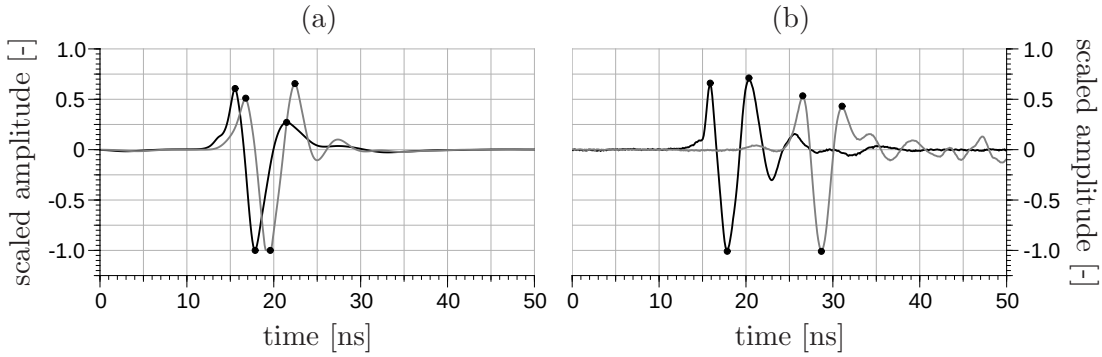

Figure 4.40: *Measured traces of the on-ground (Fig. 4.39a) and in-air measurement (Fig. 4.39b) for an internal channel (a) and an external channel (b).*

Fig. 4.40 shows a single major wavelet, at the beginning of each trace, where this wavelet is assigned to be the air wave for the in-air measurement and the ground wave for the on-ground measurement. The travel times of these two maxima and the largest minima for both waves are shown in Tab. 4.7. Here, the differences between the air and the ground wave travel times are 1.3 ± 0.4 ns for channel 1 and 10.8 ± 0.2 ns for channel 3. This underlines that the wavelet features of the large antenna separation are much more stable than for the short antenna separation.

With respect to the travel times of all wavelet features for both channels the assumption of a separately measured air wave and ground wave cannot be validated. This can be done by calculating the relative permittivity of the ground wave from the travel time difference. In order to obtain an information about the error for time zero, one can assume that channel 3 fulfills the assumption of a separate air and ground wave. This leads to a

Table 4.7: *Travel times of the wavelet features presented in Fig. 4.40.*

	channel 1		channel 3	
extremum	t_{ground} [ns]	t_{air} [ns]	t_{ground} [ns]	t_{air} [ns]
first	16.8	15.6	26.5	15.9
second	19.6	17.9	28.7	17.8
third	22.4	21.5	31.1	20.3

relative permittivity value of about 6.0. The same assumption for channel 1 would lead to a relative permittivity value of about 4.0 for the soil.

It must be noticed that the presented travel time offset data from the CMP evaluation (Tab. 4.6) and from the air measurement / evaluation of channel 3 (Tab. 4.7) should be equal, because the underlying data was measured at the same day, but not directly one after the other. Usually a stable electronic is assumed. Here, the offset values are different as well as the relative changes between the extrema, which means that the wavelet has changed. A reason could be that there were changes within the electronic due to internal heat production. This can modify the properties of single electronic components, which can alter the current density. This can change the emitted electromagnetic pulse.

4.5.2 Normal Moveout Correction

Normal moveout correction is a standard evaluation procedure in seismic applications used for CMP measurements. Extensive studies were done by Dix (1955) and Castle (1994) among others, which focus on multi-layer evaluation of CMP measurements including refraction.

Now, a short introduction will be given to the normal moveout evaluation, adapted for GPR applications. Two approaches will be presented. The first one is a slightly adapted method of the standard normal moveout procedure derived for seismic applications (Yilmaz, 2001). The presented method includes the possibility to evaluate shallow reflections. The second procedure is a modified normal moveout method, which includes the possibility to compensate uncertainties of the time zero offset.

Normal Moveout Analysis for GPR Data

The travel time t_{refl} of a reflection from a horizontal reflector in depth d with an average relative permittivity ε_c above is given by

$$t_{\text{refl}} = \frac{\sqrt{\varepsilon_c}}{c_0} \sqrt{4\,d^2 + a^2} \tag{4.43}$$

for the antenna separation a. This equation is valid for multiple reflectors as long as refraction can be neglected. Here, it is assumed that the measured travel times are zero-offset corrected, which means that the travel time offset is already subtracted. Now, Eq. (4.43) leads to a linear relationship in t_{refl}^2 and a^2,

$$t_{\text{refl}}^2 = t_0^2 + \frac{\varepsilon_c}{c_0^2}\, a^2 \quad \text{with} \quad t_0^2 = \frac{4\,d^2\,\varepsilon_c}{c_0^2} \quad , \tag{4.44}$$

with the derivative $1/v^2 = \varepsilon_c/c_0^2$, where v is the propagation velocity. t_0 is the travel time of the reflected wave, when the antenna separation is $a = 0$. Although, a measurement with $a = 0$ is in the most cases not realizable because of antenna configuration and design, the travel time $t_{0,i}$, which is the travel time from the ith reflector at zero antenna separation, can be reproduced by choosing a proper $\varepsilon_{c,i}$, which denotes the average relative permittivity above the ith reflector. Then, the amplitudes for all antenna separations, which correspond to an emission at $t = 0$, and originate from the same reflector plot on a horizontal line in the radargram, when the squared time shift $\triangle t^2$ with

$$\triangle t^2 = t_{\text{refl}}^2 - \frac{\varepsilon_c}{c_0^2}\, a^2 \tag{4.45}$$

is applied on each trace. This means each squared travel time for different antenna separations is shifted, which leads to a zero antenna separation travel time assuming a given relative permittivity

$$t_0^2(\varepsilon_c) = t_{\text{refl}}^2(a) - \triangle t^2(a, \varepsilon_c) \quad . \tag{4.46}$$

If these amplitudes for all $t_0^2(\varepsilon_c)$ are summed up, which is called stacking, then a maximum value occurs at a travel time $t_{0,i}$, when $\varepsilon_{c,i}$ is the average permittivity above an existing reflector with a depth d_i. This reflector depth d_i can be calculated due to

$$d_i = \frac{t_{0,i}\, c_0}{2\sqrt{\varepsilon_{c,i}}} \quad . \tag{4.47}$$

Note: This procedure is a bit different to the method presented by Yilmaz (2001) and Tillard and Dubois (1995). Here, they come up with the following equations starting with Eq. (4.43)

$$t_{\text{refl}} = \frac{\sqrt{\varepsilon_c}}{c_0}\sqrt{4\,d^2 + a^2} \quad \Longrightarrow \quad t_{\text{refl}} = \sqrt{t_0^2 + \frac{a^2\,\varepsilon_c}{c_0^2}}$$

$$\Longrightarrow \quad t_{\text{refl}} = t_0\sqrt{1 + \frac{a^2\,\varepsilon_c}{c_0^2\,t_0^2}} \quad \Longrightarrow \quad t_{\text{refl}} \approx t_0\left(1 + \frac{a^2\,\varepsilon_c}{2\,c_0^2\,t_0^2}\right) \tag{4.48}$$

assuming

$$\frac{t_0}{4}\left(\frac{a^2\,\varepsilon_c}{c_0^2\,t_0^2}\right)^2 = \frac{t_0}{4}\left(\frac{a^2}{4\,d^2}\right)^2 < \text{ measurement error} \quad . \tag{4.49}$$

This term is the third summand of the Taylor series. The measurement error denotes the travel time resolution of the measurement.

This leads to a time shift

$$\triangle t = \frac{a^2\,\varepsilon_c}{2\,c_0^2\,t_0} \quad , \tag{4.50}$$

where t_0 can be calculated from Eq. (4.44) without any knowledge about the reflector depth. This time shift can directly be applied to the travel time data without any quadrature.

From Eq. (4.49), it is clear that the deviation of the time shift and its applicability is only valid, if the reflector depth is larger than the antenna separation. This can not be guaranteed for all applications.

Furthermore in studies such as presented by Garambois *et al.* (2002), a semblance analysis (Neidell, 1971) is used instead of the stacking method. This semblance analysis applies the crosscorrelation between all traces. Because the wavelet structure is distorted due to the squared travel time, the application of this method was not considered in this work.

Synthetic Example: Analogous to the validation example in Sec. 3.5, a CMP measurement was simulated using the plane wave approach, Fig. 4.41a, using the material model given Fig. 4.41c. The incoming wave field is described by Eq. (3.109), using the modeling parameters given in Eq. (3.110). Because of the modeling parameter $\tau_0 = 0$, it is assumed that the results are already zero-offset corrected.

The time axis and the antenna separations are squared, which is shown in Fig. 4.42a. Afterwards, the squared travel time shift Eq. (4.45) is applied on each trace. For a relative permittivity $\varepsilon_c = 7$ the results for each trace are shown in Fig. 4.42b. With this shift, the first reflection from a depth of 0.5 m becomes a horizontal line. Now, this shifted radargram is stacked, which means that all traces are summed up. This leads to the

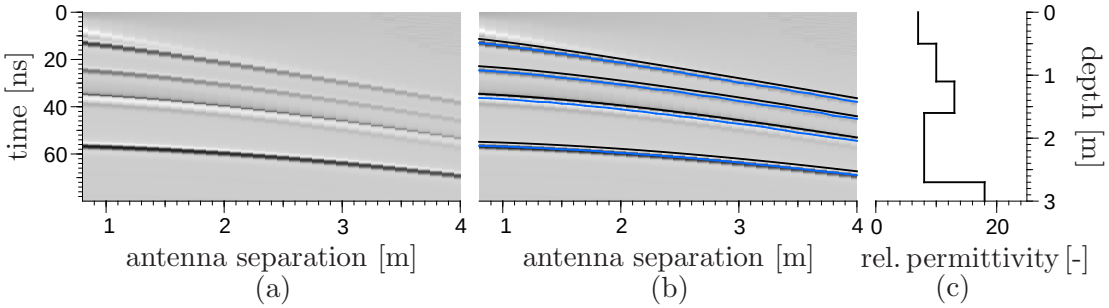

Figure 4.41: *Plane wave modeling of a CMP measurement (a) with the material model shown in (c) and the incoming field given in Eq.* (3.109) *and* (3.110)*. (b) presents the picked reflection hyperbolas (blue) and the travel times for each reflection modeled by the ray approach including refraction (black).*

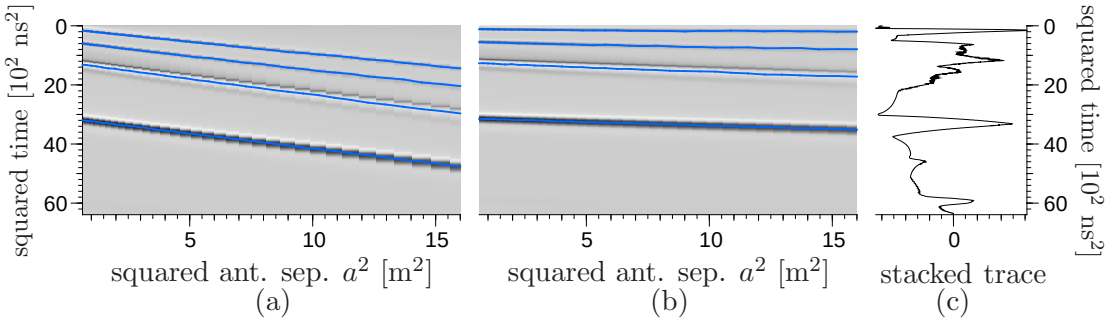

Figure 4.42: *Normal moveout procedure: (a) represents the radargram with a squared time and antenna separation axis. (b) represents a shifted radargram with the squared time shift given in Eq.* (4.45) *($\varepsilon_c = 7$). (c) is the resultant stacked trace.*

stacked traces shown in Fig. 4.42c. The numerical values of the amplitudes are neglected here, because only the positions of local maxima and minima have a relevance for this analysis.

In Fig. 4.42c, one can see that the first reflection leads to the global maximum in this stacked trace. But although, the other reflections did not lay on horizontal lines, they produce maximum values, which are very close to the global maximum. This is clear, because the amplitudes of the first reflection are in general smaller than for the others. Here, the modeled radiation pattern with a squared cosine function predicts that less energy is transmitted sidewards and the most downwards.

In a next step, the square root of the relative permittivity is changed within a reasonable range and for each value the stacked trace is calculated. Here, the square root of the relative permittivity is used instead of the velocity like it is done in Fisher *et al.* (1992) and Garambois *et al.* (2002), because the interest of this work is the water content. This water content can be given as a function of this quantity, as it is shown in Sec. 2.35.

Now, in Fig. 4.43b the stacked traces for a set of square root values of the relative permittivity values are shown. Fig. 4.43a shows the analogon with the velocity values. This kind of plot commonly used. Furthermore, the travel time axis is converted to expected reflector depth values (Fig. 4.43c) using Eq. (4.47). In all three figures, the expected and the manually estimated extremal positions are marked.

The expected extremal positions are calculated from the defined layer depths $\triangle d_i$ and the layer permittivities ε_i $(i = 1, \ldots, N)$ for a material model with N layers. For a perpendicular incidence of the wave, the two way travel time $t_{\mathrm{refl},j}(a = 0)$ to the jth

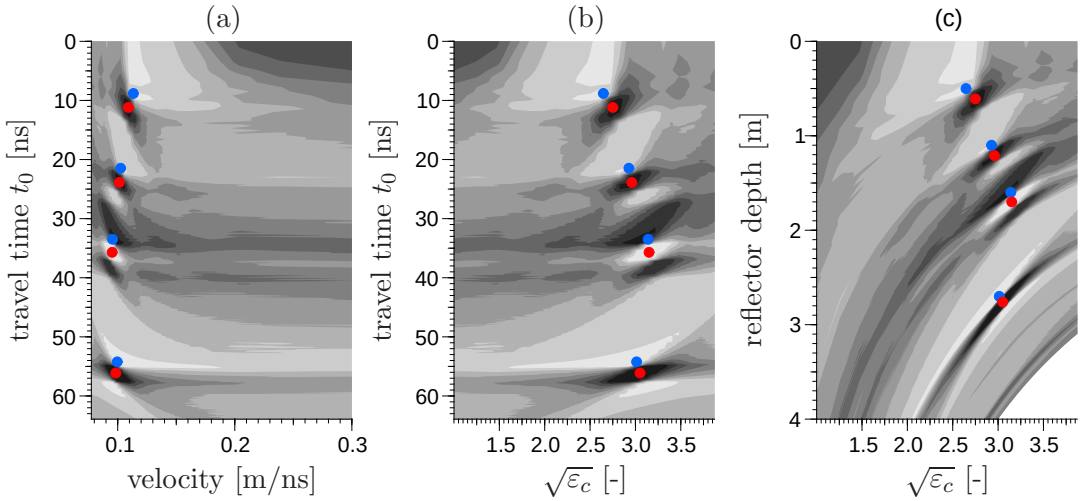

Figure 4.43: *Solution of a normal moveout procedure using the example given in Fig. 4.41. The stacked traces are shown using different velocities (a) and different values for the square root of the relative permittivity. (c) gives the converted image into expected reflector depth with Eq.* (4.47)*. The blue dots correspond to the true material model and the red dots show the manually estimated material model.*

reflector is given by

$$t_{\mathrm{refl},j}(a=0) = \frac{2}{c_0} \sum_{i=1}^{j} \triangle d_i \sqrt{\varepsilon_i} \quad . \tag{4.51}$$

On the other hand, it is expected that the true reflector depth $d_j = \sum_{i=1}^{j} \triangle d_i$ is found with only an average dielectric permittivity $\varepsilon_{c,j}$ above the jth reflector. This leads to the relationship

$$t_{\mathrm{refl},j}(a=0) = \sqrt{\varepsilon_{c,j}} \frac{2}{c_0} \sum_{i=1}^{j} \triangle d_i = \frac{2}{c_0} \sum_{i=1}^{j} \triangle d_i \sqrt{\varepsilon_i} \quad . \tag{4.52}$$

Therefore, for a given material model the expected averaged relative permittivity values are obtained by

$$\sqrt{\varepsilon_{c,j}} = \left(\sum_{i=1}^{j} \triangle d_i \sqrt{\varepsilon_i} \right) \left(\sum_{i=1}^{j} \triangle d_i \right)^{-1} \quad . \tag{4.53}$$

Otherwise the estimated averaged relative permittivity values can be used to determine the material model using

$$\sqrt{\varepsilon_j} = \frac{d_j \sqrt{\varepsilon_{c,j}} - d_{j-1} \sqrt{\varepsilon_{c,j-1}}}{d_j - d_{j-1}} \quad \text{with} \quad d_m = \sum_{i=1}^{m} \triangle d_i \quad . \tag{4.54}$$

The notation of this equation is intentionally chosen in that way, because it can be understood as an analogy to the equation of Dix (1955), who used velocity and travel time values.

Now, in Tab. 4.8 an overview of the predefined material model used for Fig. 4.41 and the estimated material model extracted from the normal moveout procedure, shown in Fig. 4.43, is given. It can be seen that the depth values are overestimated by approximately 10 cm. The relative permittivity values are reproduced reasonably.

The overestimation of the reflector depth is assumed to stem from an incorrect time zero value. This value was set to be the center maxima of the emitted wavelet. Due to

Table 4.8: *Overview of the material model used for the simulation shown in Fig. 4.41 and of the estimated material model from the normal moveout procedure (red dots in Fig. 4.43).*

layer	defined material model		manually estimated material model	
	reflector depth d_i [m]	relative permittivity ε_i [-]	reflector depth d_i [m]	relative permittivity ε_i [-]
1	0.50	7	0.61	7.56
2	1.10	10	1.21	10.07
3	1.60	13	1.70	13.10
4	2.70	8	2.76	8.35

the radiation in different direction, this wavelet seems to be distorted. Then, the resulting main maximum has a different time zero. Because of this difference, the overestimation can be explained. But in this example, the correct time zero value cannot be estimated analogous to experimental data. Because of the defined radiation characteristic, the direct wave cannot be detected sufficiently and therefore, it cannot be evaluated.

Modified Normal Moveout Approach

In a first step, a measured common midpoint radargram shall be recognized as a matrix $g(a_n, t_m)$ of N columns an M rows, where each column and row can be assigned to an antenna separation a_n $(n = 1, \ldots, N)$ and a time value t_m $(m = 1, \ldots, M)$.

A reflection, which are understood as significant amplitude values, can be observed at travel times $t_{m,n} \approx t_{\text{refl},n}$. This reflected wave travel time $t_{\text{refl},n}$ as a function of reflector depth d and relative permittivity ε_c is given as

$$t_{\text{refl},n} = \frac{\sqrt{\varepsilon_c}}{c_0} \sqrt{4\,d^2 + a_n^2} + t_{\text{off}} \quad , \tag{4.55}$$

where t_{off} is the GPR immanent travel time offset. A priori, the true values for d, ε_c and t_{off} are not known. But it is known that for the zero antenna separation $(a = 0)$ a travel time is expected as

$$t_{\text{refl},a=0} = t_{\text{refl},0} = \frac{\sqrt{\varepsilon_c}}{c_0}\, 2\,d + t_{\text{off}} \quad . \tag{4.56}$$

This leads to the idea to shift all travel times for given antenna separation a_n by

$$\triangle t_n = t_{\text{meas},n} - t_{\text{meas},0} = \frac{\sqrt{\varepsilon_c}}{c_0} \left(\sqrt{4\,d^2 + a^2} - 2\,d \right) \quad . \tag{4.57}$$

If now the chosen reflector depth d and its average relative permittivity ε_c above corresponds to a measured reflector defined by the same parameters, all amplitudes for this reflector are at $t_{\text{meas},0}$ for all antenna separations a_n $(n = 1, \ldots, N)$. Unfortunately, such horizontal amplitude lines could also occur for a wrong parameter pair, because the measured reflected wave travel time contains still the unknown offset t_{off}.

When, for a shifted radargram, all amplitudes are located at the same travel time for all antenna separations, than one would expect that these horizontal lines would lead to large number compared to the rest. This sum is called stacking, which results in a trace $g(t_m)$ from the shifted radargram $g(a_n, t_{m,n})$ by

$$g(t_m) = \sum_{n=1}^{N} g(a_n, t_{m,n}) \quad \text{with} \quad t_{m,n} = t_m - \triangle t_n \quad . \tag{4.58}$$

This resultant trace need not have its global maximum at $t_{\text{meas},0}$, because amplitudes from other reflections or travel paths could be larger and therefore, they might lead to maxima in the stacked trace $g(t_m)$ although no horizontal line was observed in $g(a_n, t_{m,n})$.

But if an offset value t_{off} is set with an uncertainty of $\pm\triangle t_{\text{off}}$, one would expect a maximum value $g_{\max}$ with

$$g_{\max} = \max_{t_m \in I} |g(t_m)| \tag{4.59}$$

$$\text{with} \quad I = [t_{\text{refl},0} - \triangle t_{\text{off}}, t_{\text{refl},0} + \triangle t_{\text{off}}] \tag{4.60}$$

within the trace in the interval I. The maximum value is still a function of reflector depth and average relative permittivity. When both values are discretized to d_k $(k = 1, \ldots, K)$ and ε_l $(l = 1, \ldots, L)$, $g_{\max}(d_k, \varepsilon_l)$ results in a matrix, where its main maxima should correspond to the describing parameters of the material model, reflector depth and average relative permittivity.

Instead of the maximum method, Eq. (4.59), one can examine the integrated amplitude g_{int} within the interval I. Mathematically, this is expressed by

$$g_{\text{int}} = \int_I |g(t_m)| \, dt_m \quad . \tag{4.61}$$

Again, the integrated amplitude is a function of the chosen reflector depth and average relative permittivity and hence, they can be illustrated in a contour plot. Maximum values should indicate the underlying material model. In contrary to the maximum method, the uncertainty $\pm\triangle t_{\text{off}}$ of the offset can be interpreted as a width of a wavelet, which is found at a travel time t_m. But this would indicate that the integral method is more sensitive to an uncertainty of the offset.

Synthetic Example: In order to show the capability of this approach, the example shown in Fig. 4.41 is used. Now, in Fig. 4.44 the result for the modified normal moveout procedure using the maximum method (Fig. 4.44a) and the integral method (Fig. 4.44b) are presented.

Here, the expected maxima are marked by blue dots. The red dots represent the estimated material model from the standard normal moveout procedure and they fit the actual maxima reasonably. Only, the deepest reflector has no localized maximum.

From Fig. 4.44, it can be seen that the integral method leads to more focused maxima. The advantage of this modified normal moveout is that the interpreter needs not to determine a reflection between maxima and minima, which are close to each other in the standard normal moveout procedure, Fig. 4.43. Furthermore, especially for the integral method, the spreading effect of the maxima (Garambois *et al.*, 2002) is less pronounced than in the standard normal moveout analysis.

4.5.3 Windowed Fourier Analysis

Electromagnetic wave phenomena can be either studied in frequency or in time domain. Because the most GPR applications operate in time domain, it could be worthwhile to take a look into the frequency domain, which is done by a Fourier analysis.

When thinking in terms of a superposition of wavelets, which sets up a measured GPR trace, then a Fourier transformation of the whole signal might not be instructive. From the point that a single wavelet is distorted during the propagation through dispersive media or from the reflection from smooth transitions, then only single wavelets should be analyzed in the frequency domain. Unfortunately, these wavelets cannot be separated

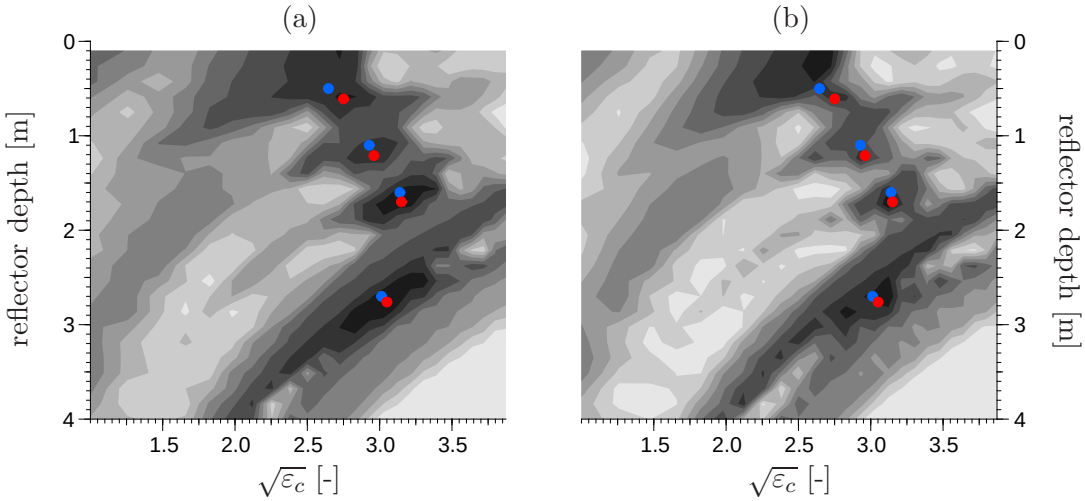

Figure 4.44: *Solutions of the modified normal moveout procedure using the maximum method (a), Eq.* (4.59) *and the integral method (b), Eq.* (4.61).

by a deconvolution method, when they all differ in shape. On the other hand, a trace can be qualitatively described. The upper part is mainly influenced by the air and the ground wave. Then for the larger travel times, it can be assumed that the signals stem from reflections from larger depth.

Under this qualitative point of perspective, a windowed Fourier / frequency analysis can be placed, which means that only a small section (window) from a whole trace is transformed into frequency domain.

There are two possibilities of windowed Fourier transformations, which each have its advantages and disadvantages. Within this work these possibilities will be named "hat-function-transformation" and "direct window transformation".

Hat-Function Transformation

The hat-function transformation denotes a method, where a hat-function is multiplied on the trace, which has a value of 1 in the region of interest, than there could be a transition to 0 and everywhere else a value of 0 is set. The product of both functions is Fourier transformed.

Mathematically, this is expressed denoting a measured trace as $r(t)$, which leads to a product trace $s(t)$

$$s(t) = g(t) \cdot r(t) \quad , \tag{4.62}$$

where $g(t)$ defines the hat-function. Two possible hat-functions shall be considered. The first one is given as

$$g(t) = u(t+t_1) - u(t+t_2) \quad \text{with} \quad t_1 < t_2 \quad \text{and} \quad u(t+a) = \begin{cases} 0 & , \text{ for } \quad t \leq a \\ 1 & , \text{ for } \quad t > a \end{cases} \quad ,$$

where $u(t)$ is the unit step function or also known as the Heaviside function. While this function has sharp edges, the second function is defined by a smooth transition, given as

$$g(t) = \begin{cases} 1 - \exp\left\{-\dfrac{(t_1-t)^2}{\tau^2}\right\} - \exp\left\{-\dfrac{(t-t_2)^2}{\tau^2}\right\} & , \quad \text{for} \quad t \in [t_1, t_2] \\ 0 & , \quad \text{for} \quad t \notin [t_1, t_2] \end{cases} \quad , \tag{4.63}$$

where τ determines the width of transition[5]. Now, the Fourier transformation of Eq. (4.62) leads to

$$s(\omega) = \int g(t) \cdot r(t)\, e^{-\mathtt{i}\,\omega\, t}\, d\omega = \int g(w - w') \cdot r(\omega')\, d\omega' \quad , \tag{4.64}$$

which results in a convolution of the Fourier transformed hat-function $g(\omega)$ and the original trace $r(\omega)$. Here, $s(\omega)$ denotes the Fourier transformed result of Eq. (4.62).

Although, this convolutional integral could lead to a distortion of the spectrum, this is not the case, if a single wavelet is assumed with a compact support approximately within $t \in [t_1 + 2\,\tau, t_2 - 2\,\tau]$. Then, this hat-function has almost no impact on the original signal.

Direct Window Transformation

The direct window transformation means that only a section of a whole trace is transformed. To be more precise, a measured trace can be understood as amplitudes being a function of time or, in a discrete sense, as amplitudes being a function of the sample. Here, a time value is assigned to each sample. Therefore, the direct window transform uses instead of all N samples only a section $N_w < N$, which includes the signal of interest.

The impact of such a restriction of samples can be highlighted by the formulation of the discrete Fourier transformation. Assuming a measured trace $r(t)$ represented in discrete form as $r(t_i)$ for $i = 0, \ldots, N-1$, where N is the number of samples, than the discrete transformation into Fourier-space is given as

$$r(\nu_j) = \sum_{k=0}^{N-1} r(t_i)\, \exp\left\{-\mathtt{i}\, \frac{2\,\pi\, j\, k}{N}\right\} \quad , \tag{4.65}$$

which gives the a complex value $r(\nu_j)$ for a discrete frequency value ν_j. The numerical value for this frequency is obtained by

$$\nu_j = \frac{j}{(N-1)\,\triangle t} \quad \text{for} \quad j = 0, \ldots, N-1 \quad , \tag{4.66}$$

where $\triangle t$ is the time step size of the measured trace.

From Eq. (4.66), it can be concluded that the truncation of the samples leads to a smaller number of frequency values, but the maximum frequency stays the same, because $\triangle t$ is not changing.

Single Trace Example

In a short example, both possible methods should be examined. For this purpose, the measurement presented in Fig. 4.33 will be used, which reveals a strong ringing for late travel times. For the windowed Fourier analysis the trace at about $x = 5.5$ m is used.

In a first step, the trace is either multiplied with a hat-function or truncated. For this purpose, a window with the center time of about $t_{\text{center}} = 52.5$ ns and a width of $\triangle t = 20$ ns was chosen. This means that either all values $t \notin [t_{\text{center}} - \triangle t/2, t_{\text{center}} + \triangle t/2]$ are truncated or set to 0 depending on the method. Furthermore for the hat-function transformation, the function given by Eq. (4.63) was used with a slope parameter $\tau = 2$ ns.

The result of this Fourier-transformed window is presented in Fig. 4.45, which shows a much higher frequency resolution for the hat-function transformation than for the direct window transformation. Furthermore, the results of both methods show a similar

[5]It must be noted that other functions for this transition are also possible. The usage of this function can only be argued by the success of this method given in the single trace example.

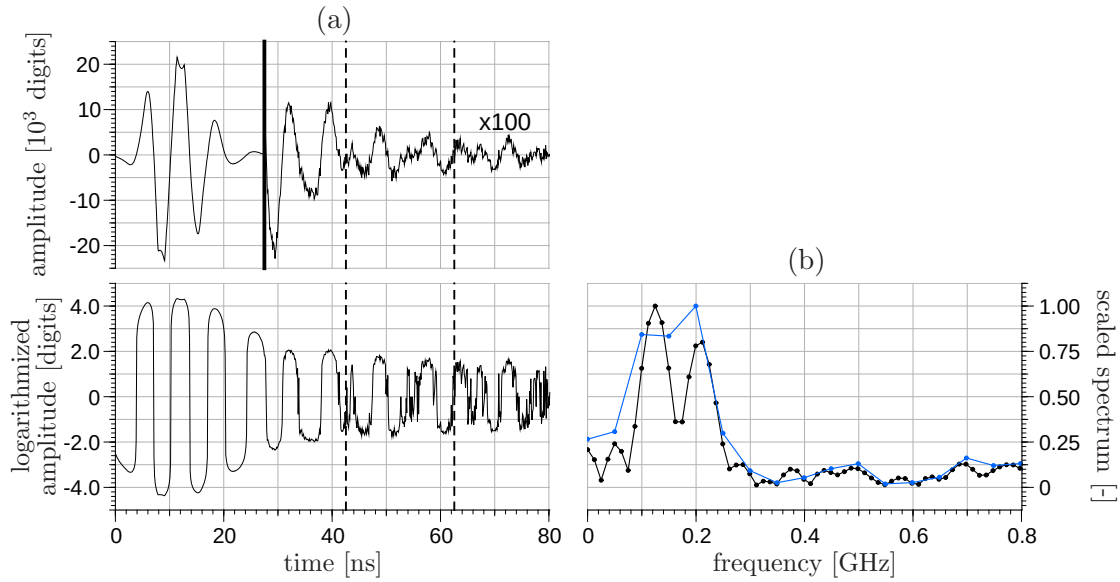

Figure 4.45: *Example of the windowed Fourier transformation of a measured trace (a) for a single window, which is marked by the vertical lines. In (b) the spectrum for hat-function method (black) and the direct window method (blue) are presented. The dots show the actual data points.*

frequency behavior. Because of the higher resolution, the hat-function method is able to detect two main frequency peaks at about 0.13 GHz and 0.22 GHz, which are close to the frequencies determined in Sec. 4.4.5 ($\nu_1 = 0.119$ GHz and $\nu_2 = 0.205$ GHz).

Another result of this single window example is that the the slope parameter τ, defined in Eq. (4.63), has only a very small impact on the result of the spectrum for the hat-function method. Because the result with either a larger or smaller τ would overlap the spectrum given in Fig. 4.45, its presentation is omitted.

At last, in Fig. 4.46 the result of a windowed Fourier transformation is shown, where the window is moved through the whole trace using both methods. The center time of each window is represented by the time axis of the contour-plots. Again, a window width of 20 ns was chosen.

Both methods show the two distinct frequencies at the lower part of the trace, but, as expected, the hat-function method reveals a much higher resolution.

Outcome: Windowed Fourier Analysis

In this section the windowed Fourier analysis was presented, which can be tool to evaluate GPR traces. With a help of an example, the possibility of this method was presented. Here, the application reveals two main frequencies, which are involved in a ringing phenomenon.

4.5.4 Evanescent Wave Evaluation / Ground Wave Evaluation

As discussed in Sec. 4.3.6, some measured waves in GPR applications show an evanescent wave behavior. Especially, the spectrum of the ground wave as a function of height seems to be describable by the analytical expression given in Eq. (4.17). Because of this finding, the idea of this section is to provide a possibility to obtain the near surface permittivity using the characteristic decay of amplitudes as a function of height.

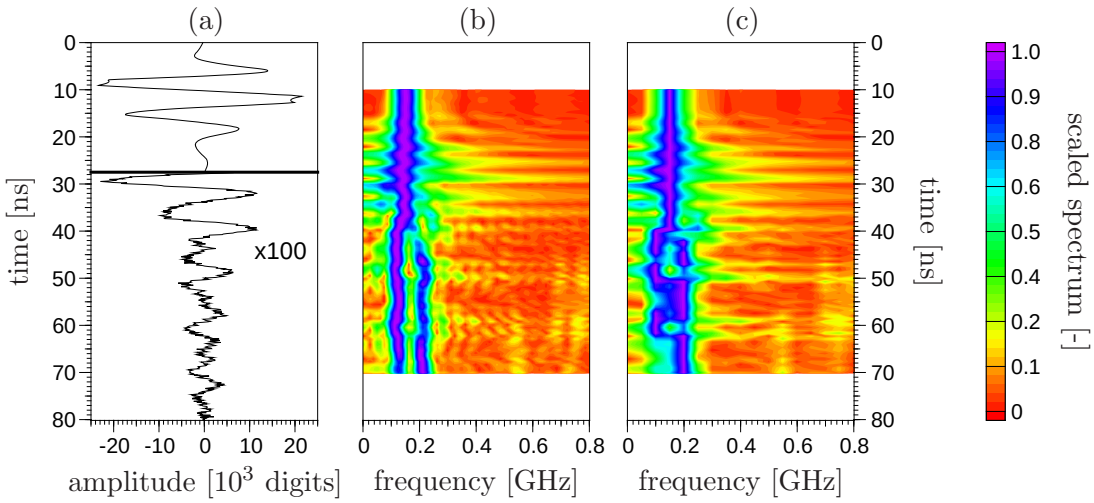

Figure 4.46: *Example of a windowed Fourier transformation of single trace (a) with a window width of 20 ns using the hat-function method (b) (with a slope parameter $\tau = 2$ ns) and the direct-window method (c). The spectra for each window are scaled independently.*

Evaluation Approach

A measurement or a simulation will be assumed, where either the transmitter, the receiver / observation point or both shall be lifted. Then the resultant trace can be recognized as a superposition of different wavelets, where some of them reveal an evanescent wave behavior and others are assumed to stay unaffected for small changes in height. Therefore, only a section $s(t)$ of the trace shall be analyzed analogous to Sec. 4.5.3, which can be obtained in the same way as presented in Eq. (4.62). Within this trace section, one can assume a two parts. On part $s_d(t,z)$ of the signal, which shows an exponential decay as a function of height z. Another part $s_c(t)$ of the signal is assumed to remain nearly constant for small changes in height.

Because the decay of the evanescent waves is a function of frequency, this trace section must be transformed into the frequency domain. This leads to

$$s(t) = s_c(t) + s_d(t,z)$$
$$\textbf{??} \Longrightarrow \quad s(\omega) = \left[s'_c(\omega) + \mathtt{i}\, s''_c(\omega)\right] + \left[s'_d(\omega,z) + \mathtt{i}\, s''_d(\omega,z)\right] \quad , \tag{4.67}$$

where s'_c, s'_d and s''_c, s''_d are the real and imaginary parts of the Fourier transformed trace section for both wave parts. From the theory presented in Sec. 3.3.2, the evanescent waves decay with

$$s_d(\omega,z) = s_d(\omega)\ \exp\{-\alpha\ z\ \omega\} \quad , \tag{4.68}$$

where α is given as

$$\alpha = \sqrt{\varepsilon_2 - \varepsilon_1}/c_0 \tag{4.69}$$

for a wave, which propagates parallelly to the interface in the medium with ε_2 and couples as an evanescent wave in the medium with ε_1. Furthermore, $s_d(\omega)$ denotes the frequency component of the wavelet directly at the surface ($z = 0$).

Now, it can be assumed that α is a function of frequency, because of the argumentation recording to the ground wave in multi-layered media, cf. Sec. 4.3.6. Under this perspective, one can assign five parameters, which determine a single frequency component $s(\omega)$ for this approach. Now, the Eq. (**??**) leads to

$$s(\omega) = \left[s'_c(\omega) + \mathtt{i}\, s''_c(\omega)\right] + \left[s'_d(\omega) + \mathtt{i}\, s''_d(\omega)\right]\ e^{-\alpha(\omega)\, z\, \omega} \quad , \tag{4.70}$$

which can be used as a modeling function for a fitting procedure. This fitting can be done by a least squares method, which minimizes the squared differences between the modeled data given by Eq. (4.70) and the measured or simulated data. This is expressed as

$$\sum_{i=1}^{N} \left\{ \left[s'_{i,\mathrm{model}}(\omega;\mathbf{p}) - s'_{i,\mathrm{meas}}(\omega) \right]^2 + \left[s''_{i,\mathrm{model}}(\omega;\mathbf{p}) - s''_{i,\mathrm{meas}}(\omega) \right]^2 \right\} \stackrel{!}{=} \min. \quad , \tag{4.71}$$

where N must be equal or larger the number of the fitted parameters in $\mathbf{p}$. Here, $\mathbf{p} = (s'_c, s''_c, s'_d, s''_d, \alpha)$ denotes the parameter vector, which is adapted such that a minimum occurs.

If the results for all $s_c(\omega)$ and $s_d(\omega)$ are transformed into time domain, the shape of both wave types in time domain can be observed. Now, when the ground wave is studied, the relative permittivity of the near subsurface can be extracted with the help of Eq. (4.69).

In the following, this approach will be tested using a synthetic and an experimental example.

Synthetic Example: The synthetic example is set up to demonstrate the capability and the limits of the approach presented above.

Setup - Underlaying Data: For the synthetic example, the simulated data set presented in Sec. 4.3.6 is used, where the observation point was lifted (Fig. 4.24d). From these traces, only the ground wave section was used by applying a hat-function Eq. (4.63) on the data with a window width of 15 ns and a transition / slope parameter of $\tau = 0.5$ ns.

The spectra of the simulated ground waves are presented in Fig. 4.47b. They show a decay and a shift of the maximum position towards lower frequencies.

Evaluation and Results: Now, the data of the real and imaginary part of the Fourier-transformed ground wave for a single frequency but for all heights were extracted. The presented data set was used to fit Eq. (4.70), which was done by a Levenberg-Marquardt algorithm (Press *et al.*, 1994). For three frequencies the result of the fitting procedure is shown in Fig. 4.47a. Here, the values are scaled, such that the maximum value of the real part is 1 (positive) and the maximum value of the imaginary part is -1 (negative). It can be seen that all components show an exponential decay. But one can also observe that there is still an amplitude offset for larger heights of the observation point. This offset is different for each frequency.

The result of the procedure for all frequencies between 0.06 and 0.37 GHz are shown in Fig. 4.48. These results are the amplitudes of the evanescent wave $s_d(t)$ and the constant wave $s_c(t)$ in the time domain at the boundary (Fig. 4.48b) as well as the exponent α (Fig. 4.48c), which includes the dielectric contrast. The truncation of the frequencies was done, because outside this range the amplitudes are very small and the fitting parameter α, which describes the decay, leads to unreasonable values after applying the Levenberg-Marquardt algorithm. Outside this range, all fitting parameters were set to zero.

In Fig. 4.48a, again all ground waves are shown for the different heights (colored lines). The dashed lines above represents the results of the fitting procedure, where these traces were obtained by a Fourier transformation into time domain of the function given by Eq. (4.70) using the fitted parameters. At the bottom of Fig. 4.48a, the absolute error between the simulated traces with the Greens function approach and the fitted ground wave sections based on plane wave theory are shown. A significant amount of this error stems from the truncation of frequencies, which was validated by changing the fitting

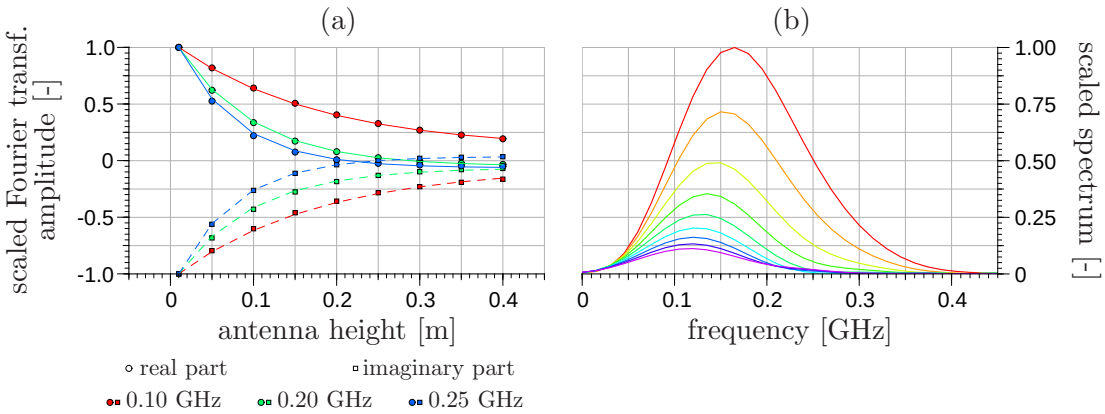

Figure 4.47: *Single frequency inversion for three different frequencies (a), where the dots represent the data points for specific heights and the lines the results of the inversion. The maximum value for the real part (circles, solid lines) was scaled to +1 and for the imaginary part (rectangles, dashed lines) to −1. The spectra for all heights are given in (b), scaled with the maximum value of all spectra. The color scheme of the spectra corresponds to Fig. 4.24.*

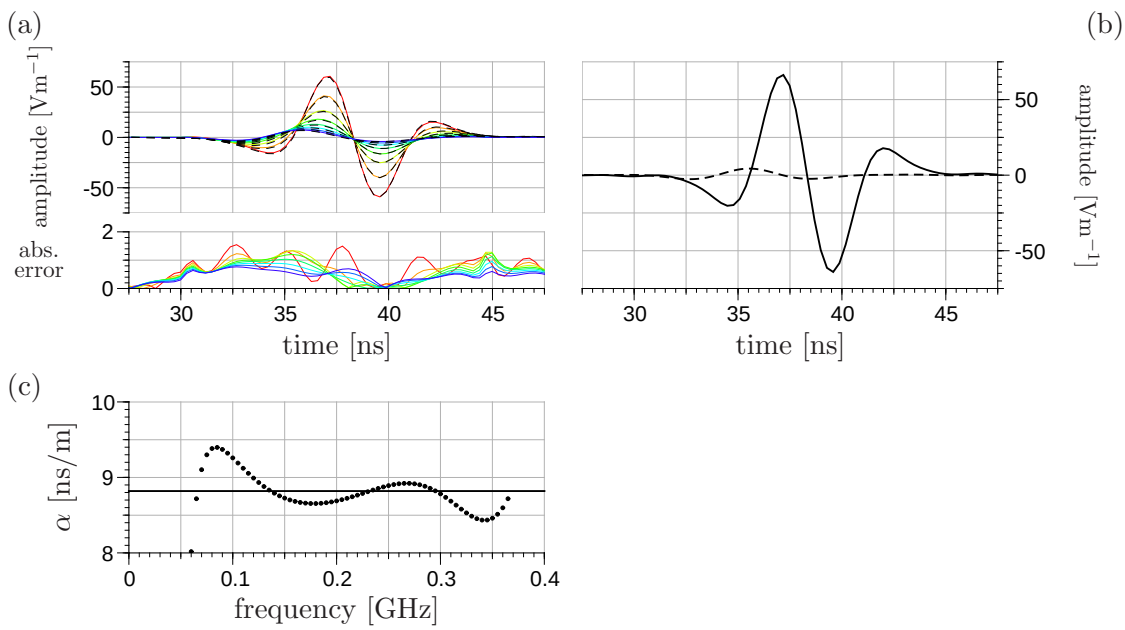

Figure 4.48: *Results of the evanescent wave analysis for the simulated data set presented in Fig. 4.24d. (a) shows the simulated data (colored lines) and the fitted results using the plane wave approach (dashed lines). At the bottom, the absolute error between both data sets is presented. Subfigure (b) shows the constant (dashed) and the decaying (solid) wavelet at the surface. (c) gives a result for the decay parameter α as a function of frequency.*

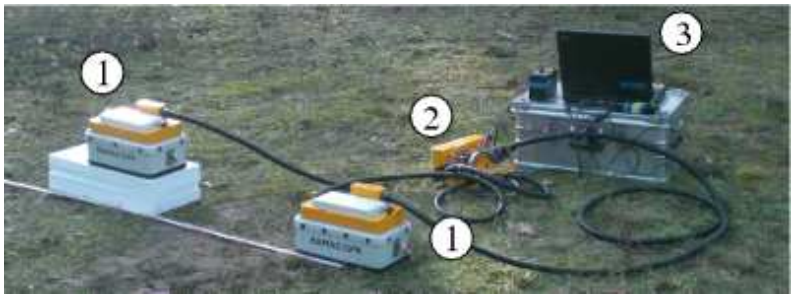

1 – 800 MHz GPR antennas

2 – control unit

3 – laptop for data acquisition

Figure 4.49: *Measurement setup for the lift measurement in order to obtain the surface relative permittivity from the evanescent behavior of the ground wave. The left antenna was lifted in equidistant steps of 0.02 m determinded by the thickness of the polystyrene plates.*

range. Although, the error is relatively high, it should be mentioned that the straight forward projection given in Fig. 4.24 has comparable errors (Fig. 4.25).

Fig. 4.48c gives the solution for the decay parameter α, which is not constant. But it is located around the expected value. This expected value was calculated with Eq. (4.69) with $\varepsilon_1 = 1$ and $\varepsilon_2 = 8$.

Discussion: Although, a simulated data set was used for this procedure, unexpected deviations are observed in Fig. 4.48. On the one hand, a constant wavelet $s_c(t)$ is not expected here, because no additional waves occur for this two-layer setup. On the other hand, the decay parameter α should be constant for this problem. A reason for these deviations could be errors within the simulation of these traces due to the integration procedure, cf. Sec. 4.3.6.

Experimental Example: In order to validate the processing approach for evanescent waves, a lift measurement was performed, cf. Sec. 4.2.1.

Setup and Data-Acquisition: The experiment was carried out in the nature protection area Hirschacker near Schwetzingen, Germany. Here, the subsurface consists of sandy soil, which is sparsely covered with mosses, grass and small plants (Fig. 4.49).

The experimental realization of the lift measurement (cf. Sec. 4.2.1) is shown in Fig. 4.49. Here, two 800 MHz RAMAC/GPR (Malå GeoScience, Sweden) antenna systems with a multi-channel unit MC4 were used in order to measure the cross-channels between both antenna systems. One antenna system was raised with underlaid polystyrene plates with a height of 0.02 m each. These plates were arranged in a way that the antenna system could be repositioned to the old place with a different height. The distance between the transmitter and the receiver, when both antennas were placed directly on the ground, was 0.79 m.

The survey result for two channels is presented in Fig. 4.50, where channel 3 denotes the measurement between the stationary transmitter and the lifted receiver and channel 4 between the lifted transmitter and the stationary receiver. As a pre-processing filter, a dewow-filter (Sec. 4.4.3) was used with a width of 30 ns in order to remove only the very low frequencies. As observed in Sec. 4.3.6 for a synthetic data set, a lifted transmitter leads also to a decay of amplitudes for the waves emitted into the soil. This is also visible in channel 4 of Fig. 4.50.

Evaluation: For the application of the evanescent wave evaluation, the ground wave of channel 3 will be analyzed, while this wavelet is assumed to be between 7.5 and 11 ns.

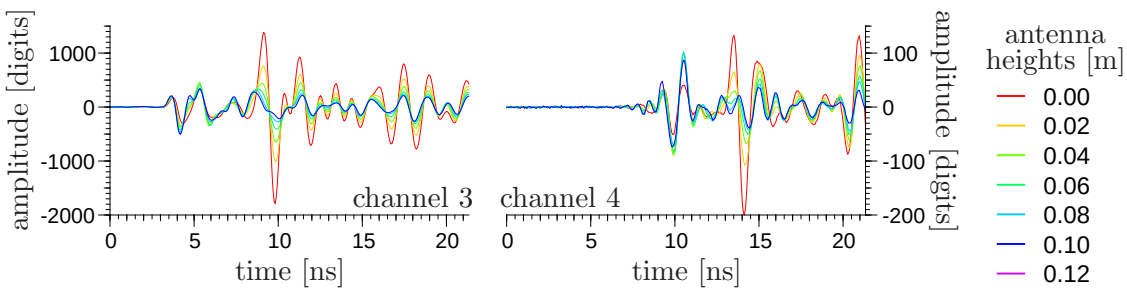

Figure 4.50: *Ground penetrating radar lift measurement, where one antenna system was lifted and another antenna system stays on the ground. Channel 3 denotes the measurement between the stationary transmitter and the lifted receiver. Channel 4 denotes the measurement between the lifted transmitter and the stationary receiver.*

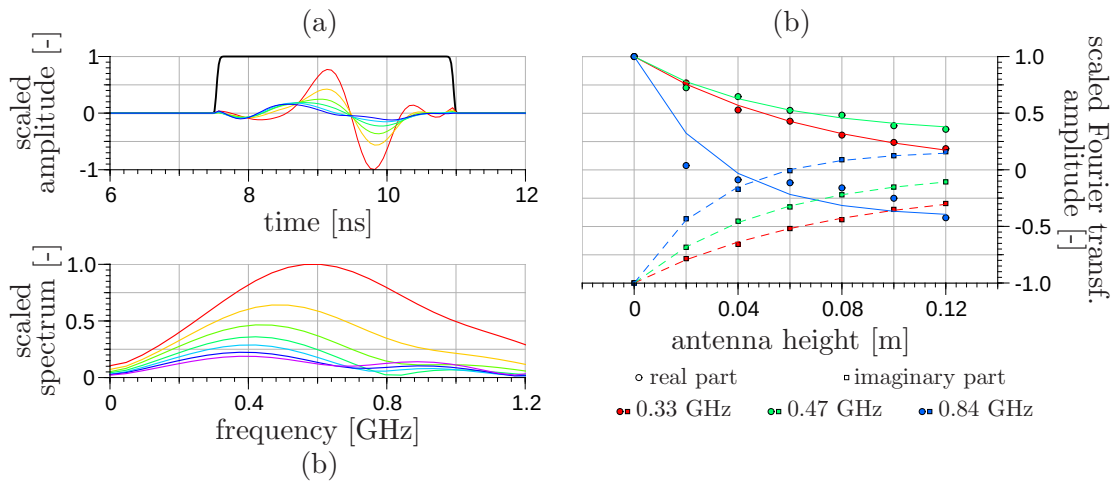

Figure 4.51: *Steps of the evanescent wave evaluation. (a) shows the extracted ground waves for different heights of the receiver using the color code of Fig. 4.50. (c) represents the corresponding spectra of these ground waves. (b) shows the real (circles) and imaginary (rectangles) parts of the Fourier-transformed ground waves for three different frequencies. The lines represent the fitted functionality for the real (solid) and the imaginary part (dashed) assuming a constant and decaying wave part.*

Therefore, the hat-function Eq. (4.63) was multiplied to all traces, using a slope parameter $\tau = 0.05$ ns. The steps of the evaluation are presented in Fig. 4.51, where the extracted ground wave, the corresponding spectra and the results of the fitting procedure in frequency domain for three frequencies are shown.

Results and Discussion: Analogous to the synthetic data set to the spectra of the experimental data show a shift towards lower frequencies. In contrast, frequencies larger 0.7 GHz show slight deviations of the spectral amplitudes. These deviations could stem from wave parts, which change with receiver height due to changing travel paths, but do not follow an evanescent behavior.

The results for the evanescent wave evaluation in time domain and the decay parameter as a function of frequency is shown in Fig. 4.52. Again, only a specific frequency range is used due to unreasonable values of the decay parameter and low amplitude values of the spectra. Here, this range was set from 0.2 to 1.2 GHz.

The results of the decay parameter as a function of frequency spreads around $\alpha \approx 6.5$ ns/m. Using the relative permittivity of polystyrene, which is given as $\varepsilon_1 = \varepsilon_{\text{polystyrene}} \approx$

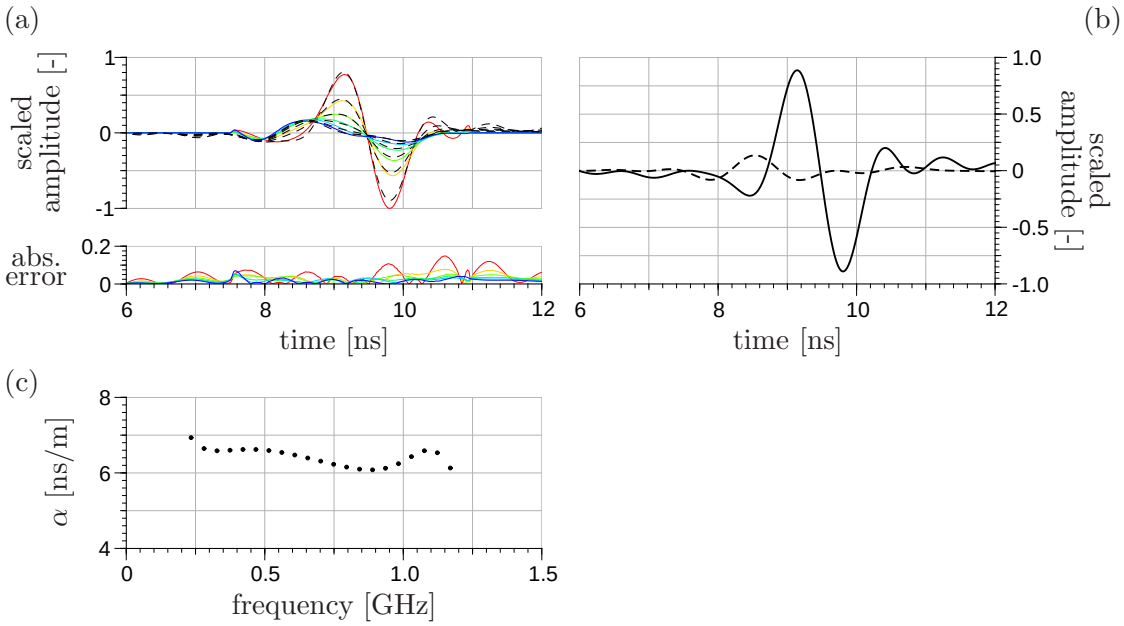

Figure 4.52: *Results of the evanescent wave analysis for the experimental data set presented in Fig. 4.50, channel 3. (a) shows the experimental data (colored lines) and the fitted results using the plane wave approach (dashed lines). At the bottom the absolute error between both are presented. (b) shows the constant (dashed) and the decaying wavelet at the surface (solid). (c) gives the result for the decay parameter α as a function of frequency.*

2.55 at 25°C and a frequency of 1 MHz (Weast, 1974), this leads to a relative permittivity of $\varepsilon_2 \approx 6.35$ for the upper soil.

In the context of this measurement, also a CMP measurement was performed. From the velocity analysis of the ground wave, a relative permittivity of $\varepsilon_2 = 6.6 \pm 0.8$ was obtained, which overlaps the relative permittivity determined by the evanescent wave evaluation, which corresponds to a volumetric water content of approximately $\theta \approx 0.09$. Here, the mixing model Eq. (2.34) was used with the parameters $\eta = 0.5$, $\varepsilon_{\text{air}} = 1$, $\varepsilon_{\text{water}} = 80$, $\varepsilon_{\text{matrix}} = 5$ and $\phi = 0.34$. This water content underlines the qualitatively observed conditions at the measurement day, which shows a dry soil, cf. Fig. 4.49.

Outcome: Evanescent Wave Evaluation / Ground Wave Evaluation

The finding of Sec. 4.3.6 that the evanescent wave behavior of the ground wave can be described analytically is applied in this evaluation approach. The assumption is based that a section of a trace is influenced by two wave parts. One wave part is an evanescent wave. The other wave is assumed to stay constant for small changes in height of the transmitter or receiver. From the decay of the evanescent wave as a function of height (from either the transmitter or the receiver), the surface relative permittivity is estimated.

The evaluation approach was validated with a synthetic and an experimental example. For the synthetic example, the modeled traces were used for a two-layer medium using the Green's function approach. A constant permittivity contrast was expected for all frequencies. The results show fluctuations from the expected contrast, which could stem from inaccuracies of the full wave modeling. The experimental example leads also to a permittivity contrast, which is not constant for the considered frequencies. Here, the assumed constant wave parts might also change slightly with antenna

height. Gradients in the near surface permittivity distribution could also cause deviations (cf. Sec. 4.3.6). At least, the average surface relative permittivity value estimated from the ground wave evaluation corresponds to a relative permittivity value obtained by a CMP measurement within the error bars.

5 Multi-Channel Ground Penetrating Radar

5.1 Overview / Introduction

For the application of ground penetrating radar, there are different measurement techniques, which are promising to obtain a remote access to subsurface structure and dielectric properties, which can be correlated to the volumetric water content. One technique is the standard common offset measurement, which is the fastest applicable method. It either gives a qualitative insight into subsurface structure (Moorman *et al.*, 2003) or with an assumption concerning the propagation velocity, it can reveal information about the reflector depth (Hinkel *et al.*, 2001; Moorman *et al.*, 2003). Furthermore, when the reflector depths are known from a soil profile, then the relative permittivity or the corresponding water content values can be obtained (Wollschläger and Roth, 2005; Lunt *et al.*, 2005). The disadvantage is that either the velocity (e.g. Greaves *et al.*, 1996) or the reflector depth can change along the survey path.

Another technique is the common midpoint (CMP) measurement, which is a localized method, which enables a detailed insight into the distribution of the relative permittivity or propagation velocity. Although, the roots of this method can be found in seismic applications (Dix, 1955), it is successfully applied in the research field of GPR (Fisher *et al.*, 1992; Garambois *et al.*, 2002), where it is extended for field scale measurements. The disadvantage of this technique is that the effort in time is much larger than common offset measurements. This extended CMP method in GPR applications, which is called multifold GPR (Bradford, 2006), is almost evaluated by collecting multiple common offset measurements with different antenna separations to CMP gathers (Fisher *et al.*, 1992). They can be evaluated with CMP normal moveout methods (Dix, 1955; Neidell, 1971; Yilmaz, 2001). This evaluation approach do not account for dipping events, which leads to distorted results (Levin, 1990). To overcome this, Bradford (2006) applied an iterative migration algorithm to correct the dipping reflectors and to focus hyperbola structures originating from point scatterers. For this method an initial velocity field must be assumed to perform the migration algorithm (e.g. Yilmaz, 2001). After the normal moveout analysis, this velocity model can be updated, which leads to an iterative procedure.

In the following, a multi-channel measurement technique is presented, which can be considered as a moving mini-CMP measurement. It will be shown that this technique opens the possibility of a fast and simultaneous access to the reflector depth and the average relative permittivity or analogous the water content. The evaluation procedure is based on simple ray approach travel times including dipping events.

This chapter is structured in two main parts. In the first part, the measurement technique and the evaluation algorithm assuming a single dipping layer is presented. Furthermore, an extension to multiple layers is introduced. With the help of a synthetic example, the difficulties concerning incorrect time zero values are presented, which can lead to a significant spreading of the results. Because of this, a heuristic approach is set up to minimize the influence of the faulty time zero values. In the second part, three experiments will

be presented, which demonstrate the efficiency but also some limits of the multi-channel evaluation method.

5.2 Multi-Channel Technique and Evaluation

5.2.1 Measurement Technique

A general setup of a multi-channel measurement can consist of multiple transmitters and receivers fixed at different antenna separations. Within the scope of this work, a setup with two transmitters and two receivers is considered (Fig. 5.1), which is realized by two GPR systems, which can be connected with a rope at a fixed distance. The setup allows to simultaneously measure four radargrams in the profiling mode with three different antenna separations (the separations for signal 1 and 4 are equal). Relocating the radargrams indicated by rays 1 or 4 such that their reflection points correspond spatially to the common midpoint of traces 2 and 3, the survey can be understood as a moving three-point CMP measurement. In order to estimate reflector depth and relative dielectric permittivity from travel time hyperbolas, analogous to a regular punctual CMP measurement, the difference between travel times to a certain reflection measured at different antenna separations should be preferably large. Hence, the maximum antenna separation should be adjusted correspondingly.

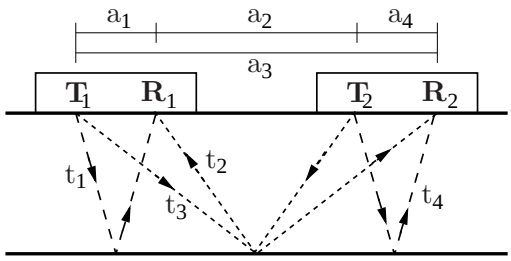

Figure 5.1: *Antenna setup of the multi-channel measurement with the four travel paths.*

5.2.2 Two-Point Evaluation of the Multi-Channel Measurement

For a horizontal reflector with a reflector depth d, the travel time t is given by

$$t = \frac{\sqrt{\varepsilon_c}}{c_0} \sqrt{4\,d^2 + a^2} \quad , \tag{5.1}$$

where ε_c and c_0 are the composite relative dielectric permittivity of the medium above the reflector and the speed of light in free space, respectively. a is the antenna separation of a single common offset measurement. Using two travel times t_2 and t_3 with a common midpoint (Fig. 5.1), d and ε_c are obtained as

$$d = \frac{1}{2} \sqrt{\frac{t_2^2\, a_3^2 - t_3^2\, a_2^2}{t_3^2 - t_2^2}} \tag{5.2}$$

$$\varepsilon_c = \frac{c_0^2\, t_i^2}{4\,d^2 + a_i^2} \qquad , \qquad i = 2, 3 \quad , \tag{5.3}$$

where a_2 and a_3 are the antenna separations corresponding to the travel times t_2 and t_3. The only effort in this approach is to obtain the absolute travel times to the reflector from measured radargrams.

In this equation, it is required that the travel paths of both signals have the same reflection point (Fig. 5.1). In order to obtain additional solutions, the information of channel 1 and 4 can also be used, when the travel times are extracted from the same location (midpoint between both antennas).

5.2.3 Multi-Point Evaluation of the Multi-Channel Measurement

Obviously, the two point evaluation does not use all available information, since for each measurement point, four rays and three different antenna separations can be used. Because more data is available than unknowns, a standard inversion technique can be used. This technique minimizes the squared differences between measured and modeled data by varying the model parameters. In this approach, statistical errors on single data points have less influence on the solutions than standard procedures such as Eq. (5.2) and (5.3). For the travel times, a dipping reflector model with the dipping angle α as an additional parameter is used. This application arises from two-point evaluations, which show significant fluctuations in reflector depth and average relative permittivity, when the data was not re-located to the common measurement location. This effect demonstrates that either the change of the reflector depth or the influence of inhomogeneities could cause these fluctuations. With the additional angle, the influence of the dipping reflector can be excluded.

Travel Time Description: Assuming a dipping reflector (Fig. 5.2) and a constant relative permittivity ε_c above that reflector, then the travel time at a measurement location x_0 is given by[1]

$$t(x_0; a) = \frac{\sqrt{\varepsilon_c}}{c_0} \cos\alpha \sqrt{4\,d^2 + a^2} \quad . \tag{5.4}$$

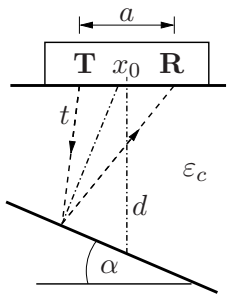

Figure 5.2: *Setup for dipping reflector.*

Here, d represents the reflector depth right beneath the measurement point x_0.

For a dipping reflector, travel times obviously change, when performing a GPR survey along the dipping direction. This information can be used as a further input for the later inverse modeling. In the surroundings of x_0, where the linear approximation is valid, the travel time at position x is given as

$$t(x; a) = \frac{\sqrt{\varepsilon_c}}{c_0} \sqrt{(4d^2 + a^2)\,\cos^2\alpha + 4\,(x_0 - x)^2\,\sin^2\alpha + 8\,d\,(x_0 - x)\,\sin\alpha\,\cos\alpha} \quad , \tag{5.5}$$

where d still denotes the reflector depth at position x_0. The convention is chosen that α is positive for reflector depths increasing along the track. Including the dipping angle in the formula for the reflected wave travel time replaces the migration procedure (Yilmaz, 2001) as a pre-processing step.

Minimization Procedure: Using N measurements around x_0 with K antenna separations from which the absolute travel times $t_{\text{refl}}(x_n, a_k)$ can be extracted for the reflected wave, the minimization problem is set up

$$\Psi_{\text{mc}} := \sum_{(n,k)}^{(N,K)} \Big(t_{\text{refl}}(x_n; a_k) - t_{\text{model}}(x_n; a_k) \Big)^2 = \min. \tag{5.6}$$

to obtain the relative dielectric permittivity ε_c of the subsurface, the dipping angle α of the reflector and the reflector depth d for a specified point x_0. Ψ_{mc} denotes the cost function for the multi-channel evaluation, which will be minimized. t_{model} is the modeled reflected

[1] The derivation of this equation is presented in the appendix, Sec. A.1.1.

wave travel time given by Eq. (5.5). Here, x_n $(n = 1 \dots N)$ denotes a measurement point near x_0 and a_k $(k = 1 \dots K)$ a particular antenna separation. For the minimization of Eq. (5.6), the Gauss-Newton method is applied. The initial values for the minimization procedure are obtained from the two-point evaluations Eq. (5.2) and (5.3) setting $\alpha = 0$.

Non-linear Reflector Correction: The approach so far assumes a constant slope of the reflector near the measurement point. If this is not the case, the calculated reflector depth d and the dipping angle α at the measurement position x_0 are not correct (Fig. 5.3). To overcome this problem, the evaluated data are transformed to the reflection position $x_{\text{refl}} = x_0 + \triangle x$ with the reflection depth d_{refl},

$$x_{\text{refl}} = x_0 + d \cos\alpha \sin\alpha \tag{5.7}$$

$$d_{\text{refl}} = d \cos^2\alpha \quad . \tag{5.8}$$

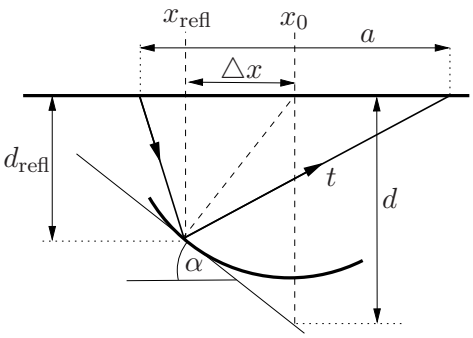

Figure 5.3: *Dipping plane model with the linear approximation around the reflection point and a global nonlinear behavior (curved line).*

Time Zero Correction: In Eq. (5.6), absolute travel times are required, which are not directly provided by the instrument used. Therefore, the offset t_{off} is introduced, which will be understood as the time when the picked characteristic of the reflected wave was emitted. When this offset is neither measured nor given by the electronics, it can be estimated from the measured travel time $t^{\text{air}}_{\text{meas}}$ of the air wave as

$$t_{\text{off}} = t^{\text{air}}_{\text{meas}} - \frac{a_k}{c_0} \quad , \tag{5.9}$$

where a_k/c_0 corresponds to the theoretical direct air wave travel time. Hence,

$$t_{\text{refl}}(x_n; a_k) = t^{\text{ref}}_{\text{meas}} - t_{\text{off}} = t^{\text{refl}}_{\text{meas}} - t^{\text{air}}_{\text{meas}} + \frac{a_k}{c_0} \quad , \tag{5.10}$$

where $t^{\text{refl}}_{\text{meas}}$ is the measured travel time of the reflected wave including the offset. t_{refl} is the required absolute travel time for Eq. (5.6). Although the air wave can be identified reasonably well, the picked air wave travel time could have a significant error. In order to calculate the absolute travel time for the reflected wave, one has to pick the corresponding point, which is chosen on the reflected wave wavelet. This procedure has some uncertainty since (i) near-field effects can disturb the air wave wavelet, (ii) the air wave can be interfered by the ground wave, and (iii) depending on the setup, the so called air wave could have traveled through the antenna box, which has a larger relative dielectric permittivity than air.

5.2.4 Multi-Layer Evaluation

In the sections above, only a single layer is assumed, but it could happen that multiple reflectors are observable. Then, two different methods can be used to obtain the material model from these reflections. In the first method, one can assume that refraction can be neglected, which is valid for small dielectric contrasts between the layers (Sec. 4.3.4). Under this assumption, the minimization procedure given in Eq. (5.6) can be applied separately for each reflector, which leads to average relative permittivity values between surface and reflector. Assuming a two-layer medium from which the average relative

permittivities $\varepsilon_{c,1}$, $\varepsilon_{c,2}$ and the reflector depth d_1, d_2 are known from a multi-channel evaluation, then the relative permittivity ε_2 of the lower layer can be calculated by[2]

$$\sqrt{\varepsilon_2} = \frac{d_2\sqrt{\varepsilon_{c,2}} - d_1\sqrt{\varepsilon_{c,1}}}{d_2 - d_1} \quad . \tag{5.11}$$

Here, it is assumed that the reflectors are horizontally layered.

The second possibility for a multi-layer evaluation can be done including refraction. Unfortunately, there is no closed form for multi-layer travel times obtained from the ray approach. Therefore, the numerical approaches presented in Sec. 3.2.2 can be used. Then, for an arbitrary reflector the travel time at a given measurement position depends on all layer thicknesses above, as well as the corresponding dielectric permittivities of each layer and the dipping angles. A closed form of the cost function Ψ_t similarly to Eq. (5.6) for S layers is given as

$$\Psi_t := \sum_{s=1}^{S} \sum_{(n,k)}^{(N,K)} \Big(t_{\mathrm{refl},s}(x_n; a_k; \mathbf{p}_1, \ldots, \mathbf{p}_s) - t_{\mathrm{model},s}(x_n; a_k; \mathbf{p}_1, \ldots, \mathbf{p}_s) \Big)^2 \quad , \tag{5.12}$$

where $t_{\mathrm{refl},s}$ and $t_{\mathrm{model},s}$ for $s = 1, \ldots, S$ are the measured and modeled travel times for the ith reflector, depending on the measurement position x_n, the antenna separation a_k and the parameters $\mathbf{p}_l$ with $l = 1, \ldots, s$. Here, $\mathbf{p}_s = (d_s, \varepsilon_s, \alpha_s)$ is the parameter vector, which includes the reflector depth d_s and the dipping angle α_s of the sth reflector as well as the relative permittivity of the sth layer.

This cost function can be minimized with standard inversion algorithms in order to obtain describing parameters $\mathbf{p}_i$. This inversion can be either done by an all at once inversion or by a successive application for each layer.

5.2.5 Inverse estimation of reflector depth: Synthetic Example

In this section, a synthetic data set will be presented in order to systematically and separately examine the influence of statistic and systematic errors, without dealing with the mentioned problems of picking.

Outline: With a given material model, the travel times of reflected waves are calculated for different antenna separations with a ray approach, using Fermat's principle (Sec. 3.2.2) adapted for non-planar media. Additionally noise is added as well as an offset that simulates the uncertainties concerning the air wave pick, mentioned previously. The noise simulates the electronic noise and the variations of the antenna separations. Although the air wave itself can also be affected by noise, this error effect is neglected here, because the air wave travel time is used as an auxiliary number to obtain the absolute travel time of the reflected wave. In this context, this air wave travel time can be understood as a substitute of the offset given in Eq. (5.9), which is assumed to be constant. Finally, the absolute travel time of the reflected wave is used, which can have both error sources, noise and offset.

The disturbed travel times represent the data set used to extract reflector depth and relative dielectric permittivity. The simplifications to real measurements are that inhomogeneities of the relative dielectric permittivity along the measurement line and reflector depth changes orthogonally to the measurement path are neglected.

[2]The derivation of the corresponding equation for arbitrary layers is given in Sec. 4.5.2.

Model Setup: A reflector depth model is chosen given as

$$d(x) = A \cdot x^2 + B \quad , \tag{5.13}$$

where A and B are set to 0.02 m^{-1} and 2.7 m, respectively. The relative dielectric permittivity above the reflector is $\varepsilon_c = 7$. The expected dipping angle α for each point is calculated by $\alpha = -\arctan[d'(x)]$, where the sign stems from the definition that $\alpha > 0$ for decreasing reflector depth and vice versa. For this synthetic example, three different channels are used with antenna separations $a_1 = 0.36$ m, $a_2 = 1.76$ m and $a_3 = 2.48$ m, in analogy to the experimental example described later in Sec. 5.3.1.

From this model, the exact travel times are obtained on which an uniformly distributed, randomly generated error as mentioned before is added. The maximal disturbance is $\triangle t_{\mathrm{max}} = 0.2$ ns. Due to the possible picking error of the air wave, each channel is disturbed separately with an arbitrary constant value ($\triangle t_{\mathrm{air},1} = -0.2$ ns, $\triangle t_{\mathrm{air},2} = 0.2$ ns, $\triangle t_{\mathrm{air},3} = -0.5$ ns).

The calculated absolute travel times per simulation point and antenna separation are shown in Fig. 5.4. The spacing between each point is 0.2 m. Here, 70 measurement points are simulated, where the starting position for each channel is set differently. They are given as $x_{\mathrm{start},1} = -4.9$ m, $x_{\mathrm{start},2} = -4.88$ m and $x_{\mathrm{start},3} = -4.72$ m.

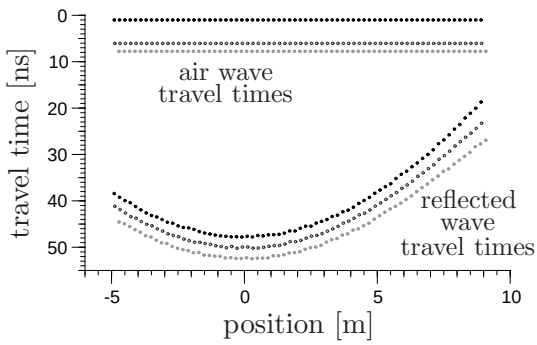

Figure 5.4: *Synthetic absolute travel times for the air and reflected wave for three different antenna separations (channels). ($a_1 = 0.36$ m - black; $a_2 = 1.76$ m - framed gray; $a_3 = 2.48$ m - gray)*

Evaluation: The travel time picks are rearranged in aggregations of measurement positions and the corresponding absolute travel time values each standing for one channel. The positions for each aggregation are chosen to be within half the spacing of the measurement points, which is 0.1 m. Each aggregation is labeled by the measurement position of channel 1. Then, the three nearest aggregations are inserted in the multi-channel evaluation, which means that the measurement points within an interval of about 0.6 m are used in this example. For all three channels, this yields 9 measurement positions and their corresponding travel times, which are taken into account for the point wise application of Eq. (5.6).

Now, the two- and the multi-point evaluation procedure is applied to the data of channel 1 and 2, as well as the multi-point evaluation procedure to the data of channel 1, 2 and 3. To both multi-channel evaluations the reflector depth correction, Eq. (5.7) and (5.8), was applied.

Results: In Fig. 5.5 the modeled reflector depths for the different evaluations are presented. They show a significant deviation from the material model and among each other. These deviations can be traced back to the erroneous values of the air wave travel time. Here, the three-channel evaluation (gray dots) fits better to the real reflector depth model than to the two-channel evaluations. Between both two-channel evaluations, the two-point evaluation (gray framed dots) shows slightly higher fluctuations, because it uses only the information of two data points, whereas the two-channel multi-point evaluation (black dots) including the dipping angle uses six data points.

In order to compensate the spreading of the solutions, the air wave adaption method is set up.

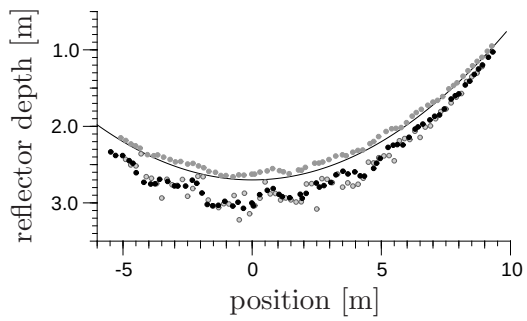

Figure 5.5: *Reflector depth without air wave adaption showing the predefined model (solid line) and the solution for the multi-point evaluation of channel 1 and 2 (black dots), for the multi-point evaluation of of all channels (gray dots) and for the two-point evaluation of channel 1 and 2 (framed gray dots).*

5.2.6 Air Wave Adaption Method

Assuming stability of the electronic equipment and constant antenna separation, the air wave travel time is a constant for each radargram. However, the extracted air wave travel time from a radargram may differ from the true value. This can lead to a significant variety of the results from different configurations (Fig. 5.5), where a configuration is a specific set of channels, which is evaluated. The variety in the solutions will be named inconsistent results. Therefore, if the solutions for different configurations match each other, then these results are called consistent.

To overcome this problem, one should conduct additional measurements to determine the air wave value as presented in Sec. 4.5.1. But it could happen that these measurements were either omitted or the results contradict each other.

Air Wave Adaption Procedure: However, one can introduce a heuristic approach assuming the air wave as a free parameter. For this approach, a minimization problem is set up. It uses L evaluation configurations and M measurement locations, given as

$$\Psi_a = \frac{1}{LM} \sum_{(l,m)}^{(L,M)} \left[\left(\frac{\bar{d}(x_m) - d_l(x_m)}{\bar{d}(x_m)} \right)^2 + \left(\frac{\bar{\varepsilon}_c(x_m) - \varepsilon_{c,l}(x_m)}{\bar{\varepsilon}_c(x_m)} \right)^2 \right] = \text{min.} \quad , \tag{5.14}$$

which minimizes the cost function Ψ_a by adjusting the air wave travel times. Here, $\bar{d}(x_m)$ and $\bar{\varepsilon}_c(x_m)$ are the mean reflector depth and the mean relative dielectric permittivity, respectively, obtained at position m by averaging over all evaluation configurations. The air wave travel times $t_{\text{meas}}^{\text{air},i}$ $(i = 1, \ldots, n_l)$ of all n_l channels used for the lth configuration are implicit variables in the solutions $d_l(x_m) = d_l(x_m, t_{\text{meas}}^{\text{air},i})$ and $\varepsilon_{c,l}(x_m) = \varepsilon_{c,l}(x_m, t_{\text{meas}}^{\text{air},i})$. From this, the mean values are calculated, which implies that these averaged values are also functions of all involved air wave travel times.

Application and Limits of the Approach: For the previously presented synthetic example, the cost function for different air wave travel times is shown in Fig. 5.6. On the right hand side of this figure, the averaged reflector depth over all possible configurations and positions is presented. The average reflector depth can be recognized as proxy for the solution. This is underlined by Fig. 5.7, where a set of consistent solutions is plotted with $\Psi_a < 0.001$ and where the air wave values are within a ± 1 ns range of the true values. Here, the shape of the reflector remains, although contrasts in reflector depth between maxima and minima are higher for solutions with greater depths. Furthermore, in this figure the solution of the multi-channel evaluation is included using the exact travel times of the air and for the reflected wave as input values. It shows an accurate reproduction of the synthetic material model.

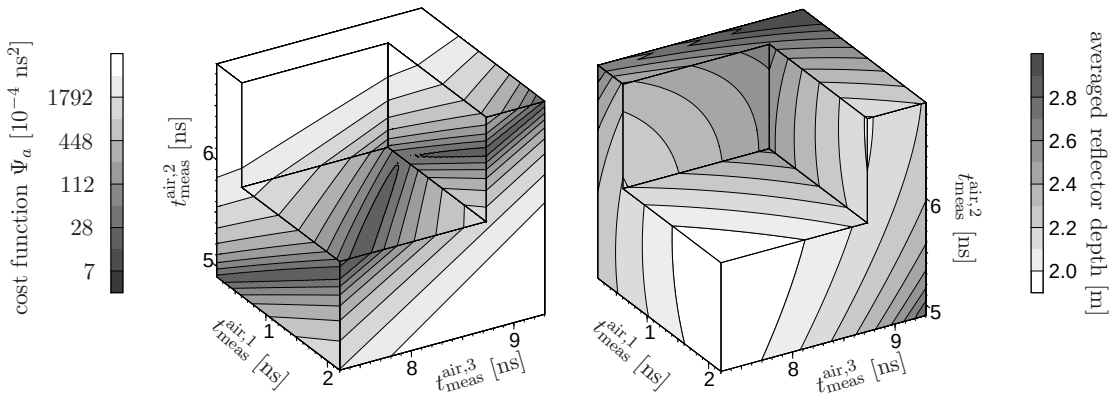

Figure 5.6: *Cost function of the synthetic example for a set of different air wave travel times (left) and their corresponding averaged solution of all configurations and all positions of the reflector depth (right). The averaged reflector depth of the true air wave values is about 2.3 m.*

In Fig. 5.6, the cost function shows a plane of minimum values, which indicates that a minimization procedure is unstable. Therefore, the new air wave values would be very close to the minimum plane, after the first step of a minimization procedure. Afterwards, the air wave values would be moved towards the small gradients on this minimum plane. For this example, decreasing reflector depths for multiple iterations are observed.

Furthermore, it is not guaranteed that the true model is found unless the air wave or the start signal of the antenna are not determined accurately. Nevertheless, the general shape of the solutions are not affected by this air wave adaption. This uncertainty in the absolute values could be overcome if a start of trace signal is logged (Arcone *et al.*, 1998). This start of trace signal needs not to correspond to the exact start of the picked signal, because from Fig. 5.6 it can be seen that different air wave travel times can lead to similar solutions, when they are shifted by the same value. At least this is only valid, if in all radargrams the same characteristic of the reflected wavelet is picked, e.g. the central maximum, and if the ratio between travel times of different channels is large enough so that a common offset does not affect the ratio much.

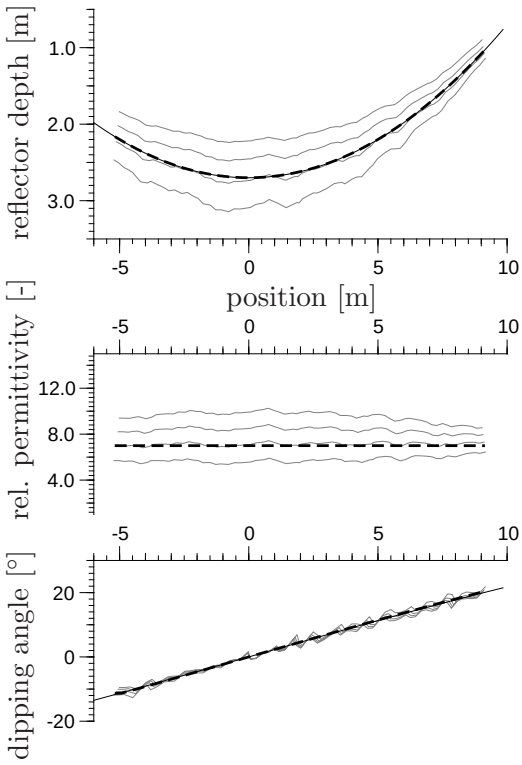

Figure 5.7: *Set of solutions for different air wave configurations with a cost function $\Psi_a < 0.001$. The thick dashed black line is the solution for the undisturbed air wave and reflected wave travel times.*

Finally, the air wave adaption method leads to consistent solutions, such that different configurations produce the same results. It is not able to yield the correct material model in absolute terms. However, the adapted solutions always reflect the correct relative shape.

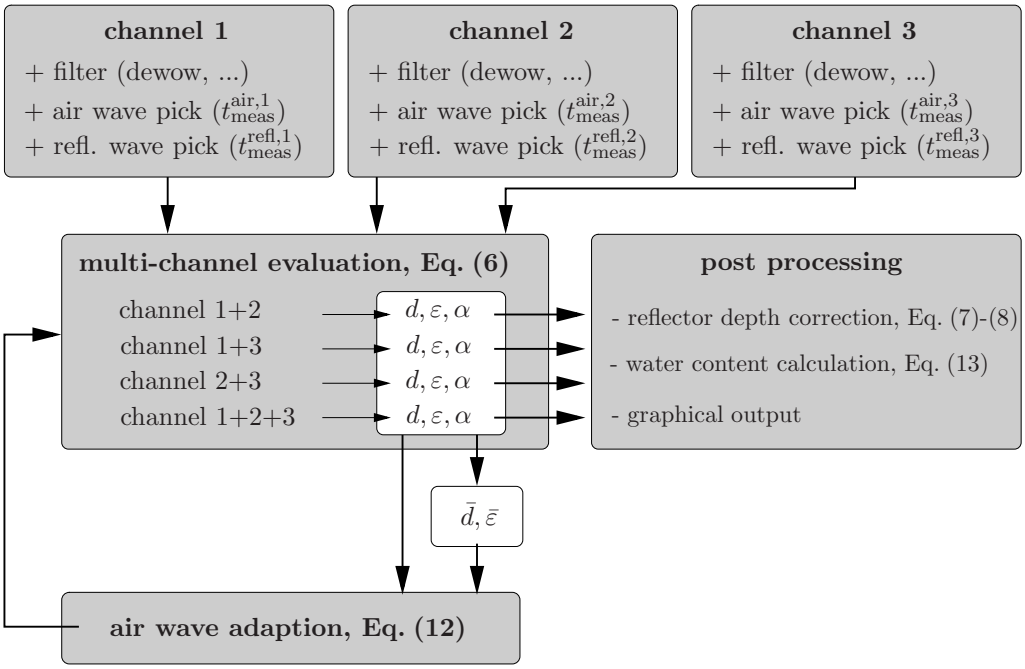

Figure 5.8: *Flow chart of the processing of a three-channel GPR measurement assuming three different antenna separations.*

5.2.7 Application of the Air Wave Adaption Method

In this section, the air wave adaption procedure is employed as shown in the flow chart (Fig. 5.8). For the air wave adaption procedure, a single Gauss-Newton iteration is applied, because the cost function has no distinct minimum, which is described above. The result of the air wave adaption is given in Tab. 5.1. The solutions for the multi-channel evaluations with the new air wave travel times are shown in Fig. 5.9. For clarity only the reflector depth, relative permittivity and dipping angle from the evaluation with channel 1 and 2 and with all channels are presented. The data of the solutions are corrected corresponding to the reflection position and reflector depth using Eq. (5.7) and Eq. (5.8). In each subfigure, the predefined material model is illustrated as a black solid line and the multi-channel solutions as dots. Because of the air wave adaption, both multi-channel solutions are consistent.

The solutions in Fig. 5.9 show a reasonable agreement with the predefined mate-

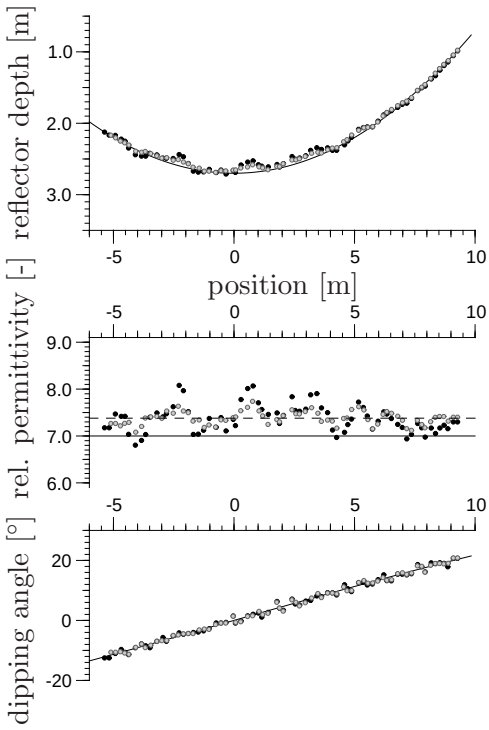

Figure 5.9: *Reflector depth, relative dielectric permittivity and dipping angle with air wave adaption showing the predefined material model (solid line) and the solution for the multi-point evaluation of channel 1 and 2 (black dots) and of all channels (framed gray dots). The dashed line in the permittivity plot represents the mean value of both configurations.*

Table 5.1: *Air wave travel times for synthetic example.*

channel	antenna separation [m]	air wave travel time [ns]		
		true values	modified values	after air wave adaption
1	0.36	1.20	1.00	0.66
2	1.76	5.87	6.07	5.20
3	2.48	8.27	7.77	7.50

rial model with only the relative dielectric permittivity showing significant deviations. Its mean value is at about 7.4. It can be found that the deviation of the relative dielectric permittivity corresponds to a water content deviation of about 0.01, which corresponds to 2.5% of the maximum range. Here, the transition from the average relative permittivity ε_c to the volumetric water content θ was done using the complex refractive index model (CRIM):

$$\theta = \frac{\sqrt{\varepsilon_c} - \sqrt{\varepsilon_s} - \phi\,(1 - \sqrt{\varepsilon_s})}{\sqrt{\varepsilon_w} - 1} \quad , \tag{5.15}$$

where ε_s and ε_w are the relative dielectric permittivities of the soil matrix and of water. ϕ is the porosity of the soil. The numerical values were set to $\varepsilon_s = 5$, $\varepsilon_w = 86.1$, corresponding to 5 °C (Kaatze, 1989), and $\phi = 0.4$.

The deviation of the relative permittivity value stems from the air wave adaption procedure. Here, the new air wave values do not correspond to the real values, cf. Tab. 5.1. They are about 0.5 to 0.8 ns smaller than the true values.

5.2.8 Synthetic Example for the Multi-Layer Evaluation

Analogous to the example in Sec. 5.2.5, the applicability of the multi-channel method for at least two layers will be presented.

Model Setup: Both reflectors d_1 and d_2 as a function of the position x are defined by

$$d_i(x) = A_i + B_i \cdot x + C_i \cdot \sin(D_i \cdot x + E_i) \quad , \tag{5.16}$$

where the parameters are given in Tab. 5.2. Again, the reflectors are assumed to be constant perpendicular to the x-direction.

The travel times are calculated with Fermat's principle. For the input data, three different antenna separations are simulated with $a_1 = 0.19$ m, $a_2 = 1.40$ m and $a_3 = 2.00$ m. 300 data points with a spacing of 0.1 m per antenna separation are calculated, where the start position for each channel is $x_1 = 0.0$ m, $x_2 = 0.3$ m and $x_3 = 0.64$ m. This denotes the midpoint between the transmitter and the receiver. For the relative permittivity of both layers, $\varepsilon_1 = 7.4$ and $\varepsilon_2 = 15.3$ is used. From these setting the travel times for both reflectors are obtained, which are disturbed by an uniformly distributed noise. This noise is ±0.2 ns at its maximum . The results of the travel times are presented in Fig. 5.10.

Table 5.2: *Describing parameters for the reflector depth using Eq.* (5.16).

		layer 1	layer 2
A_i	[m]	1.8	2.8
B_i	[–]	-0.01	0.01
C_i	[m]	0.2	0.1
D_i	[m^{-1}]	0.5	0.4
E_i	[–]	0.0	2.0

Evaluation: With these travel times as input data for the multi-channel evaluation, the cost function given in Eq. (5.12) can be set up. For the inversion procedure, a Gauss-Newton method was used. The initial values for the inversion were obtained by single two-layer inversion for each layer given by Eq. (5.2) and (5.3), which leads to an average relative permittivity between surface and reflector. The relative permittivity for the second layer is obtained by Eq. (5.11).

Results: The results for this multi-channel evaluation are presented in Fig. 5.11. It can be seen that the reflector depth values are reproduced quite accurately. Because in this example an accurate air wave travel time is assumed, no systematic error can be observed in the reflector depth values. For the first reflector, also the relative permittivity is determined quite accurate and the dipping angle can be found with reasonable errors. For the second reflector, the deviations from the true relative permittivity are remarkable. This deviation may occur due to the deep reflector depths compared to the order of the maximum antenna separation. This leads to a hardly defined hyperbola structure, when the data points are associated with a CMP gathers, conferring to Fig. 4.36a.

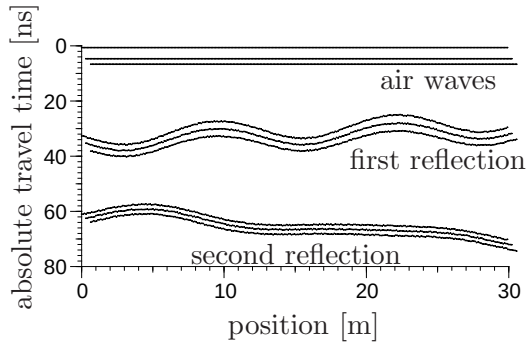

Figure 5.10: *Travel times for three different antenna separations and for a two layer material setup, where the layers are defined by Eq.* (5.16) *and Tab. 5.2.*

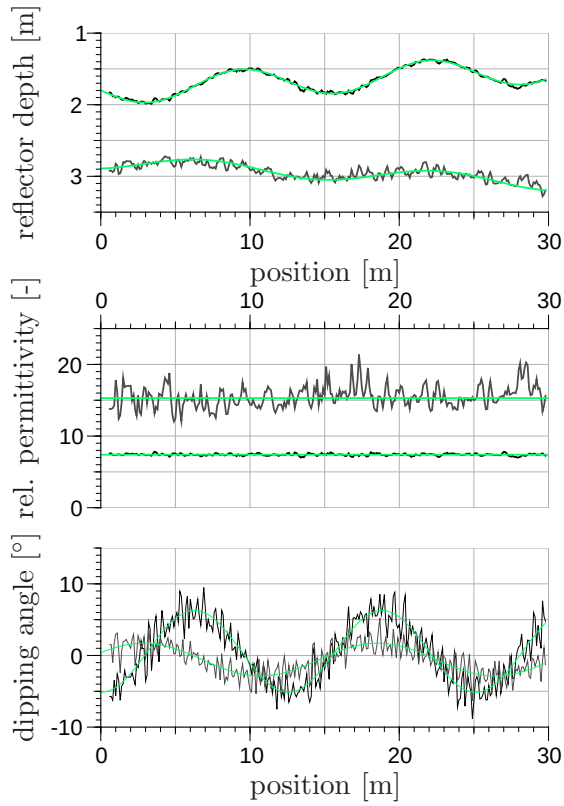

Figure 5.11: *Results of a multi-channel evaluation for the travel time data presented in Fig. 5.10 for the first (black lines) and second (gray lines) layer. The green lines represents the predefined material model.*

Outcome: Multi-Channel Technique and Evaluation

An evaluation technique for multi-channel surveys was presented. It uses the travel time values extracted from radargrams measured at different antenna separations. Clear and pickable reflections are required for the procedure. This technique enables to simultaneously obtain reflector depth and average volumetric water content without assumptions on the reflector depth behavior or the horizontal water content distribution. The limiting factor of this method is the necessary time zero value, which is required to determine absolute travel times.

5.3 Multi-Channel Surveys

In this section the multi-channel method is applied to experimental data. Three GPR surveys are presented. They are all from different sites and therefore, they all differ in the subface inhomogeneities. Where the first example shows a significant lateral variablity, in the second and third example multiple layers can be resolved and evaluated. Especially in the third example, dipping reflectors must be considered due to the special structure of the radargram. These dipping reflectors could be assigned to a subsurface structure consisting of ancient dunes.

5.3.1 Single-Layer Example from the Tibetan Plateau

Testsite: A multi-channel measurement was carried out on the Tibetan Plateau in Western China at 35°45.4'N 79°26.0'E 4950 m a.s.l. near QiTeDaBan. The site is located on an alluvial fan that is covered by several dry and water bearing rivulets. The sediments consist of alluvial sand and gravel.

Data Aquisition: Measurements were done in early October 2006, when the permafrost table was near its deepest point. For the measurements, a RAMAC/GPR (Malå Geo-Science, Sweden) multi-channel unit MC4 with two shielded 250 MHz antenna systems were used. The four measured radargrams with the setup given in Fig. 5.1 are shown in Fig. 5.12. Each radargram was measured with a spatial trace interval of 0.10 m, a time window of 110 ns and 560 samples per trace. The corresponding antenna separations were $a_1 = a_4 = 0.36$ m, $a_2 = 1.76$ m and $a_3 = 2.48$ m. From Fig. 5.1, it is clear that for the multi-channel evaluation the radargrams obtained with antenna separation a_1 and a_4 must be re-located to the common midpoint of a_2 and a_3. As the only additional pre-processing, a dewow filter was applied to each radargram.

Data Description: In the following, only a short section of the whole line will be considered where the surface water content changes drastically. The radargrams from all channels show a strong reflection from the permafrost table with a characteristic depression between 80 and 130 m. The occurrence of a permafrost table was validated in a soil profile excavated on another line, a few hundred meters away. During the measurement, at the positions between 100 and 126 m, a wet area, which in the following will be referred to as a flow system, was crossed (Fig. 5.13). It consisted of small rivulets some ten centimeters wide, surrounded by a larger area of wet soil. Due to the changing relative permittivity of the differently saturated sediments, no information on the reflector depth can be deduced from single common offset measurements.

Evaluation: For the evaluation, the reflected wave was picked. This pick was smoothed by a runmean-filter (cf. Sec. 4.4.2), which uses all data points within ±1 m. Furthermore, the air wave travel time was set to a constant value according to an extremal value of the air-ground-wave wavelet. This was done because additional measurements were not conducted to constrain the air wave travel time. The absolute travel times of

Figure 5.13: *Measurement at position $x = 126$ m. First antenna leaves flow system.*

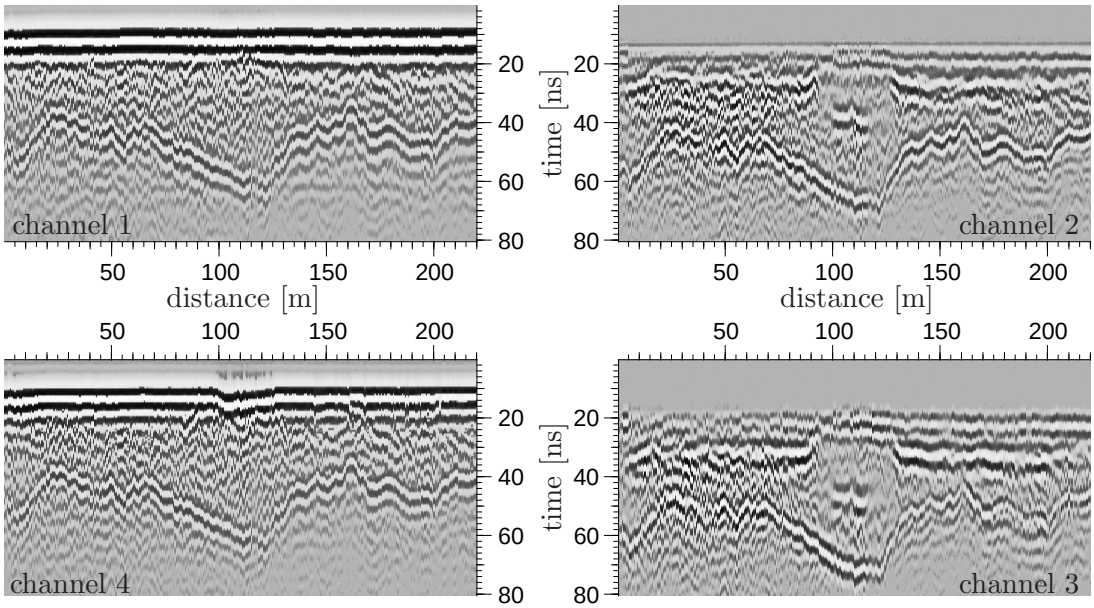

Figure 5.12: *Section of measured radargrams with 250 MHZ RAMAC/GPR antennas for different antenna separations ($a_1 = a_4 = 0.36$ m, $a_2 = 1.76$ m, $a_3 = 2.48$ m). Only dewow filtering was done for pre-processing. The channel 1 radargram shows the air-ground wave at some 12 ns and, between 35 and 65 ns, the reflections from permafrost table. Some additional, less pronounced reflections originate from intermediate soil layers but are not considered here.*

the air and reflected waves are shown in Fig. 5.14 using Eq. (5.9) and (5.10). With this data, the multi-point procedure was applied in analogy to the evaluation of the synthetic dataset in Sec. 5.2.5. For the air wave adaption, all available channels were considered except the configuration with channel 1 and 4. These both channels have the same antenna separation. Analogous to the synthetic example, a single Gauss-Newton iteration is used. The correction of the reflection position and reflector depth was applied using Eq. (5.7) and Eq. (5.8). For this survey distance no explicit changes were observed.

Furthermore, calculations were performed to analyze the cost function Ψ_a given in Eq. (5.14). The result for the cost function and the average reflector depth is presented in Fig. 5.15. For this calculation, channel 1 was neglected. For all other channels, the air wave travel time was varied by ± 1 ns, where the air wave value before the adaption algorithm was used. Corresponding to Fig. 5.6, no qualitative differences to the synthetic example are observed. Only the minimum plane is less pronounced.

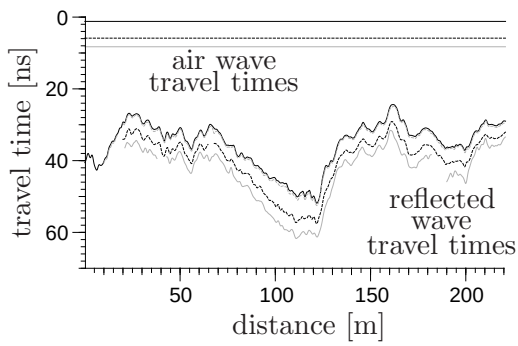

Figure 5.14: *Absolute travel times for the air and reflected wave for all four channels. The absolute air wave travel time of channel 1 and 4 are almost identical. (solid black line - channel 1; dotted black line - channel 2; solid gray line - channel 3; dotted gray line - channel 4)*

Results: The reflector depth, the average water content and the dipping angle obtained from the multi-channel evaluation is shown in Fig. 5.16. Here, the

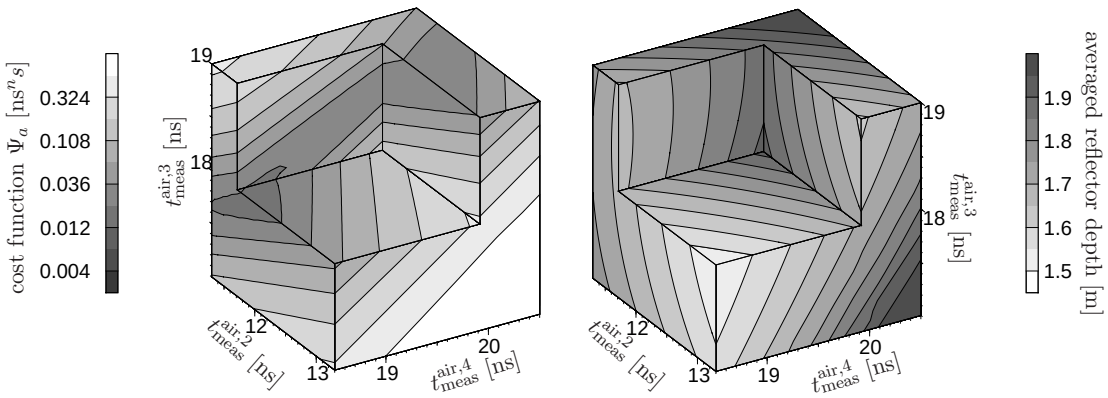

Figure 5.15: *Cost function of the experimental example for a set of different air wave travel times (left) and their corresponding averaged solution of all configurations and all positions of the reflector depth (right).*

reflector depth is only given relative to
the surface, because the surface topography was not measured during the survey. Therefore, the dipping angle is also relative to the surface. The average water content was calculated using Eq. (5.15) with $\varepsilon_s = 5$, $\varepsilon_w = 86.1$, corresponding to 5 °C (Kaatze, 1989), and $\phi = 0.4$. On these solutions, no further filter was applied. The lines within Fig. 5.16 correspond to evaluations using different numbers of channels. The evaluation with three and four channels were almost identical. This is clear, because for the used setup, channel 4 contains the same information as channel 1. The evaluation with two channels shows deviations in reflector depth and soil water content compared with the three- and four channel evaluation, which was attributed to interferences of wavelets and noise.

Discussion: Comparing the multi-channel solutions (Fig. 5.16) with the single-channel measurements (Fig. 5.14) demonstrates the qualitative advantage of the former. The measurements show a pronounced increase of travel times between 100 m and 126 m, which could easily be mistaken for a dipping permafrost table. In contrast, the long travel times are apparently caused by the water content that is a factor of three higher inside than outside the water channel (Fig. 5.16b). The multi-channel analysis indicates that the thickness of the active layer changes laterally. Because no exact topographic information exists from this measurement site, one can only state that the thickness of the active layer decreases in the 100 to 126 m interval by 0.3 m (Fig. 5.16a).

The situation becomes even more difficult outside the flow system where, except for the multi-channel analysis, one would have few clues to quantify the thickness of the active layer and the water content. For instance, the surface between 65 m and 100 m exhibits many old, dried-out channels, whereas the region between 126 m and 150 m is more of a bank, some 0.2 m high, without any sign of surface water flowing across it in the past (Fig. 5.13). Therefore, the observed flow system may be interpreted as a set of rivulets that was considerably wider during the strong snowmelt in early summer. It possibly extended from 65 m to 126 m where it was banked. This would be consistent with the GPR measurements, which indicates a gradual decrease of the active layer thickness and increase of the water content between 65 m and 100 m – the remains of the water body, which now dries out from the surface – and an abrupt drop near 126 m. A similar set of rivulets is encountered later, between 160 m and 210 m, except that here the surface is dry and white from the salt left behind by the evaporated water. Again, the multi-

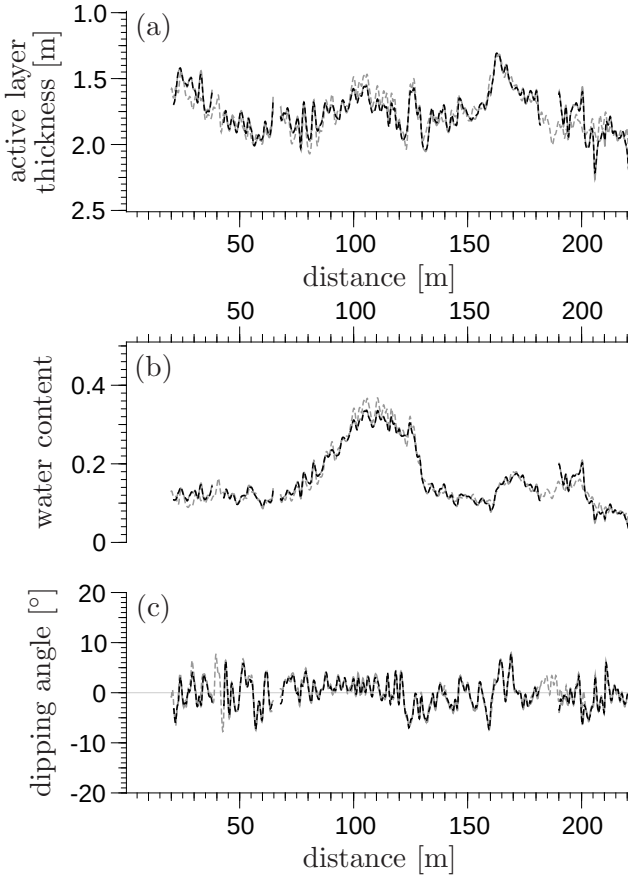

Figure 5.16: *Calculated reflector depth, which corresponds to the active layer thickness in our application, average water content and dipping angle. The gray dashed line corresponds to the multi-point evaluation of channel 1 and 2 and the black dashed line to the evaluation using all channels. The solid gray line, which corresponds to the evaluation using channel 1, 2 and 3 is almost overlapped by the black dashed line.*

channel GPR-measurements reveal the higher water content and the decreased active layer thickness.

Fig. 5.16 illustrates that the shape of the permafrost table and the water content in its wide-ranging behavior is only accessible with multi-channel GPR. On the other hand, on all solutions there are noise-like fluctuations. Beside the reflector depth, (Fig. 5.16a) also the dipping angle (Fig. 5.16c) has an unexpected variability, although the dipping angle is rather stable and reproducible in all evaluations. These fluctuations may be traced back to small antenna separation changes during the survey, as well as heterogeneities in the subsurface leading to refracted travel paths. Furthermore, the temporal resolution of the GPR measurements restricts the accuracy of the travel time determination, which may lead to these fluctuations.

5.3.2 Two-Layer Example from the Tibetan Plateau

Testsite: This example presents an evaluation for two layers. The data is obtained from Western China at 34°53.2'N 79°58.7'E 5049 m a.s.l. near QuanShuiGou. The measurement was carried out in September 2006. A RAMAC/GPR (Malå GeoScience, Sweden) multi-channel unit MC4 with two shielded 250 MHz antenna systems was used. From the

multi-channel GPR survey only a section between 220 and 280 m is presented. The whole survey path was measured at a hillslope. A representative picture of the environment is given in Fig. 5.17. This picture corresponds to the measurement position of $x = 256$ m.

Data Aquisition and Filtering: The multi-channel setup was used in the same way as presented in Fig. 5.1. Because of an antenna malfunction, only channel 1 and 2 returned analyzable data. The antenna separations were $a_1 = 0.36$ m and $a_2 = 3.39$ m. Furthermore, for both channels the time window was set to 120 ns and a sampling frequency of about 5 samples per nanosecond. 610 samples were measured per trace. The distance interval was 0.1 m.

The measured radargrams are presented in Fig. 5.18. They were filtered with a dewow filter. The time window was set to 15 ns, cf. Sec. 4.4.3, in order to remove a constant amplitude offset.

Figure 5.17: *Multi-Channel GPR measurement at a hill slope near QuanSchuiGou. Measurement position: $x = 256$ m.*

Data Description: In the radargram of channel 1 presented in Fig. 5.18, a continuous reflector can be observed between 60 and 70 ns, which can also be assigned to a reflector in channel 2 at about 80 ns. Above this reflector, another structure can be seen in both radargrams, which can be divided into two parts. They seem to stem from different reflection events. In channel 2, another reflection can be observed at distances between 240 to 275 m at times of about 55 ns. A corresponding reflection cannot be assigned in channel 1. Therefore, it cannot be evaluated.

Evaluation and Results: All reflection events are picked. They are used for the multi-channel evaluation. The necessary air wave travel time was set to a constant value at the center wiggle of the air wave wavelet. This was done, because no measurements were conducted to determine the air wave travel time. All necessary data for the multi-channel evaluation are presented in Fig. 5.18.

The multi-channel evaluation for both reflection events was carried out separately. It was performed with either three measurement points per channel and five points per channel as the input values for the local inversion, as presented in Eq. (5.6). This approach of a separate evaluation is validated by the results (Fig. 5.19), which show only small differences in the average water content for both reflectors. Therefore, refraction can be neglected. The water content was calculated with the CRIM formula (Eq. (5.15)). The parameters were set to $\varepsilon_s = 5$, $\varepsilon_w = 86.1$, corresponding to 5 °C (Kaatze, 1989), and $\phi = 0.4$.

Additionally to the reflector depth and water content results, the minimized cost function Ψ_{mc}, defined in Eq. (5.6), is presented in Fig. 5.19c. The evaluation with five measurement points per channel is underlying these graphs for both reflectors. This figure represents the reliability of the results, because these values show the quadratic deviation between the modeled and measured travel times. This indicates that the first part of the first layer is affected by significant errors. Therefore, the dipping event between 230 and 235 m is uncertain.

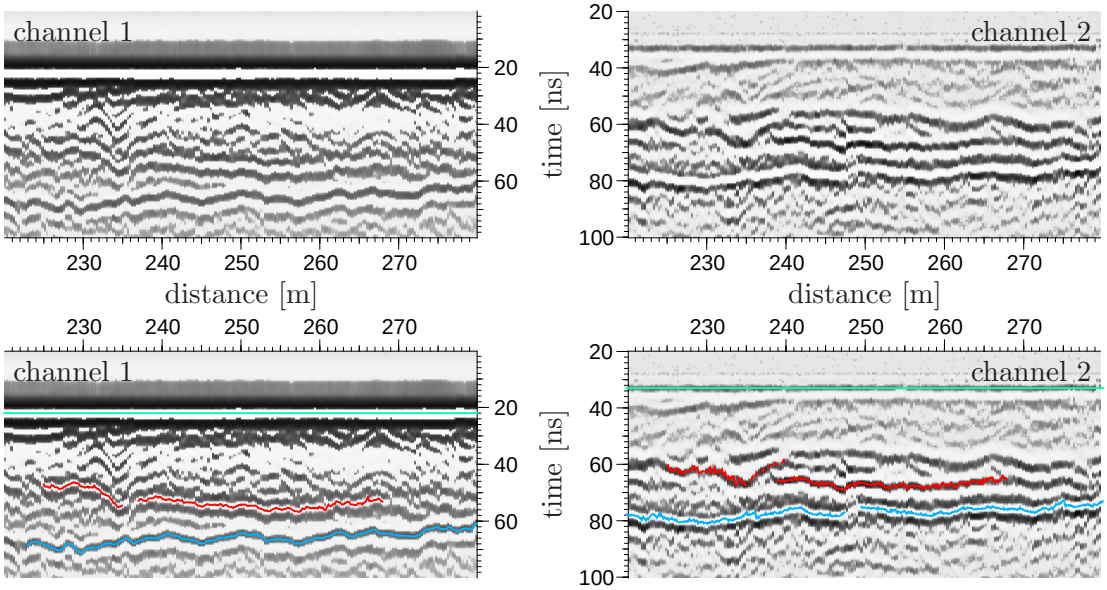

Figure 5.18: *Radargrams for a multi-channel measurement with two channels. In the lower part, the air wave pick (green) and the pick for the first (red) and the second (blue) reflection for the multi-channel evaluation are given.*

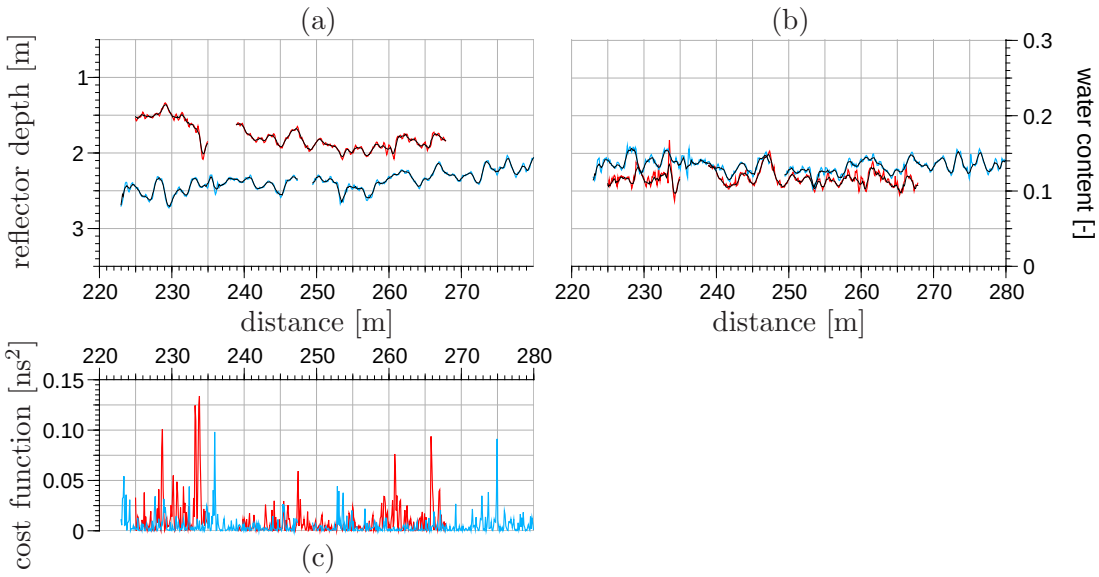

Figure 5.19: *Results of the multi-channel evaluation for the data presented in Fig. 5.18. The reflector depth (a) and the average water content (b) above the reflector is given for the first (red) and second (blue) reflector obtained from an evaluation using three measurement points per channel as the input channel. Additionally, the results with five points per channel are given as black lines. Its minimized cost function each measurement point and each channel are given in (c).*

Discussion: The most astonishing observation in this survey is that two reflectors were resolved, but the relative permittivity difference between both two layers would predict a less pronounced reflection. The assumption about the relative permittivity difference is derived from the average water content values, which are almost equal. But with respect to soil phyics, it is possible that water is ponding on top of a soil horizon. Then, a gradual increase of the water content would be assumed towards the first reflector and a sharp decrease at the boundary. From the gradual rise no reflection or only a less pronounced one would be expected. Then, the observed reflection can be assumed to stem from the sharp transition.

Furthermore, from the radargrams Fig. 5.18, one can deduce that the second reflector might stem from a ground water table. With respect to the wavelet, one can underline this presumption that the reflection stems from a transition to a medium with a higher relative permittivity. Corresponding to the air wave wavelet, the polarization of the reflected wave wavelet is reversed. This means that the reflection coefficient is negative. Because of the reflection coefficient for the perpendicular incidence

$$R_{\perp} = \frac{\sqrt{\varepsilon_1} - \sqrt{\varepsilon_2}}{\sqrt{\varepsilon_1} + \sqrt{\varepsilon_2}} \quad , \tag{5.17}$$

the relative permittivity of the lower medium has to be larger than the relative permittivity of the medium above.

The argument with the reflection coefficient can also be used for the first reflection. Here, the detected dielectric transition seems to be from a high relative permittivity to a low relative permittivity. This finding underlines the argumentation above.

5.3.3 Multi-Layer Evaluation from the Hirschacker Testsite

Testsite: The GPR survey was conducted in the nature protection area Hirschacker near Schwetzingen, Germany in October 2007. The subsurface consists almost of sandy soil, which is covered with mosses, grass and small plants such as thyme (Fig. 5.20).

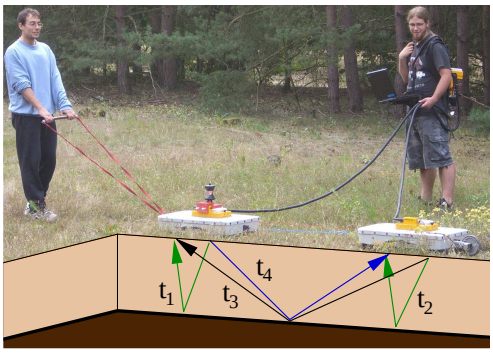

Figure 5.20: *Multi-Channel measurement at the Hirschacker testsite.*

Data Aquisition: For the GPR measurements, two 250 MHz RAMAC/GPR antenna systems were used connected with a rope. The setup is shown in Fig. 5.20. A single multi-channel survey (Fig. 5.21) was performed, resulting in four common offset measurements with different antenna separations, $a_1 = a_2 = 0.36$ m, $a_3 = 4.04$ m, and $a_4 = 3.32$ m. Furthermore, at two positions ($x = 19.8$ m and $x = 42.4$ m), two common midpoint (CMP) measurements were conducted. This resulted in four CMP radargrams using the cross-channels shown in Fig. 5.20. One for each position is shown in Fig. 5.22. For all measurements, a sampling frequency of about 10 samples per nanosecond was used and a time window of about 110 ns. The spatial trace increment for all measurements was 0.1 m.

Data Description: In the upper part of the radargrams displayed in Fig. 5.21, a large number of dipping reflectors are observable. They may origin from ancient dunes. These

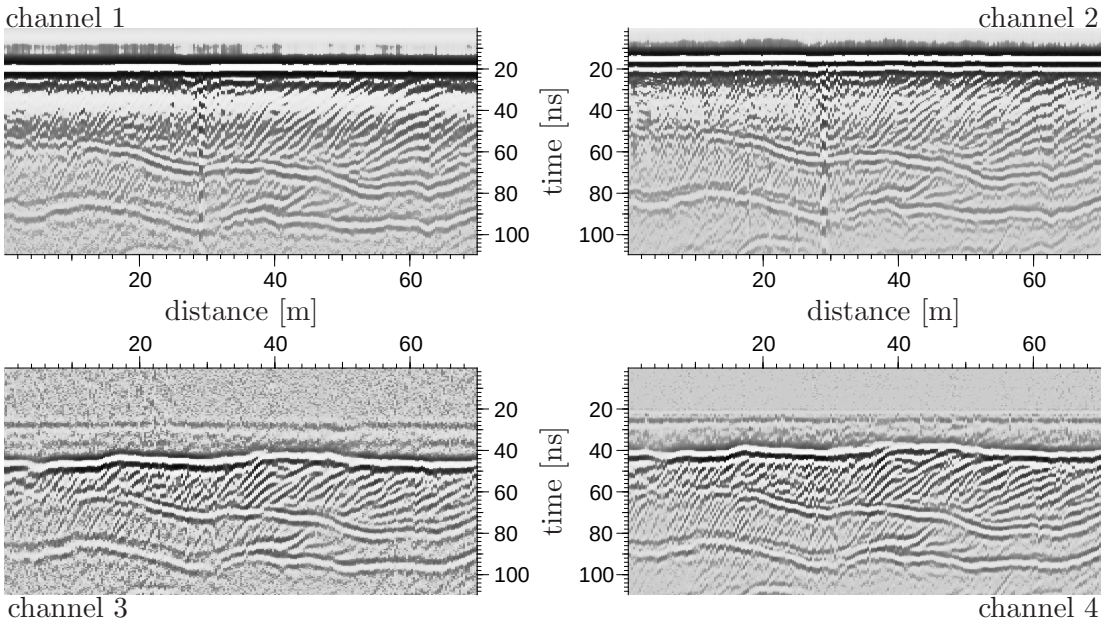

Figure 5.21: *Section of measured radargrams from the nature protection area Hirschacker near Schwetzingen with the setup shown in Fig. 5.20 using two 250 MHz RAMAC/GPR antenna systems. The antenna separations are $a_1 = a_2 = 0.36$ m, $a_3 = 4.04$ m, and $a_4 = 3.32$ m. All radargrams are shifted to a common measurement point and a dewow filter was applied to each trace.*

are underlain by a continuous reflector, which is identifiable in all radargrams between 10 and 70 m. Beneath this reflector, two further reflectors can be found, one between 33 and 44 m and a third one almost throughout the whole radargram.

In the radargrams of channel 1 and 2, at a survey position of about 29 m a significant disturbance occured. The origin of this dirturbance cannot be given because neither an abnormality was visible on the surface, nor a drilling or an excavation was performed at this position.

Multi-Channel Evaluation: The evaluation of the radargrams shown in Fig. 5.21 starts with some pre-processing steps. First, the logged measurement positions of the radargrams were shifted horizontally so that they correspond to each other. Here, a measurement position is defined as the midpoint between transmitter and receiver. In a second step, a dewow filter with a time window of 15 ns was applied in order to remove the amplitude offset.

From the filtered radargrams, the central extremum of the ground waves in channels 3 and 4 and of the three main reflectors were picked. The absolute travel times from all waves are obtained by a zero-offset correction. Here, time zero t_{off} for channel 3 and 4 was estimated from two CMP measurements (Fig. 5.22) performed at $x = 19.8$ m and $x = 42.4$ m.

The results for the air and ground wave evaluation for both channels of both CMPs are shown in Tab. 5.3. Apparently, the error of t_{off} for channels 3 and 4 is quite significant. Introducing these errors to the multi-channel evaluation, its results would spread widely, cf. Sec. 5.2.5. For the following evaluations, time zero for channels 3 and 4 were fixed to $t_{\text{off},3} = 11.9$ ns and $t_{\text{off},4} = 13.4$ ns, which are the time zero values from the ground waves of the first CMP measurement ($x = 19.8$ m). In contrast to the air wave values, the errors of these ground waves are smaller. Furthermore, the time zero from the ground

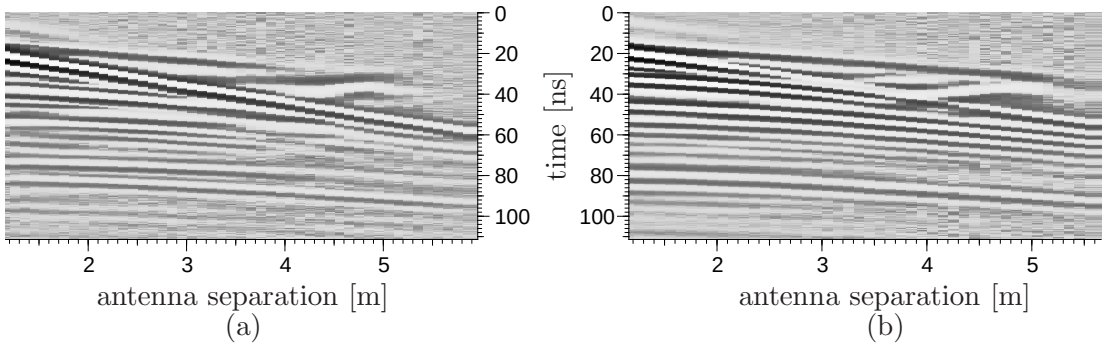

Figure 5.22: *Two of four common midpoint measurements obtained from the setup in Fig. 5.20. (a) shows channel 3 (t_3) at 19.8 m and (b) channel 3 at 42.4 m. Only a dewow filter was applied on each trace.*

Table 5.3: *Air and ground wave evaluation of common midpoint measurements to obtain time zero (t_{off}) using linear regression to fit Eq.* (3.1) *with an additional offset. The error is the standard deviation of the parameters.*

position [m]		channel 3		channel 4	
		ε_c [-]	t_{off} [ns]	ε_c [-]	t_{off} [ns]
19.8	air wave	1.3±0.4	12.4±1.5	1.4±0.2	12.7±0.8
	ground wave	5.6±0.3	11.9±0.7	5.5±0.2	13.4±0.4
42.4	air wave	1.2±0.2	12.6±1.0	1.1±0.2	13.5±0.6
	ground wave	4.5±0.4	11.4±0.6	n.d.	n.d.

wave of channel 3 of the second CMP measurement ($x = 42.4$ m) is not used, because here the ground wave is only pickable in small sections. The offset values extracted from these sections are not consistent among each other.

For channels 1 and 2, the central extremum of the air-ground-wave was picked and averaged. This averaged value is assumed to mainly stem from the air wave, which here does not propagate in air but in the medium in the antenna box. The relative permittivity of this material was set to 2.9, which was determined by a ringing analysis (Sec. 4.4.5). From this pick procedure, the time zero values are $t_{\text{off},1} = 16.9$ ns and $t_{\text{off},2} = 12.7$ ns for channels 1 and 2, respectively.

With the estimated time zero values for each channel, the absolute travel time values are obtained for all reflectors (Fig. 5.23). The additional ground waves were evaluated using Eq. (3.1) in order to obtain near surface relative permittivity and thereof, the water content.

For the multi-channel evaluation, Eq. (5.6), all four channels were used. Furthermore, for each evaluation position in each radargram five neighboring traces on each side were chosen. This means that for each position $N = 11$ measurement points are available for the multi-channel evaluation.

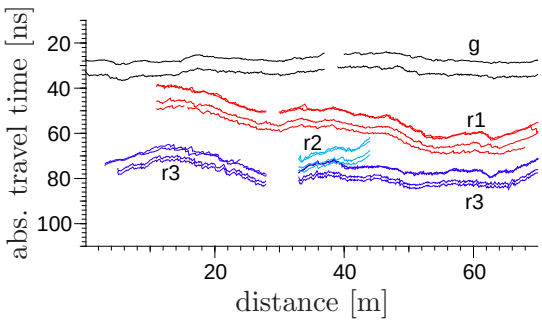

Figure 5.23: *The absolute travel times obtained from Fig. 5.21 for ground wave (g) and all reflected waves (r1, r2, r3), which can be identified in all radargrams. The two lines for the ground wave stem from channels 3 and 4. For the reflectors, 4 lines for each channel are drawn, where the absolute travel time of channels 1 and 2 overlap.*

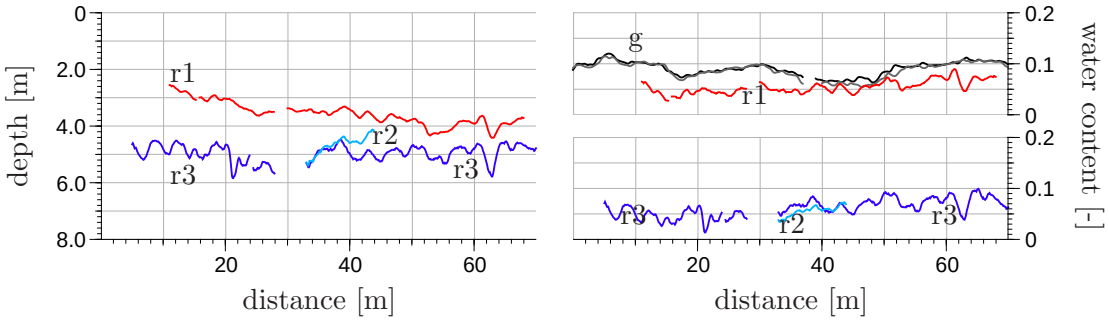

Figure 5.24: *Results of the multi-channel evaluation for reflector depth and average water content for all reflectors (r1, r2, r3). Additionally, the water content of the ground wave (g) for channels 3 and 4 is presented. The plot for the water content values was split for a better overview.*

Results: The results of the multi-channel evaluation in the reflector depth and water content for all three reflectors are presented in Fig. 5.24, where the water content θ is calculated from the composite relative permittivity ε_c with the complex refractive index model (CRIM), Eq. (5.15). The required parameters are set to $\phi = 0.4$, $\varepsilon_s = 5$ and $\varepsilon_w = 82.1$, which is the relative permittivity of water at a temperature of $\vartheta = 15°\mathrm{C}$ (Kaatze, 1989). The same conversion was applied for the composite relative permittivity of the ground wave evaluation.

The estimated reflector depth, displayed in Fig. 5.24, shows that reflectors 2 and 3 are at the same depth between a distance of 32 and 36 m. Here, the average water content values above the reflectors differ by about 0.02 volume percent. It is presumed that at least one reflection could be a side reflection, but with our measured data and with this setup and evaluation method, this dipping of the reflectors perpendicular to the survey direction cannot be extracted.

Normal Moveout Evaluation: Using the radargrams in Fig. 5.22, the zero-correction is done with the time zero values used in the multi-channel evaluation. Furthermore, the CMP radargrams were only dewow filtered with a time window of 15 ns. The normal moveout evaluation was applied as described in Sec. 4.5.2.

Results: The results are shown in Fig. 5.25, where the stacked traces for different velocities are presented in a contour plot. Additionally, the velocity axis is converted into water content values by recalculating the relative permittivity values ε_c and applying the CRIM model, Eq. (5.15), using the parameters described earlier to obtain water content values. They also represent an average water content between surface and reflector analogous to the multi-channel evaluation. Furthermore, the stacked travel times t_0 are translated to reflector depth values d using

$$d = \frac{t_0\, c_0}{2\, \varepsilon_c} \quad . \tag{5.18}$$

Although, this translation is not generally valid, because of refraction effects, only little velocity changes are observed in the measurement. Therefore, it is assumed that refraction has no significant influence on the travel time data.

In a last step, the multi-channel results are inserted at $x = 19.8$ m and $x = 42.4$ m into Fig. 5.25. For both positions, it can be observed that they are close to predicted reflections from the normal moveout analysis, but there are still deviations. A reason for

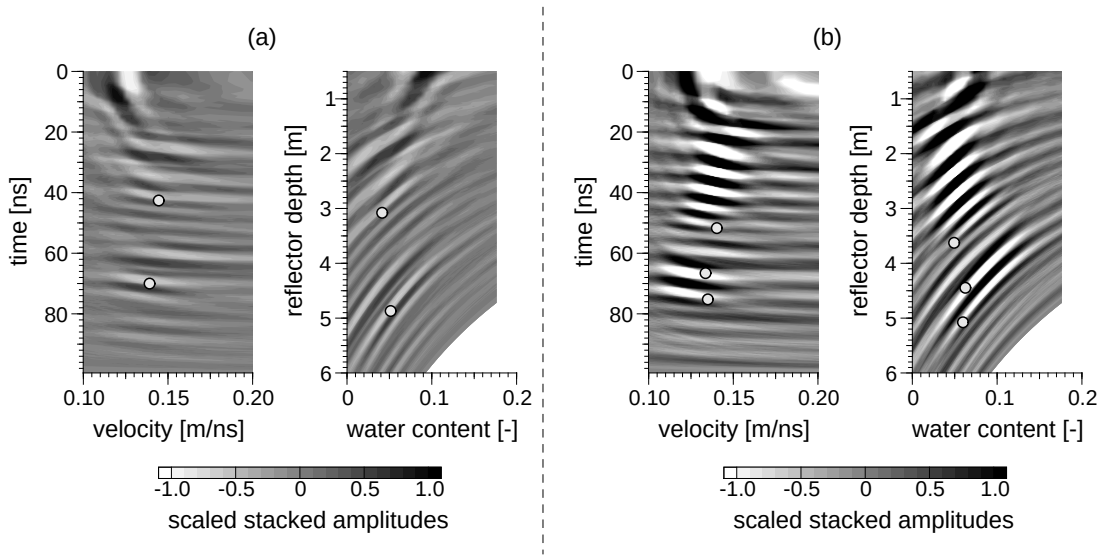

Figure 5.25: *Normal moveout analysis for offset corrected common midpoint measurements shown in Fig. 5.22 using the stacked trace method. For the measurement point at 19.8 m (a) and 42.4 m (b) the travel times of the shifted and stacked radargram for different velocities and its conversion to reflector depth and water content are presented. Furthermore, the results of the multi-channel evaluation for both measurement points are inserted as white framed dots.*

these deviations could be the restriction that normal moveout analysis only assumes flat reflectors, which is not valid for this test site.

But in contrast to the multi-channel analysis, the results of the NMO procedure reveal much more reflection events. Some of these reflection events, such as shallow reflections indicated in Fig. 5.25b, stem from the dipping reflectors, which may result from the ancient dunes. They cannot be evaluated by the multi-channel method because these reflectors cannot be uniquely assigned in at least two radargrams. Another reflection, which can be seen in Fig. 5.25a at about 60 ns, cannot be observed in the radargrams of Fig. 5.21. A reason could be that the measurement position of the CMP measurement was not directly on the survey path. This can result that both reflection may interfere each other for the GPR measurement on the survey path.

Outcome: Multi-Channel Surveys

Three examples of multi-channel surveys were presented. In the first example, the advantage of the multi-channel technique against a single common offset measurement was presented. Here, lateral changes in the water content could be observed either visually at the testsite as well as in the results of the multi-channel evaluation. In the second example, two reflectors were evaluated. The results show a similar average water content between soil surface and the corresponding reflector. From this finding, the detection of the first reflector would not be expected assuming homogeneous layers. Therefore, this reflector is assumed to stem from a small layer of ponded water. In the last example, a multi-layered system was analyzed. Here, the multi-channel evaluation returns that two reflectors are at the same depth but the average water content above is different. From this, it is assumed that at least one detected reflection is a side reflection.

6 Summary

This work represents a combined theoretical and experimental approach to expand the boundaries for the evaluability and processability of ground penetrating radar (GPR) measurements. The main focus is on the applications in soil hydrology with a special interest in the vadoze zone.

[a] In the first part, the dielectric properties which determine the propagation of electromagnetic waves are examined. The fundamentals of the description for the relative permittivity and the conductivity are given. Additionally, these properties are discussed with respect to their numerical values in specific soil types. In this context, the linkage between the relative permittivity and the water content is described. This requires a short introduction in soil physics, which is presented with a special focus on the capillary fringe. This capillary fringe is a representative for continuously changing water content.

A specific outcome of this chapter is the description of the electric conductivity as a complex function of frequency. This originates from the assumptions of free moving charge carriers. With the help of an example, assuming a potassium chloride solution, it is shown that this conductivity function reduces to a constant for frequencies used in GPR applications. This constant is the direct current conductivity.

[b] In the second part, an introduction to different modeling methods for electromagnetic waves is given. Three specific approaches are presented, which provide the simulation of electromagnetic waves in horizontally layered media. These simulation techniques are based on a ray approach, a plane wave description and a Green's function approach. This chapter represents a toolbox for GPR simulations, which are applied in the third part.

[c] The third part gives a detailed overview of the fundamentals of GPR applications. It describes the measurement principle and some measurement techniques. This is followed by a list of specific aspects of electromagnetic wave propagation. First, the propagation of a wavelet pulse in dispersive media is exemplary given, which shows the effects of wavelet distortion. Furthermore, the refraction and reflection at sharp and smooth relative permittivity transitions are studied. For the special case of a reflection from a sharp interface, the occurrence of a penetration depth is quantitatively analyzed. Another focus is on the ground wave, especially on the evanescent behavior, when the ground wave couples into the air. Furthermore, several filter and processing methods are presented. For instance, the normal moveout correction adapted for GPR applications is described. At last, the novel technique of lift measurements are evaluated with respect to the properties of evanescent waves. For the ground wave, the surface relative permittivity is extracted for one example. This correspondes to the relative permittivity obtained from a common midpoint measurement.

The major findings of the chapter are:

[1] The refraction at the air soil interface due to air gaps is not crucial for travel time evaluations for the reflected and for the refracted-reflected wave. On the other hand, the amplitudes of these waves are affected by the air gaps.

[2] The analysis of refraction in media with smooth gradients of the relative permittivity shows that the average water content extracted from reflected wave travel times is a

function of antenna separation. This results from the travel path distortion.

[3] The analysis of reflection at sharp transitions reveal that a penetration depth can be found, when either total reflection occurs or when one medium is dispersive. Except for highly dispersive media (for instance some clay minerals) this penetration depth has no significant influence on GPR travel times.

[4] The reflection from a capillary fringe shows a significant wavelet distortion, which represents the properties of low-path filter. The analysis reveals that an associated sharp transition can have different depths depending on the soil material. Here, this associated sharp transition assumes the surface relative permittivity as a value for the whole layer. Analyzing the reflectivity and transmissivity for different frequencies from such a smooth transition shows that high frequencies can pass without a reflection. In a low frequency limit, this transition appears to be sharp.

[5] When the capillary fringe is approximated as a linear ridge, then the reflection coefficient is only a function of the ridge width per wavelength. Here, a small quotient lead to a higher reflection coefficient. This model also indicates that the reflection need not to stem from the point of the largest gradient of the permittivity distribution. Here, it seems to stem from the point of the largest second derivative of the permittivity profile.

[6] A next outcome of this chapter is that the ground wave is an evanescent wave and that it can be described analytically.

[7] Simulations with a lifted transmitter and separately lifted receiver reveal that the excitation of the ground wave in the ground is symmetric to the coupling from the ground into the air.

[8] A similar symmetry was found for the reflected-refracted wave path, where typically the reflection point is not assumed to be between the transmitter and the receiver.

[9] The last both findings indicate that the excitation of electromagnetic waves in the ground, when the emitter is placed in the air, is symmetric to the coupling and transition from the ground into the air. This contradicts a current opinion that the radiation of an antenna and also the receiving of an antenna is a function of the surrounding material. This is validated with a measurement, where a transmitting and a receiving antenna are involved. This measurement corresponds to a simulation, where only a transmitting dipole is involved, without including the receiving process. This means that the receiving process is not a function of surrounding material, but a function of the electromagnetic fields directly at the antenna. Because the receiving and the transmitting is a symmetric process, the radiation pattern of an antenna is only a consequence of the coupling in the sourrounding materials.

[d] In the last part, the multi-channel technique is presented. The evaluation approach is based on an inversion technique, which compares measured travel times with modeled ray approach travel times assuming dipping reflectors. The results are significantly disturbed, when the time zero is not determined accordingly. A heuristic approach is set up to minimize this influence. Although, this approach reduces the spreading of the solutions, it does not guarantee the right solution. At least, relative changes in the obtained material model stay unaffected. This multi-channel method is validated with two synthetic and three experimental examples, which have different complexities in the subsurface structure.

The statements of this chapter are that the multi-channel method leads to a simultaneous determination of the reflector depth and an average water content above this reflector. No additional assumptions concerning the material model are required. The experiments reveal that this method is capable of resolving complex subsurface structures, which are hardly evaluable with standard single channel measurements. Another outcome is found

from the analysis of a radargram with two reflectors. The results show a similar average water content above both reflectors. This would contradict the occurrence of the strong first reflection. Therefore, one can assume that this reflection comes from a material change, where some water was ponding on top of the interface. Furthermore, the evaluation of a multi-layer example leads to solutions for different reflectors with a comparable reflector depth but with different average water content values above. Here, at least one reflection could be a side reflection. A normal moveout analysis indicated the same finding.

A Calculations and Derivations

A.1 Small Calculations

A.1.1 Travel Time from a Dipping Reflector

Here, the derivation of the travel time is presented, which stems from a reflection of a dipping plane. Therefore, the travel time will be a function of relative permittivity of the subsurface ε_c, the reflector depth d at a specific point and the dipping angle α. A sketch of the reflection from dipping plane is given in Fig. A.1, where all necessary variables are defined.

First, the travel time t from the reflector is defined as

$$t = \frac{l}{c_0}\sqrt{\varepsilon_c} = \frac{l_1 + l_2}{c_0}\sqrt{\varepsilon_c} \quad , \tag{A.1}$$

where l_1 and l_2 are the travel paths from the emitter to the reflection point and from the reflection point to the receiver. At the reflection point, both reflection angles are equal

$$\varphi_1 = \varphi_2 = \varphi \quad . \tag{A.2}$$

This leads to the relationships

$$\sin\varphi = \frac{s_1}{l_1} = \frac{s_2}{l_2} \quad \text{and} \quad \cos\varphi = \frac{g_1}{l_1} = \frac{g_2}{l_2} \quad \Longrightarrow \quad \frac{s_1}{s_2} = \frac{l_1}{l_2} = \frac{g_1}{g_2} \quad . \tag{A.3}$$

Now, from trigonometric considerations concerning the dipping angle, we obtain

$$\sin\alpha = \frac{g_1}{x_0 - a/2} = \frac{g_2}{x_0 + a/2} \quad \text{and} \quad \cos\alpha = \frac{s_0}{x_0 - a/2} = \frac{s_0 + s_1 + s_2}{x_0 + a/2} \tag{A.4}$$

$$\Longrightarrow \quad \frac{g_1}{g_2} = \frac{x_0 - a/2}{x_0 + a/2} = \frac{s_0}{s_0 + s_1 + s_2} \tag{A.5}$$

When Eq. (A.3) is inserted into Eq. (A.5), it yields

$$\frac{s_0 + s_1(1 + g_1/g_2)}{s_0} = 1 + \frac{s_1}{s_0}\left(1 + \frac{x_0 + a/2}{x_0 - a/2}\right) = \frac{x_0 + a/2}{x_0 - a/2}$$

$$\Longrightarrow \quad \frac{s_1}{s_0}\frac{2x_0}{x_0 - a/2} = \frac{a}{x_0 - a/2} \quad \overset{\text{(A.4)}}{\Longrightarrow} \quad s_1 = \frac{a}{2x_0}(x_0 - a/2)\cos\alpha \quad . \tag{A.6}$$

Furthermore, we can formulate the Pythagorean theorem between l_1, g_1 and s_1, which yields

$$l_1^2 = g_1^2 + s_1^2 = (x_0 - a/2)^2 \sin^2\alpha + \frac{a^2}{4x_0^2}(x_0 - a/2)^2\cos^2\alpha \tag{A.7}$$

$$\Longrightarrow \quad l_1^2 = (x_0 - a/2)^2\left(\sin^2\alpha + \frac{a^2}{4x_0^2}\cos^2\alpha\right) \quad , \tag{A.8}$$

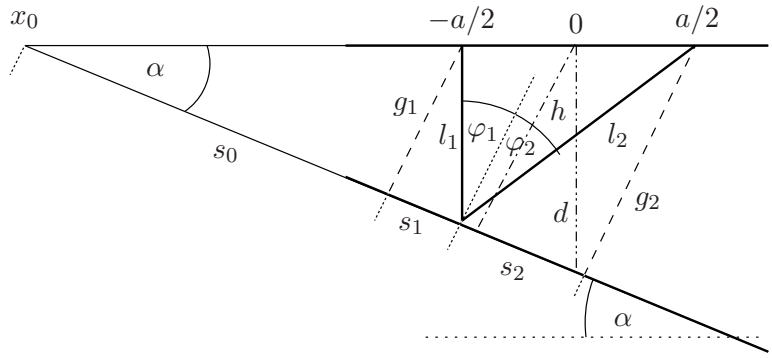

Figure A.1: Setup for the dipping reflector calculation; definition of all quantities

where Eq. (A.4) and (A.6) was used. For the travel path l_2, we obtain

$$l_2 = l_1 \frac{x_0 + a/2}{x_0 - a/2} \tag{A.9}$$

$$\Longrightarrow \quad l_2^2 = (x_0 + a/2)^2 \left(\sin^2\alpha + \frac{a^2}{4x_0^2}\cos^2\alpha \right) \quad , \tag{A.10}$$

which is derived from a comparison between Eq. (A.3) and (A.5). Then the travel path is described by

$$l = l_1 + l_2 = 2\,x_0 \sqrt{\sin^2\alpha + \frac{a^2}{4x_0^2}\cos^2\alpha} = \sqrt{4x_0^2\,\sin^2\alpha + a^2\cos^2\alpha} \quad . \tag{A.11}$$

Now, one x_0 is no well defined value for experimental investigations. Therefore, one can either use the parameter h defined in Fig. A.1

$$h = x_0\,\sin\alpha \quad , \tag{A.12}$$

which leads to a travel time

$$t = \frac{\sqrt{\varepsilon_c}}{c_0}\sqrt{4h^2 + a^2\cos^2\alpha} \quad . \tag{A.13}$$

A more adequate parameter is the reflector depth d, which is right under the measurement point, which yields to another expression for the travel time, given as

$$t = \frac{\sqrt{\varepsilon_c}}{c_0}\,\cos\alpha\,\sqrt{4d^2 + a^2} \tag{A.14}$$

using

$$h = d\,\cos\alpha \quad . \tag{A.15}$$

If, we emitter and receiver are moved equally by a distance $\triangle x$, then Eq. (A.14) stays valid, but the used reflector depth in this equation is changing, which leads to a different travel time. For some purposes, it is necessary to express this equation as a function of the reflector depth at the measurement point x=0, which we will call d. For d and the reflector depth at the position $\triangle x$, which we will call $d_\triangle$, the following equations are set up

$$\tan\alpha = \frac{d}{x_0} = \frac{d_\triangle}{x_0 + \triangle x} \quad \Longrightarrow \quad d_\triangle = d + \triangle x\,\tan\alpha \quad . \tag{A.16}$$

This leads to

$$t = \frac{\sqrt{\varepsilon_c}}{c_0} \cos\alpha \sqrt{4\,(d + \triangle x\, \tan\alpha)^2 + a^2}$$

$$\Longrightarrow \quad t = \frac{\sqrt{\varepsilon_c}}{c_0} \sqrt{(4\,d^2 + a^2)\, \cos^2\alpha + 4\,\triangle x\, \sin^2\alpha + 8\,d\,\triangle x\, \sin\alpha\, \cos\alpha} \quad . \tag{A.17}$$

A.1.2 Attenuation of Plane Waves for a Small Imaginary Part of the Relative Permittivity

The attenuation β of a plane wave as a function of real (ε') and imaginary part (ε') of the relative permittivity is given as

$$\beta = \frac{\omega}{c_0\,\sqrt{2}} \sqrt{-\varepsilon' + \sqrt{\varepsilon'^2 + \varepsilon''^2}} \quad . \tag{A.18}$$

Assuming an imaginary part near zero, β can be given as a taylor expansion

$$\beta \approx \; \beta_{\varepsilon''=0} + \left[\partial_{\varepsilon''}\beta\right]_{\varepsilon''=0} \varepsilon'' \quad . \tag{A.19}$$

Where $\beta_{\varepsilon''=0}$ can be easily found to be 0, an analysis of the limit of the second term is required:

$$\lim_{\varepsilon''=0} \partial_{\varepsilon''}\beta = \lim_{\varepsilon''=0} A\,\partial_{\varepsilon''} \sqrt{-\varepsilon' + \sqrt{\varepsilon'^2 + \varepsilon''^2}} = A \cdot B \quad \text{with} \quad A = \frac{\omega}{c_0\,\sqrt{2}} \quad , \tag{A.20}$$

where B is defined as the limit of the square root, which is not known yet. The calculation of B is given as

$$\begin{aligned} B = \frac{1}{A} \lim_{\varepsilon''=0} \partial_{\varepsilon''}\beta &= \lim_{\varepsilon''=0} \frac{\varepsilon''}{2\sqrt{-\varepsilon' + \sqrt{\varepsilon'^2 + \varepsilon''^2}}\sqrt{\varepsilon'^2 + \varepsilon''^2}} \\ &= \frac{\lim_{\varepsilon''=0} \partial_{\varepsilon''}\varepsilon''}{2\,\lim_{\varepsilon''=0} \partial_{\varepsilon''} \left(\sqrt{-\varepsilon' + \sqrt{\varepsilon'^2 + \varepsilon''^2}}\sqrt{\varepsilon'^2 + \varepsilon''^2}\right)} \\ &= \frac{1}{2(B\,\varepsilon' + 0)} \\ \Longrightarrow \quad B = \frac{1}{A} \lim_{\varepsilon''=0} \partial_{\varepsilon''}\beta &= \frac{1}{\sqrt{2\,\varepsilon'}} \quad , \end{aligned} \tag{A.21}$$

which leads to

$$\lim_{\varepsilon''=0} \partial_{\varepsilon''}\beta = \frac{\omega}{2\,c_0\,\sqrt{\varepsilon'}} \quad . \tag{A.22}$$

A.2 Hertzian Potential and Hertzian Dipole

Here, a short introduction to the concept of the Hertzian potential will be given. First, it is started with the relevant Maxwell's equations in frequency domain for an isotropic media:

$$\nabla \times \mathbf{E} = -\mathtt{i}\,\omega\,\mu\,\mathbf{H} \tag{A.23}$$

$$\nabla \times \mathbf{H} = \mathbf{J} + \mathtt{i}\,\omega\,\varepsilon\,\mathbf{E} \quad . \tag{A.24}$$

The Hertzian potential $\boldsymbol{\pi}_e$ for the electrical case is now introduced by the relationships

$$\mathbf{E} = k^2\,\boldsymbol{\pi}_e + \nabla\nabla\cdot\boldsymbol{\pi}_e \tag{A.25}$$
$$\mathbf{H} = \mathtt{i}\,\omega\,\varepsilon\,\nabla\times\boldsymbol{\pi}_e \tag{A.26}$$

with

$$k^2 = \omega^2\,\mu\,\varepsilon \quad , \tag{A.27}$$

which is the dispersion relation. When Eq. (A.25) and Eq. (A.26) are substituted in Eq. (A.23), this equation is directly fulfilled. Furthermore, Eq. (A.24) yields

$$\begin{aligned}\mathtt{i}\,\omega\,\varepsilon\,\nabla\times\nabla\times\boldsymbol{\pi}_e &= \mathbf{J} + \mathtt{i}\,\omega\,\varepsilon\,(k^2\,\boldsymbol{\pi}_e + \nabla\nabla\cdot\boldsymbol{\pi}_e)\\ \Longrightarrow\quad (\nabla^2 + k^2)\,\boldsymbol{\pi}_e &= -\frac{\mathbf{J}}{\mathtt{i}\,\omega\,\varepsilon}\quad ,\end{aligned} \tag{A.28}$$

which is a wave equation for the Hertzian potential.

Radiating Free Dipole

The meaning of the Hertzian potential can be illustrated by assuming a radiating dipole in z-direction ($J_x = 0$, $J_y = 0$ and $J_z = \delta(\mathbf{r})$) placed at the origin, which is called Hertzian dipole. The surrounding medium shall be homogeneous and isotropic, which leads to constant k. Than, the Hertzian potential has also only a z-component $\rightarrow \boldsymbol{\pi}_e = (0, 0, \pi_z)$. The solution of the wave equation (A.28) is given as

$$\pi_z = C(\omega)\,\frac{e^{-i\,k\,r}}{r} \quad \text{with} \quad r = \sqrt{x^2 + y^2 + z^2} \quad . \tag{A.29}$$

Before inserting this equation into Eq. (A.28), I'd like to examine the effect of ∇^2 to this solution:

$$\begin{aligned}\nabla^2\frac{e^{\mathtt{i}kr}}{r} &= \frac{1}{r}\,\nabla^2 e^{\mathtt{i}kr} + 2\left(\nabla\frac{1}{r}\right)\cdot\left(\nabla e^{\mathtt{i}kr}\right) + e^{\mathtt{i}kr}\,\nabla^2\frac{1}{r}\\ &= -\frac{k^2}{r}\,e^{\mathtt{i}kr} - 4\pi\,e^{\mathtt{i}kr}\,\delta(\mathbf{r})\end{aligned} \tag{A.30}$$

Here, the only the term, which can not solved by pure intuition, is $\nabla^2 r^{-1}$. That's why I will show a short calculation, which shows its solution:

$$\int_\Omega \nabla^2\frac{1}{|\mathbf{r}-\mathbf{r}'|}\,d\Omega' \quad\Longrightarrow\quad \int_\Omega \nabla\cdot\nabla\frac{1}{|\mathbf{r}-\mathbf{r}'|}\,d\Omega' = \oint_{\partial\Omega'=\Gamma'} \mathbf{n}\cdot\nabla\frac{1}{|\mathbf{r}-\mathbf{r}'|}\,d\Gamma' \quad .$$

Now, the surface integration will be done over a sphere with the center point $\mathbf{r}'$ and the radius $|\mathbf{r}-\mathbf{r}'|$. This leads to

$$\begin{aligned} d\Gamma' &= |\mathbf{r}-\mathbf{r}'|^2\sin\vartheta'\,d\varphi'\,d\vartheta'\\ \mathbf{n}\cdot\nabla'\frac{1}{|\mathbf{r}-\mathbf{r}'|} &= -\partial_{|\mathbf{r}-\mathbf{r}'|}\frac{1}{|\mathbf{r}-\mathbf{r}'|} = \frac{1}{|\mathbf{r}-\mathbf{r}'|^2}\\ \Longrightarrow\qquad \int_0^\pi\int_0^{2\pi}\frac{1}{|\mathbf{r}-\mathbf{r}'|^2}\,|\mathbf{r}-\mathbf{r}'|^2\sin\vartheta\,d\varphi\,d\vartheta &= -\,4\pi \quad .\end{aligned}$$

With the finding of Eq. (A.30), the approach Eq. (A.29) for the Hertzian dipole can be validated, because the wave equation (A.28) yields

$$\text{for} \quad r \neq 0 \qquad \left(\nabla^2 + k^2\right) C(\omega)\, \frac{e^{\mathtt{i}kr}}{r} = 0 \tag{A.31}$$

$$\text{for} \quad r = 0 \qquad -4\pi\, e^{\mathtt{i}kr}\, C(\omega)\, \delta(\mathbf{r}) = -\frac{J(\omega)\, \delta(\mathbf{r})}{\mathtt{i}\omega\varepsilon}$$

$$\Longrightarrow \qquad C(\omega) = \frac{J(\omega)}{4\pi\, \mathtt{i}\omega\varepsilon} \quad . \tag{A.32}$$

In a last step, I will show the solution of the electrical field for the Hertzian dipole using the Hertzian potential. For this purpose, all relevant equations are transformed into spherical coordinates, which leads to the representation of the Hertzian potential

$$\boldsymbol{\pi}_{\text{Hertz}} = \begin{pmatrix} \pi_r \\ \pi_\vartheta \\ \pi_\varphi \end{pmatrix} = \begin{pmatrix} \pi_z\, \cos\vartheta \\ -\pi_z\, \sin\vartheta \\ 0 \end{pmatrix} \quad . \tag{A.33}$$

Furthermore, Eq. (A.25) yields

$$\tilde{E}_r = k^2 \pi_r + \partial_r \nabla \cdot \boldsymbol{\pi}_{\text{Hertz}} \tag{A.34}$$

$$\tilde{E}_\vartheta = k^2 \pi_\vartheta + \frac{1}{r}\, \partial_\vartheta \nabla \cdot \boldsymbol{\pi}_{\text{Hertz}} \tag{A.35}$$

$$\tilde{E}_\varphi = k^2 \pi_\varphi + \frac{1}{r\, \sin\vartheta}\, \partial_\varphi \nabla \cdot \boldsymbol{\pi}_{\text{Hertz}} \quad , \tag{A.36}$$

where

$$\nabla \cdot \boldsymbol{\pi}_{\text{Hertz}} = \frac{1}{r^2}\, \partial_r (r^2\, \pi_r) + \frac{1}{r\, \sin\vartheta}\, \partial_\vartheta (\sin\vartheta\, \pi_\vartheta) \tag{A.37}$$

$$= -C(\omega)\, \cos\vartheta\, e^{-\mathtt{i}\,k\,r} \left(\frac{\mathtt{i}\,k}{r} + \frac{1}{r^2} \right) \quad . \tag{A.38}$$

Then, the solution of the electrical field in spherical coordinates is given as

$$E_r = \frac{2\, J(\omega)\, \cos\vartheta}{4\,\pi\,\mathtt{i}\,\omega\,\varepsilon}\, e^{-\mathtt{i}\,k\,r} \left(\frac{1}{r^3} + \frac{\mathtt{i}\,k}{r^2} \right) \tag{A.39}$$

$$E_\vartheta = \frac{J(\omega)\, \sin\vartheta}{4\,\pi\,\mathtt{i}\,\omega\,\varepsilon}\, e^{-\mathtt{i}\,k\,r} \left(\frac{1}{r^3} + \frac{\mathtt{i}\,k}{r^2} - \frac{k^2}{r} \right) \tag{A.40}$$

$$E_\varphi = 0 \quad . \tag{A.41}$$

This corresponds to the standard solution of the Hertzian dipole (Balanis, 1997; Kraus and Marhefka, 2002).

Vertical Dipole in a Horizontally Layered Medium

The derivation of the transition conditions for the vertical dipole in a horizontally layered medium will be given. Here, the Hertzian potential for the vertical dipole is defined as $\boldsymbol{\pi}_e = (0, 0, \pi_z)$ and the interface are located in the x-y-plane, which leads to a normal vector on the interfaces as $\mathbf{n} = (0, 0, 1)$.

The transition conditions for the Hertzian potential can be derived from the condition for the electric and magnetic field given as

$$(\mathbf{E}_2 - \mathbf{E}_1) \times \mathbf{n} = 0 \tag{A.42}$$

$$\text{and} \quad (\mathbf{H}_2 - \mathbf{H}_1) \times \mathbf{n} = \mathbf{J}_{\text{surface}} \quad , \tag{A.43}$$

where the subscript denotes the field in one of the neighboring half-spaces. $\mathbf{J}_{\text{surface}}$ represents the surface current densities, which are set to zero in the following analysis.

Now, Eq. (A.25) and the transition condition Eq. (A.42) leads to

$$\begin{aligned} & E_{x,1} = E_{x,2} \quad \text{and} \quad E_{y,1} = E_{y,2} \\ \Longrightarrow \quad & \partial_x \partial_z \pi_{z,1} = \partial_x \partial_z \pi_{z,2} \quad \text{and} \quad \partial_y \partial_z \pi_{z,1} = \partial_y \partial_z \pi_{z,2} \\ \Longrightarrow \quad & \partial_z \pi_{z,1} = \partial_z \pi_{z,2} \quad . \end{aligned} \tag{A.44}$$

Furthermore, Eq. (A.26) and the transition condition Eq. (A.42) leads to

$$\begin{aligned} & H_{x,1} = H_{x,2} \quad \text{and} \quad H_{y,1} = H_{y,2} \\ \Longrightarrow \quad & \mathtt{i}\,\omega\,\varepsilon_1\,\partial_y \pi_{z,1} = \mathtt{i}\,\omega\,\varepsilon_2\,\partial_y \pi_{z,2} \quad \text{and} \quad \mathtt{i}\,\omega\,\varepsilon_1\,\partial_x \pi_{z,1} = \mathtt{i}\,\omega\,\varepsilon_2\,\partial_x \pi_{z,2} \\ \Longrightarrow \quad & \varepsilon_1\,\pi_{z,1} = \varepsilon_2\,\pi_{z,2} \end{aligned} \tag{A.45}$$

In the following step, the transition conditions for the adjoint eigenfunctions are derived, using the definition for these function given as

$$\big(\mathcal{L}u(z), v(z)\big) := \int_\Omega \mathcal{L}u(z)\;\bar{v}(z)\,d\Omega = \int_\Omega u(z)\;\mathcal{L}^\star \bar{v}(z)\,d\Omega =: \big(u(z), \mathcal{L}^\star v(z)\big) \tag{A.46}$$

$$\text{with} \quad \mathcal{L} = -\left(\partial_z^2 + k_j^2\right) \quad \text{and} \quad \mathcal{L}^\star = -\left(\partial_z^2 + \bar{k}_j^2\right) \quad . \tag{A.47}$$

In order to fulfill Eq. (A.46), the following calculation is set up:

$$\begin{aligned} -\int d\Omega\,\left[(\nabla^2 + k^2)\,u_z\right]\overline{v}_z &= -\int d\Omega\,\left[\nabla^2 u_z\right]\overline{v}_z - \int d\Omega\,u_z\overline{\bar{k}^2 v_z} \\ \int d\Omega\,\left[\nabla^2 u_z\right]\overline{v}_z &= \int d\Omega\,\Big(\nabla\cdot\left[(\nabla u_z)\,\overline{v}_z\right] - (\nabla u_z)\cdot(\nabla\overline{v}_z)\Big) \\ &= \int d\Omega\,\Big(\nabla\cdot\left[(\nabla u_z)\,\overline{v}_z\right] - \nabla\cdot\left[u_z(\nabla\overline{v}_z)\right] + u_z(\nabla^2\overline{v}_z)\Big) \\ (\mathcal{L}\underline{u}^z, \underline{v}^z) &= \int d\Omega\,\Big(-\nabla\cdot\left[(\nabla u_z)\,\overline{v}_z\right] + \nabla\cdot\left[u_z(\nabla\overline{v}_z)\right]\Big) + (\underline{u}^z, \mathcal{L}^*\underline{v}^z) \\ \Longrightarrow \quad 0 &= \int d\Omega\,\nabla\cdot\Big(-(\nabla u_z)\,\overline{v}_z + u_z(\nabla\overline{v}_z)\Big) = \oint_{\partial\Omega=\Gamma} d\Gamma\cdot\Big(\cdots\Big) \quad . \end{aligned}$$

This leads to a surface integral, which must equal to zero.

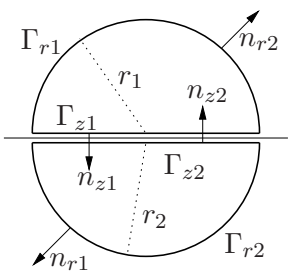

$\Gamma_1 = \Gamma_{r1} \oplus \Gamma_{z1}$
$\Gamma_2 = \Gamma_{r2} \oplus \Gamma_{z2}$

Figure A.2: *Definition for the surface integral.*

The integration surface can be defined as sketched in Fig. A.2, which consists of to half spheres and an integration along on the interface. These integration paths can be evaluated separately

$$\begin{aligned} 0 &= \oint_{\Gamma_1} d\Gamma_1\,n_1\cdot\Big(\cdots\Big)_1 + \oint_{\Gamma_2} d\Gamma_2\,n_2\cdot\Big(\cdots\Big)_2 \\ &= \int_{\Gamma_{r1}} d\Gamma_{r1}\,n_{r1}\cdot\Big(\cdots\Big)_1 + \int_{\Gamma_{z1}} d\Gamma_{z1}\,n_{z1}\cdot\Big(\cdots\Big)_1 \\ &\quad + \int_{\Gamma_{r2}} d\Gamma_{r2}\,n_{r2}\cdot\Big(\cdots\Big)_2 + \int_{\Gamma_{z2}} d\Gamma_{z2}\,n_{z2}\cdot\Big(\cdots\Big)_2 \quad , \end{aligned}$$

where the integration over the half Γ_1 and Γ_2 spheres vanishes, because r_1 and $r_2 \to \infty$. At infinity, it is assumed that the numerical value of the eigenfunctions is zero. The integrals at the interface remain. Here, it is defined that $n_{z1} = -n_{z2} = n_z$,

$n_{z2} = (0,0,1)$ and $\Gamma_{z1} = \Gamma_{z2} = \Gamma_z$, which leads to

$$
\begin{aligned}
0 &= \int_{\Gamma_z} d\Gamma_z \, n_z \cdot \Big(-(\nabla u_{z,1})\, \overline{v}_{z,1} + u_{z,1}\, (\nabla \overline{v}_{z,1}) + (\nabla u_{z,2})\, \overline{v}_{z,2} - u_{z,2}\, (\nabla \overline{v}_{z,2}) \Big) \\
&= \int_{\Gamma_z} d\Gamma_z \Big(-(\partial_z u_{z,1})\, \overline{v}_{z,1} + u_{z,1}\, (\partial_z \overline{v}_{z,1}) + (\partial_z u_{z,2})\, \overline{v}_{z,2} - u_{z,2}\, (\partial_z \overline{v}_{z,2}) \Big) \\
\overset{\text{(A.44)-(A.45)}}{\Longrightarrow} \quad 0 &= \int_{\Gamma_z} d\Gamma_z \Big((\partial_z u_{z,1}) \Big[\overline{v}_{z,2} - \overline{v}_{z,1} \Big] + u_{z,1} \Big[\partial_z \overline{v}_{z,1} - \frac{\varepsilon_1}{\varepsilon_2}\, \partial_z \overline{v}_{z,2} \Big] \Big) \\
\Longrightarrow \quad & \underline{v_{z,2} = v_{z,1}} \quad \text{and} \quad \underline{\overline{\varepsilon}_2\, \partial_z v_{z,1} = \overline{\varepsilon}_1\, \partial_z v_{z,2}}
\end{aligned}
\tag{A.48}
$$

Bibliography

al Hagrey, S. A. and Müller, C., 2000. GPR study of pore water content and salinity in sand, *Geophysical Prospecting* **44**:63–85.

Amente, G., Baker, J. M. and Reece, C. F., 2000. Estimation of soil solution electrical conductivity from bulk soil electrical conductivity in sandy soils, *Soil Science Society of America Journal* **64**:1931–1939.

Arcone, S. A., Lawson, D. E., Delany, A. J., Strasser, J. C. and Strasser, J. D., 1998. Ground-penetrating radar reflection profiling of groundwater and bedrock in an area of discontinuous permafrost, *Geophysics* **63**:1573–1584.

Artmann, K. 1948. Berechnung der Seitenversetzung des totalreflektierten Strahls, *Annalen der Physik* **437**:87–102.

Balanis, C. A. 1997. *Antenna Theory: Analysis and Design*, Wiley New York.

Birchak, J. R., Gardner, C. G., Hipp, J. E. and Victor, J. M., 1974. High dielectric constant mircrowave probes for sensing soil moisture, *Proceedings of the IEEE* **62**:93–98.

Bittelli, M., Salvatorelli, F. and Pisa, P. R., 2008. Correction of TDR-based soil water content measurements in conductive soils, *Geoderma* **143**:133–142.

Bohidar, R. N. and Hermance, J. F., 2002. The GPR refraction method, *Geophysics* **67**:1474–1485.

Bradford, J. H. 2006. Applying reflection tomography in the postmigration domain to multifold ground-penetrating radar data, *Geophysics* **71**:doi:10.1190/12159051.

Bradford, J. H. and Deeds, J. C., 2006. Ground-penetrating radar theory and application of thin-bed offset-dependent reflectivity, *Geophysics* **71**:doi:10.1190/1.2194524.

Cassidy, N. J. 2007. A review of practical numerical modelling methods for the advanced interpretation of ground-penetrating radar in near-surface environments, *Near Surface Geophysics* **5**:5–12.

Castle, R. J. 1994. A theory of normal moveout, *Geophysics* **59**:983–999.

Chen, C., Berini, P., Feng, D., Tanev, S. and Tzolov, V. P., 2000. Efficient and accurate numerical analysis of multilayer planar optical waveguides in lossy anisotropic media, *Optics Express* **7**:260–272.

Chen, H.-W. and Huang, T.-M., 1998. Finite-difference time-domain simulation of GPR data, *Journal of Applied Geophysics* **40**:139–163.

Chen, Y. and Or, D., 2006a. Effects of maxwell-wagner polarization on soil complex dielectric permittivity under variable temperature and electrical conductivity, *Water Resources Research* **42**:doi:10.1029/2005WR004590.

Chen, Y. and Or, D., 2006b. Geometrical factors and interfacial processes affecting complex permittivity of partially saturated porous media, *Water Resources Research* **42**:doi:10.1029/2005WR004744.

Chew, W. C. 1990. *Waves and Fields in Inhomogeneous Media*, IEEE press, New York.

Chiu, K. W. and Quinn, J. J., 1972. On the Goos-Hänchen effect: A simple example of a time delay scattering process, *American Journal of Physics* **40**:1847–1851.

Clement, W. P. and Knoll, M. D., 2006. Traveltime inversion of vertical radar profiles, *Geophysics* **71**:doi:10.1190/1.2194527.

Cole, K. S. and Cole, R. H., 1941. Dispersion and absorption in dielectrics, *Journal of Chemical Physics* **9**:341–351.

Davis, J. L. and Annan, A. P., 1989. Ground-penetrating radar for high-resolution mapping of soil and rock stratigraphy, *Geophysical Prospecting* **37**:531–551.

de Loor, G. P. 1968. Dielectric properties of heterogeneous mixtures containing water, *Journal of Microwave Power* **3**:67–73.

Debye, P. 1929. *Polare Molekeln*, Hirzel, Leipzig.

Dix, C. H. 1955. Seismic velocities from surface measurements, *Geophysics* **20**:68–86.

Dobson, M. C., Ulaby, F. T., Hallikainen, M. T. and El-Rayes, M. A., 1985. Microwave dielectric behavior of wet soils - part II: Dielectric mixing models, *IEEE Transactions on Geoscience and Remote Sensing* **GE-23**:35–46.

Drude, P. 1900. Zur Elektronentheorie der Metalle, *Annalen der Physik* **306**:566–613.

Dudley, D. G. 1994. *Mathematical Foundations for Electromagnetic Theory*, IEEE Press.

Ferré, T. P. A., Rudolph, D. L. and Kachanoski, R. G., 2003. The electrical conductivity response of a profiling time-domain reflectometry probe, *Soil Science Society of America Journal* **67**:494–496.

Fisher, E., McMechan, G. A. and Annan, A. P., 1992. Acquisition and processing of wide-aperture ground-penetrating radar data, *Geophysics* **57**:495–504.

Fuentes, C., Haverkamp, R. and Parlange, J.-Y., 1992. Parameter constraints on closed-form soilwater relationships, *Journal of Hydrology* **134**:117–142.

Galagedara, L. W., Redman, J. D., Parking, G. W., Annan, A. P. and Endres, A. L., 2005. Numerical modeling of gpr to determine the direct ground wave sampling depth, *Vadoze Zone Journal* **4**:1096–1106.

Garambois, S., Sénéchal, P. and Perroud, H., 2002. On the use of combined geophysical methods to assess water content and water conductivity of near-surface formation, *Journal of Hydrology* **259**:32–48.

Gerhards, H., Wollschläger, U., Yu, Q., Shiwek, P., Pan, X. and Roth, K., 2008. Continuous and simultaneous measurement of reflector depth and average soil-water content with multichannel ground-penetrating radar, *Geophysics* **73**:doi:10.1190/1.2943669.

Goodman, D. 1994. Ground-penetrating radar simulation in engineering and archaeology, *Geophysics* **59**:224–232.

Goos, F. and Hänchen, H., 1947. Ein neuer fundamentaler Versuch zur Totalreflektion, *Annalen der Physik* **436**:333–346.

Grasmueck, M. 1996. 3-D ground-penetrating radar applied to fracture imaging in gneiss, *Geophysics* **61**:1050–1064.

Greaves, R. J., Lesmes, D. P., Lee, J. M. and Toköz, M. N., 1996. Velocity variations and water content estimated from multi-offset, ground-penetrating radar, *Geophysics* **61**:683–695.

Grégoire, C. and Hollender, F., 2004. Discontinuity characterization by the inversion of the spectral content of ground-penetrating radar (GPR) reflections - application of the jonscher model, *Geophysics* **69**:1414–1424.

Grote, K., Hubbard, S. and Rubin, Y., 2003. Field scale estimation of volumetric water content using ground-penetrating radar ground wave techniques, *Water Resources Research* **39**:1321.

Hansen, T. B. and Johansen, P. M., 2000. Inversion scheme for ground penetrating radar that takes into account the planar air-soil interface, *IEEE Transactions on Geoscience and Remote Sensing* **38**:496–506.

Hansma, P. K. and Tersoff, J., 1987. Scanning tunneling microscopy, *Journal of Applied Physics* **61**:R1–R23.

Hanson, G. W. 2004a. Dyadic eigenfunctions in natural modes for hybrid waves in planar media, *IEEE Transactions on Antennas and Propagation* **52**:941–947.

Hanson, G. W. 2004b. Dyadic green's function for multilayerd planar medium - a dyadic eigenfunction approach, *IEEE Transactions on Antennas and Propagation* **52**:3350–3356.

Herkelrath, W. N., Hamburg, S. P. and Murphy, F., 1991. Automatic, real-time monitoring of soil moisture in a remote field area with time domain reflectometry, *Water Resources Research* **27**:857–864.

Hinkel, K. M., Doolittle, J. A., Bockheim, J. G., Nelson, F. E., Paetzold, R., Kimble, J. M. and Travis, R., 2001. Detection of subsurface permafrost features with ground-penetrating radar, barrow, alaska, *Permafrost and Periglacial Processes* **12**:179–190.

Hugenschmidt, J., Partl, M. N. and de Witte, H., 1998. GPR inspection of mountain motorway in switzerland, *Journal of Applied Geophysics* **40**:95–104.

Huisman, J. A., Hubbard, S. S., Redman, J. D. and Annan, A. P., 2003. Measuring soil water content with ground penetrating radar: A review, *Vadose Zone Journal* **2**:476–491.

Ishida, T., Makino, T. and Wang, C., 2000. Dielectric-relaxation spectroskopy of kaolinite, montmorillonite, allophane, and imogolite under moist conditions, *Clay and Clay Minerals* **48**:75–84.

Jones, D. S. 1994. *Methods in Electromagnetic Wave Propagation*, IEEE Press.

Jonscher, A. K. 1977. The 'universal' dielectric response, *Nature* **267**:673–679.

Kaatze, U. 1989. Complex permittivity of water as a function of frequency and temperature, *Journal of Chemical and Engeneering Data* **34**:371–374.

Kraus, J. D. and Marhefka, R. J., 2002. *Antennas for All Applications*, McGraw-Hill.

Kung, K.-J. S. and Lu, Z.-B., 1993. Using ground-penetrating radar to detect layers of discontinuous dielectric constant, *Soil Science Society of America Journal* **57**:335–340.

Lambot, S. 2003. *Hydrogeophysical characterization of soil using ground penetrating radar*, PhD thesis, Université catholique de Louvain; Faculté d'Ingéniere Biologique, Agronomique et Environnementale; Département des Sciences du Milieu et de l'Aménagement du Teritoire.

Lambot, S., Slob, E. C., van den Bosch, I., Stockbroeckx, B. and Vanclooster, B. S. M., 2004. Estimating soil electric properties from monostatic ground-penetrating radar signal inversion in the frequency domain, *Water Resources Research* **40**:doi:10.1029/2003WR002095.

Lambot, S., Weihermüller, L., Huisman, J. A., Vereecken, H., Vanclooster, M. and Slob, E. C., 2006. Analysis of air-launched ground-penetrating radar techniques to measure the soil surface water content, *Water Resources Research* **42**:doi:10.1029/2006WR005097.

Lampe, B., Holliger, K. and Green, A. G., 2003. A finite-difference time domain simulation tool for ground-penetrating radar antennas, *Geophysics* **68**:971–987.

Levin, F. K. 1990. Reflection from a dippling plane - transversely isotropic solid, *Geophysics* **55**:851–855.

Löwy, H. 1912. Eine elektrodynamische Methode zur Erforschung des Erdinneren, *Jahrbuch der drahtlosen Telegraphie und Telephonie* **5**:386–390.

Löwy, H. 1927. Über das Grundproblem der angewandten Geophysik und den elektrischen Nachweis von Erdöl, *Die Naturwissenschaften* **15**:921–928.

Lunt, I. A., Hubbard, S. S. and Rubin, Y., 2005. Soil moisture content estimation using ground-penetrating radar reflection data, *Journal of Hydrology* **307**:254–269.

Maetzler, C. 1998. Mircowave permittivity of dry sand, *IEEE Transactions on Geoscience and Remote Sensing* **36**:317–319.

Meincke, P. 2001. Linear GPR inversion for lossy soil and a planar air-soil interface, *IEEE Transactions on Geoscience and Remote Sensing* **39**:2713–2721.

Moorman, B. J., Robinson, S. D. and Burgess, M. M., 2003. Imaging periglacial conditions with ground-penetrating radar, *Permafrost and Periglacial Processes* **14**:319–329.

Neal, A. 2004. Ground-penetrating radar und its use in sedimentology: principles, problems and progress, *Earth-Science Reviews* **66**:261–330.

Neidell, N. S. 1971. Semblance and other coherency measures for multichannel data, *Geophysics* **36**:482–497.

Nguyen, B.-L., Bruining, J., Slob, E. C. and Hopman, V., 1998. Delination of air/water transition zone from GPR data, *SPE Reservoir Evaluation and Engineering* **1**:319–327.

Nigmatullin, R. R. and Ryabov, Y. E., 1997. Cole-davidson dielectric relaxation as a self-similar relaxation process, *Physics of the Solid State* **39**:87–90.

Nolan, M. and Fatland, D. R., 2003. Penetration depth as a dinsar observable and proxy for soil moisture, *IEEE Transactions on Geoscience and Remote Sensing* **41**:532–537.

Nuzzo, L., Leucci, G., Negri, S., Carrazzo, M. T. and Quarta, T., 2002. Application of 3D visualization techniques in the analysis of gpr data for archaeology, *Annals of Geophysics* **45**:321–337.

Olhoeft, G. R. and Capron, D. E., 1994. Petrophysical causes of electromagnetic dispersion, *Proceedings of the 5th International Conference on Ground Penetrating Radar*, Kitchener, Ontario, Canada, S. 145–152.

Ori, G. G. and Ogliani, F., 1996. Potentiality of the ground-penetrating radar for the analysis of the stratigraphy and sedimentology of mars, *Planetary and Space Science* **44**:1303–1315.

Peplinski, N. R., Ulaby, F. T. and Dobson, M. C., 1995. Dielectric properties of soils in the 0.3-1.3 ghz range, *IEEE Transactions on Geoscience and Remote Sensing* **33**:803–807.

Press, W. H., Teukolsky, S. A., Vetterling, W. T. and Flannery, B., 1994. *Numerical Recipes in C*, Cambridge University Press.

Reddick, R. C., Warmack, R. J. and Ferrell, T. L., 1989. New form of scanning optical microscopy, *Physcal Review B* **39**:767–770.

Reppert, P. M., Morgan, F. D. and Toksöz, M. N., 2000. Dielectric constant determination using ground-penetrating radar reflection coefficients, *Journal of Applied Geophysics* **43**:189–197.

Richards, L. A. 1931. Capillary conduction of liquids through porous media, *Physics* **1**:318–333.

Roberts, R. L. and Daniels, J. J., 1997. Modeling near-field GPR in three dimensions using the FDTD method, *Geophysics* **62**:1114–1126.

Robinson, D. A., Jones, S. B., Wraith, J. M., Or, D. and Friedman, S. P., 2003. A review of advances in dielectric and electrical conductivity measurements in soils using time domain reflectometry, *Vadoze Zone Journal* **2**:444–475.

Roth, K., Schulin, R., Flühler, H. and Attinger, W., 1990. Calibration of time domain reflectometry for water content measurement using a composite dielectric approach, *Water Resources Research* **26**:2267–2273.

Rucker, D. F. and Ferré, T. P. A., 2003. Near-surface water content estimation with borehole ground penetrating radar using critically refracted waves, *Vadoze Zone Journal* **2**:247–252.

Samouëlian, A., Cousin, I., Tabbagh, A., Bruand, A. and Richard, G., 2005. Electrical resistivity survey in soil science: a review, *Soil and Tillage Research* **83**:173–193.

Sommerfeld, A. 1926. Über die Ausbreitung der Wellen in der drahtlosen Telegraphie, *Annalen der Physik* **386**:1135–1153.

Sposito, G. and Prost, R., 1982. Structure of water absorbed on smectites, *Chemical Reviews* **82**:553–573.

Strobbia, C. and Cassiani, G., 2007. Multilayer ground-penetrating radar guided waves in shallow soil layer for estimating soil water content, *Geophysics* **72**:doi:10.1190/1.2716374.

Taflove, A. and Hagness, S. C., 2000. *Computational Electrodynamics, The finite-difference time-domain method*, Artech House.

Tillard, S. and Dubois, J.-C., 1995. Analysis of GPR data: wave propagation velocity determination, *Journal of Applied Geophysics* **33**:77–91.

Tip, A. 2004. Linear dispersive dielectrics as limits of drude-lorentz systems, *Physical Review E* **69**:doi:10.1103/PhysRevE.69.016610.

Topp, G. C. 1980. Electromagnetic determination of soil water content: Measurements in coaxial transmission lines, *Water Resources Research* **16**:574–582.

Turner, G. 1994. Modelling antenna-ground interactions, *Proceedings of the 5th International Conference on Ground Penetrating Radar*, Kitchener, Ontario, Canada, S. 205–221.

Ulaby, F. T., Moore, R. K. and Fung, A. K., 1982. *Microwave Remote Sensing*, Vol. 2, Addison-Wesley, Reading, MA.

van der Kruk, J. 2006. Properties of surface waveguides derived from inversion of fundamental and higher mode dispersive GPR data, *IEEE Transactions on Geoscience and Remote Sensing* **44**:2908–2915.

van der Kruk, J., Arcone, S. A. and Liu, L., 2007. Fundamental and higher mode inversion of dispered GPR waves propagating in an ice layer, *IEEE Transactions on Geoscience and Remote Sensing* **45**:2483–2491.

van Genuchten, M. T. 1980. A closed-form for predicting the hydraulic conductivity of unsaturated soils, *Soil Science Society of America Journal* **44**:892–898.

Vidulich, G. A., Evans, D. F. and Kay, R. L., 1967. The dielectric constant of water and heavy water between 0 and 40°, *Journal of Physical Chemistry* **71**:656–662.

Vogel, H. J. and Roth, K., 1998. A new approach for determining effective soil hydraulic functions, *European Journal of Soil Science* **49**:547–556.

Volakis, J., Chatterjee, A. and Kempel, L., 1998. *Finite Element Method for Electromagnetics*, IEEE Press.

Wagner, K. W. 1913. Zur Theorie der unvollkommenen Dielektrika, *Annalen der Physik* **345**:817–855.

Wagner, K. W. 1914. Erklärung der dielektrischen Nachwirkungsvorgänge auf Grund Maxwellscher Vorstellungen, *Electrical Engineering (Archiv fur Elektrotechnik)* **2**:371–387.

Wait, J. R. 1998. The ancient and modern history of EM ground-wave propgation, *IEEE Antennas and Propagation Magazine* **40**:7–24.

Weast, R. C. (ed.) 1974. *Handbook of Chemistry and Physics*, CRC Press.

Wollschläger, U. and Roth, K., 2005. Estimation of temporal changes of volumetric soil water content from ground-penetrating radar reflections, *Subsurface Sensing Technologies and Applications* **6**:207–218.

Yelf, R. 2004. Where is true time zero?, *Proceedings of the 10th International Conference on Ground Penetrating Radar*, Delft, Netherlands, S. 279–282.

Yilmaz, Ö. 2001. *Seismic Data Analysis*, Society of Exploration Geophysicists, Tusla.

Zenneck, J. 1907. Über die Fortpflanzung ebener elektromagnetischer Wellen längs einer ebenen Leiterfläche und ihrer Beziehung zur drahtlosen Telegraphie, *Annalen der Physik* **328**:846–866.

Acknowledgments

The difference between try and triumph
is just a little umph!

(unknown author)

This work would not have been possible, if I had no personal support of several people as well as the financial support of the *Deutsche Forschungsgemeinschaft* (through project RO 1080/10-2). To honor all, who accompanied and helped me on the journey to this thesis, I would like to say thanks to

- *Prof. Kurt Roth* who offers me the opportunity to work on theoretical aspects concerning ground penetrating radar. I would like to thank for all discussions, the support and especially for the possibility for follow own ideas and concepts.
- *Dr. Ute Wollschläger* for all discussions, comments, the scientific help on the practical and experimental aspects of this work and also for all hints concerning the language and the content of this thesis.
- *Prof. Bernd Jähne* who agreed to be the second referee for my thesis.
- *Dr. Benedikt Oswald* who led the first steps of this thesis.
- *Felix Heimann* who worked with me on the `PG` software-project.
- *Dr. Andreas Bayer* and *Klaus Schneider* who helped me with the initial steps as well as with crucial things concerning linux and programming.
- *all colleagues of the soil physics group in Heidelberg* for the friendly atmosphere, the jokes and the discussions on scientific and non-scientific concerns.
- *the Taekwondo group of the university of Heidelberg* for the hours of recreation by doing this marvelous sport.

Special thanks I would like to address to *Sandra* who was very patient and heartily during the exhausting time of writing. Thanks not only for correcting the language, but just by lightening my life with humor, kindness and insightful discussions.

Finally, I have to state that without the support of my family I would not have reached so far with my work. Thanks a lot to my mother as well as to my two siblings for the confidence in me.

For all who are not named here but have given some kind of contribution to this work, for example with scientific hints, personal discussions or some refreshing and constructive cake, I hope I can give personally my cordial thanks to you, if you have not already received them.